

**DEVELOPMENT OF AN ONLINE TRACK FINDING ALGORITHM
FOR THE PANDA LUMINOSITY DETECTOR
AND
SEARCH FOR THE DECAY CHANNEL $e^+e^- \rightarrow h_c\eta\pi^+\pi^-$ AT THE
CENTER OF MASS ENERGY OF 4.6 GeV AT BESIII**

Dissertation
zur Erlangung des Grades eines
Doktors der Naturwissenschaften
in der Fakultät für Physik und Astronomie
der Ruhr-Universität Bochum

vorgelegt von
Stephan Maldaner
aus Mainz

Bochum, September 2020

Abstract

Quantum chromodynamics is the current quantum field theory used to describe the strong interaction. For a long time it has been able to successfully explain all newly discovered hadron states. During this time it was possible to understand all hadron states as baryons and mesons with a basic configuration of qqq and $q\bar{q}$ respectively. Despite this quantum chromodynamics has always allowed for more complex internal structures even though they have been difficult to identify. These so called exotic states are very interesting as they allow for additional testing of quantum chromodynamics. The charmonium sector provides an excellent environment for the search of these exotic hadron states. The reason for this is that the charm quark is heavy causing the states to be more narrow and therefore have little overlap. In recent years many candidates for exotic states such as the $X(3872)$, $Y(4260)$, $Z_c(3900)^{\pm/0}$ and $Z_c(4020)^{\pm/0}$ have been found in the charmonium sector. Identifying their inner structure is an important task which needs dedicated studies of their decay properties and line shapes. Hence, searching for more resonances in the charmonium sector is necessary in order to extend our knowledge about the underlying theory. The future PANDA experiment in Darmstadt and the BESIII experiment in Beijing are crucial and complementary experiments for this task.

The PANDA experiment will utilize a high precision antiproton beam and a proton target for searching new resonances and investigating known states. PANDA will provide the energy scan method which allows for the determination of line shapes of resonances with high precision. To normalize the separate scan points of these measurements it is necessary to exactly determine the luminosity. Therefore a dedicated luminosity detector will be used at the PANDA experiment. It has four layers of active silicon pixel sensors to measure the tracks of elastically scattered antiprotons in an angular range from 3.5 mrad to 8 mrad. As the amount of data collected in this measurement is very large it must be processed quickly to have the possibility to reduce the amount of data stored for further analysis. For this processing an online track finding algorithm was developed based on the principle of the cellular automaton. The algorithm has been implemented on a GPU and CPU and characterized in terms of processing speed, efficiency and ghost track percentages.

In the second part of this thesis a new resonance is searched for at the BESIII experiment. BESIII is an e^+e^- collider experiment running for almost 10 years. Some examples for the interesting resonances which are observed at BESIII are the charmonium-like states $Z_c(3900)^{\pm/0}$ and $Z_c(4020)^{\pm/0}$ which have been seen decaying to both open and hidden charm final states. The decays $Z_c(3900)^{\pm/0} \rightarrow J/\psi\pi^{\pm,0}$ and $Z_c(4020)^{\pm/0} \rightarrow h_c\pi^{\pm/0}$ suggest that both sets of states belong to an isospin triplet. If so, one would expect that an isospin singlet state decaying to $J/\psi\eta$ or $h_c\eta$ also exists. For this reason the reaction channel $e^+e^- \rightarrow h_c\eta\pi^+\pi^-$ has been used to search for a resonant structure decaying into $h_c\eta$. This decay has been searched for in the high statistic dataset of the BESIII collaboration at a center of mass energy of 4.6 GeV. As no significant signal was observed, an upper limit at 90% confidence level is established for the reaction channel $e^+e^- \rightarrow h_c\eta\pi^+\pi^-$. Since the number for reconstructed events does not allow for looking into the subsystem no conclusion can be drawn if an isospin singlet state can be produced in this channel.

Kurzfassung

Die aktuell zur Beschreibung der starken Wechselwirkung verwendete Quantenfeldtheorie ist die Quantenchromodynamik. Diese war lange Zeit dazu in der Lage alle neu entdeckten Hadronenzustände zu erklären, da diese entweder als Baryonen und Mesonen mit den jeweiligen Basiskonfigurationen qqq und $q\bar{q}$ identifiziert werden konnten. Prinzipiell erlaubte die Quantenchromodynamik schon immer auch Zustände mit komplexeren inneren Strukturen. Diese sind aber schwierig zweifelsfrei nachzuweisen. Was diese sogenannten exotischen Zustände sehr interessant macht ist, dass sie zusätzliche Möglichkeiten bieten die Quantenchromodynamik zu überprüfen. Der Charmoniumsektor ist eine ausgezeichnete Umgebung um nach solchen Hadronenzuständen zu suchen, denn die große Masse des Charm Quark führt zu schmaleren und weniger überlappenden Zuständen. In den letzten Jahren wurden im Charmoniumsektor viele Kandidaten für exotische Zustände gefunden wie zum Beispiel die Zustände $X(3872)$, $Y(4260)$, $Z_c(3900)^{\pm/0}$ und $Z_c(4020)^{\pm/0}$. Um die inneren Strukturen solcher Zustände zu identifizieren, müssen ihre Zerfallseigenschaften gemessen und die Linienformen bestimmt werden. Zudem ist die Suche nach weiteren Resonanzen wichtig, um unser Wissen über die Quantenchromodynamik zu erweitern. Das zukünftige \bar{P} ANDA Experiment in Darmstadt und das BESIII Experiment in Peking sind hier wichtige Experimente um diese Aufgabe zu bewältigen.

Das \bar{P} ANDA Experiment wird einen Antiprotonenstrahl mit hoher Präzision und ein Protonentarget nutzen, um nach neuen Resonanzen zu suchen und bekannte Zustände z.B. mit der Energiescan Methode präzise zu vermessen. Zur Normierung der einzelnen Messwerte wird \bar{P} ANDA die Luminosität mit einem dedizierten Luminositätsdetektor bestimmen. Dieser besitzt vier Lagen von aktiven Silizium-Pixelsensoren, um Spuren von elastisch gestreuten Antiprotonen in einem Winkelbereich von 3.5 mrad bis 8 mrad zu messen. Da die zu erwartende Datenmenge sehr groß sein wird, müssen diese Daten sehr schnell verarbeitet und gefiltert werden, um, wenn es nötig ist, nur eine Untermenge der Daten zu archivieren. Für diese Verarbeitung wurde ein Algorithmus zum Auffinden von Spuren entwickelt, der sowohl auf einer GPU als auch auf einer CPU implementiert wurde. Die Verarbeitungsgeschwindigkeit, die Effizienz und der Prozentsatz an Geisterspuren wurden verglichen.

Im zweiten Teil dieser Arbeit wurde eine neue Resonanz bei BESIII gesucht. BESIII ist ein e^+e^- Kollisionsexperiment das bereits seit fast 10 Jahren in Betrieb ist. Ein Beispiel für einige neuere interessante Resonanzen sind die charmoniumartigen Zustände $Z_c(3900)^{\pm/0}$ und $Z_c(4020)^{\pm/0}$ die mit BESIII zum ersten mal gemessen worden sind. Die Zerfälle $Z_c(3900)^{\pm/0} \rightarrow J/\psi\pi^{\pm,0}$ und $Z_c(4020)^{\pm/0} \rightarrow h_c\pi^{\pm/0}$ sind ein Hinweis darauf das jeweils beide Sammlungen von Zuständen zu einem Isospintriplett gehören. Sollte das der Fall sein würde man erwarten, dass ebenso ein Isospinsinglett Zustand existiert der zu $J/\psi\eta$ oder $h_c\eta$ zerfallen könnte. Aus diesem Grund wurde nach der Reaktion $e^+e^- \rightarrow h_c\eta\pi^+\pi^-$ bei einer Schwerpunktsenergie von 4.6 GeV gesucht, wo eine resonante Struktur im $h_c\eta$ subsystem auftreten könnte. Da kein signifikantes Signal beobachtet wurde, wurde eine obere Grenze für den Wirkungsquerschnitt des Kanals $e^+e^- \rightarrow h_c\eta\pi^+\pi^-$ mit einer statistischen Sicherheit von 90% bestimmt. Aufgrund der geringen Zahl von rekonstruierten Ereignissen kann jedoch keine Aussage getroffen werden, ob ein Isospin-Singulett-Zustand in dieser Reaktion erzeugt werden kann.

Contents

1	Motivation	1
2	Quantum Chromodynamics	5
2.1	The QCD Lagrangian	5
2.2	Light Meson Systems	8
2.3	Charmonium Spectroscopy	10
3	Charmonium Spectroscopy Experiments	15
3.1	The $\bar{\text{PANDA}}$ Experiment	15
3.2	The BESIII Experiment	25
4	Luminosity Determination at $\bar{\text{PANDA}}$	33
4.1	Luminosity	33
4.2	Luminosity Measurement at $\bar{\text{PANDA}}$	34
4.3	The Luminosity Detector	39
4.4	Sensors	43
4.5	DAQ Scheme	46
5	CPU and GPU Architectures	49
5.1	CPU Architecture	49
5.2	GPU Architecture	54
6	Online Track Finding	65
6.1	Online track finding at other experiments	65
6.2	Track Finding Algorithm and Implementation Platform	67
6.3	Triplet Reconstruction	69
6.4	Implementation	71
7	Performance of the track finding algorithm	77
7.1	Efficiency and ghost tracks	78
7.2	Float versus Double precision performance	86
7.3	Processing times	87
7.4	Summary and Discussion	93
8	Event selection for the decay $e^+e^- \rightarrow h_c\eta\pi^+\pi^-$ at BESIII	95
8.1	Datasets and Monte Carlo Simulations	95
8.2	Criteria for Particle Selection	96
8.3	Event Selection	98
8.4	Background Estimation	103

9	Results of the Analysis	107
9.1	Correctness	107
9.2	Method for cross section determination	108
9.3	Efficiency and Resolution	111
9.4	Channel Cross Feed	112
9.5	Cross section	113
9.6	Systematic Uncertainties	114
9.7	Initial State Radiation and Vacuum Polarization	122
9.8	Upper Limit	127
9.9	Summary and Discussion	129
10	Summary	133
A	Track Reconstruction Efficiencies	151

Chapter 1

Motivation

The currently accepted model describing our knowledge in the field of elementary particles is the standard model of particle physics. Its basic building blocks are grouped as 17 different particles organized in three categories as shown in figure 1.1. These categories are quarks, leptons and gauge bosons. Particles out of the first two groups, quarks as well as leptons, are spin $S = \hbar/2$ particles and therefore fermions. They are further categorized in three generations which are clearly separated by their mass. The different quarks can be identified by their flavor of which there are currently 6 known types: up (u), down (d), strange (s), charm (c), bottom (b) and top (t). The latter 4 differ significantly in mass and have distinct quantum numbers associated with their flavor. However, the mass of the up and down quarks is very similar and to account for this symmetry they carry a quantum number called isospin which is described by an SU(2) group. For leptons there are three quantum numbers. The electron lepton number identifies electrons, positrons, electron neutrino and electron anti-neutrino while muon and tau lepton number classify the rest of leptons accordingly. The first and lightest generation of quarks and leptons contains the constituents of natural matter while the second generation particles only form unstable states. In the third generation the heaviest of elementary particles are grouped together. All quarks except the top quark form bound states. The reason why the top quark does not form bound states is its short life time which is caused by its large mass.

In the standard model these particles can interact with each other through three forces described by Quantum Field Theory (QFT)s. Each of these forces is mediated by a gauge boson. The interaction of electrically charged particles is described with Quantum Electrodynamics (QED) which is mediated by the massless photon. This masslessness results in an infinite range for this force. Its strength though is limited by a factor of $1/r^2$. The massive W^\pm and Z bosons mediate the weak interaction between weakly charged particles. A prominent example of an effect caused by the weak interaction are radioactive decays. As the name indicates the strength of it is weak compared to the other forces and its range is limited by its massive gauge bosons. To describe both the weak interaction and QED they can be unified into the electroweak theory [1, 2].

The strongest of the fundamental forces included in the standard model is the strong force described by Quantum Chromodynamics (QCD) which couples to the color charge and is mediated by the massless gluons. Color charge is carried by quarks and contrary to other mediating bosons by gluons themselves. As gluons interact with all particles carrying color they do also interact with themselves. This leads to the unique effect that the strength of the interaction increases with distance rather than decreases. At small distances it is so weak that quarks can be considered to not interact with each other

which is called asymptotic freedom. In contrast to this the increasing strength with distance makes it impossible for quarks to exist independently of each other as free quarks. Separating a quark-antiquark pair sufficiently requires so much energy that new quark antiquark pairs are generated out of energy rather than achieving a separation. Quarks and antiquarks being unable to exist independently is called confinement. Bound states of quarks are called hadrons and are effectively colorless. They are classified either as mesons with a baryon number $B = 0$ or baryons with a baryon number $B = 1$. Conventional mesons are composed of an quark antiquark pair while conventional baryons are three quark states.

Besides the gauge bosons resulting from the fundamental forces there is also the Higgs boson. Historically it has been introduced to solve the problem of the W^\pm and Z bosons being massive particles which according to gauge theory should be massless. A scalar field has thus been introduced which explains the mass through spontaneous symmetry breaking. The introduction of this field lead to the prediction of the Higgs boson in 1964 [3, 4] which has been discovered 2012 at CERN [5, 6].

Gravitation is another fundamental force but it is very weak compared to the other forces and can therefore be neglected for all scenarios in this work. Gravity can be described with a hypothetical graviton as gauge boson. However, this has not been experimentally verified yet.

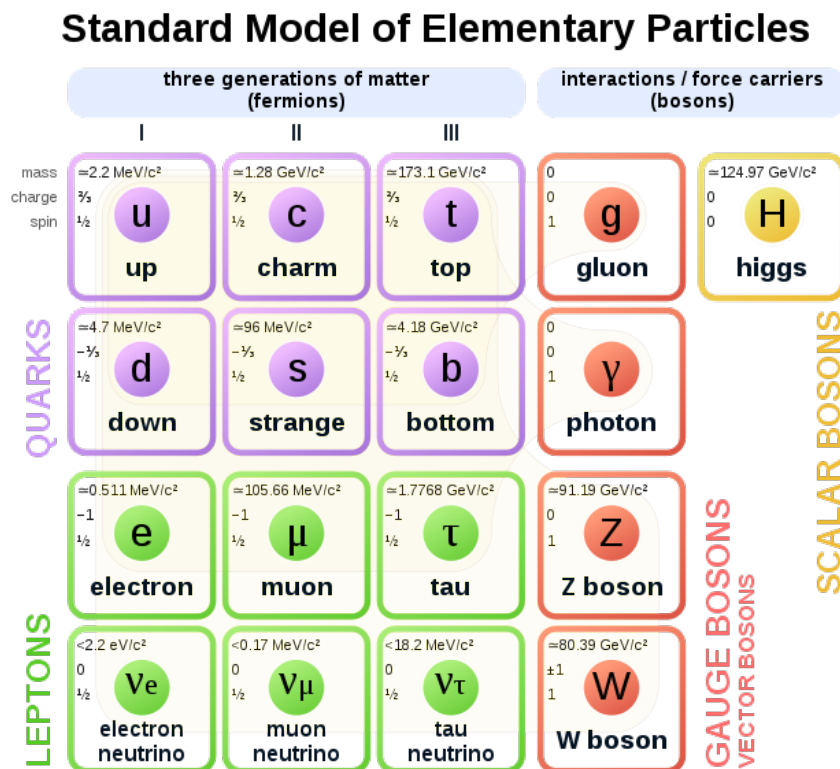


FIGURE 1.1: Standard model of elementary particles [7]. 16 particles are grouped into the three categories, quarks, leptons and gauge bosons. The higgs boson is a scalar boson which does not fit into the other categories.

Beside the commonly found mesons and baryons composed out of a quark antiquark pair and three quarks respectively, QCD also allows for other states made of different components [8]. Examples for these are tetra- and pentaquarks states containing two quarks and 2 antiquarks (tetra) and four quarks and an antiquark (penta), glueballs which are bound states entirely built out of gluons or hybrid states made of a quark-antiquark pair and additional gluons. These states are called exotic states as there had been no evidence for their existence for a long time and only conventional mesons and baryons had been found. However, in recent years multiple discoveries have been made in the mass region of charmonium states. This is the general term for $c\bar{c}$ (charm quark and anticharm quark) pairs. Prominent examples of these states are the $X(3872)$ (discovered by Belle in 2003 [9]), the $Y(4260)$ (discovered by BaBar in 2005 [10]), the $Z_c(3900)^\pm$ (discovered by both BESIII [11] and Belle in 2013,[12]), the $Z_c(3900)^0$ (first evidence seen in CLEO-c data [13] and discovered by BESIII [14]) and the $Z_c(4020)^{\pm/0}$ (observed by Beijing Spectrometer III (BESIII) in 2014 [15][16]). These new states exhibit decay properties which do not fit into a description with conventional internal structure.

To get a more complete picture of QCD proper insights into the internal structure of bound states like these described above have to be obtained and additional exotic states must be discovered. For this purpose precision measurements with high statistics and searches for new resonances have to be performed. As can be seen through the past discoveries of exotic states, the BESIII experiment in Beijing is a current key experiment in this scientific endeavor. A fundamental reason for this is the enormous amount of data in the charmonium region it has recorded. Mass, width of bound states and their quantum numbers are examples of properties which need to be determined with high precision for any future advancement in disentangling their internal structure.

The first two can be extracted via the determination of their line shape which in turn is accessed by energy scans. In this method the center of mass energy of the initial reaction is increased in small steps while the resulting event rate is observed. If a bound state exists which can be produced resonantly in the energy range used by the experiment it will show up as a peak in the measured spectrum. As BESIII is an e^+e^- collider the quantum number of the resonant structures produced in an energy scan are limited to $J^{PC} = 1^{--}$. Therefore, other experiments are needed to investigate states with other quantum numbers. The future PANDA experiment at the Facility for Antiproton and Ion Research (FAIR) in Darmstadt will be able to do this kind of measurement very effectively. The reason for this is that the energy resolution of PANDA will be at least an order of magnitude higher than with any e^+e^- colliders and therefore allowing a more precise measurement of lineshapes. In addition, it also provides access to states with $J^{PC} \neq 1^{--}$ by its use of an antiproton proton reaction.

Measurements at PANDA like the aforementioned energy scan require a precisely determined integrated luminosity for each scan point for the normalization of the scan points among each other. This requirement is the reason that a dedicated luminosity detector will be part of the PANDA detector instead of just a simple monitor. The difference to luminosity monitors commonly used in other experiments is that the luminosity will be determined by measuring the differential cross section of the elastically scattered antiprotons in dependence on the scatter angle. To measure the scattering angle the tracks of the scattered antiprotons have to be reconstructed. For this four layers of silicon pixel sensors are positioned inside the vacuum close to the beam axis. Reducing

the amount of data this detector delivers to a more manageable level and discriminating tracks of elastically scattered antiprotons from background channels requires a fast track finding system as part of the data acquisition system. One goal of this thesis was the design and characterisation of such a system.

The existence of the charmoniumlike states $Z_c(3900)^\pm$ and $Z_c(3900)^0$ decay to $J/\psi\pi^\pm$ or $J/\psi\pi^0$ respectively as well as the decays of $Z_c(4020)^{\pm/0} \rightarrow \pi^{\pm/0}h_c$ leads to the assumption both could be isospin triplets. Then singlet states might exist which decay to $J/\psi\eta$ or $h_c\eta$.

As the underlying structure of all the Z_c states is not understood yet observations of the mentioned resonances would add valuable information. The search for a resonant structure decaying to $h_c\eta$ is therefore the goal of the second part of this thesis. To achieve this the reaction channel $e^+e^- \rightarrow h_c\eta\pi^+\pi^-$ is chosen. Since a minimum energy of the recoiling pions is required the high luminosity dataset collected by the BESIII collaboration at a center of mass energy of 4.6 GeV is used.

Chapter 2 at the beginning of this thesis briefly covers the theoretical background of QCD and summarizes the contemporary knowledge in the field of hadron spectroscopy. In chapter 3 the two hadron spectroscopy experiments BESIII and PANDA relevant for this work are introduced. Both detectors are described in the necessary detail and their physics programs are briefly outlined. Chapter 4 explains the concept of the determination of luminosity, how its measurement is planned at PANDA in general and afterwards in which way the detector for it is currently designed. Chapter 5 describes Graphics Processing Unit (GPU) and Central Processing Unit (CPU) architectures which is necessary for understanding the choices made in terms of the online track finding algorithm. After a short survey through already existing online track finding algorithms chapter 6 describes how the online track finding algorithm for the luminosity detector was chosen and implemented. Afterwards the performance of the track finding algorithm in terms of efficiency, ghost track percentage and processing times on GPU and CPU is presented in chapter 7. Chapter 8 describes the event selection of the decay $e^+e^- \rightarrow h_c\eta\pi^+\pi^-$ from the BESIII dataset. This is followed by chapter 9 covering the performance of the event reconstruction in terms of correctness, efficiency, resolution and background rejection capabilities. The chapter also finally presents the results of the data analysis including the decay cross section, systematic uncertainties and an upper limit on the decay cross section. A summary of this work is given in chapter 10.

Chapter 2

Quantum Chromodynamics

2.1 The QCD Lagrangian

During the middle of the last century an enormous number of new particles which are called hadrons have been discovered with particle physics experiments. All these particles needed to be classified according to their properties. Introducing a model with three new particles, called quarks, with only a fractional instead of integer charge seemed to allow this [8, 17]. For a long time all states which have been found were identified as quark antiquark pairs called mesons or three quark combinations called baryons. However, exotic states with another internal structure are not forbidden in QCD. To prevent contradicting the Pauli principle there were more qualities needed than just the three types of quarks. There are some hadrons with a completely symmetric wave function while being fermions at the same time. A new quantum number called color charge does provide a way to solve that contradiction [18, 19]. All quarks carry a color charge while the hadrons formed by their combination have to be colorless. The three u, d and s quarks lead to 9 quark antiquark pairs and can be organized into an octet and a singlet with the SU(3) symmetry while neglecting mass differences.

The currently accepted way to formulate this model as a gauge field theory is QCD. Its Lagrangian density [20] is given by:

$$\mathcal{L}_{QCD} = \sum_q \bar{\psi}_{q,a} (i\gamma^\mu \partial_\mu \delta_{ab} - g_s \gamma^\mu t_{ab}^C \mathcal{A}_\mu^C - m_q \delta_{ab}) \psi_{q,b} - \frac{1}{4} \mathcal{F}_{\mu\nu}^A \mathcal{F}^{A\mu\nu} \quad (2.1)$$

in this $\bar{\psi}_{q,a}$ are quark-field spinors with a quark flavor q and a color index a ranging from 1 to $N_c = 3$ as there are three color charges. γ^μ are the Dirac matrices. The mass of the quarks is given by m_q . \mathcal{A}_μ^C represent the gluon fields and t_{ab}^C represent the 3×3 matrices which are the generators of the SU(3) color group. The index C ranges between $C = 1$ to $N_c^2 - 1 = 8$ accounting for the 8 gluons. A gluon interacting with a quark rotates the color of the quark in SU(3) space. The g_s is the QCD coupling constant (which can also be written as $\alpha_s = \frac{g_s^2}{4\pi}$) and $\mathcal{F}_{\mu\nu}^A$ is the field tensor which is given by

$$\mathcal{F}_{\mu\nu,a} = \partial_\mu \mathcal{A}_{\nu,a} - \partial_\nu \mathcal{A}_{\mu,a} - g_s f_{abc} \mathcal{A}_\mu^b \mathcal{A}_\nu^c \quad (2.2)$$

where f_{abc} are the structure constants of the SU(3) color group.

As the field strength tensors contain a quadratic term in the gluon fields there are

interaction terms between three and four gluon fields besides the usual interaction between gauge field and matter. This self interaction of gluons is the cause of both confinement and asymptotic freedom of quarks. In figure 2.1 all possible interactions which are described by equation (2.1) and (2.2) are shown. A gluon can be created by radiation from a quark, decay into a quark antiquark pair or interact with itself. The coupling g_s at the vertices is the same for each of the interactions and it is dependent on the momentum transfer Q^2 of an interaction. The reason for this dependence is twofold. Gluons decaying into quark antiquark pairs are leading to a charge screen effect. Viewed by itself this would mean that the effective coupling strength increases with Q^2 . Another effect does put restrictions on that though. Self interaction of gluons means that they can decay into gluon loops which in turn means that there will be an anti charge screening effect resulting in a reduced net charge for larger Q^2 and thus a smaller coupling strength. Making use of perturbation theory [21] this dependence on Q^2 can be quantified as

$$\alpha_s(Q^2) = \frac{12\pi}{(11n_c - 2n_f) \ln(Q^2/\Lambda^2)} \quad \text{with } Q^2 \gg \Lambda^2 \quad (2.3)$$

in which n_c and n_f are the numbers of colors and quark flavor. It decreases with increasing Q^2 for $n_c > 2/11 \cdot n_f$. The parameter Λ is free and experiments have estimated it to be in the range of 100 MeV – 500 MeV. α_s increases with decreasing momentum transfer, meaning longer distances, which results in quark pairs being unable to be separated from each other as the colorless state is preserved which is the so called confinement. Increasing momentum transfer on the other hand leads to a decreasing coupling strength. Thus quarks are asymptotically free at short distances. This theoretical Q^2 dependence and data taken by experiments are shown in figure 2.2 and both are compatible with each other.

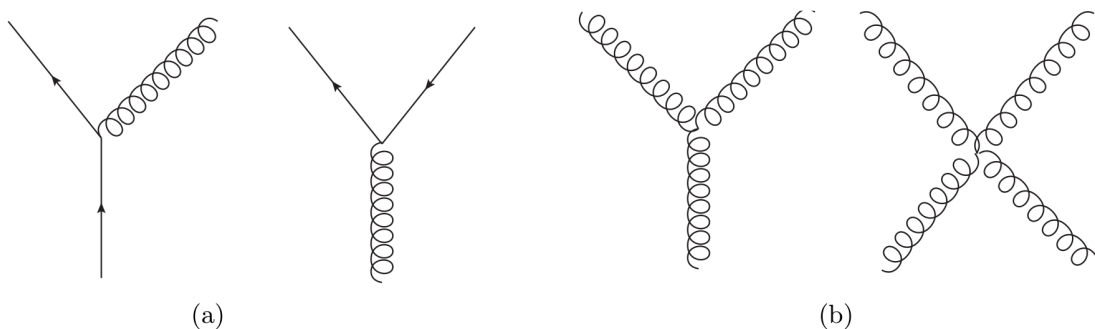


FIGURE 2.1: Possible interactions of quarks and gluons [22]. (a) Radiation of a gluon by a quark and decay of a gluon into a quark antiquark pair. (b) Self coupling of quarks.

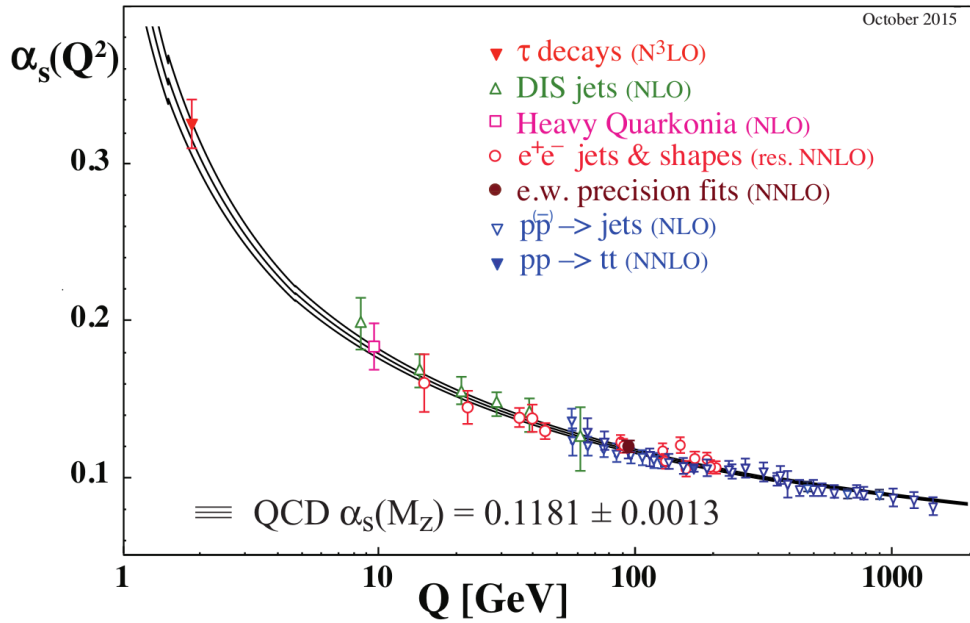


FIGURE 2.2: Strong coupling constant α_s in dependence on the momentum transfer Q [23]. The black curves are theoretical predictions of QCD for different Λ values. The data points are measurements taken from various experiments with the degree of QCD perturbation theory denoted in brackets.

As perturbation theory is only valid for low coupling strengths it can only be used for high Q^2 . At low Q^2 where hadrons are described the coupling constant α_s is too large for perturbation theory to be applied. Thus an alternative approach has to be used. One such an approach is lattice QCD. Lattice QCD uses a discretized space time which reduces the problem to a numerical one [24]. This way QCD effects can be calculated from first principles as long as enough computation power is available. Another way to approach the problem is to use effective field theories by neglecting the masses of light mesons and using them as degrees of freedom instead. One of these effective field theories is chiral perturbation theory [25]. In heavier quarkonia such as charmonium consisting out of a $c\bar{c}$ pair relativistic effects in bound states are small. Thus a non relativistic approach to QCD can be taken. For this an interaction potential like the Cornell potential can be used with the Schrödinger equation. It is given by

$$V = -\frac{4}{3} \frac{\alpha_s(r)}{r} + k \cdot r$$

where r is the distance between the quark and antiquark pair and k the string tension. The first term is a coulomb like potential as one gluon exchange interaction dominates at small distances analogous to one photon exchanges in QED. As this potential dominates for small r it is compatible with asymptotic freedom. Taking into account the contribution of the different colors gluons can have leads to the factor $\frac{4}{3}$. Confinement is realized with the second term as it is growing linear with distance. For an accurate description of the masses of bound states the potential is modified with terms representing spin-orbit and spin-spin interaction of quarks.

2.2 Light Meson Systems

Light mesons consist of the three lightest quarks u , d and s as well as their respective antiquarks. They have only a small mass in comparison to the binding energy and thus bound states composed out of them must be handled relativistically. On the other hand a negligible mass means that effective field theories like chiral perturbation theory can be used as an approach to calculating the coupling strength. Low masses also mean that comparatively low beam momenta are sufficient to access them experimentally. As mesons consist of quark antiquark pairs and each quark carries a spin of $1/2$ any resulting meson can only have a spin of either 0 or 1. A common way to describe these states are the J^{PC} quantum numbers. J is there total angular momentum, P is the eigenvalue of their wave function under parity transformation and C is the eigenvalue under charge conjugation. For ground states with an angular momentum of $L = 0$ there are two types of mesons. Vector mesons with the quantum numbers $J^P = 1^-$ and pseudoscalar mesons with $J^P = 0^-$. The possible combinations of the light quarks to bound states are governed by the $SU(3)$ group. This results in 8 particles in an octet and one in a singlet for both kinds of mesons. As can be seen in figure 2.3 they are ordered by their strangeness and the third component of the isospin. The isospin was introduced as a means to describe the proton and neutron as a doublet state motivated by their similar masses. It is conserved under strong interaction and follows the same rules as angular momentum. u quarks carry the isospin $|I, I_3\rangle = |1/2, +1/2\rangle$ while d quarks carry $|1/2, -1/2\rangle$ respectively. Both of them lack a specific flavor quantum number like the strangeness only carried by the s quark which in turn does not have an isospin. Strangeness is a simple additive quantum number and like all flavors can only be violated through weak processes.

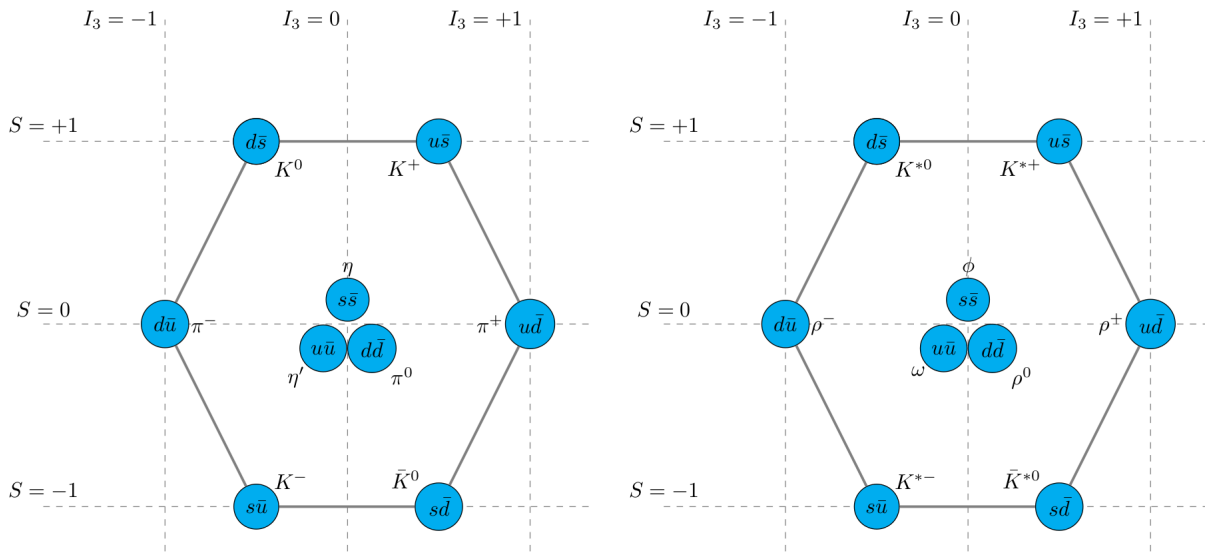


FIGURE 2.3: Isospin and strangeness multiplets for light pseudoscalar (left) and vector (right) mesons [22].

The lightest known mesons are pions. They fall into the category of pseudoscalar mesons and form an isospin triplet [26] with the following combinations.

$$\pi^+ = |1, +1\rangle = -u\bar{d}$$

$$\pi^0 = |1, 0\rangle = \sqrt{\frac{1}{2}}(u\bar{u} - d\bar{d})$$

$$\pi^- = |1, -1\rangle = d\bar{u}$$

As is typical for such triplets all different pion states differ only slightly in mass. The reason for this is found in the similar masses of the u and d quarks which only leads to a weak symmetry breaking of the underlying $SU(2)$. With a perfect symmetry all these states would have the same mass. For vector mesons a corresponding triplet can be found in the ρ mesons.

By including the s quark kaons become part of the multiplet. These form isospin doublets with $S = \pm 1$. As the mass of the s quark is noticeably larger than that of the u and d quark the $SU(3)$ symmetry is broken. This broken symmetry leads to mixing of the singlet η_1 and octet η_8 with $I_3 = 0$ and $S = 0$. The unmixed states are given by

$$|\eta_1\rangle = \sqrt{\frac{1}{3}}(u\bar{u} + d\bar{d} + s\bar{s})$$

$$|\eta_8\rangle = \sqrt{\frac{1}{6}}(u\bar{u} + d\bar{d} - 2s\bar{s})$$

Mixing for pseudoscalar mesons is weak enough that η and η' can be considered pure states with the following singlet and octet state:

$$|\eta\rangle \approx \eta_8$$

$$|\eta'\rangle \approx \eta_1$$

In the case of vector mesons both states mix in the following way:

$$|\phi\rangle = \eta_8 \cos \theta_v - \eta_1 \sin \theta_v \approx |s\bar{s}\rangle$$

$$|\omega\rangle = \eta_8 \sin \theta_v + \eta_1 \cos \theta_v \approx \frac{1}{2}(|u\bar{u}\rangle + |d\bar{d}\rangle)$$

with a mixing angle of $\theta_v = 36.4^\circ$ [27]. ϕ is approximately an $s\bar{s}$ state and the ω a linear combination of u and d quarks without contribution of s quarks.

2.3 Charmonium Spectroscopy

The second generation of quarks does not only contain the strange quark but also a significantly heavier one called charm (c) quark. Historically its existence has been accepted through the discovery of a meson now called J/ψ . This particle has been discovered independently at Stanford Linear Accelerator Center (SLAC) in an e^+e^- annihilation and at Brookhaven in the reaction $p + \text{Be} \rightarrow e^+ + e^-$ [28, 29]. Both observations have been published virtually at the same time in December 1974. The mass of this new-found particle is very high with $m_{J/\psi} = 3.096 \text{ GeV}/c^2$, doesn't have charge and has an enormous lifetime of about $10 \times 10^{-20} \text{ s}$ compared to other particles found in that mass region. Its internal structure has been determined as $c\bar{c}$ and it was the first member of the new meson family called charmonium, named similarly to positronium (bound states of e^+e^-). Before it has been observed a fourth quark had already been proposed by the Glashow–Iliopoulos–Maiani (GIM)-mechanism [30] and the new important finding lead to the acceptance of the quark model. In fact the contribution of the J/ψ to particle physics was of such an extent that its discovery commonly dubbed *November Revolution* of particle physics.

The spectrum of experimentally established charmonium states is shown in figure 2.4. These states are sorted by their J^{PC} quantum numbers and their respective masses. Labeling is either done with $X(m)$ where m is the approximate mass at which the state has first been observed or with $X(nL)$. In the latter notation n is the radial excitation with values 1,2,3, etc. and L is the angular momentum between the quark antiquark pair using a capital letter notation (S,P,D, etc.). Singlet states are called η_c and h_c while triplets are labeled as ψ and χ_c . Below the threshold of two D mesons (which are the lightest mesons with charm content) at $3.730 \text{ GeV}/c^2$ long lived charmonium states can be found. The reason for this is that their strong decays are suppressed by the Okubo-Zweig-Iizuka (OZI) rule. It says that if Feynman diagrams describing the decay can be cut in half by just severing internal gluon lines the decay is suppressed. Additionally these states have a very narrow width and can be described well with the Breit-Wigner model. Beginning with $\psi(3770)$ states above the $D\bar{D}$ threshold have decreased lifetime as strong decays into two D mesons are possible. As D mesons are composed of a c quark and one of the lighter quarks the OZI rule does not apply anymore.

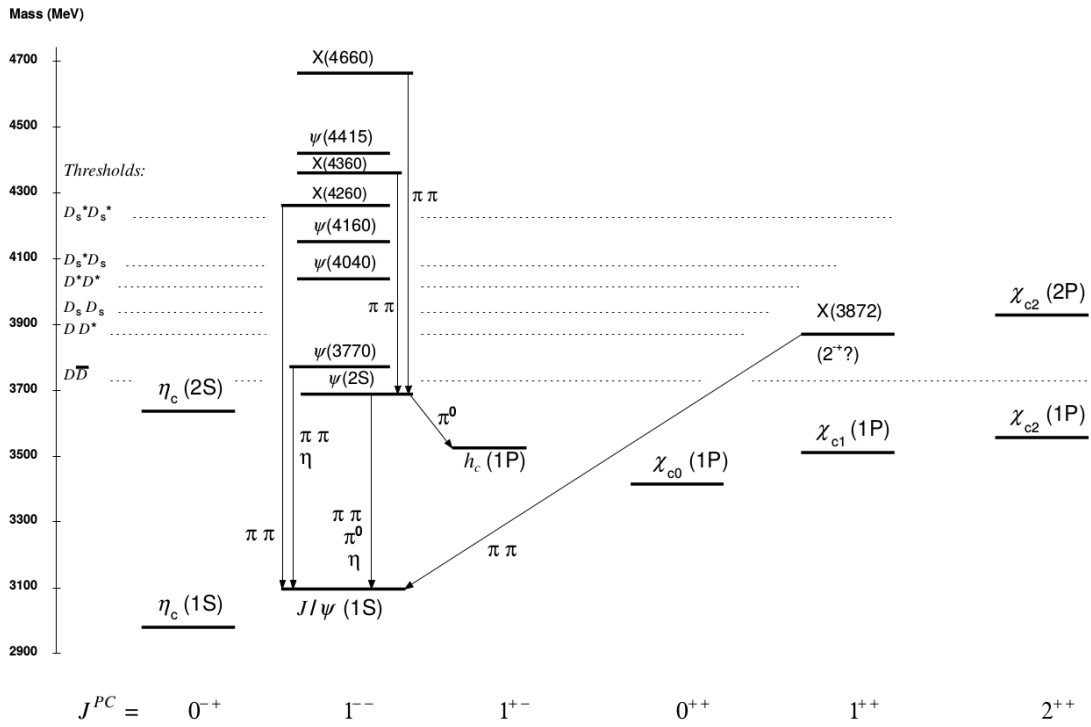


FIGURE 2.4: Spectrum of established $c\bar{c}$ states ordered by J^{PC} quantum numbers and mass. η_c and h_c are singlet states. Triplets are labeled as ψ and χ_c . States not fitting into the common $c\bar{c}$ scheme are labeled X. Arrows mark hadronic transitions. [31].

Over time more states than expected have been measured in the charmonium region and they have exhibited uncommon characteristics compared to conventional charmonium states such as being too narrow, decays not including D meson pairs or even being charged. These states are usually named with the letters X, Y, Z and are candidates for exotic states. QCD allows for a multitude of bound states described in the following and some are depicted in figure 2.5.

tetraquark Bound state consisting of one quark and one antiquark pair $qq\bar{q}\bar{q}$.

pentaquark Bound state consisting of a baryon and a quark antiquark pair $qqqq\bar{q}$.

molecular state Bound state formed by two separate mesons held together by gluon exchange at short distances and pion exchange at long distances $(q\bar{q})(q\bar{q})$.

hadro-quarkonium Bound state formed by a heavy quarkonium (e.g. $c\bar{c}$) surrounded by a cloud of light mesons [32].

hybrid state Bound state of quarks and an excited gluon e.g. $q\bar{q}g$.

glueball Bound state entirely formed by gluons gg or ggg .

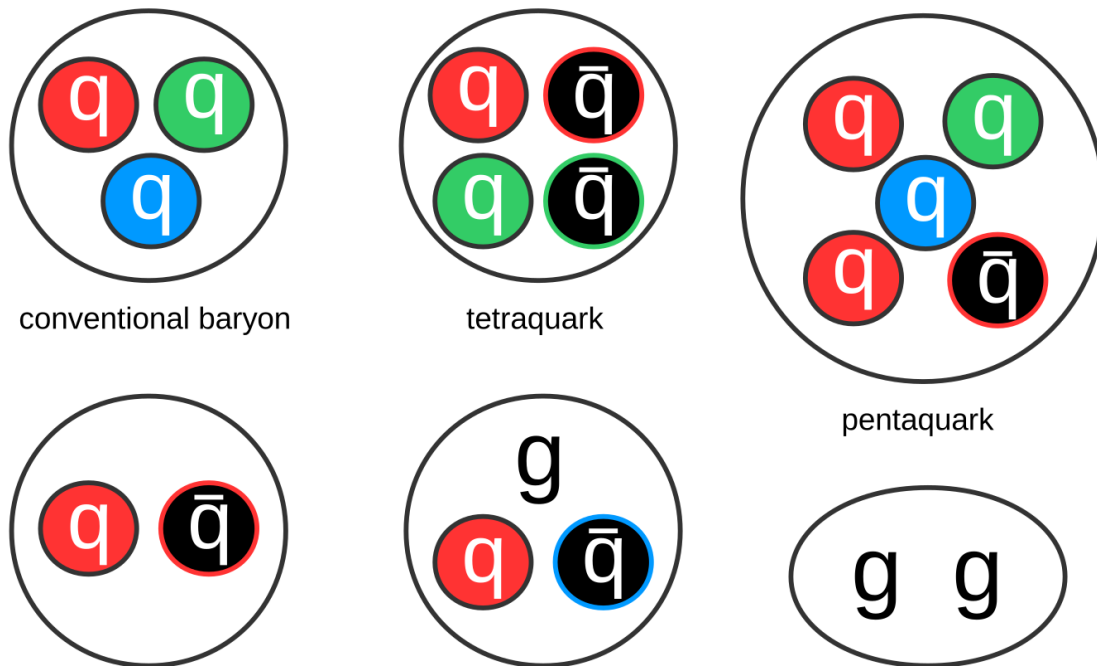


FIGURE 2.5: Illustration of a few possible bound state configurations using the quark model. [33].

The fact that mesons can not carry the quantum numbers $J^{PC} = 0^{--}, 0^{+-}, 1^{-+}, 2^{+-}$ etc. means that any state with these numbers is likely to be one of the mentioned exotic states. Unfortunately this is not the case in reverse. It is possible for exotic states to carry conventional quantum numbers shared with mesons and baryons. Thus their internal structure can't be determined in a simple way. In addition mixing between exotic and conventional states can occur. Because of the large amount of mesons found so far the mass region of up to $2.5 \text{ GeV}/c^2$ is a challenging environment for any search for exotic states. A way to circumvent this problem is to take a closer look at the charmonium region. One of the reasons for this is that charmonium states are narrower than the states composed of lighter quarks. Additionally the density of these states is also much lower.

A spectrum of charmonium states including exotic resonances (e.g. glueballs) from lattice QCD calculations together with a comparison with experimentally observed resonant states is shown in figure 2.6. Below the $D\bar{D}$ threshold the lattice QCD calculations and the conventional states found by experiments such as various χ_c or the J/ψ are in good agreement with each other. For glueballs and states above the $D\bar{D}$ threshold most of the calculated states have not been measured so far.

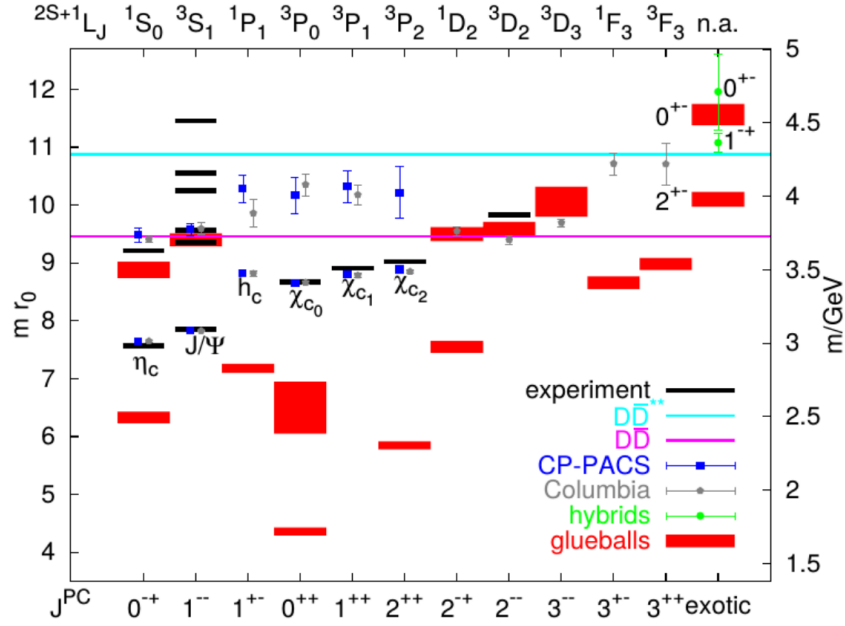


FIGURE 2.6: Comparison of the charmonium spectrum resulting from lattice QCD calculations with $r_0^{-1} \approx 394$ as scale parameter and experimental results [34].

A prominent example for an X, Y, Z state is the $X(3872)$. It is a neutral state which has been discovered by Belle in the decay $B^\pm \rightarrow K^\pm X, X \rightarrow J/\psi \pi^+ \pi^-$ [9] and is very narrow. The LHCb collaboration has determined the quantum numbers of the $X(3872)$ to be $J^{PC} = 1^{++}$ [35]. As it is very close to the $D^0 \bar{D}^{0*}$ threshold one candidate for its internal structure would be a molecular state of an D^0 and \bar{D}^{0*} . It has also been speculated to be a tetra quark state but so far no charged partner to it has been observed. Likewise the possibility of it being a classical $c\bar{c}$ has not been ruled out yet either. Contrary to its rather precisely known mass its width is only known as an upper limit of $2.3 \text{ MeV}/c^2$. [31]. As the PANDA experiment is designed for the precise determination of lineshapes in the charmonium mass region it may provide considerable insight into the riddle of the $X(3872)$ structure [36]. In the processes $e^+e^- \rightarrow \gamma_{ISR} J/\psi \pi^+ \pi^-$ and $e^+e^- \rightarrow \gamma_{ISR} \psi' \pi^+ \pi^-$ the BaBar collaboration observed the two states $Y(4260)$ and $Y(4360)$ respectively [37, 38] and afterwards both have been confirmed by other experiments [39, 40, 41]. The decay $Y(4260) \rightarrow \gamma X(3872)$ observed with the BESIII experiment [42] strongly suggests that the $Y(4260)$ and $X(3872)$ both have the same quark configuration. While their quantum numbers are known as $J^{PC} = 1^{--}$ their masses and width lack a precise determination and their decay properties are only vaguely known. For example the possible internal configuration of the $Y(4260)$ could be a hybrid [43, 44], a tetraquark [45, 46], a molecular state [47] or a hadro-charmonium [32, 48]. While previous measurements of the decay $e^+e^- \rightarrow \pi^+ \pi^- J/\psi$ have only shown one broader resonance at the mass region of the $Y(4260)$ [12] a more precise measurement at BESIII [49] has shown two resonances close by. The first matching the $Y(4260)$ with a much narrower width while the second one might be the $Y(4360)$ suggesting a new decay channel for it. One of the exotic states not fitting into the common meson scheme is the $Z_c(3900)^\pm$ discovered by both BESIII and Belle in 2013 [11],[12]. Evidence of its neutral partner $Z_c(3900)^0$ has first been seen by the analysis of CLEO-c data [13] and it has later

been confirmed by BESIII [14]. The preferred decay channel of this triplet is $\pi^{\pm/0}J/\psi$. A resonance which is consistent with $Z_c(3900)^{\pm} \rightarrow (D\bar{D}^*)^{\pm}$ has also been found by BESIII [50]. This indicates that these resonances contain a $c\bar{c}$ as well as an additional quark which is carrying the necessary electric charge. Besides the previously mentioned $Z_c(3900)^{\pm}$ a similar charged resonance $Z_c(4020)^{\pm}$ has been found by BESIII [15] in the decay $e^+e^- \rightarrow h_c\pi^+\pi^-$ and $e^+e^- \rightarrow (D^*\bar{D}^*)^{\pm}\pi^{\mp}$ [51] while its neutral partner has been found later in $e^+e^- \rightarrow h_c\pi^0\pi^0$ also by BESIII [16].

Motivated by all these discoveries of exotic states there have been many diligent searches for further resonant structures. These searches in the charmonium mass region are usually done via final states including well known charmonium resonances as is the search described later in this thesis.

Chapter 3

Charmonium Spectroscopy Experiments

To access the physics described in chapter 2 large and complex detector setups are necessary. For each of these detectors the concrete physics program dictates the requirements which must be satisfied when building it. Two experiments will be described in detail as studies for both of them are part of this work: The $\bar{\text{P}}\text{ANDA}$ and BESIII experiment. $\bar{\text{P}}\text{ANDA}$ has yet to be build and the High Energy Storage Ring (HESR) will offer high quality beams. The already existing BESIII experiment offers very high statistics datasets.

3.1 The $\bar{\text{P}}\text{ANDA}$ Experiment

The $\bar{\text{P}}\text{ANDA}$ detector is a planned experiment to investigate a multitude of hadron physics topics by using antiproton-proton annihilation. It is part of the new FAIR [52] which is currently under construction at the GSI Helmholtzzentrum für Schwerionenforschung GmbH (GSI) in Darmstadt, Germany. Funded by 16 countries FAIR is an international project and it will be hosting various particle accelerators and experiments. In figure 3.1 an overview of the research center can be seen. The starting point of the whole complex is the already existing Universal Linear Accelerator (UNILAC) and the heavy ion synchrotron Schwerionen Synchrotron (SIS)18. They are going to serve as injectors for the accelerator SIS100. The circumference will be 1100 m. In addition to the UNILAC the new linear injection accelerator Proton linear accelerator (p-LINAC) will be built. Beside the $\bar{\text{P}}\text{ANDA}$ experiment there will be other experiments running in parallel, Atomic, Plasma Physics and Applications (APPA), Compressed Baryonic Matter (CBM) and Nuclear Structure, Astrophysics and Reactions (NUSTAR).

$\bar{\text{P}}\text{ANDA}$ will be located at the HESR which provides it with an antiproton beam allowing for a unique physics program. To produce this antiproton beam a procedure of multiple steps is necessary. At first protons are created in the proton source and accelerated by the p-LINAC. They are then injected into and further accelerated by the SIS18. Afterwards they will be accelerated further by the SIS100. This results in a final energy of 29 GeV/c [53]. The protons are then shot in bunches of $2 \cdot 10^{13}$ particles onto a nickel (or iridium) antiproton production target [54] and thus create a variety of secondary particles via hard processes. To extract the antiprotons created this way with high efficiency a magnetic horn in combination with a momentum separation station will be used. The Collector Ring (CR) collects, cools and debunches the antiproton beam [55]. In the beginning years of the experiment the CR will feed the beam directly into the HESR which accumulates the antiprotons. When FAIR will be upgraded at a later stage

with the Recuperated experimental storage ring (RESR) to take over the accumulation it will be possible to simultaneously take data and accumulate antiprotons thus resulting in a higher integrated luminosity for the $\bar{\text{P}}\text{ANDA}$ experiment [52, 56].

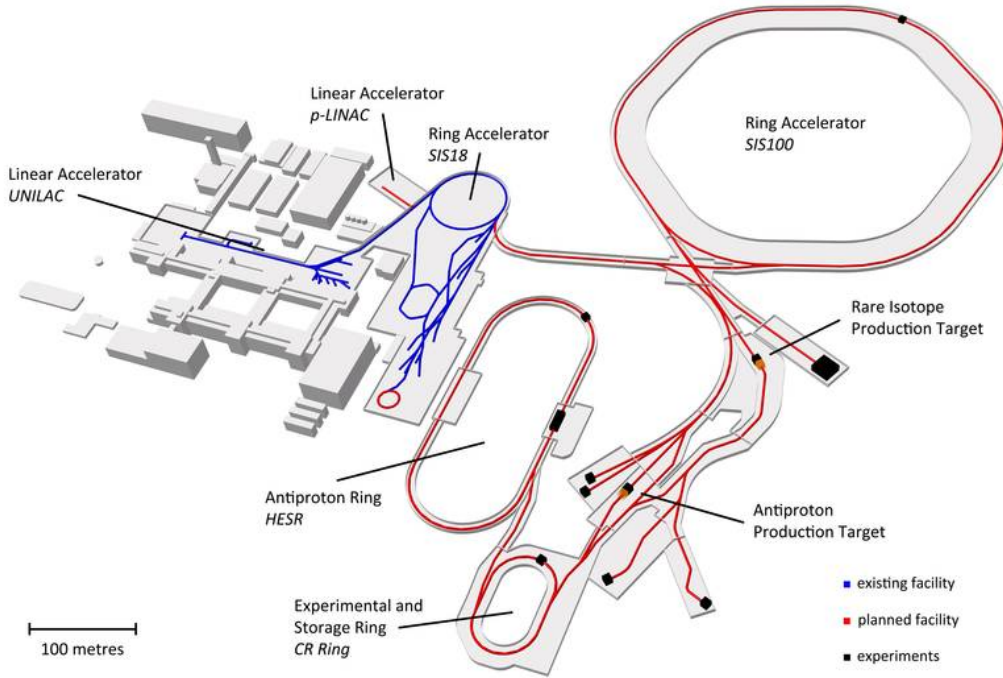


FIGURE 3.1: The accelerator complex FAIR [52] at GSI in Darmstadt. The blue parts are the already existing accelerators while the planned ones are displayed in red. The $\bar{\text{P}}\text{ANDA}$ detector is located at the HESR

3.1.1 The HESR

The HESR is a storage ring with a circumference of 575 m with two straight parts of 130 m. $\bar{\text{P}}\text{ANDA}$ is located at one of these straight sections which can be seen in figure 3.2. Along with $\bar{\text{P}}\text{ANDA}$ the KOALA [57] and SPARC [58] experiment will be situated at the HESR. KOALA is an experiment necessary for preparatory measurements. It will determine parameters of elastic antiproton proton scattering cross section needed for the extraction of the luminosity at $\bar{\text{P}}\text{ANDA}$. The purpose of SPARC is to determine properties of highly charged nuclei. To achieve this techniques from atomic physics like doppler boosts of optical laser beams to the X-ray regime [58] are used.

The HESR will be able to acc- and decelerate antiprotons in a momentum range of 1.5 – 15.0 GeV/c. It will offer the two operation modes high luminosity and high resolution. The former mode will deliver a peak luminosity of $2 \cdot 10^{32} \text{ cm}^{-2}\text{s}^{-1}$ with a momentum resolution of about $\delta p/p \approx 10^{-4}$ though it will not be available in the initial setup of FAIR. The high resolution mode available in the initial state improves the momentum resolution to $\delta p/p \leq 5 \cdot 10^{-5}$ but only offers a peak luminosity of up to $2 \cdot 10^{31} \text{ cm}^{-2}\text{s}^{-1}$. To achieve these resolutions a stochastic cooling system is used.

The position of the particle beam will be measured at the stochastic pick up and from this a correction signal is derived which will be send to the stochastic kickers which get antiprotons with a larger emittance closer to an ideal orbit. In the future an electron cooler will be added to the HESR to further improve the resolution in high resolution mode to a value of $\delta p/p \leq 2 \cdot 10^{-5}$. The parameters of these HESR operation modes are summarized in table 3.1.

beam parameters	High luminosity mode	High resolution mode	starting mode
p [GeV/c]	1.5 – 15	1.5 – 15	1.5 – 15
$\delta p/p$	$\approx 10^{-4}$	$\leq 2 \cdot 10^{-5}$	$\leq 5 \cdot 10^{-5}$
N antiprotons	10^{11}	10^{10}	10^{10}
\mathcal{L}_{peak} [$cm^{-2}s^{-1}$]	$2 \cdot 10^{32}$	$2 \cdot 10^{31}$	$2 \cdot 10^{31}$

TABLE 3.1: Design goals of the antiproton beam parameters for the HESR in the starting mode at the beginning of operation and the high luminosity and resolution mode [59, 60].

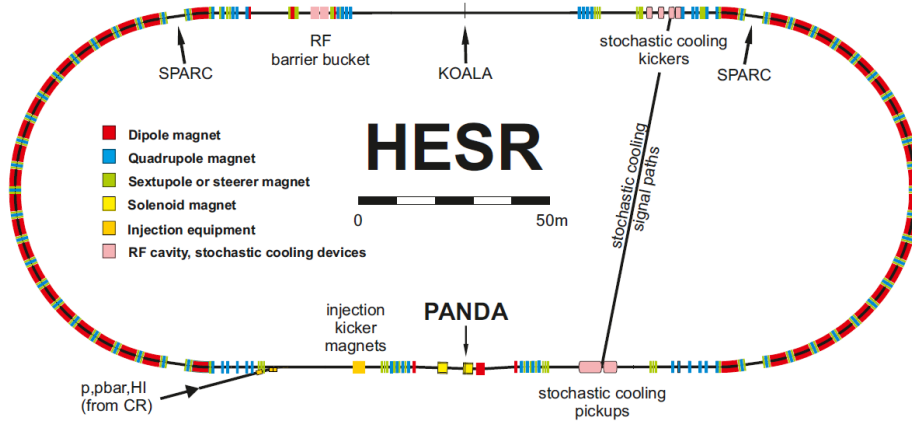


FIGURE 3.2: Schematic view of the HESR. It is a racetrack shaped storage ring equipped with RF cavities to acc- and decelerate the beam. Stochastic pickups and kickers are present to provide stochastic cooling. The electron cooler to further reduce the beam emittance will be added at a later stage opposite to the position of the $\bar{\text{P}}\text{ANDA}$ detector itself. The indicated locations of the KOALA and SPARC experiments are not final yet [61].

3.1.2 The $\bar{\text{P}}\text{ANDA}$ Physics Program

The physics program of the $\bar{\text{P}}\text{ANDA}$ experiment comprises a varied spectrum of physics subjects from the field of nuclear and hadron physics. Other experiments like BESIII use e^+e^- collisions and can therefore only produce initial states with the same quantum numbers as a virtual photon. However, due to using proton antiproton annihilation $\bar{\text{P}}\text{ANDA}$ will be able to directly access states with arbitrary mesonic quantum numbers via formation. With an additional recoil particle it is also possible to produce hadronic particles with exotic quantum numbers. This is illustrated in figure 3.3. Combined with

the HESRs high momentum resolution this makes it possible measure the line shape of a resonance with a high precision. To do this the energy scan method illustrated in figure 3.4 is applied. A resonance is scanned at different center of mass energies and its production cross section is determined. By systematically varying the beam momentum a resonance is scanned at various center of mass energies and at each of these scan points the number of events is determined. However, the integrated luminosity needs to be known to normalize each scan point and to calculate the production cross section. Deconvoluting the measured resonance shape and the momentum distribution of the beam provides the true line shape of the resonance. Additionally the integrated luminosity allows for the absolute cross section of a reaction channel to be measured. The PANDA physics program consists of four main areas which will be explained in the following paragraphs.

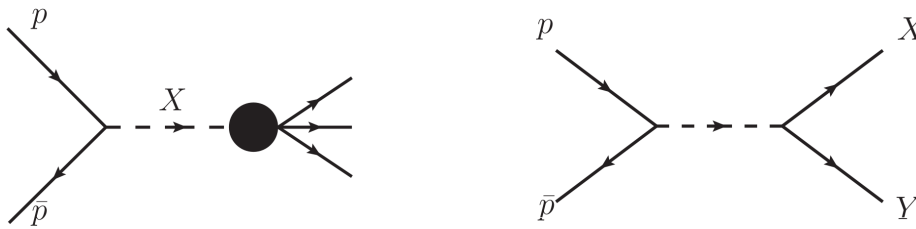


FIGURE 3.3: Creation of a resonance X through direct formation (left) and in production via an additional recoil particle (right) [22].

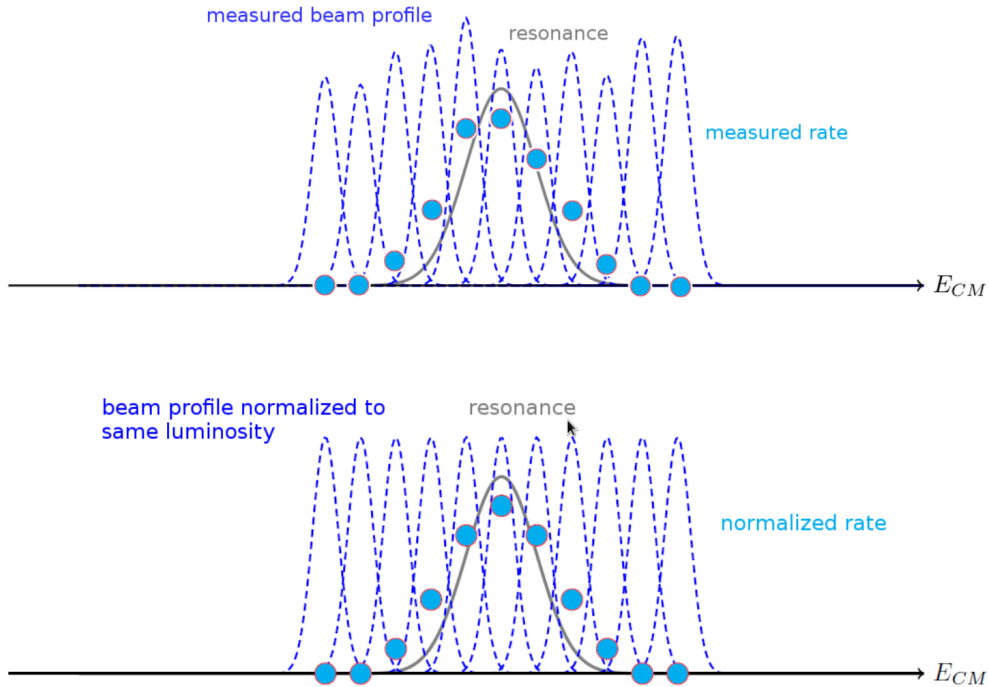


FIGURE 3.4: Determination of the line shape of a resonance with the energy scan method. The measured rate varies for each measured energy point varies as the integrated luminosity is different. Normalizing the points with knowledge of the integrated luminosity allows the extraction of the cross section. Deconvoluting them with the beam profile allows for the determination of the resonance shape [62].

Hadron Spectroscopy

The main physics topic of \bar{P} ANDA is hadron spectroscopy. It includes the measurement of hadron properties and the search for exotic particles. In this case exotic means that the particle content deviates from the usual 2 or 3 constituent quarks e.g. glueballs, hybrid or tetra quark states. Conventional charmonium states are well understood and as a result of the large mass of the charm quark mixing with light quarks is negligible. Therefore exotic charmonium states which are expected in the mass region of $3 \text{ GeV}/c^2$ to $5 \text{ GeV}/c^2$ can be better identified than corresponding states in the light quark region. An example for predicted states in the charmonium mass region are charmed hybrid states [44].

The high beam momentum resolution and direct production (formation) of any set of meson quantum numbers made possible by the proton antiproton annihilation offers opportunities to improve existing measurements. Line shape widths will be measured down to 100 keV which can be used to further investigate already discovered states such as the h_c and $\eta_c(2S)$. For the very narrow $X(3872)$ resonance the width of the line shape is only known with an upper limit of a few MeV. The possibility of improving the measurement of this value down to 100 keV by doing a fine grained energy scan [63] will allow to distinguish between different proposed models for the $X(3872)$ resonance. Another sub topic are hadrons in which only gluons contribute to their quantum numbers. About 15 glueballs are predicted to exist in the momentum region of \bar{P} ANDA [64].

Hadrons in matter

To understand the origins of hadron masses in the context of chiral symmetry breaking in QCD and the changes of them in an hadronic environment hadrons formed by light quarks have been used. \bar{P} ANDA will expand this research by making use of hadrons containing charm quarks which is made possible by its higher center of mass energy. Determining the dissociation cross sections of J/ψ is another possibility of \bar{P} ANDA. This can be achieved by measuring J/ψ and D meson production cross sections in $p\bar{p}$ annihilation on a series of nuclear targets. This is a fundamental parameter to understand J/ψ suppression in relativistic heavy ion collisions.

Nucleon Structure

Using wide angle Compton scattering and reactions as $p\bar{p} \rightarrow e^+e^-$ \bar{P} ANDA will be able to provide additional insights in the internal structure of the nucleon. With crossed-channel Compton scattering and related exclusive annihilation processes the generalized parton distributions [65] can be accessed while the reaction $p\bar{p} \rightarrow e^+e^-$ provides the possibility to measure the time-like form factor of the proton. Comparing the differential cross sections of the assorted processes and the generalized parton distribution based models will make it possible to gain new insights into the annihilation process of quark models and QCD. \bar{P} ANDA will be able to determine the form factors $|G_M|$ and $|G_E|$ independent of each other in a wide range of momentum transfer. Improvements in the regions of high momentum transfer are expected to be significant as other current measurements provide limited statistics.

Hypernuclei

A hypernucleus is formed when a strange quark replaces an up or down quark in a proton or neutron which is bound in a normal nucleus. This additional quantum number extends the nuclear chart by another axis. Only a limited amount of Λ -hypernuclei are presently known despite the fact that they have first been discovered almost 70 years ago [66]. To investigate hypernuclei a change of the experimental setup of \bar{P} ANDA will be made. A primary solid carbon target having a partial overlap with the circulating beam will be introduced for the reaction $\bar{p} \rightarrow \Xi^- \bar{\Xi}$. In a secondary target the Ξ will be captured and an excited $\Lambda\Lambda$ -nucleus will be created via $\Xi^- p \rightarrow \Lambda\Lambda$. As the number of antiprotons in the HESR decreases during a run it is necessary to determine the instantaneous luminosity and move the secondary target closer to the beam center accordingly to keep a constant interaction rate. The \bar{p} -beam of \bar{P} ANDA leads to the expectation of an ample production of hypernuclei making it possible to determine the $\Lambda\Lambda$ strong interaction strength which is not practical with direct scattering experiments. Hyperons are an excellent probe for the structure of nucleons and the hyperon-nucleon interaction because they can populate all possible nuclear states as they are not bound by the Pauli principle.

3.1.3 The \bar{P} ANDA Detector

\bar{P} ANDA is a fixed target experiment designed to have a high momentum and energy resolution, good particle identification at high reaction rates of up to 20 MHz and a solid angle coverage close to 4π . As it is a fixed target experiment the detector is split into a target- and a forward spectrometer to deal with the event topology. It is 15 m long with a width of 5 m and a height of 10 m. Around the target spectrometer is a 2 T superconducting solenoid magnet and a dipole magnet is constructed around the tracking detectors of the forward spectrometer. The luminosity detector is located approximately 11 m behind the interaction point and after the forward spectrometer. A schematic view of the \bar{P} ANDA detector shown in figure 3.5. The following paragraphs describe its main components.

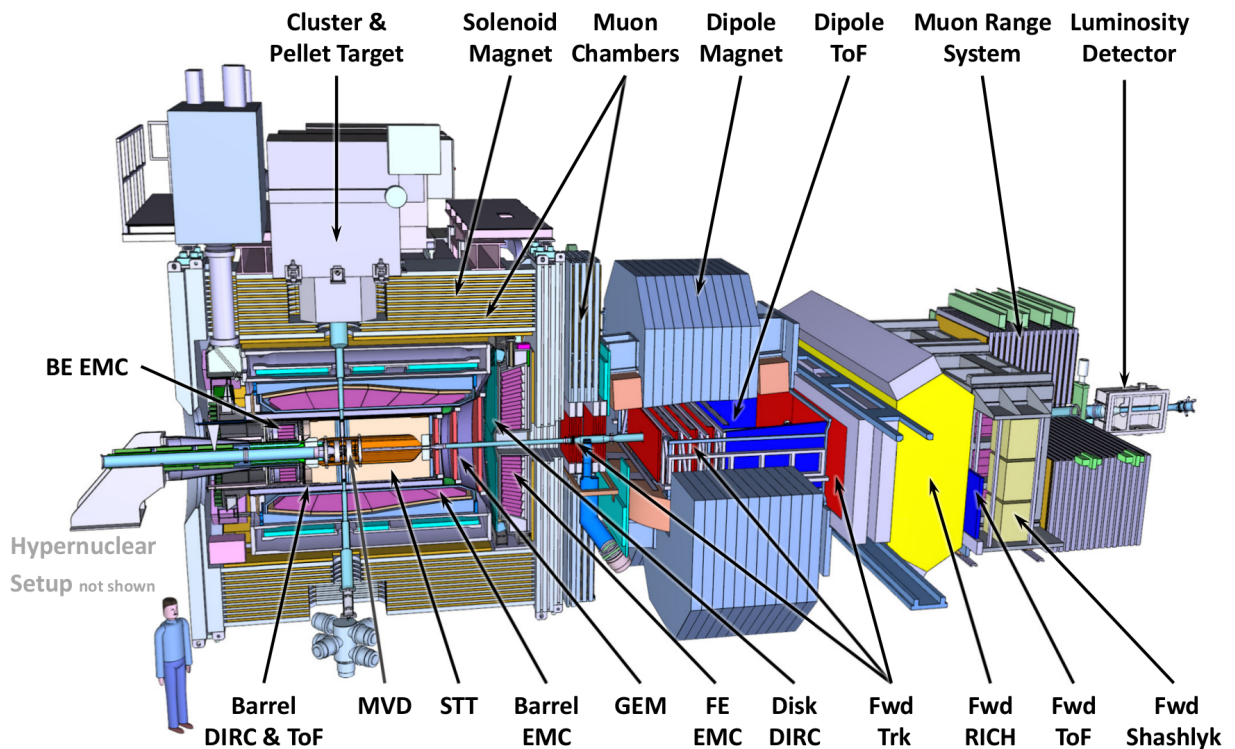


FIGURE 3.5: Schematic view of the complete \bar{P} ANDA detector. The location of the LMD is 11 m behind the interaction point [67].

\bar{P} ANDA Target

To achieve the high design peak luminosity of $\mathcal{L} = 2 \cdot 10^{32} \text{ cm}^{-2}\text{s}^{-1}$ at an interaction rate of 20 MHz it is necessary to have a hydrogen target with a density of $5 \cdot 10^{15} \text{ atoms/cm}^2$. Two target versions are in development: A cluster jet target and a pellet target [68].

Using a narrow jet of pre-cooled hydrogen the cluster jet target creates clusters by expanding the pressurized gas into the beam pipe vacuum. About 10^3 to 10^6 hydrogen molecules are usually contained in such a cluster. The density inside of a cluster is homogeneous and the amount of clusters injected is adjustable allowing for a constant luminosity in the detector. The disadvantage with this target is that the position of the interaction point has an uncertainty of a few millimeters. This uncertainty can be measured with the tracking detectors.

The pellet target has a triple-point chamber in which a gas is kept at the triple-point. A jet of cryogenic liquid is injected into this chamber via a periodically vibrating nozzle which creates droplets. This process leads to the production of frozen micro-spheres called pellets with a size between $25 - 40 \mu\text{m}$. An additional optical tracking system is foreseen to record the beam direction thus allowing for a determination of the position of the interaction point with a resolution of $50 \mu\text{m}$. However, the non-uniform time and thickness distribution of the pellets leads to variations of the instantaneous luminosity. Both described targets can be used with other gaseous substances, for example nitrogen or argon.

Micro Vertex Detector

The innermost detector enclosing the beam pipe covering an angle of 3° to 150° is the Micro Vertex Detector (MVD) which measures tracks of charged particles. It is currently foreseen to consist of a barrel with four layers and an endcap with six layers. The detector is composed of radiation hard double sided strip and silicon pixel detectors with a single hit resolution of $6.9\ \mu\text{m}$ for the pixel sensors and $12.4\ \mu\text{m}$ for the strip sensors. The spatial resolution of the reconstructed primary vertex is $100\ \mu\text{m}$ in the beam direction and $50\ \mu\text{m}$ in the x-y plane [69]. In addition the MVD also improves the momentum resolution of the single tracks and the Particle Identification (PID) determination. As it is the first detector particles pass the effect of multiple scattering is still minimal.

Straw Tube Tracker

The Straw Tube Tracker (STT) is positioned around the MVD. It serves as the central tracking chamber of the PANDA detector [70]. It consists out of 4636 self-supporting straws. Each straw is a 10 mm thick aluminised mylar tube filled with an ArCO_2 gas mixture at an 1 bar overpressure. In the center of each straw tube is a single anode wire responsible for the collection of the charge cloud created by passing charged particles. Most of the straw tubes are aligned in parallel to the beam axis to measure parameters in the xy-plane while some skewed layers will be used to get information on the z-position along the beam axis. The STT is expected to achieve a track reconstruction efficiency above 90% and a position resolution of $< 150\ \mu\text{m}$. Together with information from the MVD and by using the magnetic field of the solenoid a momentum resolution of $\delta p/p \approx 1\%$ can be achieved. In addition to measuring tracks and the primary vertex it will also be used to reconstruct secondary vertices of particle decays occurring outside of the MVD.

Gaseous Micro-Pattern Detectors

To detect charged particles tracks with an angle closer to the beam axis (3° to 20°) the MVD and STT are complemented by three gaseous micro-pattern detectors based on the principle of Gas electron multiplier (GEM)s. These are situated at 1.1 m, 1.4 m and 1.9 m away from the interaction point and can operate with high particle rates in the forward direction occurring because of the relativistic boost intrinsic to the fixed target setup. The expected position resolution for this detector system is $< 100\ \mu\text{m}$. Besides the reconstruction of tracks the GEM tracker will also be used for secondary vertex reconstruction.

Electromagnetic Calorimeter

Detection and energy measurement of electrons, positrons and photons is performed with an Electromagnetic Calorimeter (EMC). It is composed of a barrel part, a forward and a backward endcap. About 15744 Lead tungsten crystals (PbWO_4) are aligned to the proximity of the interaction point and read out by large avalanche photodiodes. The crystals are cooled to a temperature of -25°C for an increased light yield. An energy resolution of $1.54\%/\sqrt{E/\text{GeV}} + 0.3\%$ is achieved. For energy deposits of larger than

100 MeV a time resolution below 1 ns is possible. The shape and energy deposits of electromagnetic showers also allow for the separation of electrons from hadrons and muons [71].

Particle Identification Systems

Identification of charged particles is done with a multitude of PID detectors over a wide kinematic range. Systems dedicated to this task are Cherenkov and time-of-flight detectors. Integrated into the barrel part of \bar{P} ANDA is a Detector of Internally Reflected Cherenkov light (DIRC) [72] and a Disc DIRC [73] into the forward end caps of the target spectrometer. Both are constructed out of a highly polished fused-silica radiator with quartz bars holding the readout system attached to it. The DIRC makes use of the Cherenkov radiation emitted by charged particles to provide a π/K separation of at least three standard deviations for a momentum of 1 GeV/c up to 5 GeV/c. The barrel part of the DIRC covers polar angles in the range of $22^\circ - 140^\circ$ while the polar angle range of $5^\circ - 22^\circ$ is covered by the Disc DIRC. The DIRC is also used to discriminate between photons and charged particles entering the EMC behind it.

For the identification of low momentum particles below 1 GeV/c a Time of Flight (TOF) [74] system is used. The barrel TOF covers an angle of $|\cos(\theta)| < 0.83$ and consists out of 88 plastic scintillators readout by photomultipliers. With the planned timing resolution of about 100 ps a separation of π/K at up to 430 MeV/c at 90° and 760 MeV/c at 22° is achievable with three standard deviations. In addition the detection of slow kaon decay products by the TOF provides information which increases the trigger performance for the hypernuclei program.

As the capability of muons to penetrate material without being stopped is extremely high compared to other particles a typical absorber-detector combination is used at \bar{P} ANDA. This muon detection system is located in the iron flux-return yoke of the solenoid magnet [75]. The barrel part of the muon detection system contains 13 sensitive layers with a thickness of 3 cm which are surrounded by 3 to 6 cm thick iron absorbers. Due to the higher energies of muons more absorber material is required in the forward endcap. In this region 6 detection layers are surrounded by 6 cm iron layers. The sensors making up the sensitive layers are made out of rectangular aluminum Mini drift tube (MDT)s. Overall this system contains enough detector layers and absorber material to stop any remaining pions thus allowing for the remaining particles to be identified as muons.

Forward Spectrometer

Behind the target spectrometer in the direction of the antiproton beam, \bar{P} ANDA has a forward spectrometer composed of similar components as the target spectrometer. A dipole with a magnetic field of 1 T offers a bending power of up to 2 Tm. It is used to bend the tracks of charged particles to measure their momentum with the Forward Tracker (FT) [76]. This tracking system is based on straw tubes similar to the STT. There are three pairs of tracking stations and each tracking station is made out of four double layers of straw tubes [76]. The two inner layers of these tracking stations contain tubes inclined by $\pm 5^\circ$. This construction allows for the reconstruction of tracks separately with each pair of tracking stations even in the case of multi track events. At 3 GeV/c a

momentum resolution of $\delta p/p \approx 0.2\%$ is expected. Identification of particles is achieved with a Ring Imaging Cherenkov (RICH) and an Forward Time of Flight (FToF) detector [77]. This FToF detector has an angular acceptance of $\pm 10^\circ$ horizontally and $\pm 5^\circ$ vertically. It consists of 44 plastic scintillators and allows for a three standard deviation separation of π/K at particle momenta below 2.8 GeV/c and below 4.7 GeV/c for K/p . In the momentum range of 2 – 15 GeV/c the RICH provides the necessary separation ability. A silica aerogel and a C_4F_{10} gas mixture makes up the material in which charged particles emit the Cherenkov radiation which is then reflected onto attached Photomultiplier tube (PMT)s. In the forward region the particle energy is going to be measured with a Shashlyk type EMC. It is composed of alternating layers of lead for absorption and scintillating material with embedded wavelength shifting fibres. PMTs are attached to the end of the fibers to detect the scintillation photons. A resolution of $4\%/\sqrt{E}$ is expected. Behind the calorimeter another muon detection system is situated. As the system in the barrel part of the detector it allows for the differentiation of muons and other particles via a setup of interleaved absorber layers and MDTs. The last component of \bar{P} ANDA placed 11 m downstream of the interaction point after every other subdetector is the LMD. It will be discussed in detail in chapter 4.

Data Acquisition System

The \bar{P} ANDA experiment has an expected interaction rate of 20 MHz and the Data Acquisition (DAQ) system has to be able to cope with high data rates of up to 200 GB/s [78]. This amount of data can't be written to disk and thus a sophisticated event filter and trigger system is needed to differentiate between interesting events and background reactions. \bar{P} ANDA will not rely on a global hardware trigger to achieve this task. Instead partially reconstructed events will be used to determine the trigger decisions. The front end electronics of every detector component will be free running and select the data to be passed on with a feature extraction algorithm. This preprocessed data will be sent to data concentrators which will in turn send chunks of data to an event building network composed of two stages. In these event building stages compute nodes will continuously reconstruct events in order to form the trigger decisions. Any interesting events found this way will be written to disk. This can be seen schematically in figure 3.6. The compute nodes can in theory be systems using GPUs, CPUs or Field-Programmable Gate Array (FPGA)s depending on the data rate and the algorithms used. For synchronization of the DAQ across the different sub detectors, the Synchronisation of Data Acquisition (SODA) protocol will be used [79]. It provides a global clock which has a jitter of less than 20 ps and time stamps coupled to the HESR beam structure. These global time stamps are necessary for assembling the complete events out of data from the individual detector components. SODA also controls the whole DAQ via a predefined set of common commands [79].

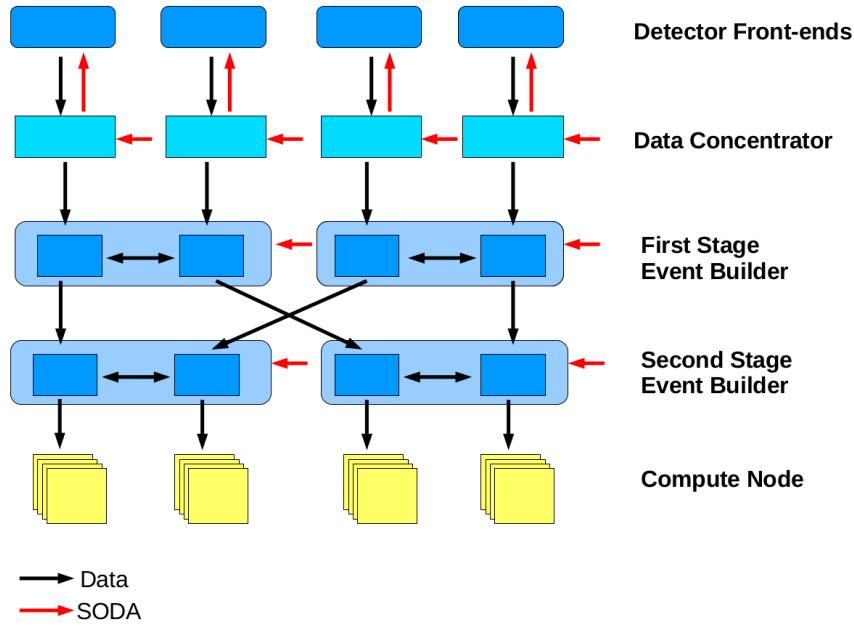


FIGURE 3.6: Schematic view of the complete PANDA data acquisition system [80].

3.2 The BESIII Experiment

The BESIII detector is located in Beijing at the Beijing Electron-Positron Collider (BEPCII) of the Institute of High Energy Physics (IHEP). The BEPCII is a multi-bunch collider with an available center of mass energy range of $\sqrt{s} = 2 - 4.6 \text{ GeV}$. It has two separate accelerator rings with a circumference of 237.5 m and has a design luminosity of $\sim 10^{33} \text{ cm}^{-2} \text{ s}^{-1}$ which was surpassed in April 2016 at a center of mass energy of $2 \cdot 1.89 \text{ GeV}$. It uses a top-off injection system with which the collider can reuse the remaining bunches. Additionally the BEPCII can be used to accelerate only electrons and thus work as a source of synchrotron radiation. In table 3.2 the operation parameters of BEPCII are summarized.

Parameter	Design	Achieved	
		e^- ring	e^+ ring
E [GeV]	1.89	1.89	1.89
I_{beam} [mA]	910	650	700
I_{bunch} [mA]	9.8	>10	>10
bunches	93	93	93
crossing angle [mrad]	11	11	11
injection rate [$\frac{\text{mA}}{\text{min}}$]	$200(e^-) 50(e^+)$	>200	>50

TABLE 3.2: Design and operation parameters of the BEPCII accelerator [81]

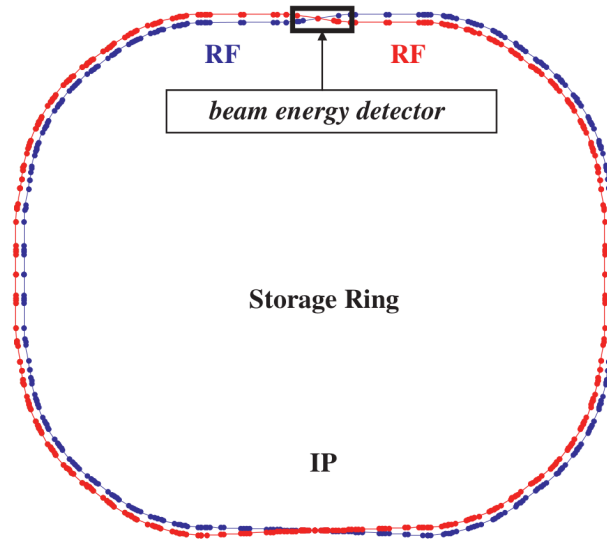


FIGURE 3.7: Schematic view of BEPCII double ring accelerator at the IHEP in Beijing. The detector of the BESIII experiment is situated at the lower part while the synchrotron light can be found opposite of that in the upper part[82].

3.2.1 The BESIII Physics Program

The BESIII physics program contains a wide range of topics which can be divided into several categories [83][84]. Some examples out of the extensive range of topics will be given for each listed category.

Light Hadron Physics

In the low and medium energy regime QCD is still a very challenging piece of the standard model. Asymptotic freedom in the high energy regime allows for systematic calculations with perturbation theory but for lower energies this is not the case. While the low energy regime can be explored with established theoretical methods such as chiral perturbation theory the medium energy regime requires a non-perturbative approach in form of effective field theories. Lattice QCD and QCD-motivated models predict a broader spectrum of mesons as it also takes into account gluonic degrees of freedom compared to just quark degrees of freedom. For these reasons studying light hadrons is an important part for achieving a better description of confinement physics. Radiative decays of the J/ψ provide a so called gluon-rich environment in which gluons are expected to appear. Lattice QCD calculations predict that a partial width of the J/ψ of $1.01(22)(10)$ keV is decaying into a tensor glueball [85] and 0.35 keV into a pure gauge scalar glueball [86]. Therefore the high-statistics sample of J/ψ makes BESIII an excellent choice for systematic research on glueballs. Scalar mesons are also an interesting example area in which BESIII can contribute through the the high-statistics sample of J/ψ . A large production of scalar mesons have been observed at BESIII in $J/\psi \rightarrow \gamma\eta\eta$ [87], $J/\psi \rightarrow \gamma\pi^0\pi^0$ [88] and $J/\psi \rightarrow \gamma K_s K_s$ [89] around $2.1 \text{ GeV}/c^2$ and so BESIII can

contribute to clearing up the nature of the $f_0(2100)$. Exploring how many distinct resonances exist around $1.7 \text{ GeV}/c^2$ and discovering if the $f_0(1370)$ is a true $q\bar{q}$ resonance or generated by $\rho\rho$ molecular dynamics are also open questions to be answered.

Charmonium Physics

The topic in which the analysis is performed in this thesis is part of Charmonium physics. Analogous to positronium mesons with $c\bar{c}$ content are called charmonium. Both charmonium states above and below the open charm threshold are accessible in the BESIII energy range. The broad scale of this energy range makes it an excellent tool to explore both perturbative and non-perturbative QCD. On the lower end QCD and QCD inspired models can be subjected to precision tests. Studies mainly include the decay properties of the $J/\psi, \psi(3686)$ and $\psi(3770)$ such as the total decay widths, which are supposed to be measured with a precision below the percent level. The ability to measure the many different decay modes of the $J\psi$ more precisely than before allows for insight into problems as for example the $\rho\pi$ puzzle and decays of the $\psi(3770)$ into states other than $D\bar{D}$. Higher mass states however can be used to investigate non standard configurations of quarks and gluons, for instance, tetraquark states consisting out of two quarks and two antiquarks, hadronic molecules formed by two hadrons, and hybrid mesons which are made of quark antiquark pair and an excited gluonic field. The first example for these is the $X(3872)$ as every meson between a mass of 2.9 and $4.5 \text{ GeV}/c^2$ could be described as a $c\bar{c}$ bound state before it has been discovered in 2003 with $X(3872) \rightarrow \pi^+\pi^-J/\psi$ [9]. At a center of mass energy of 4.26 GeV BESIII produces many $Y(4260)$. These $Y(4260)$ allow access to the $X(3872)$ via the process $e^+e^- \rightarrow \gamma X(3872)$ [42]. The $Y(4260)$ is another prominent example of a non standard meson discovered about 2 years later than the $X(3872)$ [37]. In recent years further unexpected discoveries have been made in this area with the BESIII detector. For example resonances decaying into states suggesting exotic internal structure, have been found. One of these is the $Z_c(3900)^\pm$ [11],[12] manifesting in a decay to a charged pion and a J/ψ . This discovery was made in the reaction $e^+e^- \rightarrow J/\psi\pi^+\pi^-$. The decay to J/ψ suggests $c\bar{c}$ content while the fact that the net charge is non-zero implicates additional $q\bar{q}$ content. The other one found in the channel $e^+e^- \rightarrow h_c\pi^\pm$ is the $Z_c(4020)^\pm$ [15] which has similar implications. In addition to that the uncharged partners $Z_c(3900)^0$ [13] and $Z_c(4020)^0$ [16] have been observed which complete both isospin triplets.

Charm Physics

The high statistics sample at 4.18 GeV containing many $\psi(3770)$ which mainly decay into D meson and D_s meson pairs respectively is also used for high precision measurements as it allows background suppression by tagging one $D_{(s)}$ -meson. Studying the leptonic decays of D and D_s mesons it is expected to measure the decay constants f_D and f_{D_s} with systematic errors of 0.8% and 1.4% [84]. Measurements of the semi-leptonic decays allow for the extraction of Cabibbo-Kobayashi-Maskawa (CKM) matrix elements V_{cs} and V_{cd} and with 20 fb^{-1} of $\psi(3770)$ data the uncertainties are expected to reach the 0.5% level. The ratio of the branching fractions $B(D^0 \rightarrow \pi^-\mu^+\nu_\mu)/B(D^0 \rightarrow \pi^-e^+\nu_e) = 0.82 \pm 0.08$ [90] deviates from standard model predictions of 0.985 ± 0.002 [91] by 2.1σ and therefore hinted at a violation of lepton flavour universality. BESIII

provided more accurate measurements with $B(D^0 \rightarrow \pi^- \mu^+ \nu_\mu)/B(D^0 \rightarrow \pi^- e^+ \nu_e) = 0.922 \pm 0.030 \pm 0.022$ and $B(D^+ \rightarrow \pi^0 \mu^+ \nu_\mu)/B(D^+ \rightarrow \pi^0 e^+ \nu_e) = 0.964 \pm 0.037 \pm 0.026$ [92] which are more consistent with the predictions. Having 20 fb^{-1} of $\psi(3770)$ data will allow for studies improving the efficiency further.

τ Physics

Another area for which BESIII provides good experimental conditions is the study of properties of τ -leptons such as the τ mass which is measured via an energy scan. This energy scan consisted of a scan of the J/ψ and $\psi(3686)$ resonances at several data points and a scan near the τ pair production threshold with one scan point below the threshold and four above it. With a total amount of 100 pb^{-1} it is expected to measure the τ mass with an uncertainty of less than $0.1 \text{ MeV}/c^2$ [84]. The τ lepton is the only lepton heavy enough to decay into hadrons and about 65% of its decay width contain hadrons in the final state. These decays offer an opportunity to study the non-perturbative regime of QCD. Second class QCD currents can be searched for via the decay $\tau \rightarrow \pi^- \eta \nu_\tau$. Studying decays of the τ into three pseudoscalar particles can be used to obtain information on the Wess-Zumino anomaly, hadronic form factors and to study CP violation in the leptonic sector. The CKM matrix element $|V_{us}|$ and the mass of the strange quark can both be directly determined via decays of the τ lepton which involve three kaons. Through the study of $\psi(3686)$ decays as $\psi(3686) \rightarrow e^+e^-$, $\mu^+\mu^-$, $\tau^+\tau^-$ all three lepton generations can be compared. A fine scan of the $\psi(3686)$ leading to 67 pb^{-1} of data allows for a direct measurement of the branching fraction of each lepton generation separately instead of relying on the relationship between them as an earlier study has done [93].

Exotic Decays and New Physics

Besides high energy hadron colliders low energy electron positron collision experiments can also provide hints to new physics beyond the standard model of particle physics. One class of processes which can hint at new physics are processes which are allowed in the standard model but do not occur at all or at very different rates in other models. Below the open charm threshold strong or electromagnetic interactions are prevalent for the decays of $\psi(nS)$ ($n = 1, 2$). Flavour changing weak decays through a virtual W boson are still possible. The standard model predicts J/ψ inclusive weak decays of $J/\psi \rightarrow D(\bar{D})X$ (X denotes any hadrons) with a branching fraction in the order of 10^{-10} [94] but other models allow for larger branching fractions [95, 96, 97]. As with the more conventional physics the high statistics sample of J/ψ leads to BESIII being in a good position to measure valuable results. Any type of dark matter would be in a class of processes not allowed in the standard model in any way. Should there be dark matter particles with masses only in the keV-MeV range they are implied to be allowed to be emitted and absorbed by standard model particles. As these dark matter particles would have extremely small couplings to standard model particles any experimental search for light dark matter particles requires large sample sizes and a good ability to resolve missing energy. The BESIII experiment can search for such particles in the helicity suppressed leptonic $D/D_s \rightarrow l\bar{\nu}$ decays. The helicity suppression of these decay

could be lifted by an axion-like particle a which would change the energy spectrum of the lepton [98]. In a similar fashion a flavour changing transition as $D \rightarrow a\pi$ could have a two body like spectrum of pions in $D \rightarrow \pi + \text{invisible}$ [99]. Searching for dark photons is also a possibility. At BESIII the radiative decay $e^+e^- \rightarrow \gamma V^* \rightarrow \gamma e^+e^-$ has been analysed on the $2.9fb^{-1} \psi(3770)$ sample resulting in an upper limit [100] compatible to an earlier result of BaBar [101].

3.2.2 The BESIII Detector

The BESIII detector is optimized for the expected event topology, multiplicity, types of primary particles and energy spectra of the physics program described in the previous section. Additionally the high data rate has also been taken into consideration. The most probable momentum of charged particles is around $0.3 \text{ GeV}/c$ while the average photon energy is 100 MeV [102]. For most particles the upper limit on the energy is 1.0 GeV . The detector is build with a 1 T superconducting solenoid. Its solid angle coverage is 93% . To reduce multiple scattering the beam pipe is made out of beryllium. In figure 3.8 a profile view of the BESIII detector can be seen and the shown main detector components are described in the following sections.

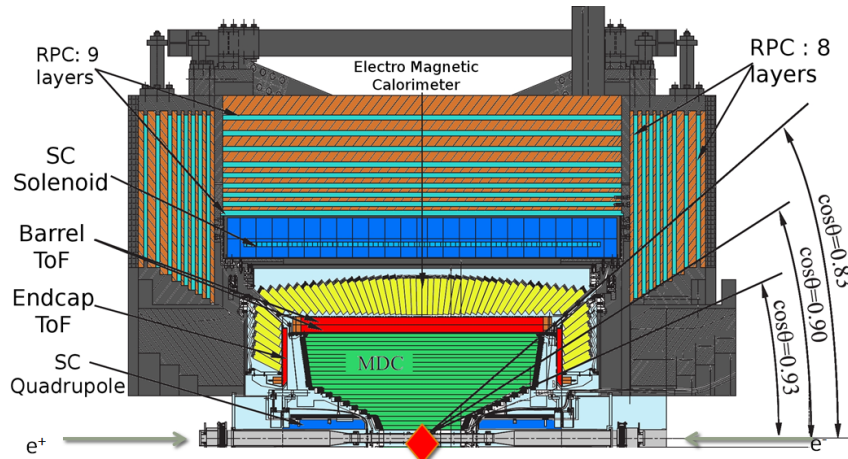


FIGURE 3.8: Side view of the upper half of the BESIII detector [103]. The detectors starting from the innermost to the outermost layer are the multilayer drift chamber, the time-of-flight system, an electromagnetic calorimeter and the muon detector

Multilayer Drift Chamber

The innermost detector surrounding the beam pipe is the Multilayer Drift Chamber (MDC). Its purpose is to measure the momentum of charged particles by the curvature of their tracks inside a solenoidal magnetic field. Measuring from the beam pipe the detector has an inner radius of 59.2 mm and an outer radius of 810 mm with covering a θ -range down $\cos \theta = 0.93$. It is constructed out of an inner and an outer chamber. The former can be replaced in case of too much radiation damage. 43 layers of drift cells organized into 11 superlayers make up the MDC. The majority of 35 layers form the outer chamber while the remaining 8 are part of the inner chamber. Individual drift

cells contain one sense wire which is surrounded by eight field wires. This results in a total of 6796 sense wires. They have a diameter of $25\ \mu\text{m}$ and are constructed out of gold plated tungsten. To reduce multiple scattering the surrounding field wires are produced out of $110\ \mu\text{m}$ thick gold plated aluminum. Neighboring cells share the field wires if they are part of the same superlayer. Each of these superlayers consists of four layers each except for the last one which has only three. The cells are filled with a helium-propane mixture ($\text{He} : \text{C}_3\text{H}_8 = 60 : 40$) which serves to minimize multiple scattering of low momentum particles while maintaining a good dE/dx resolution. At $1\ \text{GeV}/c$ the momentum resolution is $\delta p/p = 0.5\%$. In the r - ϕ plane the spacial resolution is $130\ \mu\text{m}$ and in beam direction $2\ \text{mm}$. The energy loss resolution for particles is 6% .

Time-Of-Flight

The TOF system measures the flight duration of particles using the bunch crossing time as the starting time and thus allows for particle identification. The TOF is build around the MDC and consists out of a barrel layer and two end caps. The barrel layer has a mean radius of $870\ \text{mm}$ and covers an angle up to $|\cos\theta| < 0.83$ while the end caps with an inner radius of $410\ \text{mm}$ and an outer radius of $890\ \text{mm}$ cover the region $0.85 < |\cos\theta| < 0.95$. The former is constructed from two layers of staggered scintillating bars and the latter from only one. These scintillators are read out via fine mesh photomultiplier tubes achieving a timing resolution of $110\ \text{ps}$ in the end caps and $90\ \text{ps}$ in the barrel [83]. $3\sigma\pi/K$ separation for momenta up to $0.7\ \text{GeV}/c$ is achieved. Additionally the TOF provides a fast trigger signal for charged particles.

Electromagnetic Calorimeter

The EMC is used to measure the energy and flight direction of photons, electrons and positrons and to provide trigger signals. It surrounds the TOF and is also split into a barrel part and two end caps. The former covers a solid angle of $|\cos\theta| < 0.82$ while the latter covers $0.83 < |\cos\theta| < 0.93$. It is made out of 6272 CsI(Tl) crystals with a length of $28\ \text{cm}$ which corresponds to 15 radiation lengths. They are read out by two silicon photo-diodes each. At $1\ \text{GeV}$ the EMC has an energy resolution of $\sigma_e/E = 2.5\%$ and a position resolution of $6\ \text{mm}/\sqrt{E[\text{GeV}]}$. Via their energy deposition, pions and electrons can be separated for momenta higher than $200\ \text{MeV}/c$.

Muon System

The outermost detector component is the muon system which identifies muons and discriminates them from other charged particles by their hit patterns. The system is composed out of multiple interleaving absorption and detection layers. Iron plates which are responsible for the magnetic flux return of the superconducting solenoid serve as the passive absorption layer stopping most particles except for muons. The detection layers are realized by Resistive plate chamber (RPC)s. RPCs consist out of two electrodes which are separated by an isolating gas (Argon(50%), Freon 134a(42%) and iso-butane(8%)). Charged particles passing through an RPC ionize the gas and thus create a detectable voltage signal. Nine layers of RPCs and iron plates comprise the barrel system and 8 the two end caps. As the muon tracks are bend in the solenoidal magnetic

field and loose energy in the EMC the muon system is effective for momenta above 0.4 GeV/c.

Trigger System and Event Filter

High interaction rates dominated by background reactions make it necessary to have a trigger and event filter system in place to suppress these background reactions. The trigger system is realized in two stages. The first level (L1) is hardware based mainly implemented on FPGA based electronics. It processes information of the MDC, TOF and EMC in a global trigger logic. The clock of the L1-trigger is synchronized to the accelerator and runs at 41.65 MHz. The maximum trigger rate of the L1-trigger is 4 kHz. Events passing the L1-trigger are then processed by a software trigger (L2) implemented on a commercial server farm. This second stage partially reconstructs events to form a trigger decision and brings down the rate even further to 2 kHz.

Luminosity Determination

To determine the luminosity the three QED processes $e^+e^- \rightarrow e^+e^-, \mu^+\mu^-, \gamma\gamma$ are exploited. For these reactions the cross sections are well known and they are very large. After the correction for detection efficiency and acceptance the rate of these reactions allows a measurement of the integrated luminosity with a precision of 1%. The main limitation on this measurement is the determination of the trigger efficiency, radiative corrections and background event suppression. Additionally luminosity monitors made out of fused silica blocks are mounted near the interaction point. Using the rate of incident photons from radiative Bhabha scattering these measure the relative bunch-by-bunch luminosity.

Chapter 4

Luminosity Determination at $\bar{\text{P}}\text{ANDA}$

Several topics in the $\bar{\text{P}}\text{ANDA}$ physics program require a precise measurement of the luminosity. To determine the time-dependent luminosity the differential cross section in dependence on the scattering angle of elastically scattered antiprotons is measured. This reaction is used as it has a well known cross section. This can be done by measuring the tracks of these antiprotons. Measuring tracks instead of just counting the tracks offers the advantage of allowing for the correction of systematic uncertainties and identifying possible background contributions. In turn this makes it possible to determine the luminosity with a high level of precision. Thus a tracking detector has been developed allowing for the reconstruction of the tracks. It uses silicon pixel sensors operating in a vacuum very close to the antiproton beam.

4.1 Luminosity

As quantum mechanics only allows for probabilities instead of predictions of individual reactions multiple identical and independent measurements have to be taken to determine these probabilities. In particle physics this probability under ancillary conditions for reactions is expressed in terms of a cross section σ . Together with the instantaneous luminosity \mathcal{L} it determines the event rate \dot{N} at which a reaction happens. It is given by

$$\dot{N} = \mathcal{L} \cdot \sigma \quad (4.1)$$

As event rates are measured through counting a number N of events during a time period dt the time-integration yields

$$N = L \cdot \sigma \quad (4.2)$$

with

$$L = \int \mathcal{L} dt \quad (4.3)$$

For a fixed target experiment the luminosity is defined as

$$\mathcal{L} = \phi_{beam} \cdot n_{target} \quad (4.4)$$

where ϕ_{beam} is the beam particle flux and n_{target} the target density per unit area. Therefore observing these two quantities could provide the instantaneous luminosity.

Alternatively the event rate of a reference channel with a well known cross section can be measured to determine the luminosity.

4.2 Luminosity Measurement at \bar{P} ANDA

At \bar{P} ANDA both methods mentioned in the previous section will be used to some extent. In the HESR the luminosity will be determined via monitoring the target and the beam. The thickness of the target is going to be measured by the emittance growth and energy loss of the antiproton beam and the beam particle flux by calibrated beam current transformers. This has been done at the COSY accelerator for the luminosity measurement for the ANKE experiment and a hydrogen cluster-jet target and resulted in a precision of about 5% [104]. As the beam is required to lose energy for this method due to the target material it can't be accelerated and cooled to its nominal energy at each revolution. Therefore it provides the disadvantage that luminosity measurements can only be taken punctually for different runs instead for concurrently measuring the luminosity while taking physics data and thus the time integrated luminosity has to be determined by interpolating between runs.

In order to provide a continuous measurement of the luminosity the luminosity detector will constantly measure tracks of antiprotons elastically scattered at the target protons to determine the luminosity with high precision. Advantages of this approach are the simple kinematic dependencies between interacting particles and a large cross section of 5 – 40 mb in the momentum range of \bar{P} ANDA's antiproton beam. There are three different components to the differential cross section with varying contributions depending on the momentum transfer $|t|$. This is shown in figure 4.1.

The differential cross section of this process is given by:

$$\frac{d\sigma_{total}}{dt} = \frac{d\sigma_{Coul}}{dt} + \frac{d\sigma_{had}}{dt} + \frac{d\sigma_{int}}{dt} \quad (4.5)$$

where t denotes the momentum transfer, σ_{Coul} the Coulomb part, σ_{had} the hadronic contribution and σ_{int} the interference part of the differential elastic proton-antiproton cross section. The momentum transfer is directly related to the scattering angle θ of the process in the center of mass system:

$$|t| = |p - p'|^2 = 4p^2 \cdot \sin^2\left(\frac{\theta}{2}\right) \quad (4.6)$$

p is the momentum of the antiproton before scattering and p' after scattering. All three contributing parts can be parameterized according to [105]. For the long ranged Coulomb part the parameterization is:

$$\frac{d\sigma_{Coul}}{dt} = \frac{4\pi\alpha_{em}^2 G^4(t) \hbar c^2}{\beta^2 t^2} \quad (4.7)$$

It is well understood and within QED it can be analytically calculated. $\beta = \frac{v}{c}$ is the relativistic speed expressed as a ratio of the velocity v and the speed of light c . \hbar is the reduced Planck constant, α_{em} the electromagnetic fine structure constant and $G(t)$ the proton dipole form factor given by:

$$G(t) = \left(\frac{1}{1 + (|t|/\Lambda^2)} \right)^2 \quad (4.8)$$

with $\Lambda = 0.71 \text{ GeV}^2/c^2$. The short ranged hadronic part can be described with:

$$\frac{d\sigma_{had}}{dt} = \frac{\sigma_{tot}^2(1 + \rho^2)}{16\pi(\hbar c)^2} e^{-bt} \quad (4.9)$$

It dominates at large scattering angles and can't be calculated analytically. This is the case because it is mediated by gluons which are self-coupling. Thus, the description of the hadronic part is based on empirical models. Equation 4.9 is valid for a momentum transfer range $-t > 10^{-4} \text{ GeV}^2/c^2$. σ_{tot} is the total hadronic cross section which has to be determined experimentally as well as the slope parameter b and the ratio ρ of the real to imaginary part of the scattering amplitude at a momentum transfer of zero.

$\frac{d\sigma_{int}}{dt}$ is the last component of the total cross section for elastic proton-antiproton scattering and represents the interference part given by:

$$\frac{d\sigma_{int}}{dt} = \frac{\alpha_{em}\sigma_{tot}G^2(t)}{\beta|t|} e^{-\frac{1}{2}bt} (\rho \cos(\delta) + \sin(\delta)) \quad (4.10)$$

where δ denotes the Coulomb phase which also depends on ρ and the slope parameter b and can be parameterized by

$$\delta = \alpha_{em} \left(\gamma + \ln\left(\frac{b|t|}{2}\right) + \ln\left(1 + \frac{8}{\Lambda^2 b}\right) + \frac{4|t|}{\Lambda^2} \ln\left(\frac{4|t|}{\Lambda^2}\right) + \frac{2|t|}{\Lambda^2} \right) \quad (4.11)$$

with $\gamma \approx 0.577$. The interference part is only a minor contribution to the total cross section as it is dominated by the Coulomb part at lower momentum transfers and the hadronic part at higher ones. The model independence of the Coulomb interaction makes it an ideal candidate for a precise luminosity determination.

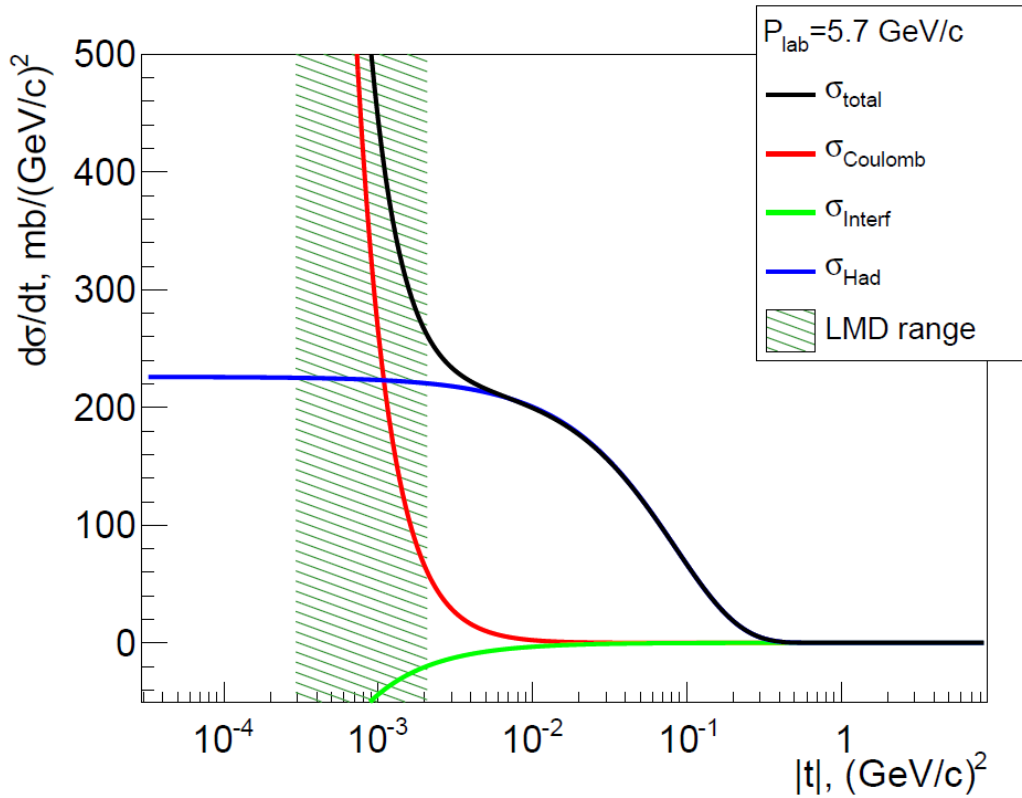


FIGURE 4.1: Differential cross section of elastic proton antiproton scattering in dependence on the momentum transfer $|t|$ with contributing hadronic, Coulomb and interference part at $p_{lab} = 5.7 \text{ GeV}/c$ [106].

As the hadronic part can't be calculated analytically it must be modeled otherwise. Two possible models are the Dual Parton Model (DPM) model [107] and the E760 model which is named after the E760 experiment in which it was used to extract the luminosity. In figure 4.2 the contributing parts to the differential cross section (4.5) are shown integrated over 3-9 mrad for both models in dependence on the beam momentum. Both models predict only slightly different results in terms of relative contributions of the different parts contributing to the cross section.

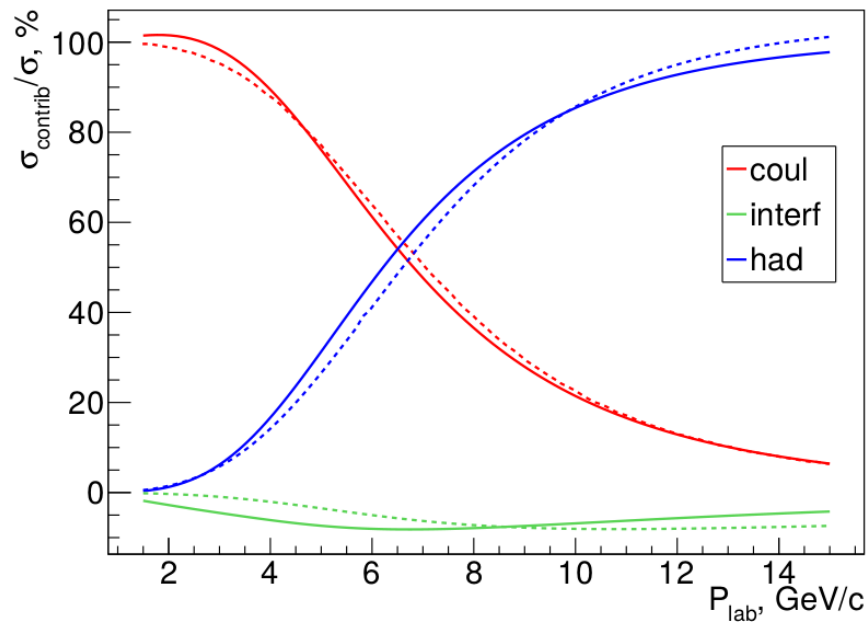


FIGURE 4.2: Contribution of the terms of the elastic $p\bar{p}$ scattering cross section integrated over the scattering angle θ between 3-9 mrad (solid line - estimation according to DPM elastic scattering model [108, 107], dashed line - estimation according to E760 model) [106].

Regardless of which model is used it will result in an uncertainty on the cross section. For the DPM model the relative uncertainty of the cross section integrated over several small polar angle θ ranges in dependence on the beam momentum is shown in figure 4.3. At low beam momenta where the coulomb part is the preminent contribution the uncertainty is expected to be lower than 2%. For beam momenta between 3.5 GeV/c and 12 GeV/c both the coulomb and hadronic part contribute and the uncertainty fluctuates with the largest values reaching almost to 10%. For beam momenta over 12 GeV/c rises to up to 20%.

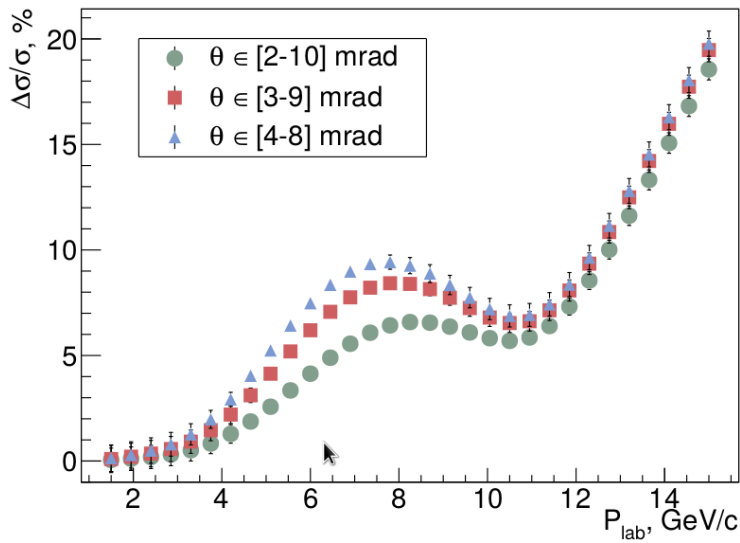


FIGURE 4.3: The relative uncertainty of the cross section integrated over different polar angle range in dependence on the beam momentum P_{lab} (for the DPM model) [106].

In figure 4.4 the relative uncertainty of the cross section integrated over several polar angle θ ranges in dependence on the beam momentum is presented for the E760 model. For low beam momenta it is larger than with the DPM model with the largest value slightly above 2% while it decreases to about 0.1% in the range of 3-6 GeV/c. The E760 model is so precise in the range of 3-6 GeV/c as the data to which the model was adjusted has been taken between 3.7 GeV/c and 6.2 GeV/c [105]. In the region above 6 GeV/c the uncertainty rises with the largest uncertainty reached at 15 GeV/c with about 2% again.

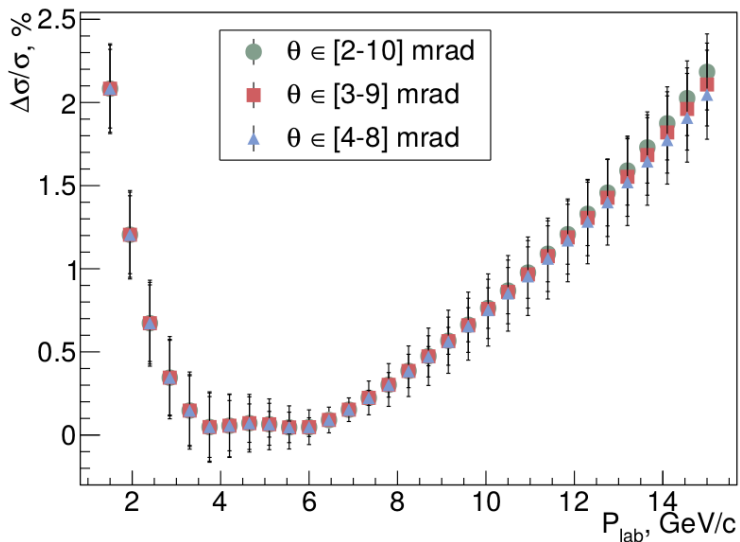


FIGURE 4.4: The relative uncertainty of the cross section integrated over different polar angle range in dependence on the beam momentum P_{lab} (for the E760 model) [106].

As the model dependence is not negligible and the luminosity detector measures the angular distribution of the elastically scattered antiprotons and not just the rate it is crucial to measure antiproton-proton elastic scattering in the relevant momentum transfer range. This will be done in the beginning of the operation of HESR and in parallel to the $\bar{\text{P}}\text{ANDA}$ measurements by the KOALA experiment dedicated to this task [57]. In figure 4.5 the measurement range of the KOALA experiment and luminosity detector in dependence on the beam momentum is shown. The blue line marks the momentum transfer at which the hadronic and coulomb part of the cross section are equal. It can be seen that the measurement range of the KOALA experiment covers the momentum transfer range of the luminosity detector at higher beam momenta. KOALA will measure the scattered antiprotons of the beam at forward angles with the prototype of the luminosity detector. The polar angle and kinetic energy of recoil target protons will be measured with a recoil detector positioned at 90° . Using a coincidence between the recoil detector and the prototype of the luminosity detector leads to the $|t|$ values of down to $\approx 10^{-3} \text{ (GeV/c)}^2$ being reached. It is expected that the parameters ρ , b and σ_{total} can be extracted with a precision better than 1% [57]. As can be seen from figure 4.5 for high beam momenta the distribution of the cross section measurement from the KOALA experiment can be taken directly for the luminosity determination of $\bar{\text{P}}\text{ANDA}$. For lower beam momenta the parameters ρ , b and σ_{tot} from KOALA will be used together with equation 4.11 to calculate the differential cross section.

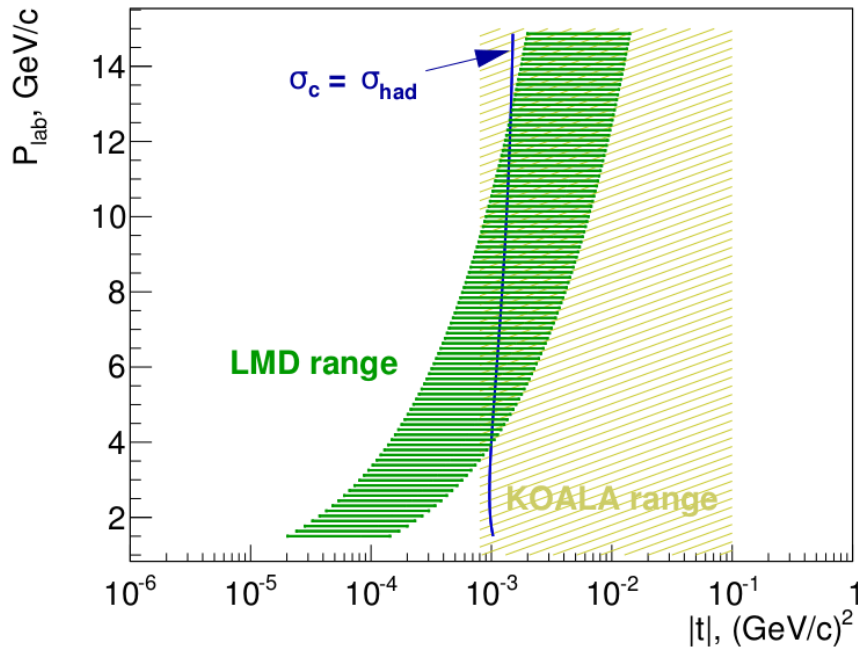


FIGURE 4.5: Luminosity measurement region in terms of momentum transfer $|t|$ at $\bar{\text{P}}\text{ANDA}$ (green) and the KOALA experiment (yellow)[106].

4.3 The Luminosity Detector

To minimize the systematic uncertainty introduced by the hadronic part of the elastic scattering cross section the measurement is performed at low momentum transfers

where the Coulomb cross section dominates. Therefore the antiprotons have to be measured at very low scattering angles. This leads to a placement of the sensors of the luminosity detector as close as possible to the primary beam in the vacuum without influencing the beam and far away from the interaction point. At 11 m behind the interaction point the luminosity detector covers an angular range of $3.5 - 8$ mrad. At larger angles the scattered antiprotons would have already interacted with the beam pipe or the forward spectrometer. Thus multiple scattering would have made them unusable for the luminosity determination. This is also the reason why the width of the beam pipe increases in steps until it reaches the luminosity detector. This prevents interaction with the beam pipe prior to the measurement of the track. Antiprotons at lower angles will be reintegrated into the beam to keep the instantaneous luminosity at high level.

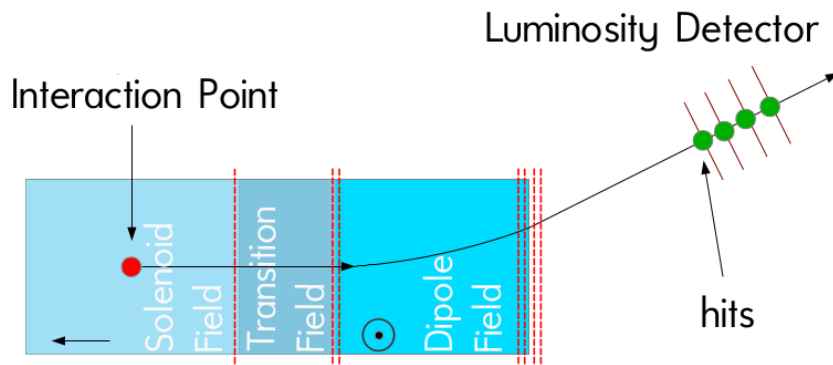


FIGURE 4.6: Schematic view of particle track from the interaction point through the magnetic fields to the detector planes of the luminosity detector[106].

In order to reconstruct the tracks of the antiprotons at least three hit positions must be measured. In principle this means that a setup of three detection layers could be used but to achieve a higher reliability in case of dead sensors or dead pixels four detection layers will be used instead. Figure 4.6 illustrates the path which the elastically scattered antiprotons take from the interaction point to the detection layers of the luminosity detector. In order to reach the luminosity detector antiprotons have to fly along the entire \bar{P} ANDA setup and hence pass through the magnetic fields of the solenoid and dipole magnet as well as the transitional field caused by the overlapping of both magnetic fields. This complicates the measurement as they have to be propagated back to the original interaction point to access the distribution of elastic scattering angles. The design of the luminosity detector as a tracking detector allows for this back propagation.

As other particles also have to pass through the dipole field tracks from concerning background reactions are suppressed. The requirements set for the systematic uncertainty for the luminosity measurement are $\leq 5\%$ for the absolute and $\leq 1\%$ for the relative time integrated luminosity between runs [109]. Also the instantaneous luminosity during a run has to be measured since the information about the bunch structure of the HESR antiproton beam should be monitored. Important factors influencing the precision of the measurement are the statistics of the reconstructed angular distribution, the precision of the measured scattering angles themselves, which is influenced by multiple scattering caused by material of the detector planes and the resolution of

the hit positions, and for the measurement of the absolute time-integrated luminosity the knowledge about the parameters ρ , b and σ_{tot} of the hadronic part of the elastic scattering model as mentioned above.

A Computer-aided design (CAD) drawing of the luminosity detector design is shown in 4.7. Preventing multiple scattering as much as possible is crucial. Therefore the detector consists of a stainless steel box containing a vacuum in which the sensors and the beam pipe reside. At the entrance to the box the main beam pipe has a diameter of 200 mm and is connected to a smaller beam pipe with a diameter of 65 mm by a very thin transition foil. This foil allows the scattered antiprotons to stay in the vacuum and interact with the sensors without passing through the beam pipe material thus reducing multiple scattering. Both the beam pipe and the detector box contain a vacuum with potentially different pressures as out-gassing of detector components may affect the quality of the vacuum. Therefore a coupled pumping scheme between box and beam pipe is used to prevent the thin transition foil from ripping. The foil is made out of a 20 μm thin layer of Biaxially-oriented polyethylene terephthalate (boPET) and a 10 μm thin conducting aluminum layer. The latter serves as electromagnetic shielding between the primary antiproton beam and the sensors of the luminosity detector.

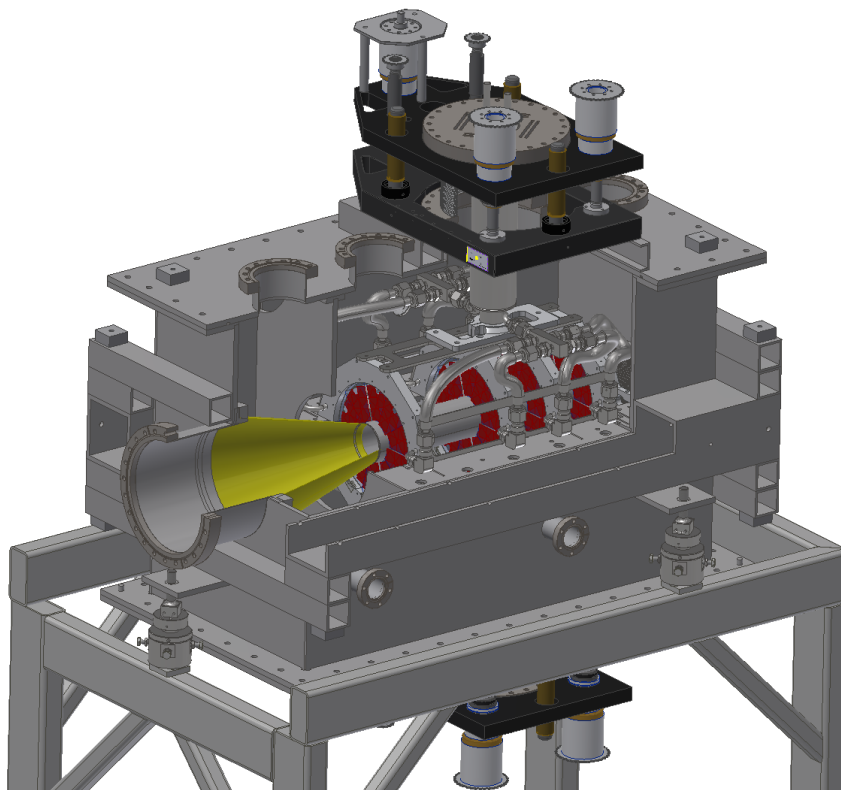


FIGURE 4.7: CAD drawing of the $\bar{\text{P}}\text{ANDA}$ luminosity detector. Elastically scattered antiprotons enter the detector through a thin transition foil (yellow) to minimize multiple scattering. They are then detected by four tracking planes based on silicon pixel sensors (red). The tracking planes can be retracted via the linear shift mechanism to prevent damage during the filling of the HESR[110].

After passing through the transition cone the elastically scattered antiprotons traverse through the four detector planes where their scattering angles are measured by silicon active pixel sensors. The first plane is located at $z = 11.24$ m behind the interaction point and it is followed by three more planes with a distance of 20 cm, 10 cm and 10 cm apart from each other. As minimal multiple scattering is crucial for a high angular resolution great care has been taken to keep the material budget as low as possible. The sensors themselves only have a thickness of $50\ \mu\text{m}$. They are glued onto $200\ \mu\text{m}$ thin Chemical Vapor Deposition (CVD) diamond wafers as support structure which provides the necessary thermal conductivity for cooling purposes while adding a minimal amount of material budget. For the electrical connection of the sensors flex cables with aluminum traces are used, as aluminum offers the right conductivity while having a lower radiation length than copper. The distance between the first and the second layer is larger to have a larger lever arm for the measurement making maximum use of the fact that the antiprotons have been affected the least by multiple scattering compared to having passed through more detection layers already. The following 10 cm distances are a compromise between mechanical spacing requirements and a compact design. Three consecutive hits would be enough to reconstruct a track but a missing hit on one plane would then prevent a proper reconstruction. Hence a design with four detector planes is chosen. Each detector half plane is composed of an aluminum support structure which is shown in figure 4.8.

The electronics to read out, control and provide power to the sensors are directly attached to this structure. 5 sensor modules with sensors are clamped into the inner part. A sensor module is a CVD diamond wafer with 3+2 sensors glued onto each side of leading to a total of 400 sensors. To cool all active components a stainless steel pipe is melted into the support structure. As a coolant Ethanol at a temperature of $-20\ ^\circ\text{C}$ is flowing through this pipe. Both half detectors are connected to a linear shift mechanism responsible for retracting the corresponding half planes. This is done to prevent excessive radiation damage to the sensors caused by bad beam conditions during injection into the HESR.

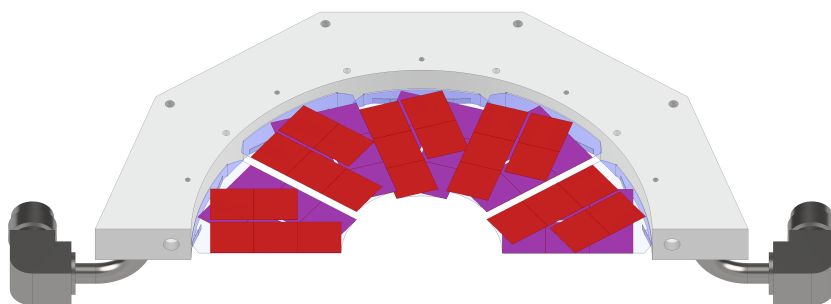


FIGURE 4.8: CAD drawing of a detector half plane without electronics attached to it. HVMAPS are glued onto CVD diamonds which are in turn clamped into an aluminum support structure containing a stainless steel pipe for the cooling liquid[110].

4.4 Sensors

The pixel sensors used for the detection of particle hits are HVMAPS [111]. They are based on normal semiconductor Monolithic Active Pixel Sensors (MAPS) technology [112] and therefore are also produced with a standard Complementary Metal-Oxide-Semiconductor (CMOS) process. The active detection area consists of radiative sensitive diode structures arranged as distinct pixels and it is integrated with the necessary readout electronics on a single piece of silicon.

The detection of particles with a semiconductor sensors relies on the formation of a pn-junction (see figure 4.9). Such a pn-junction is formed by having a contact between a p-doped and an n-doped semiconductor. As both types of material contain a surplus of free charge carriers, electrons in the n- and holes in the p-doped material, these charge carriers diffuse into the opposite material and recombine there. The net charge of the complete semiconductor is zero which means that the recombination of free charge carriers leads to stationary positively charged ions in the n-doped material and negatively charged ions in the p-doped material. Therefore an electric field is created which opposes the diffusion and eventually stops it after an equilibrium is reached at a certain depth. This charged zone devoid of free charge carriers is called the depletion zone. Applying a bias voltage increases the depth of the depletion zone. When a particle crosses the depletion zone it loses energy by creating a proportional number of electron hole pairs. The electric field inside the depletion zone causes the free charge carriers to drift towards the side with the opposite charge. As no other free charge carriers are available for recombination in the depletion zone a signal is created at the electrodes. Figure 4.9 illustrates a basic pn-junction used as a particle detector.

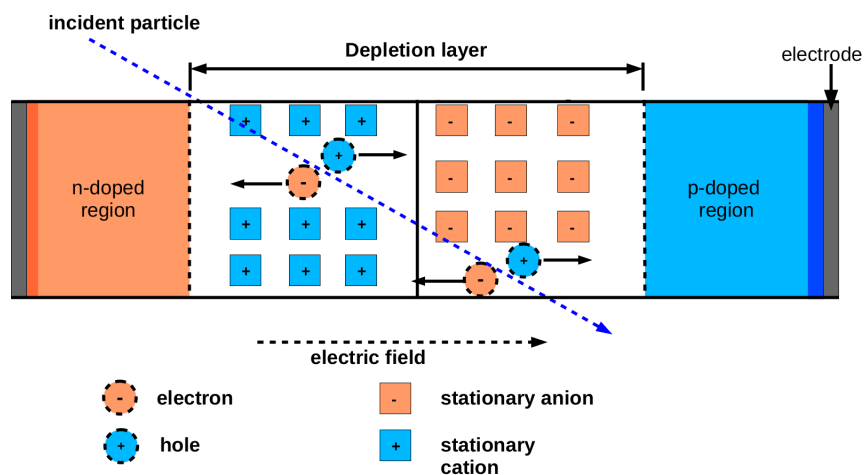


FIGURE 4.9: Usage of a pn-junction for the detection of ionizing radiation. [22]

In figure 4.10 the basic structure of a pixel on a MAPS is shown. A good charge collection is achieved by using a highly p-doped p^{++} substrate onto which a lightly p-doped epitaxial layer is grown. This structure of different dopant concentrations creates a barrier between the layers which serves to guide the electrons released by traversing charged particles. Inside of the epitaxial layer an n-well is placed to sense these electrons which pass it due to diffusion. The readout electronics for each pixel are placed

inside the p-well in form of n-type metal–oxide–semiconductor (NMOS) transistors. The pixel sizes of MAPS can be as low as $20\ \mu\text{m} \times 20\ \mu\text{m}$ and they reach an efficiency of almost 100%. The sensors can be thinned down to a depth of $50\ \mu\text{m}$ reducing the amount of multiple scattering significantly. A downside of the charge collection via diffusion is that it leads to high charge collection times of about 20 to 150 ns. Another disadvantage of the structure of MAPS is that it is not possible to place any p-type metal–oxide–semiconductor (PMOS) based structures such as discriminators in the active area as the necessary n-wells would result in parasitic charge collection. Therefore any PMOS transistor must be placed in the periphery of the silicon chip. For these reasons one set of readout electronics per column is placed outside of the active area. All pixels of a row are readout in parallel and each row is then readout one after the other which is called rolling shutter. This rolling shutter mode of readout leads to long readout cycles with typical values of $180\ \mu\text{s}$ [113] rendering standard MAPS unsuited for the luminosity detector.

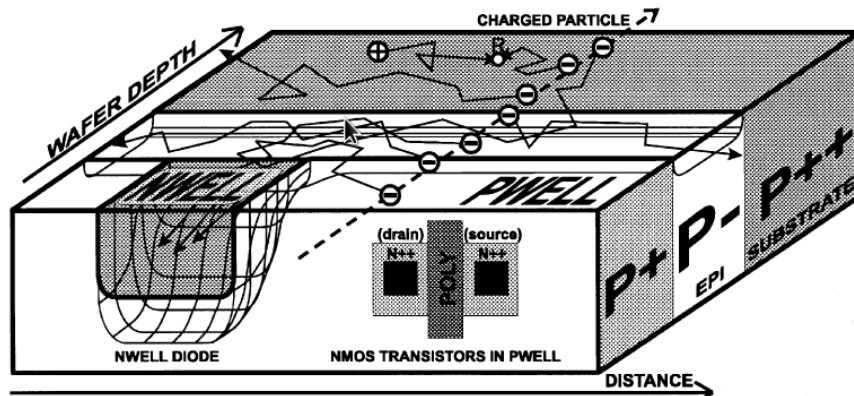


FIGURE 4.10: Scheme of the pixel structure of a MAPS. The sensing n-well is grown into a p-epitaxial layer while the front end electronics transistors are integrated into the p-well [112].

Figure 4.11 shows the basic structure of HVMAPS. They use high voltage CMOS technology to circumvent the disadvantages of standard MAPS. Pixels consist of lowly doped n-wells placed inside of a p-substrate. To these a reverse bias voltage in the order of about 60 V to 120 V can be applied leading to a depletion zone thickness of about $10\ \mu\text{m}$. NMOS as well as PMOS transistors are located inside of the n-well in low-voltage CMOS technology which allows for complex circuits. The electron hole pairs caused by passing charged particles are collected by drift as there is a high electric field in the depletion zone. This process results in a faster charge collection in the order of a few nano seconds compared to the slower 20 to 150 ns of MAPS. Thus the sensors are capable of keeping up with the planned read out rate of 40 MHz.

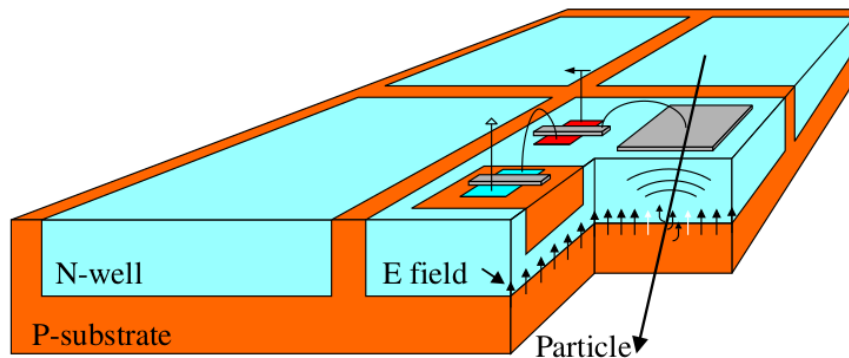


FIGURE 4.11: Structure of HVMAPS [111].

The sensor chosen for use in the luminosity detector is the MuPix which is also used in the Mu3e experiment [114]. Figure 4.12 shows the layout of a MuPix. It is divided into the analog part, containing the pixels responsible for the collection of the charge left behind by passing particles and a digital part which converts these signals into digital row and column hit information. The dimensions of such a sensor are $2.3 \times 2 \text{ cm}^2$ with a pixel size of $80 \times 80 \mu\text{m}^2$ and a part for digitization with a width of 3 mm below the active area of $2 \times 2 \text{ cm}^2$. Power consumption is a downside of the HVMAPS which lead to the requirement of high thermal conductivity for the material they are glued to. The expected value which has been seen in measurements is $2.5 \text{ mW}/\text{mm}^2$. It has been shown with simulations and prototype measurements that up to $7 \text{ mW}/\text{mm}^2$ are acceptable for the cooling system of the luminosity detector[62].

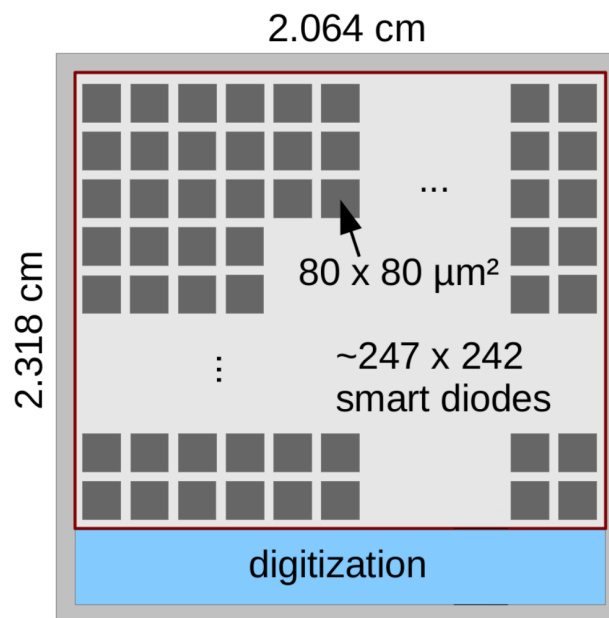


FIGURE 4.12: Layout of an HVMAPS showing the analog pixels and the digitization part [109].

In every electrical component there is a time difference between an input signal and its output signal. This is called latency and has to be accounted for when designing a system. The most simple reason for this is cable length. As this is constant it can easily

be adjusted for. Another influence on the latency is the energy deposition of a particle in a sensor pixel. Depending on the total amount of energy deposited in one pixel the number of generated electron-hole pairs changes and therefore the amplitude of the input signal varies while the basic signal shape stays the same. A comparator compares the signal at its input to a certain threshold. If the height of this signal exceeds the threshold the comparator will produce a signal at its output which will finally result in a timestamp determining the time at which the particle hit the sensor. For larger signal amplitudes the signal reaches the threshold faster than for smaller ones. Therefore the total latency until a response can vary. This means that two particles passing different sensors or even different pixels of the same sensor at the same time are measured at a slightly different time depending on their energy deposition. As the sensor is thin the energy deposition inside of it has a broad Landau shape which leads to large timing distribution. This effect is generally called time walk. The time until a signal falls below the threshold is affected in the same way so the Time over Threshold (ToT) is measured in addition to the latency to quantify the effect. In figure 4.13 the resulting distribution of latencies is shown for the MuPix 6 prototype [22] in itself and as time walk by showing it in dependence on the time over threshold. The latency is spread over approximately 75 ns. This spread means that all hits belonging to the same physical particle track can be assigned different time stamps. Looking at the distribution of the latency and assuming a time stamp granularity of 25 ns shows that most particle tracks are covered by three adjacent time stamps. Such a combination of adjacent time stamps is called a time window. It is not certain if time walk will be corrected in the final version of the sensors or if a time over threshold information will be available with enough precision to allow for a later correction of time walk. For these reasons a worst case scenario with no time walk correction is assumed.

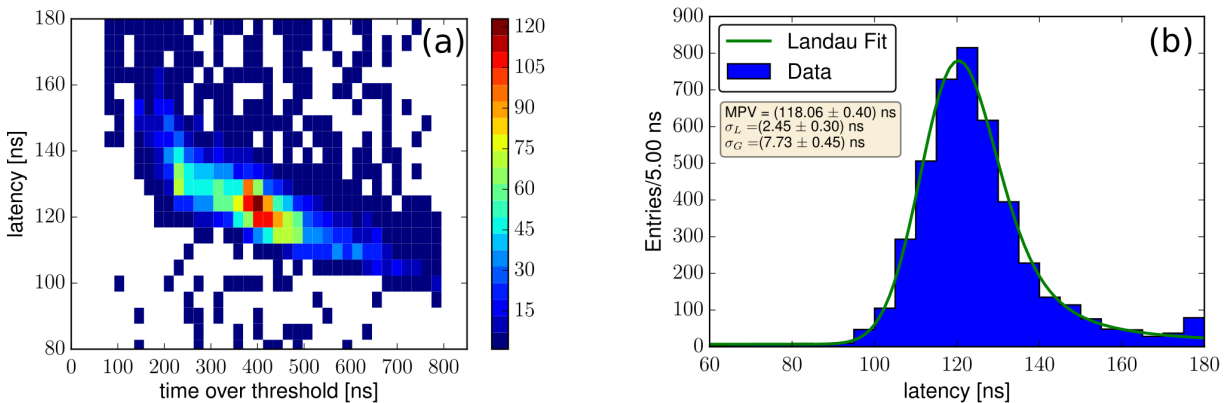


FIGURE 4.13: Time walk (a) and latency (b) distribution for a 1 GeV electron beam measured with the MuPix 6 prototype [22]. The latency of the signal is spread over ≈ 75 ns.

4.5 DAQ Scheme

Data which are registered by the 400 sensors will be transferred by the Data Acquisition (DAQ) system to storage. Within this processing could be necessary which may include sorting, filtering and online track reconstruction. To reduce the amount of data

collected by the luminosity detector to a more manageable level a software trigger will be used. Besides spatial information a detector hit also includes timing information. The timing information of each sensor will be correlated with timing information of the SODA network [115]. SODA is a system to distribute a common clock and control signals and therefore is responsible for synchronizing the data of all sub detectors of the $\bar{\text{P}}\text{ANDA}$ experiment. It uses a point-to-multipoint optical network to achieve this.

As the LMD operates with antiproton proton elastic scattering events exclusively its data is disjoint with the events relevant for the $\bar{\text{P}}\text{ANDA}$ physics program. Therefore the event building network does not require the data from the LMD. This allows for a separate DAQ independent of the main DAQ except for the integration of SODA.

Figure 4.14 shows a sketch of the data acquisition scheme for the $\bar{\text{P}}\text{ANDA}$ luminosity detector. Elastically scattered antiprotons are detected by the 400 MuPix HVMAPS which are distributed over the four planes of the luminosity detector. Each plane of the detector contains 100 sensors and is build of two half planes with 5 modules each. Onto both sides of the module 5 sensors are glued. This leads to each plane effectively having two layers of sensors with a slightly different z coordinate. The sensors are sending a serial data stream to FPGA-boards via Low-voltage differential signaling (LVDS). The main purpose of these boards is to de-serialize the data stream and perform a clock recovery. Additionally the SODA signals will be received by these boards and a first sorting of data by timestamp will be performed followed by combining hits in adjacent pixels to clusters and merging hits from front and backside sensor modules. The TRBv3 [116] with four peripheral and one central FPGA was chosen for this. As there are only 6 serializer/deserializer circuits per peripheral FPGA about 17 boards have to be used to collect the data streams from all sensors. The data streams from all TRBv3s will be send via an optical switch to an altera FPGA board where sorting of all hits by time and plane is performed. This FPGA board for hit processing will be connected to a conventional PC via a Peripheral Component Interconnect Express (PCIe) connection. On this PC it will be possible to perform further calculations such as track finding on either a CPU or a GPU. The found tracks will then be used to decide which hits will be saved to storage.

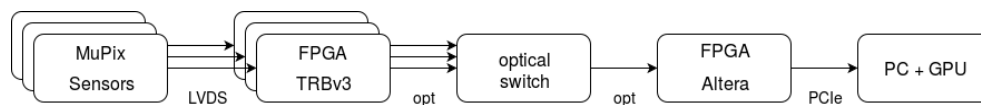


FIGURE 4.14: Sketch of the data acquisition scheme for the $\bar{\text{P}}\text{ANDA}$ luminosity detector showing the different levels of hardware to process data acquired by the sensors.

Chapter 5

CPU and GPU Architectures

In this chapter two types of processors used in modern computers will be described in detail. The first is the Central Processing Unit (CPU) which is the component responsible for all general calculations in a computer. Beside the CPU most modern computers also contain some kind of Graphics Processing Unit (GPU). GPUs are used for calculations needed for graphical output. For general calculations it is often the case that they are dependent on each other. Therefore they have to be executed sequentially. Calculations for graphical output on the other hand are usually independent from each other and can be calculated in parallel. This difference for general purpose and graphical calculations is the reason why CPUs and GPUs have different architectures. In the beginning of their existence GPUs have been exclusively used for their original purpose of graphical calculations. As independence from each other is not just a feature of graphical calculations GPUs are nowadays also used for different purposes.

5.1 CPU Architecture

The central part of a computer is the CPU. As it is responsible for most calculations happening in a computer it has very general design to handle all tasks reasonably well. A central part of a CPU or other types of processors which performs the actual calculations is called an Arithmetic Logic Unit (ALU). It gets and returns data via so called input and output nets while receiving the instructions of what to do with the data as so called opcode. In addition the ALU also has status inputs and outputs conveying information such as if arithmetic overflows occurred, if all bits of a result are zero or if the number of set bits is even or odd. In general any type of processor can contain multiple ALUs.

For the longest time the most visible improvement in performance has come through ever increasing clock frequencies. In 1971 Intel released the Intel 4004 with an initial clock frequency of 108 kHz [117]. The fastest base clock frequency of an Intel processor has so far been 4.3 GHz reached by the Core i7-7740X in 2017 [118]. Considering that such a base clock frequency is rare and that the Xeon E3-1290 v2 already reached 3.7 GHz in 2012 [119] a limit in this formerly ever increasing clock frequency seems to have been reached. The clock frequency is not the only thing which has been improved. Over the years the number of transistors in a CPU has increased tremendously, allowing for improvements in architecture. This is described by Moore's law which states that the number of transistors on one physical chip doubles approximately every two years [120].

The limit for clock frequency can be explained when examining the power consumption of a CPU. It can be approximated by the following equation [121]:

$$P = C \cdot V^2 \cdot f$$

where P is the consumed power, C the capacity, V the voltage and f the frequency. As transistors need to accumulate charge to switch their state raising just the frequency is not enough. As the current and thereby the voltage is not high enough anymore to reach the required charge level the frequencies can only be increased in connection to an increase in voltage. The relation between these two quantities is $f \sim V$. This means that a linear increase in frequency results in cubic growth of the power consumption. At a certain limit it becomes impractical to remove the excess heat generated by the CPU so changes in CPU architecture [122] itself are necessary for increasing the overall performance.

Instruction Level Parallelism

A category of improvements used for single core CPUs is Instruction Level Parallelism (ILP). A processor which can handle ILP is called superscalar. One technique of ILP is called instruction pipelining. Every high level instruction coming from software consists of smaller instructions handled by different parts of the CPU. This means different sub-instructions can be executed at the same time. To keep the whole CPU busy a pipeline is implemented. This pipeline is filled with sub-instructions from different high level instructions.

Branch prediction

Another technique is branch prediction which works on the control structures used in software. As the name suggests a CPU tries to guess which of the different branches in a control structure is the most likely to occur before the preceding condition has been evaluated. The related instructions are then executed speculatively. To a certain degree this can be anticipated statically at compile time but CPUs also contain hardware to make these decisions. As software usually contains instructions which are not data dependent on each other a lot of sub-instruction can also be executed in a different order than suggested by the original program. This is called out-of-order execution. Techniques like these can already be done statically by the compiler. This way no action has to be taken by the hardware to handle instructions differently than presented to it.

Single Instruction Multiple Data

In contrast to instructions being handled in parallel it is also possible for data to be independent. This is called data parallelism. When parallel data is processed with the same instruction in one processing unit this is called Single Instruction Multiple Data (SIMD). In figure 5.1 it is schematically shown how one processing unit handles multiple parallel data streams with one instruction stream resulting in parallel result streams. In practice this concept has been implemented in several ways. Processors implementing this concept with a very large amount of data are called vector processors. A historical

example for this is the Cray-1 [123] released in the 1970's. As Data parallelism is a very common occurrence in software development this concept has also been integrated into modern multipurpose CPUs. Modern CPUs usually contain processing units which are SIMD capable although on a much smaller scale.

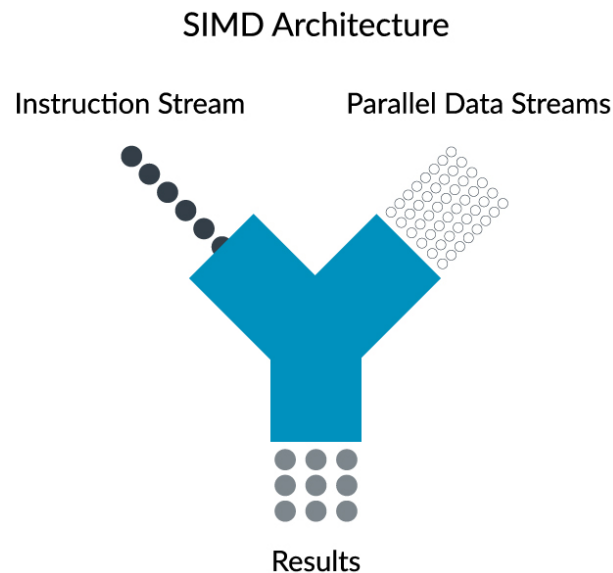


FIGURE 5.1: Schematic of SIMD architecture [124]. Instructions are executed on multiple parallel data streams at the same time yielding parallel result streams.

Memory

Another very important point impacting the performance of a CPU is the memory structure. In general there are several different stages when it comes to storing data. For permanent storage a computer contains disk storage. While these offer an enormous amount of storage space they are also incredibly slow (in the order of ms) compared to the duration of a CPU clock cycle. For this reason a computer also contains volatile main memory with faster access times of $\approx 10^2$ ns which is located on the mainboard. It is made of Dynamic Random Access Memory (DRAM) and usually in the order of $10^1 - 10^2$ GB. These access times are still quite slow so a CPU contains some on-chip memory made of Static Random Access Memory (SRAM) called cache. It is organized in several levels (usually three) with both increasing size and access times. The first two levels (L1 and L2) are in the order of $10^1 - 10^2$ kB while the third (L3) is in the low MB range. Access times are $10^0 - 10^1$ ns. Whenever the CPU would read or write data to a location in the main memory it will check if the data is already available in the cache. If this is not the case this is called a cache miss and increasingly higher levels of memory are accessed. Data is transferred to these caches in blocks and every time it gets new data while already being full a decision has to be made which data to keep and which to delete or send to a higher level. In general L1 cache is specific to a single CPU core while the L3 cache is shared between multiple cores. L2 cache can either be used by only a single core or multiple cores depending on the architecture of a specific CPU. An example of this kind of memory architecture is shown in figure 5.2. Some CPUs that

have integrated GPUs have an additional L4 cache which serves as a cache to which both the CPU part and the GPU part have access. The exact structure of these caches and the algorithms used to fill them have a huge impact on the performance of the software running on a CPU and it varies between different CPU models. The fastest and smallest type of storage is a register. All data directly being involved in calculations is stored there. In contrast to the main memory or cache these are not made Random Access Memory (RAM) but instead are constructed out of circuits called flip-flops. Registers are very specialized and only contain data in scale of bits. There are registers holding the instructions which need to be performed as well as user accessible registers containing values to be processed, addresses or different status values.

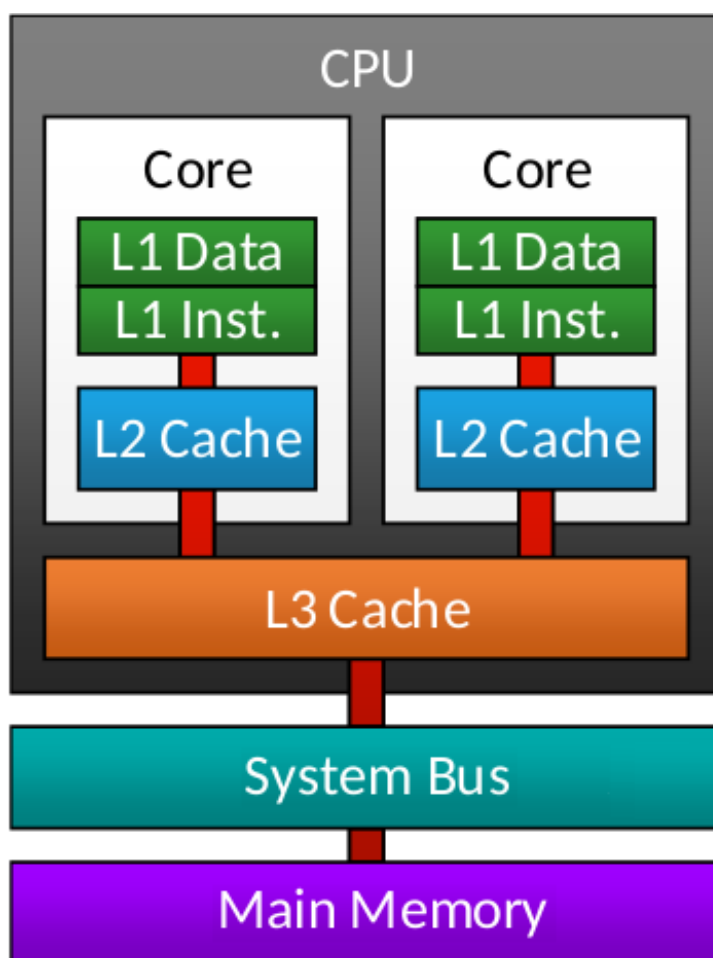


FIGURE 5.2: Example schematic of a CPU memory structure. L1 and L2 caches are part of a specific core while the L3 cache is shared between the two cores. The whole CPU is connected to the main memory via the system bus [125].

Thread Level Parallelism

Besides the already mentioned levels of parallelism there is also Thread Level Parallelism (TLP). In the most extreme case this can mean that two completely independent programs are running at the same time but it also includes a single program running

multiple threads doing different or similar things. This is opposed to data parallelism in which the exact same instructions are executed on multiple data. TLP exists in several different conceptual forms.

Without any form of TLP only one thread can be executed by a CPU at a time. In case of cache misses this means that there are some cycles during which the CPU does not execute any instructions and just waits for new data (illustrated in figure 5.3 (a)). The simplest form is multithreading. In this case a single CPU core contains the component to control multiple threads at once but is only able to handle multiple instructions of one thread at the same time. This is useful when a thread encounters a cache miss causing a longer latency. While parts of the CPU are busy waiting for data the other functional units can be used to process another thread. This concept is shown in figure 5.3 (b) still does not use all components a CPU has available. An extension of multithreading is called Simultaneous Multithreading (SMT). In this case different functional units of a CPU core can handle instructions from multiple threads at once instead of completely switching between independent threads. This is illustrated in figure 5.3 (c). However SMT means that threads on a CPU with SMT capabilities still have to share functional units and can not be processed completely in parallel. To achieve this level of parallelization chip multiprocessing is needed. This usually means that a single CPU contains multiple identical cores which can act independently from each other. The concept of chip multiprocessors is shown in figure 5.3 (d). Each of the separate cores of a multiprocessor has one or two levels of cache for itself while there is also some cache which is shared between multiple processors. This further complicates cache management and has an impact on computational performance. Real problems tend to fall on a continuum of all the different types of parallelism. For this reason modern CPU architectures contain most of the presented concepts at the same time.

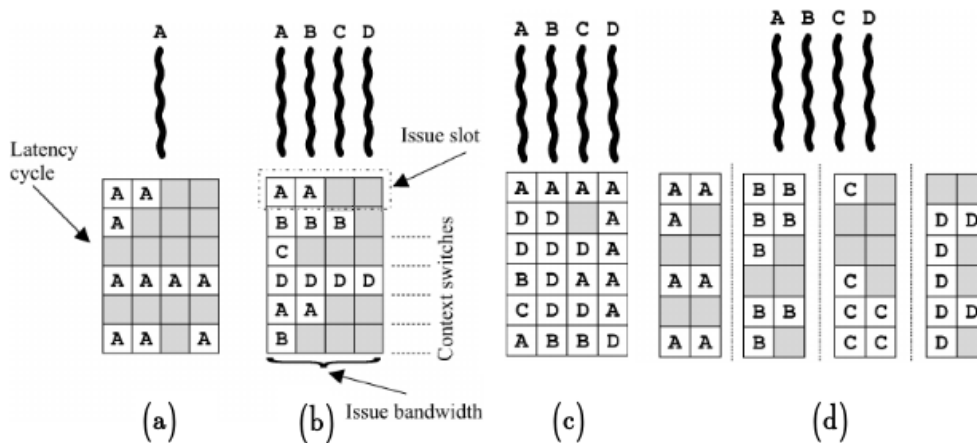


FIGURE 5.3: Examples of TLP. Each row represents a latency cycle with different functional units shown as squares. The instructions of different threads are shown as letters. (a) Singlethreaded, (b) basic multithreaded, (c) simultaneous multithreading, (d) chip multiprocessor. Modified from [126].

5.2 GPU Architecture

Another processing component of a computer is a GPU. As the name suggests it was originally developed exclusively for graphical computations. The nature of graphical computations is highly parallel and at some point it was realized that the architecture of GPUs could be used for non graphic computations as well. The most obvious difference between CPU and a GPU is the number of ALUs. Figure 5.4 is a simplified schematic illustrating this. A CPU contains a lower number of cores which are more complicated to be able to handle a lot of different tasks in a fast way. Contrary to that a GPU has a lot of simpler cores with less control structure which enable it to handle more specific tasks faster. Besides the difference in number of cores the schematic also illustrates that the memory architectures differ. There is a relatively large amount of DRAM as main memory for both processors but the cache on a GPU is smaller and more distributed.

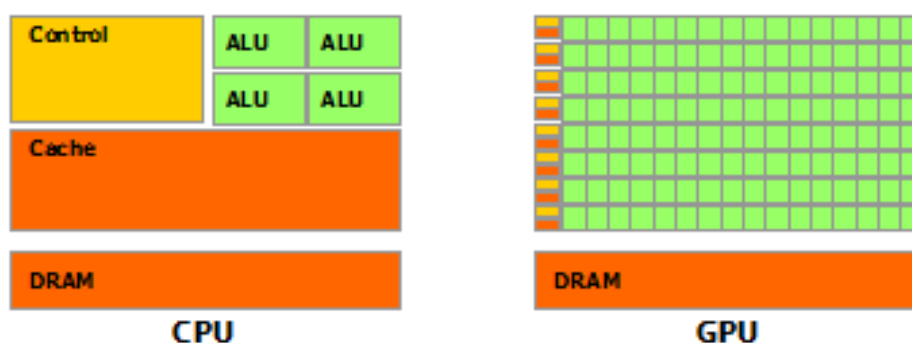


FIGURE 5.4: Schematic of CPU and GPU. A CPU has a few very powerful components while a GPU has lot of basic components [127].

When looking at the structure in more detail more distinctions have to be made including what a core actually is. The Fermi architecture of Nvidia GPUs will serve as an example case. It has to be kept in mind though that details vary between different architectures. The layout of the Fermi GPU is sketched in figure 5.5. In general GPUs contain a number of Streaming Multiprocessor (SM)s in roughly the same order of magnitude as there are cores in a CPU. Fermi has 16 of these SMs arranged around a common L2 cache between blocks of main memory. The L2 cache receives its data via a host interface which also connects the CPU and GPU via PCI-Express. The different threads which are executed are distributed to the different SMs thread schedulers by the GigaThread global scheduler. A SM itself is shown in more detail in figure 5.6. Similar to a CPU core it has a L1 cache but in this case this lowest level cache is shared between 32 calculation units Nvidia calls CUDA cores. These in turn contain basic floating point and integer units performing the actual calculations. In addition to these CUDA cores a SM contains a number of Special Function Units (SFUs) which contain circuits for calculating functions like sin or cos. For floating point operations it must be kept in mind that the number of units handling single or double precision can vary significantly between GPUs. Another component of a SM are the Load/Store Units (LD/ST) which are responsible for calculating source and destination addresses for the threads. When it comes to running actual threads on a GPU they are organized as groups of 32 threads

which Nvidia calls a warp. However a SM does not contain any structure for branch prediction or even the necessary logic to execute different branches of the same if-else statement in different threads belonging to the same warp. If conditional branches diverge in warp related threads only the threads taking the same branch will be executed while the others will be suspended until all threads containing the first branch have completed it. This is illustrated in figure 5.7. If one type of branch is done the other types of branches will be executed.

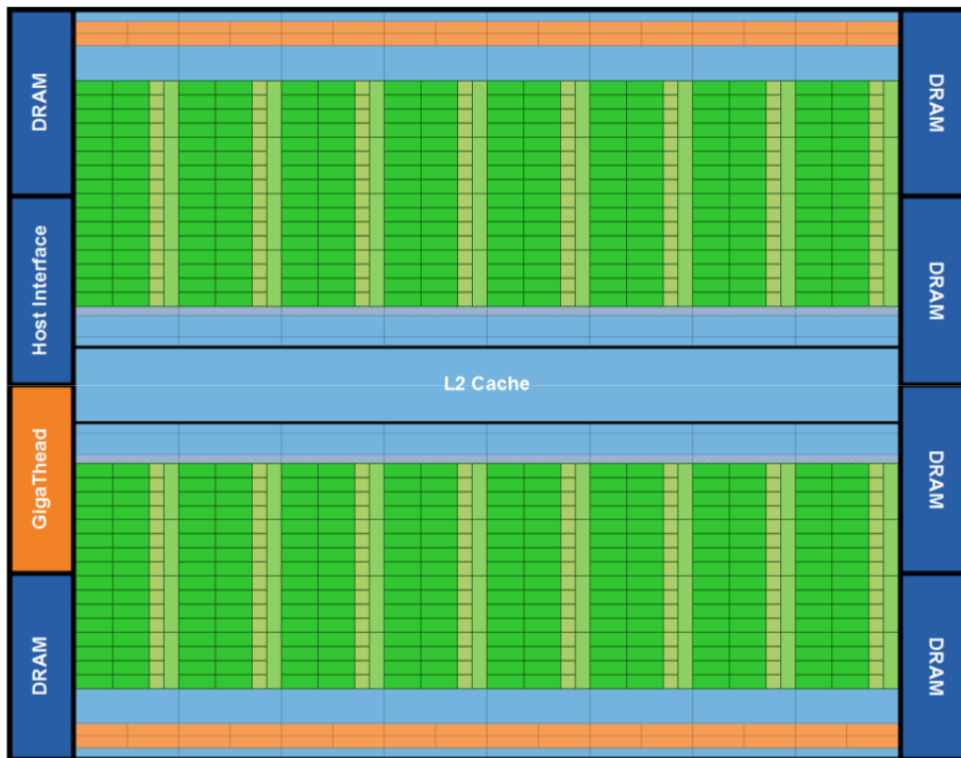


FIGURE 5.5: Schematic view of the Fermi GPU architecture. Basic processing units are shown in green and are grouped into 16 SMs [128].

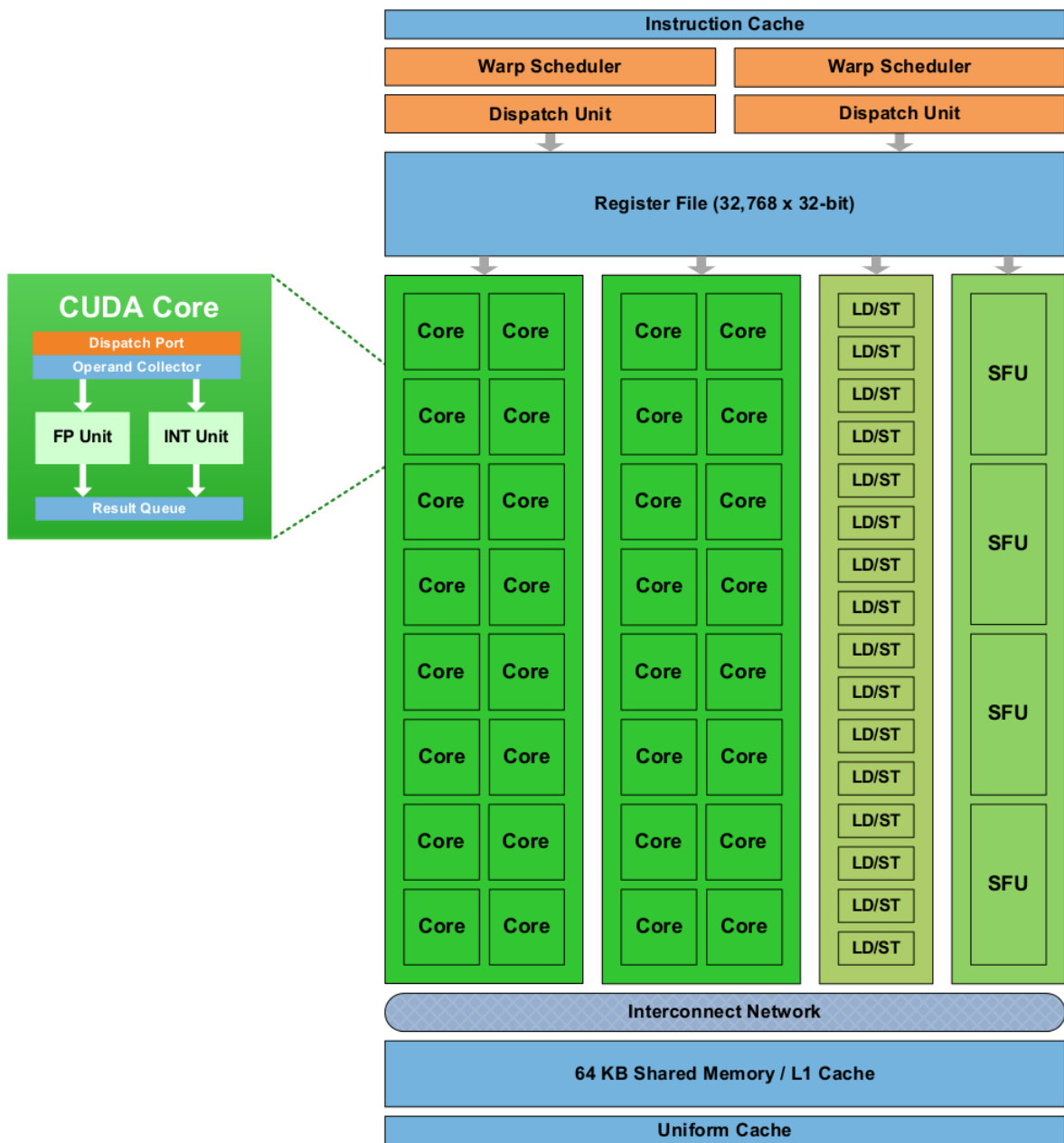


FIGURE 5.6: Schematic of a SM consisting of memory, control units and cores for the actual calculations [128].

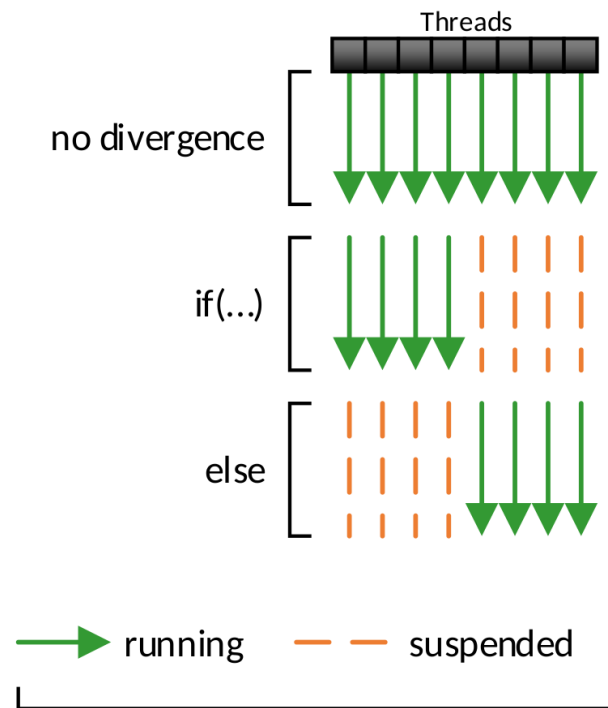


FIGURE 5.7: Whenever conditionals are processed and different branches are taken by different threads they are not processed in parallel [125].

CUDA programming model

To use their GPUs for a general purpose Nvidia provides a general purpose parallel computing platform and programming model called CUDA. With CUDA C it offers an extension to the C programming language which allows programmers to define C functions to run on the GPU. These functions are called kernels. The parallelism on the software level is introduced as threads and blocks. In general kernels are started from C code executing on the CPU which is usually called host in this context. Kernels themselves are executing on the GPU. The level of parallelism is given to a kernel via the number of threads n_t and blocks n_b while the complete structure is called a grid [127]. This is shown schematically in figure 5.8. Since CUDA version 5.0 kernels do have the option to also invoke kernels themselves. This is called dynamic parallelism. The initial kernel call still needs to be done by the host device though. Some devices also have the ability to execute multiple kernels in parallel.

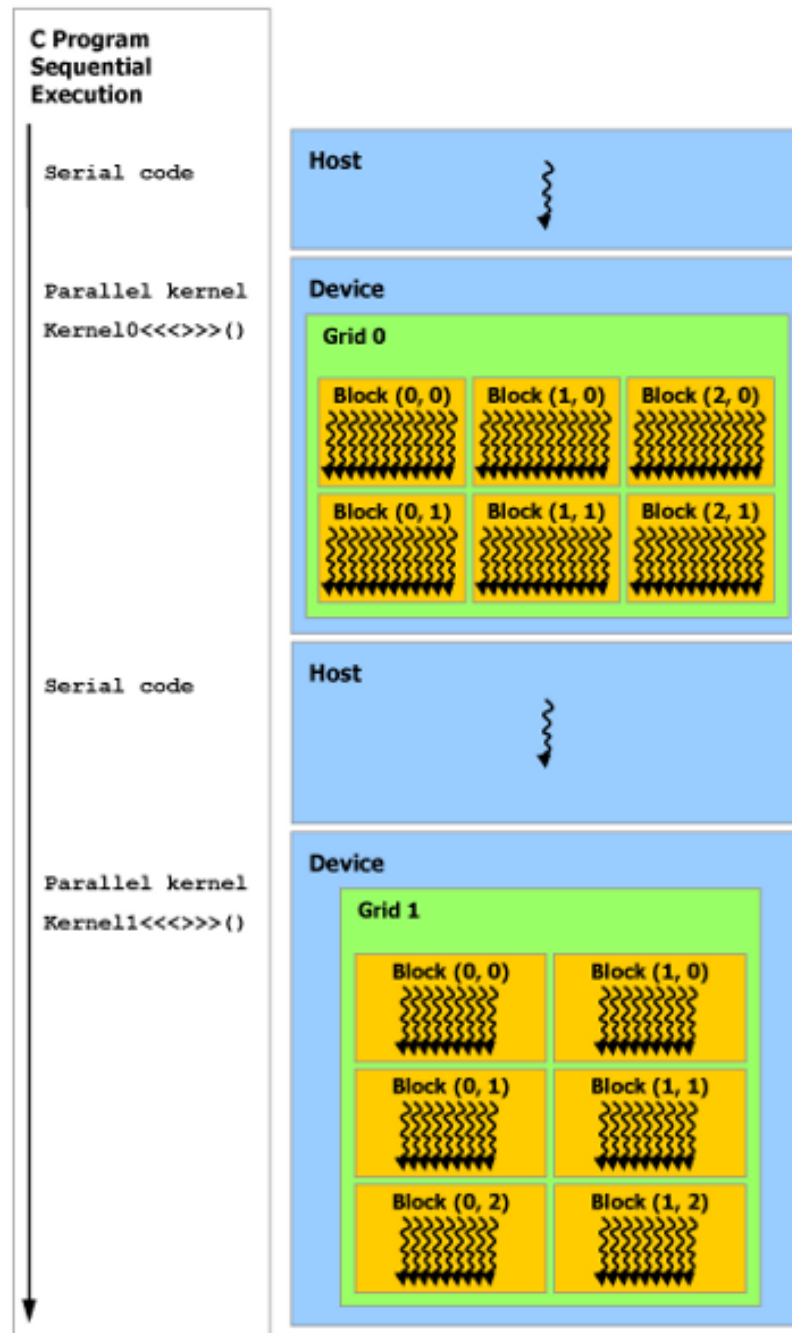


FIGURE 5.8: CUDA programming model. Serial code executes on the host (CPU) while parallel code executes on the device (GPU). Threads are represented by wavy arrows. [127]

A block contains the number of specified threads n_t so that the total number of threads is $n_{threadsTotal} = n_t \cdot n_b$. Each block is handled by a single SM. Starting a kernel with more blocks than there are SMs leads to the additional blocks being processed sequentially by the SMs. This is schematically illustrated in figure 5.9.



FIGURE 5.9: CUDA program block structure. Each block is assigned to one SM for processing [127]. Depending on the number of SMs in the GPU more blocks can be processed in parallel.

Memory

Concerning memory there are things to be considered in general when comparing CPUs and GPUs. The main memory connected to CPU and GPU are separate entities. Therefore any data which is to be processed on the GPU needs to be transferred to the GPU main memory first. In principle this introduces latency but a data transfer can happen in parallel to a kernel execution on different data. It is possible to mitigate this to a certain degree if a continuous data stream needs to be processed. The latency of a data transfer also depends on how the data is structured. Transferring large chunks of data is faster than transferring data which is more structured. The memory structure of a GPU is illustrated in figure 5.10. The main memory of the GPU is called global memory and is located off-chip and consists of DRAM. It is comparable to the main memory used by a CPU. Global memory is accessible to all threads. Local memory on the other hand is only accessible by a single thread and only used for temporary data storage during the lifetime of a thread. Contrary to the name local memory is also located off-chip as DRAM and has the same access times as global memory. A special kind of memory related to the originally intended use of GPUs as devices for processing graphics is texture memory. It also consists of DRAM located off-chip. It is specifically designed for two dimensional spatial locality. Analog to main memory and cache there is also a texture cache located on-chip. Depending on the specific GPU architecture the texture memory could be part of the global memory with a different readout scheme or a separate memory chip. Texture cache could also be a part of the existing L1 or L2 caches or be a separate block of cache. Unfortunately the specific design is usually not published by the GPU vendor. Threads belonging to the same warp reading data from memory

addresses close to each other in a two dimensional sense achieve the best performance with this type of memory. Sometimes threads all require the same constants so instead of using inefficient general purpose global or local memory there is also constant memory and cache available. When threads from the same warp all request memory from the same location the memory access can be as fast as access to a register. Both texture and constant memory are accessible by all threads. Another feature of the memory organizational structure is that all threads in a block have access to a shared memory. This access enables them to cooperate on certain tasks. This type of memory actively usable by the programmer is unique to a GPU. It is in principle a cache which can be explicitly accessed by the programmer. Shared memory and registers are specific to individual Multiprocessors located on the GPU chip.

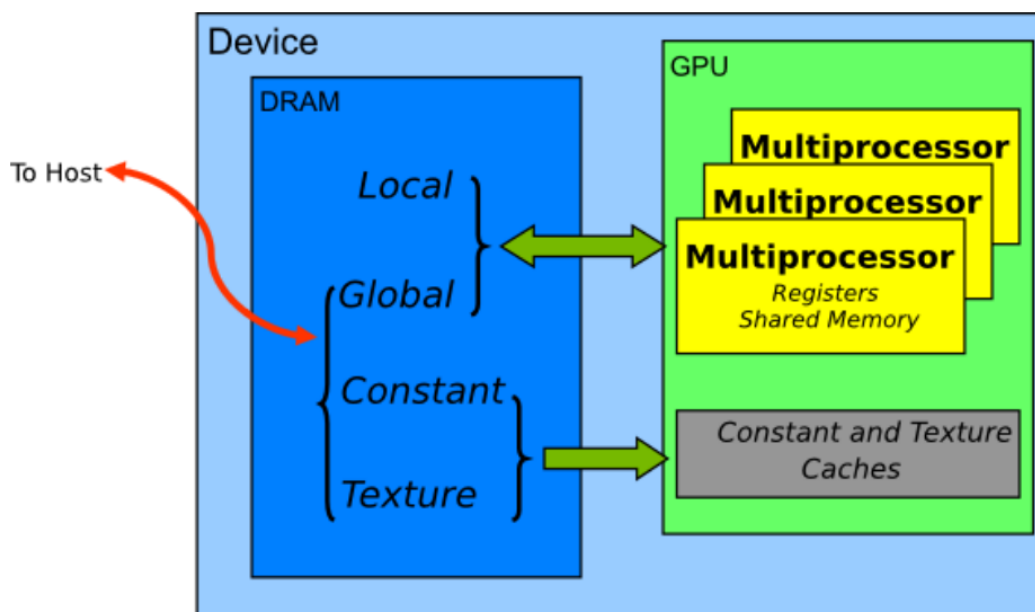


FIGURE 5.10: Schematic of different types of memory on an Nvidia GPU.[129].

The way in which data on the GPU is accessed has a strong effect on computation time. The large number of cores on a GPU results in a memory design leaving only limited resources for a single thread. To gain high performance neighboring threads should be restricted to a certain degree of locality when accessing memory cells. Some examples for memory access are shown in figure 5.11. The simplest option to achieve optimal memory access is when adjacent threads access adjacent memory locations. As long as adjacent threads access only a very limited range of memory random access also yields optimal performance. This limited range is based on the fact that data is transferred from off-chip memory to caches in groups of defined byte lengths. These groups of data are aligned to each other. Should adjacent threads access more than one group of data an additional memory transfer is required. The number of independent memory transfers increases with the range which adjacent threads need to access. Each of these memory transfers might contain a lot of data which is not needed by individual threads. Therefore this leads to less than optimal performance. This negative effect on performance of more distributed memory access is more severe on a GPU as there are less sophisticated

control structures than on a CPU. In the case when only read operations are performed many threads accessing the same memory location is also an optimal memory access. Several threads trying to write to the same memory location are also a problem. The different threads are either overwriting data from each other in an unpredictable way or the write actions have to be performed as atomic operations. Atomic operations are executed sequentially. This means that threads effectively block each other and the advantages of performing calculations in parallel are lost. So in contrast to reading data the same access pattern as for write operations has to be avoided.

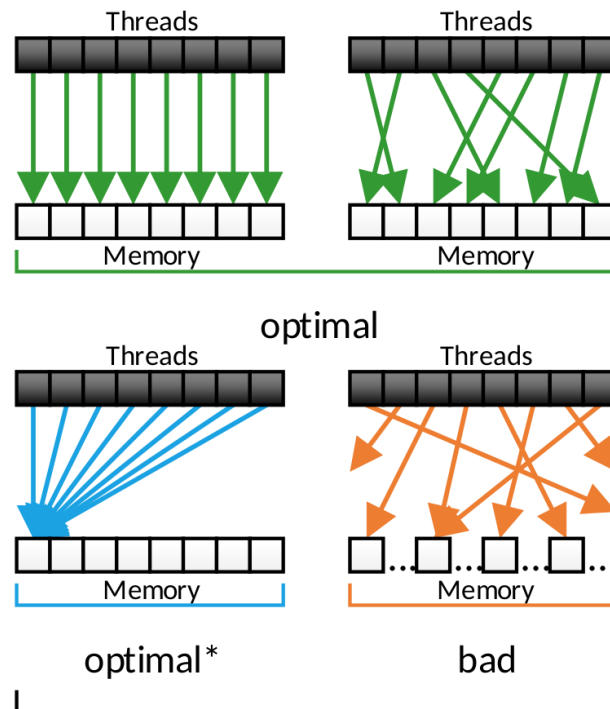


FIGURE 5.11: Different possibilities of related threads accessing memory. A more distributed access shown in orange offers the worst performance. The pattern shown in blue is only optimal for read operations [125].

GPU Occupancy and Performance Considerations

Keeping as many multiprocessors working at the same time as possible is a good way to attain better performance. To achieve this the amount of threads and blocks must be balanced for specific tasks. Instructions in individual threads are executed in sequence. Therefore the only way to hide latencies and fully utilize the hardware when a warp is stalled is to execute other warps. A metric for this is the number of warps which are active on a multiprocessor. It is expressed in terms of occupancy. Occupancy is the ratio of warps active per multiprocessor and the maximum amount of possible active warps. In general it is true that a low occupancy reduces the possibility to hide memory latencies. However a higher occupancy does not always result in higher performance. Registers in which local variables are stored are shared on a multiprocessor. This is done to access them with the lowest possible latency. When a block of threads requires a lot of registers the amount of blocks which can occupy a multiprocessor is reduced.

There is a certain granularity to register allocation and the amount of registers and simultaneous threads can vary between different devices. Therefore the relation between occupancy and register allocation is not a trivial matter. An example in which the occupancy changes in irregular steps dependent on the used register per thread is shown in figure 5.12. Another factor influencing the occupancy similar to the number of used registers is the shared memory. As mentioned above shared memory also resides on the multiprocessor and can be accessed by all threads of a block. As it therefore has to be allocated to a specific block the amount of shared memory used by a block also changes the occupancy. An example for this is given in figure 5.13. It shows how the the occupancy changes in irregular steps depending on used shared memory and the amount of shared memory available in total. A very prominent aspect when it comes to performance of code on a GPU is the number of threads in a block as it is one of the starting parameters for a kernel launch. Figure 5.14 shows how the occupancy changes dependent on the amount of threads per block. An irregular sawtooth structure can be seen that shows that neither a large number of threads nor a small number of threads necessarily results in a high occupancy. This sawtooth structure can sometimes be seen directly in the performance of a given code running on a GPU.

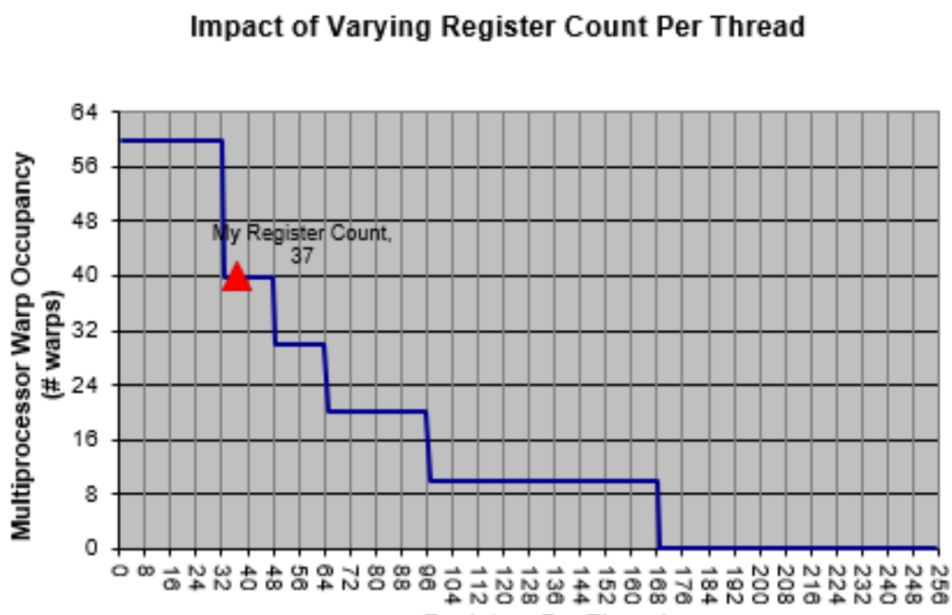


FIGURE 5.12: Multiprocessor Warp Occupancy in relation to Registers Per Thread. The figure is taken from an occupancy calculation tool and the red triangle marks a specific occupancy for a certain number of used registers [129]

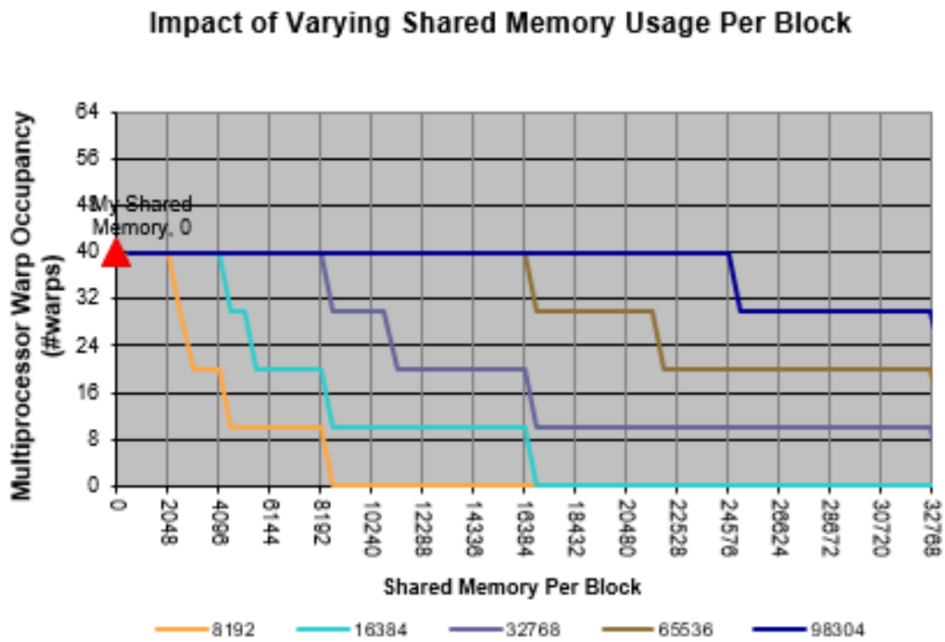


FIGURE 5.13: Multiprocessor Warp Occupancy in relation to Shared Memory Per Block. The figure is taken from an occupancy calculation tool and the red triangle marks a specific occupancy for a certain used shared memory [129]

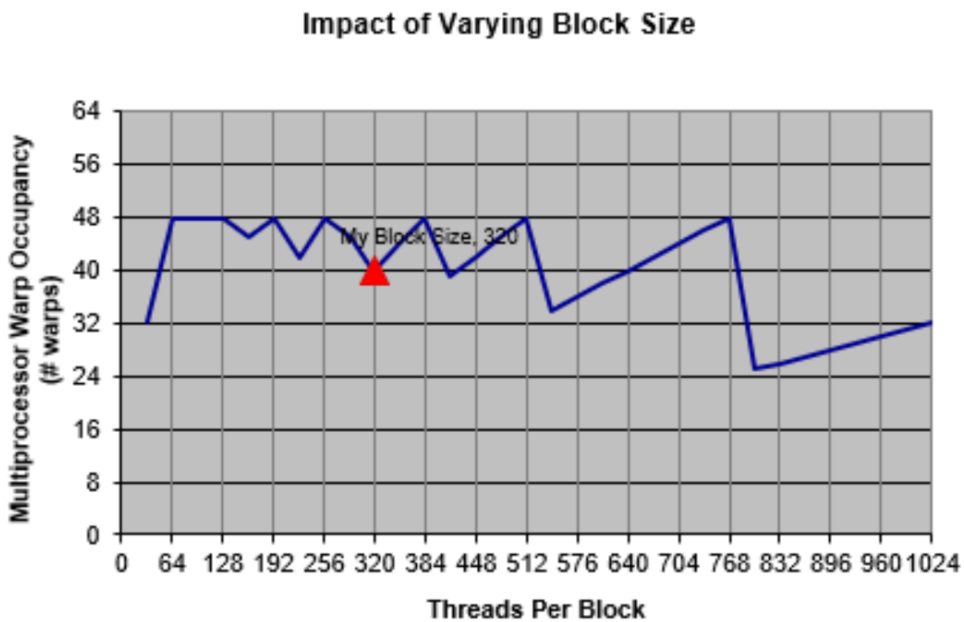


FIGURE 5.14: Multiprocessor Warp Occupancy in relation to Threads per Block. The figure is taken from an occupancy calculation tool and the red triangle marks a specific occupancy for a certain number of threads per block [129]

Chapter 6

Online Track Finding

At a worst case assumption the luminosity detector will produce approximately 5.5 TByte of data a day [109]. It is unclear how much storage capacity will finally be available for the luminosity detector. For this reason it must be possible to reduce the data rate accordingly. While it is expected that secondary particles, tracks from background events and electrical noise will leave signals in the luminosity detector the majority of data will be from elastically scattered antiprotons. Therefore the only way to reduce the amount of data is to pre-scale the detected events we are actively looking for. To do this in a clearly defined way only the lists of every n -th elastically scattered antiproton candidate will be permanently recorded. Identifying these candidates is achieved by reconstructing their tracks. As this needs to be done in real time during data taking this process is called online track finding. It is not necessary for the track parameters to be known at this stage. Thus a simple track finding approach can be taken compared to the track calculations needed for the precise determination of the luminosity.

6.1 Online track finding at other experiments

The determination of particle tracks and their parameters is a common task in particle physics. Many different detectors and algorithms exist to conduct it. As with other tasks there are multiple things to take into account when judging their performance. The most obvious performance metric is simply the number of tracks which can be successfully reconstructed. However, not all tracks which are reconstructed have been caused by a real particle. Fake tracks or ghost tracks as they will be called here can be caused by combinations of sensor hits from different tracks or by sensor noise. The more particles are going through a detector at once the higher the chance for unphysical combinations of hits which lead to ghost tracks.

If a more complete track reconstruction besides simple track finding is required the resolution with which track parameters e.g. spatial position, angles and momentum can be determined must also be taken into account. Not all algorithms used in the field of track finding are capable of reconstructing tracks and determining track parameters at the same time. With the huge amount of data produced by modern particle physics experiments the computation time for the track finding algorithms has also become an important factor. All the collected data needs to be analyzed at some point so the algorithms need to terminate in a sensible amount of time. If track information is to be used in early stages of the DAQ computation time becomes crucial as it must be able to keep up with the rate at which the experiment produces new data. For this use in

the early stages of the DAQ it can be beneficial to forgo algorithms which return precise track parameters and rely only on track finding.

Some examples for algorithms commonly used for track finding are hough transform, track following and cellular automaton. For the hough transform [130] a model for the track must exist. A discrete parameter space is created for that model. For every hit in the detector an entry for all possible model parameters it might belong to is made into the parameter space. After this has been done the parameter space is examined for clusters of parameters. These are then identified as representations of the track.

Track following is another simple routine that starts by connecting two hits to form a track seed. The track related to this seed is extended to the next detector layer. If a hit is found within a certain distance of the intersection with this layer it will be included into the track and a further extension to the next layer is constructed.

Cellular automaton based algorithms have been used for track finding in many different particle physics experiments including the experiments NEMO-2 [131], HERA-B [132] and ALICE [133]. It is also planned to use it for future experiments e.g CBM [134]. The cellular automaton is illustrated in figure 6.1 for the luminosity detector with four layers of sensors. In a first step cells are constructed as segments out of a hit from one layer and one from the next or second next detector layer. This is shown in 6.1 (a). Each cell has an intrinsic state represented by an unsigned integer which starts at zero. After all cells have been formed their state is updated in an iterative process. In each iteration a cells state will be updated if a neighbor with an equal state can be found on its left side. All cells are updated at the same time. There are two requirements for cells to be considered neighbors. The first one is that they need to have a hit in common in a shared detector layer. The second is that the breaking angle α between the cells must be small enough to satisfy the condition $(1 - \cos \alpha) < A_{max}$. In Figure 6.1 (b) an angle between two different cells not satisfying this condition is marked with a dashed red circular line. The parameter A_{max} has to be non zero for two main reasons. The numerical values of hit positions are defined by the middle of the sensor pixels and as pixels can be shifted relative to each other between detector layers even a straight track would have a non zero breaking angle between its cells. The second and dominating reason is multiple scattering in the detector material as every interaction between particles and material causes the particle to deviate from its original path. The iterative process stops as soon as cell states are no longer updated. A track is then reconstructed by starting with a rightmost cell. To this cell neighboring cells to the left are added by looking for neighbors with a state $cell_{n-1} = cell_n - 1$. This is repeated for the newly added cell and the track ends when no more cells can be added. Figure 6.1 (c) shows such a track constructed from cells with the states two, one and zero with a dashed red line. This procedure with cell states has turned out to be very effective in environments with high track multiplicity.

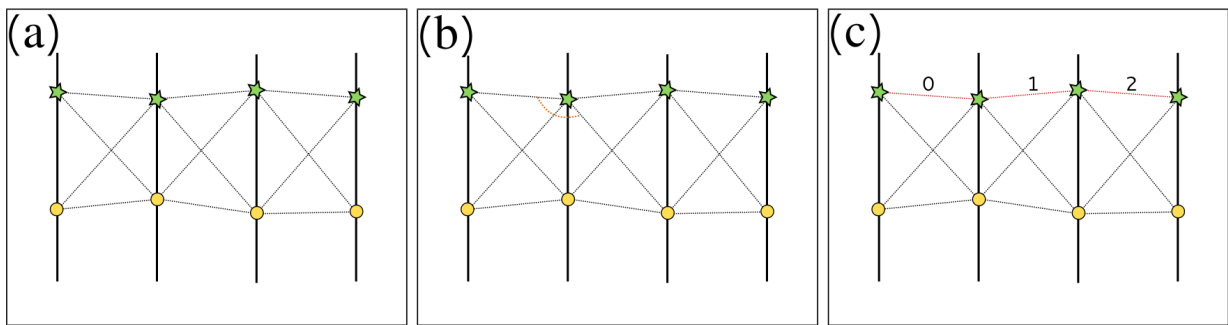


FIGURE 6.1: Illustration of the a cellular automaton algorithm [106]. (a) Possible Cells are constructed from hits in neighboring layers. (b) Angles between cells are checked to find neighboring cells. The red dotted line shows the angle between two cells which are not neighbors. (c) Final situation after the iterative process is complete. A track found through adding cells with decreasing internal state is shown in red.

6.2 Track Finding Algorithm and Implementation Platform

The hough transform is simple to implement in hardware but for cases with only a low numbers of detector layers no suitable clusters are formed in parameter space when applied to a real world problem. Thus it is not applicable to the luminosity detector. The track finding algorithms which have already been investigated for the luminosity detector offline track reconstruction of recorded data are the track following algorithm and the cellular automaton [106]. They have been quantified in terms of number of found, ghost and missing tracks for non online usage. The cellular automaton has been presented as preferable. Therefore it has been taken as a basis for implementing the online track finding to be used for possible pre-scaling of data. As time related issues have not been a priority for the previous studies this means choosing a platform for the algorithm, removing algorithm steps in favor of computation speed and parallelizing the code were the issues to solve.

The degree to which it can be parallelized must be determined by answering the following questions. Are there many independent calculations inside of one event? Should several threads cooperate? Is it reasonable to collect a certain number of events before processing to hide latencies? Can the data be arranged in such a way to fit the memory model of the hardware? Which programming language and frameworks to use? Some times it is not possible to choose the best way theoretically and several things have to be compared in practice.

After an algorithm has been chosen to deal with a certain problem the question remains how and where to implement it. There is a multitude of target options to implement an algorithm on. In principle an Application-Specific Integrated Circuit (ASIC) could be designed for a specific problem. This way a very low computing time can be achieved but it has a lot of practical disadvantages. Designing circuitry takes more time than writing software. The production of an ASIC is a very costly process that also consumes additional time. As prototypes also need to be produced this slows the development even further. The final product is then so specialized it can not easily be

reused. If it is damaged after some time it can not be replaced easily. Should the requirements on the algorithm change it is also not possible to just modify the implementation. Instead a new ASIC needs to be developed.

An alternative approach is to use an FPGA. This is an Integrated Circuit (IC) which can be programmed on hardware level. As with ASICs the function is usually implemented with hardware description languages which are used to describe actual circuitry. In contrast software uses instructions which will be interpreted by hardware. The main building blocks of an FPGA are Look-Up-Table (LUT)s. These LUTs can hold any logic relating their input ports to their output ports. The number of input ports and output ports is rather small and limits the complexity of functions one LUT can have. To build more complex functions an FPGA has a programmable network of connections between these LUTs. In addition to these two main components there is also some more specialized circuitry e.g. RAM blocks, modules for clock management or Input/Output (I/O) modules. This offered flexibility comes with the cost of having larger structures than ASICs so they contain less logic and are slower. This is offset by much lower costs for non mass production and the flexibility meaning changes to algorithms can be implemented without redesigning large parts of the electronics of the experiment. Nevertheless developing with hardware description languages is more time consuming than using programming languages. While it is possible to move firmware from one type of FPGA to another the differences between the individual models and the boards they are based on makes it a non trivial process.

The most flexible solution which results in the easiest maintenance is implementing the algorithm as software running on more general purpose ASICs. The two types relevant for the application in this work are CPUs and GPUs. Software written for a CPU can simply be run on any other model. For a GPU this is less trivial but still a lot easier than porting FPGA code.

Traditionally cellular automaton tracking algorithms have been implemented in a sequential way for a CPU but recently other experiments have implemented them in parallel. In principal it can also be implemented on an FPGA. The cell states could be stored in the RAM blocks and an iterating circuit could be build around these. However the amount of RAM on an FPGA is usually quite limited. Having the same structure working repeatedly on the same data blocks until the calculation is done also has the potential to be slower than desired. An alternative to this could be a pipeline structure. This way new independent calculations could be done before the current ones are completely done. As the amount of combinatorics is potentially quite large this might result in a rather large amount of used LUTs which is also not optimal. For this reasons and the flexibility provided by software the decision has been made to investigate if a software solution is viable.

The algorithm derived from the cellular automaton has both been implemented for a GPU and for a CPU. For the GPU implementation CUDA (Compute Unified Device Architecture) is used. It is a parallel computing platform and programming model created by NVIDIA to use their GPUs for general purpose computations. The CPU version of the algorithm has been implemented with openMP which is an application programming interface to write portable and multithreaded code. It can be used with the programming languages C, C++ or Fortran and it contains a set of compiler directives, library routines, and environment variables influencing the run-time behavior

of the code. For simplicities sake the algorithm has first been implemented in CUDA and later been ported to openMP. As modern consumer GPUs do not contain as many double precision as single precision floating point units it also has to be checked if the precision difference noticeably influences the results. If the algorithm relies on double precision calculations a more expensive professional GPU would have to be used.

6.3 Triplet Reconstruction

The basis for the online track finding algorithm of the luminosity detector is the cellular automaton. It has been chosen based on a previous work comparing the track following algorithm and the cellular automaton [106]. The cellular automaton has proven useful for an environment with a very high multiplicity of tracks. In the case of the luminosity detector the amount of tracks is about 1 – 2 per time stamp in over 90% of the cases [109] with noise not yet being taken into account.

A track in the luminosity detector is defined as a set of three or four hits fulfilling an angle requirement. For this small number of hits the concept of cell evolution over time has been abandoned. Every combination of two cells will instead just be checked once for its validity and then saved as a triplet consisting out of three hits from three different planes. The validity of a triplet depends on the angle α between the two cells it is constructed of

$$(1 - \cos \alpha) \leq \delta\Psi_{max} \quad (6.1)$$

and describes the deviation of the two cells from a straight line. Due to multiple scattering in the sensor material and non-zero spatial resolution of sensors in general an angle of 0° would prevent any triplet from being reconstructed while an angle of 90° leads to every hit combination in the detector being valid as a triplet. A pixel with a length of $80\ \mu\text{m}$ and a distance of 10 cm between detector planes results in an angle of $\alpha_{res} \approx 8 \cdot 10^{-4}$ rad [106]¹. The multiple scattering angle θ_{MS} depends on the momentum of the antiprotons and has been estimated from $5.2 \cdot 10^{-4}$ rad to $4.4 \cdot 10^{-5}$ rad for 1.5 to 15 GeV/c. Adding α_{res} and θ_{MS} and calculating $\delta\Psi_{max}$ via 6.1 leads to a range of $2 \cdot 10^{-6}$ to $8 \cdot 10^{-7}$ chosen for the offline study [106]. However, the material the antiprotons pass in the detector is not uniform as there are overlapping sensors and holes between sensors. These values have only been taken as an estimate for the scale of $\delta\Psi_{max}$. Figure 6.2 shows the influence of the parameter $\delta\Psi_{max}$ on a logarithmic scale on the percent of events with missed tracks and ghost tracks simulated with $P_{beam} = 15\ \text{GeV}/c$. The percentage of events with missed tracks follows an S-curve. The orange dashed line representing the estimated value due to multiple scattering and spatial resolution is located at the point where the curve starts flattening to a minimum. The gray dashed line shows the actually chosen $\delta\Psi_{max}$ for the offline study. With just one track per event the percentage of events with ghost tracks is flat while it rises sharply from that baseline when multiple tracks are simulated in an event. After that sharp rise the increase appears linear.

If two adjacent triplets share two hits they are then combined and saved as a complete track. Triplet combination is illustrated in figure 6.3. Two complete tracks are

¹this is called α_{digi} in the original publication

shown in blue and yellow. Their constituting triplets share two hits in the middle layers. The red dotted line shows a triplet which is rejected in the triplet construction stage as its angle is too large. It is expected that tracks sometimes don't produce a hit in each sensor layer of the luminosity detector. Thus if no matching triplet pair is found the single triplet will be accepted as a short track. As not only the first and last sensor layer may be missing hit triplets will also be constructed out of hits from layers which are not directly adjacent. These special triplets are not checked for potential matches with other triplets. The green triplet in figure 6.3 is an example for such a special triplet counted as a short track as it is missing a hit in the middle.

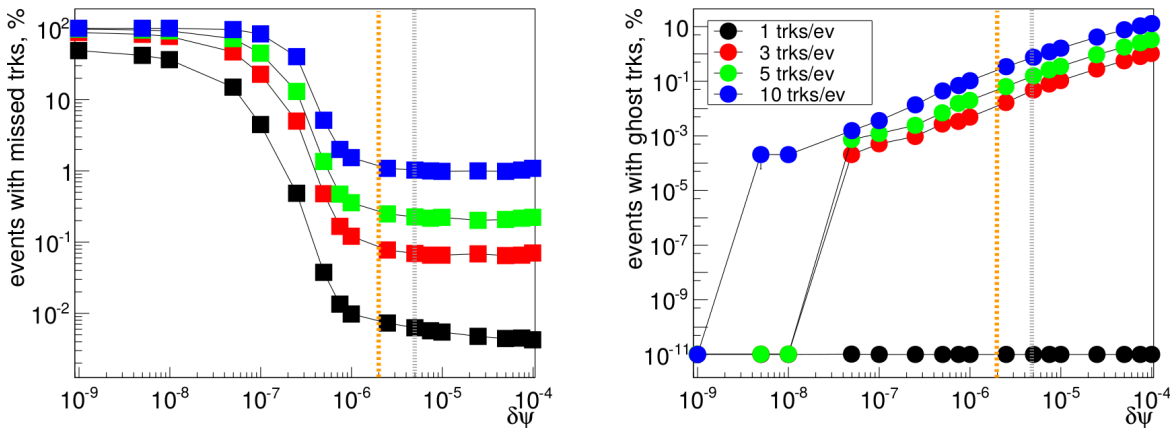


FIGURE 6.2: Offline study of the influence of the parameter $\delta\Psi_{max}$ on the percentage of events with missed tracks (left) and ghost tracks (right) simulated with $P_{beam} = 15 \text{ GeV}/c$. The orange dashed line is the estimated value and the gray dashed line is the chosen value for the offline study [106].

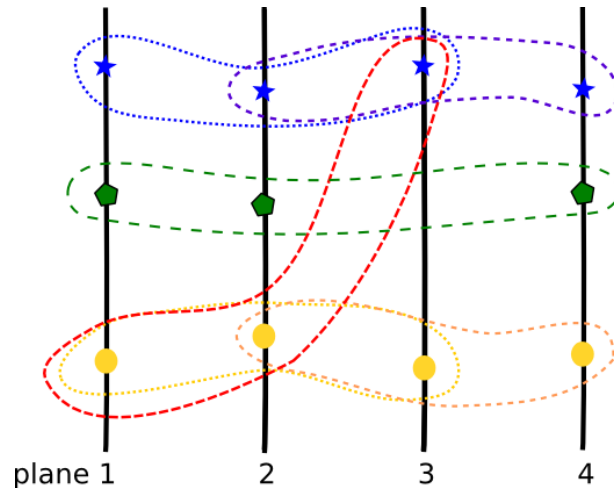


FIGURE 6.3: Illustration of possible triplets and triplets being combined to complete tracks. Possible triplets are shown by dotted and dashed lines.

The low expected track multiplicity in the complete luminosity detector also means that there is not enough data in one event to fully exploit parallelism in either a GPU

or a CPU. To counter that and achieve a reasonable computation time per event by exploiting parallelism data will be accumulated over a period of time and processed as one bunch. In case of a calculation on a GPU this is obviously needed to avoid unnecessary latency when transferring data to the GPU and to make use of its many cores. For a CPU it is not quite as obvious but creating threads to work in parallel also produces some computational overhead. This is one of the reasons why data accumulation is also beneficial in this case. Beside the requirements of efficient hardware use there is another factor why at least some data accumulation is necessary. In chapter 4 the time walk of the sensors has been shown. The latency of signals is spread over about 75 ns in such a way that the majority are within 50 ns. With the planned readout frequency of 40 MHz time stamps will have a resolution of 25 ns. This means that individual hits belonging to one track can be attributed to three different adjacent time stamps. To be able to correctly find such tracks it is necessary to search for corresponding hits in at least three subsequent time stamps. To account for that a moving time window is introduced to the algorithm. It has the corresponding length of three time stamps and moves in steps of one time stamp. As the hits of a track are not necessarily spread over three time stamps the moving time window can lead to finding one track multiple times. In figure 6.4 this problem is illustrated for a track spread over two time stamps. At T_0 an antiproton passes the detector and each sensor layer detects a hit (blue). The hits are spread over two time stamps and the moving time window does not include any hits. The red hit represents a faulty hit. At T_1 another antiproton passes the detector and leaves only 3 hits also distributed over 2 time stamps. The moving time window progresses and contains 2 hits of the blue particle track. At T_2 no further particles pass the detector and the moving time window completely contains the blue particle track and parts of the pink one. At T_3 the pink particle track is completely contained for the first time and the blue one for a second time. The blue track would now have been reconstructed for a second time. This would now require to filter the tracks afterwards to prevent double counting. To avoid this it should be avoided to construct multiples of the same track in the first place. This is achieved by associating each time window with its first time stamp. A triplet will only be reconstructed in a moving time window if it contains at least one hit in the first time stamp of it. Making this association with the first time stamp is completely arbitrary as the second or third could also be chosen. As there is no definite way to determine the true time stamp to which all hits should belong any of these choices is acceptable.

6.4 Implementation

When implementing the described steps on a GPU the first step is to think about the appropriate data structure. As CUDA does not offer higher level containers such as vectors, maps, etc. the data is arranged in simple arrays. As mentioned in chapter 5 data transfers to a GPU are fastest if done in large chunks. Hence data is arranged as structure of arrays instead of an array of structures. Each spatial hit coordinate has its own array and the coordinates of a hit are associated by the same index. This means that hit coordinates belonging to different sensor layers and different time stamps are all contained in the same array. Therefore accessing the correct data for triplet calculation must be managed explicitly. This means that offsets for the index to access data

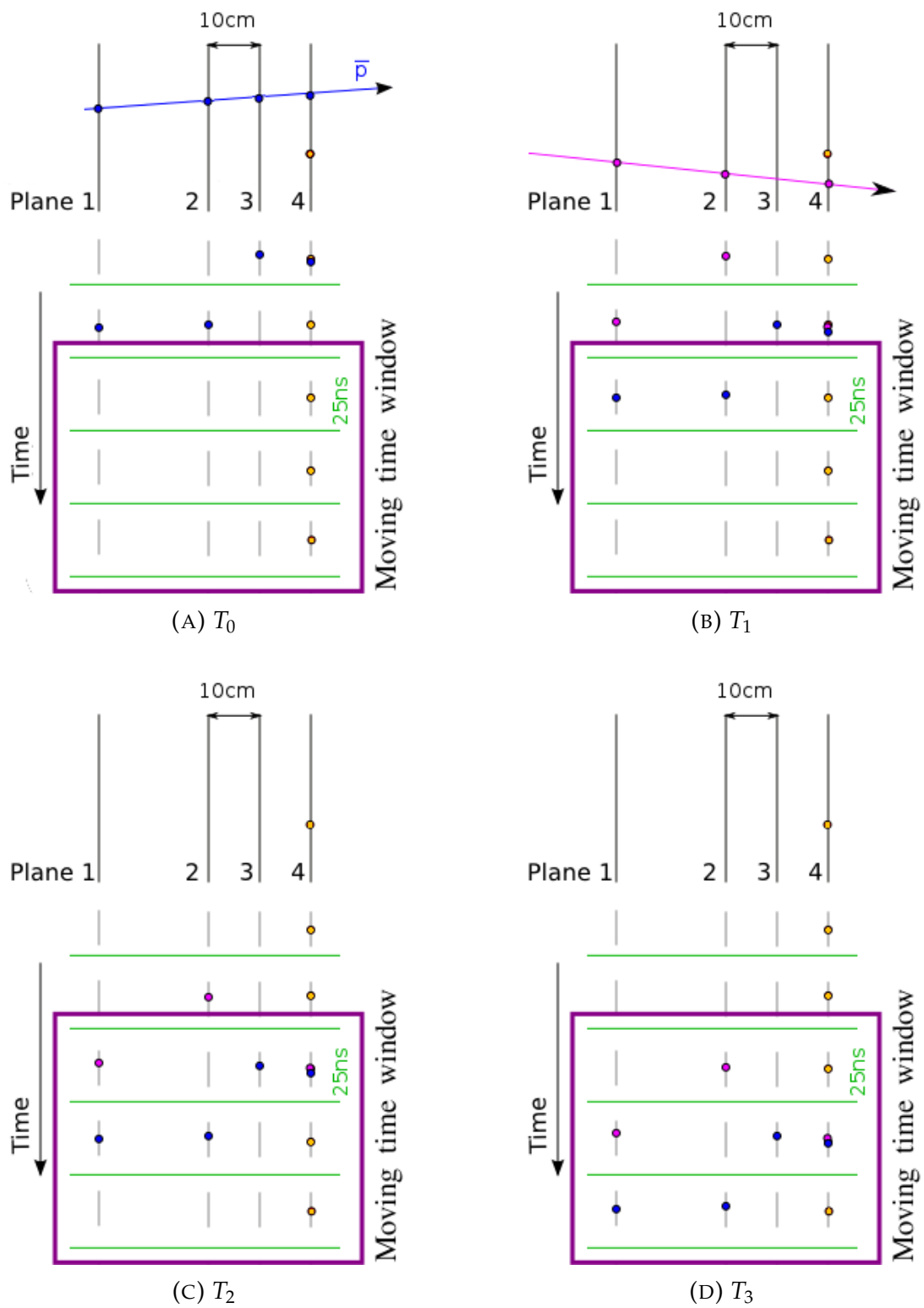


FIGURE 6.4: Illustration of a moving time window to find tracks which have hits spread over up to 75 ns with a time stamp size of 25 ns. Shown are subsequent time windows T_0 , T_1 , T_2 and T_3 .

must be calculated to be able to individually access different time stamps and planes. Not every time stamp contains hits and if it does the amount varies. Thus data is sorted by time stamp as primary criterion and by sensor layer as a second. Offsets are then calculated for finding the correct data (see figure 6.5 (a)). As hits are distributed over time and sensor layers a two dimensional organization has to be mapped to one dimensional memory. To exploit parallelization the different combinations of hits for triplet construction are distributed to different threads for calculation of the angles. The amount of combinatorics in conjunction with the structure of the problem leads to a suboptimal spread of memory access on a GPU (see figure 5.11) for individual triplet calculations. Constructing all triplets from a specific combination of hits from three time stamps and three planes taken from a moving time window is considered a triplet building task. Figure 6.5 (b) shows some example combinations for these triplet building tasks. All calculations of a triplet building task are handled by one thread. The number of triplet building tasks each thread handles varies depending on the number of threads and total amount of data processed at the same time. In the case of just one thread this would mean that one thread would handle all tasks. On a GPU threads are organized in blocks. The total amount of threads and blocks used on the problem can be varied. As soon as all calculations of one task have been completed a thread continues with one of the remaining tasks. This continues until all tasks have been finished.

On a CPU there is no organization of threads into blocks. Therefore the triplet building tasks are distributed differently to threads than on a GPU. Figure 6.6 (a) shows how the triplet building task to thread distribution would look like for a large amount of available threads. As the amount of threads on a CPU is a lot lower than on a GPU a thread has to handle more triplet building tasks. An example how this would look like for a CPU with two physical cores running two threads is illustrated in figure 6.6 (b).

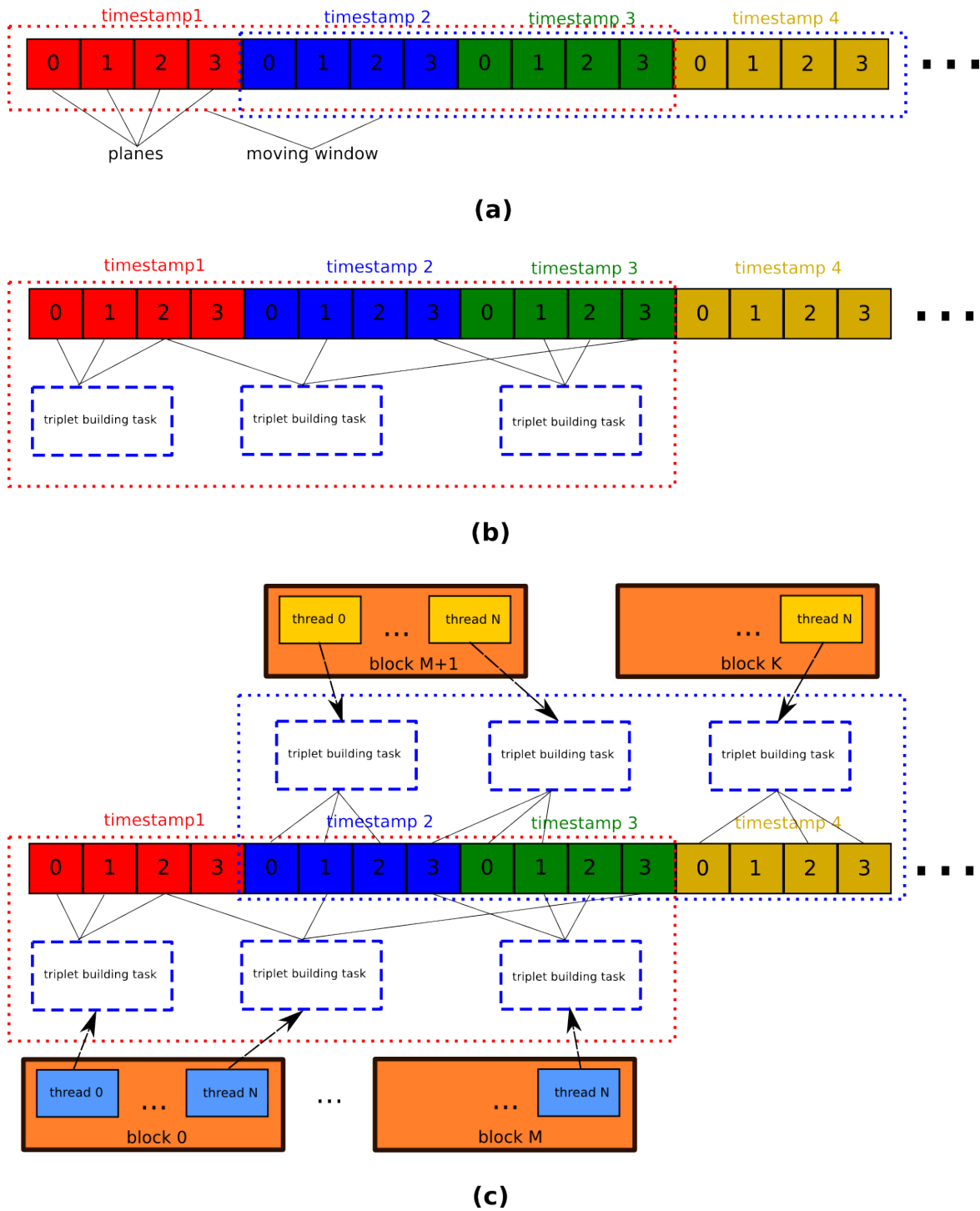


FIGURE 6.5: Schematic view of data structure and distribution of calculations. (a) Structure of data in memory. Sensor hits are ordered by time stamp and plane (indicated by the number) a sensor belongs to. A time window spans three time stamps. The triplet building task is building triplets out of three sensor hits. On a GPU all the calculations of a task are handled by one thread. These threads are organized in blocks.

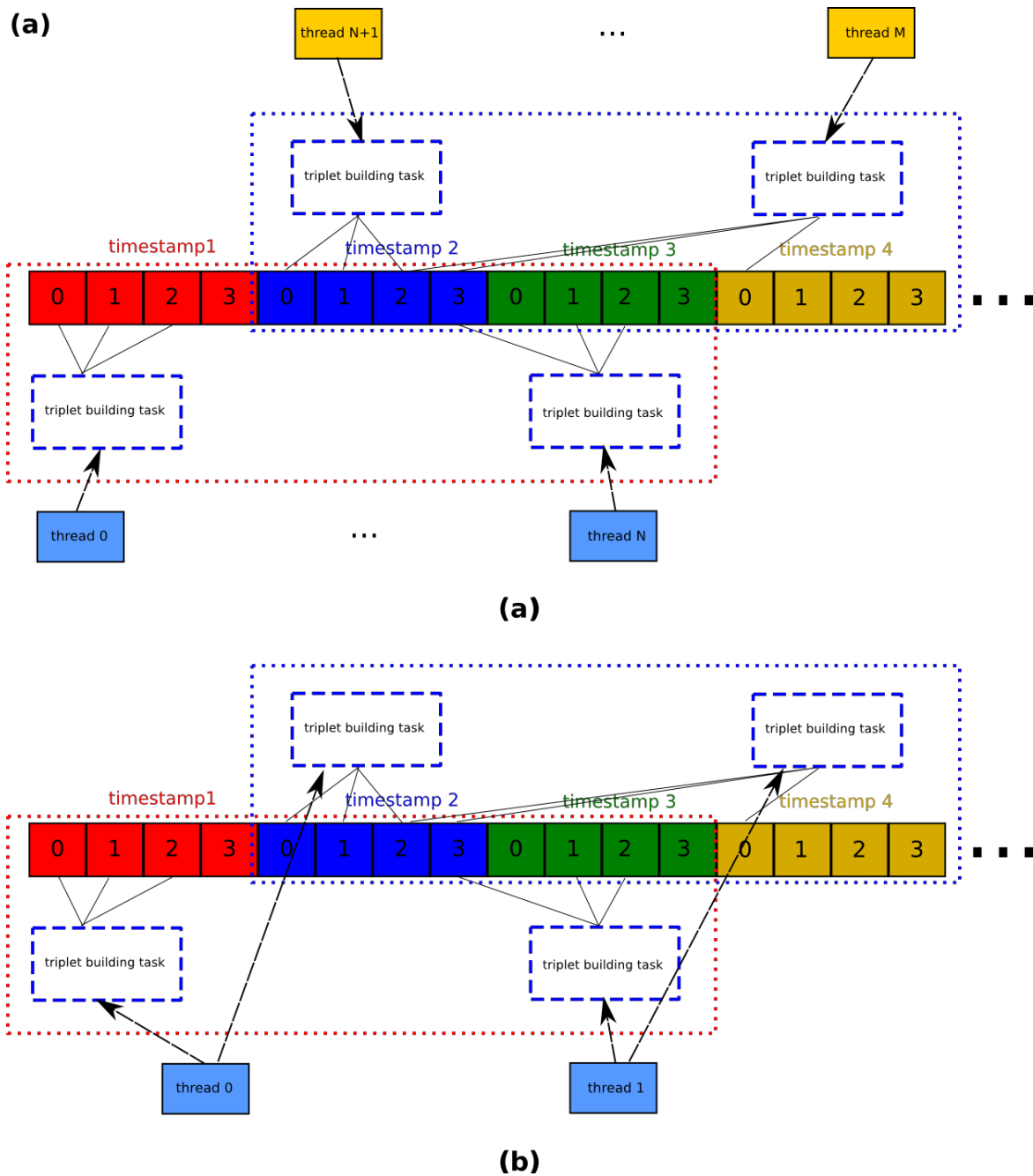


FIGURE 6.6: Calculation distribution on a CPU. (a) Ideal structure with an unlimited amount of threads. Each task is handled by a different thread. (b) Example for a practical case on a CPU with two physical cores running a thread each.

After all triplets satisfying the angular condition are found they are combined to full tracks whenever possible or else saved as short tracks. This is schematically illustrated in figure 6.7. A thread is assigned to all triplets which are built from hits from three adjacent time stamps. Triplets containing a hit from the first of three these time stamps will be the basis for a complete track assigned to that time stamp. Such a triplet is then combined with matching triplets which contain hits from all three time stamps.

Uncombined triplets are saved as a short tracks. This scheme prevents the multiple reconstruction of tracks which are completely contained in one time stamp.

As a moving time window requires three time stamps the last two time stamps of the currently processed data lack neighboring time stamps for finding all possible tracks. Therefore this data needs to be fed into the algorithm again as a start of the next accumulated data bunch to prevent missing any tracks.

Not all duplications stemming from the same track in form of different short tracks can be avoided by explicit construction. The reason for this is that complete tracks can leak short tracks into later time stamps. An example for this is when one triplet is associated with a time stamp because one of the hits is associated to the first time stamp and all other hits of the other planes are associated to the second and/or third time stamp. The complete track will be reconstructed in the first time stamp but the next thread running in parallel only sees the second triplet and therefore reconstructs it as a short track in a later time stamp. Thus an additional step of filtering the newly acquired tracks is still needed. This is also done in parallel with each thread being responsible for its assigned time stamp. For each short track found in a certain time stamp the previous and next to previous time stamp are checked for complete tracks with four hits which contain all hits of the short track. If this is the case the short track it is deleted from its associated time stamp to avoid unnecessary duplication. The hits of all tracks are stored.

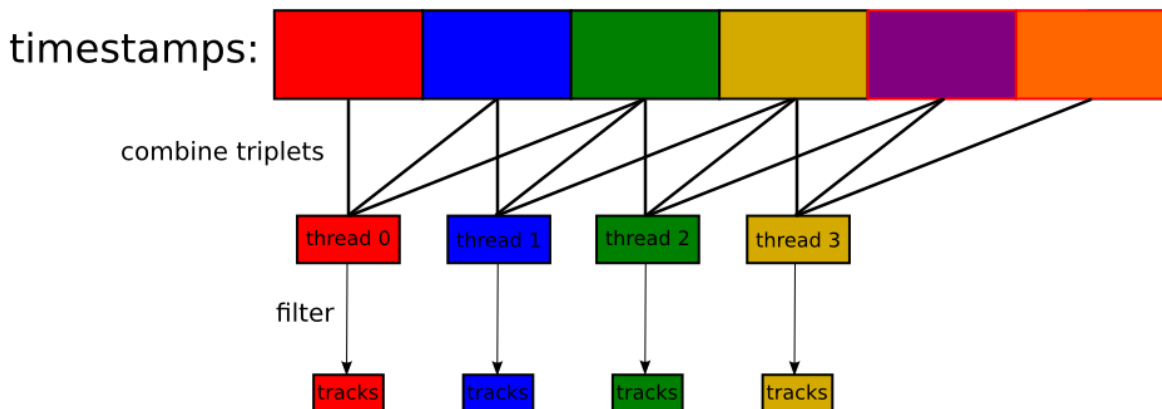


FIGURE 6.7: Triplet combination step of the tracking algorithm. Threads construct tracks associated with time stamps. The combination starts with a triplet containing at least one hit from the current time window. Such a triplet is then combined with matching triplets from this and the two following time stamps.

Chapter 7

Performance of the track finding algorithm

When having implemented an algorithm for a specific situation the performance of this implementation has to be evaluated. The main metrics are the efficiency of the track finding algorithm, the relative number of ghost tracks and the computation time. For this evaluation multiple steps are executed.

At first realistic Monte Carlo tracks have to be generated. For this the software framework $\bar{\text{PANDA}}$ ROOT [135] is used. With it elastic antiproton proton scattering events are simulated. The framework only offers a limited amount of beam momenta as the magnetic field has only been provided for these. The following three beam momenta $P_{beam} = 1.5, 4.06, 15 \text{ GeV}/c$ have been chosen. The elastically scattered antiprotons are propagated through the magnetic fields of the $\bar{\text{PANDA}}$ detector until they reach the luminosity detector. There the passage through the transition cone and the sensor layers is simulated including multiple scattering. Particles originating from secondary reactions are also simulated as these might also result in hits in the detector and thus influence the reconstruction of antiproton tracks. For the luminosity detector $\bar{\text{PANDA}}$ ROOT does not offer a realistic time based simulation. Therefore event based data is taken and hits belonging to the same track are arbitrarily spread over the event time stamp and the next two following time stamps. Then data is sorted by the timestamp and plane as described in chapter 6. After the sorting the offsets for the array access index are calculated. These offsets are needed to know the data positions of the different time stamps and sensor layers in memory. It has to be noted that sorting and offset calculation are not included in the computation time as this is expected to be done during earlier steps of the DAQ. The three algorithm steps triplet reconstruction, triplet combination and filtering are then individually timed. In case of the GPU the time needed for the data transfer to and from the GPU is also measured. The resulting tracks are compared to the originally simulated ones to estimate the efficiency and the amount of ghost tracks.

7.1 Efficiency and ghost tracks

The efficiency of the track finding algorithm is defined as

$$\varepsilon = n_{correctTracks} / n_{mcTracks} \quad (7.1)$$

where $n_{mcTracks}$ is the number of Monte Carlo tracks of elastically scattered antiprotons which have at least one hit in the active area of the luminosity detector. This means that tracks which are missed completely because they are outside of the investigated angular range do not distort the efficiency. Missing hits through the reduced acceptance through inactive material in the sensor planes and multiple scattering is taken into account. $n_{correctTracks}$ is the number of tracks the tracking algorithm found which have been successfully matched to a simulated track. A track is matched successfully if it either has four hits which all match hits coming from one simulated track or if it contains only three hits and these are all coming from the same simulated track.

The tracking algorithm might also find tracks consisting out of hits from different particles which therefore have no physical equivalent. These are called ghost tracks. To study their influence the number of ghost tracks n_{ghosts} is given relative to the total number of reconstructed tracks $n_{foundTracks} = n_{correctTracks} + n_{ghosts}$. The tracking algorithm returns the ghost percentage

$$v = n_{ghosts} / n_{foundTracks} \quad (7.2)$$

In table 7.1 the contributions of different types of ghost tracks to the total amount of tracks reconstructed by the tracking algorithm is summarized. Depending on the specific combinations of parameters (e.g. beam momentum P_{beam} , number of simulated tracks per event $n_{generatedTracks}$ and maximally accepted scattering $\delta\Psi_{max}$ between hits) the percentage varies for each type.

Ghost track type	Total contribution to reconstructed tracks [%]
Split hit tracks	0.45 ~ 0.5
Secondary particle contribution	0.41 ~ 0.5
Time mixing	< 4.8
Secondary particle and time mixing	< 0.26

TABLE 7.1: Contribution of different types of ghost tracks to the total amount of tracks reconstructed by the track finding algorithm. Percentages vary for different combinations of parameters e.g. beam momentum P_{beam} , number of simulated tracks per event $n_{generatedTracks}$ and maximally accepted scattering $\delta\phi_{max}$ between hits

Wrong hits contributing to ghost tracks have several different sources. Figure 7.1 shows some examples for ghost track types. Detector simulation includes merging hits from the front and the back side of the sensor module. Sometimes this process fails resulting in a track with five hits despite only having four detector layers (see figure 7.1 (a)). This is called a split hit track. In these cases the track finding algorithm returns

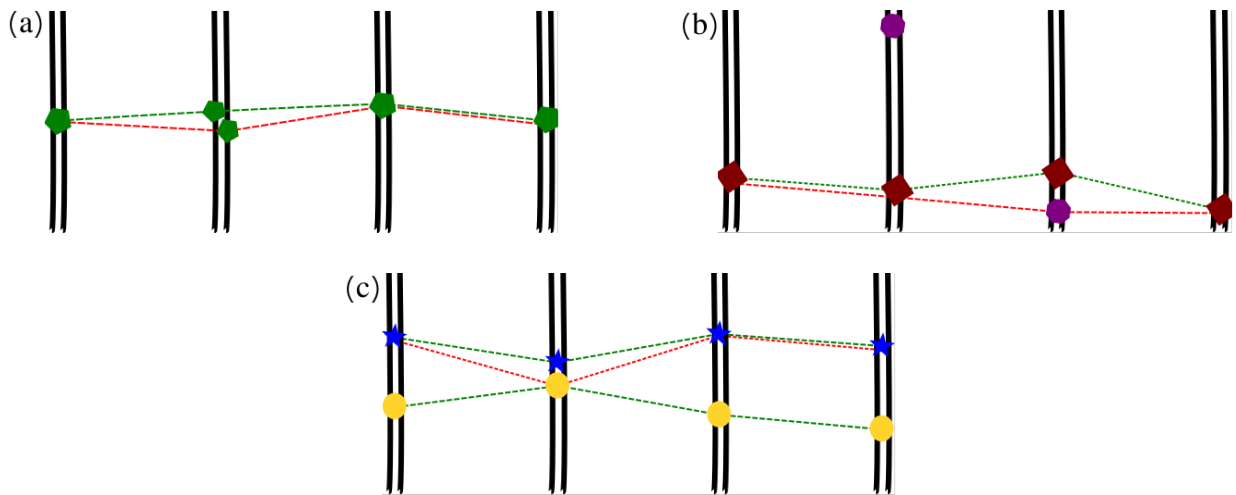


FIGURE 7.1: Examples for different kinds of ghost track types. Each of the four detector planes has two layers of sensors with partial overlap. Hits on both layers in close vicinity get merged into one hit. Correctly reconstructed tracks are marked with a green dotted line and ghosts with a red dotted line. Hits coming from the same source use the same marker. (a) Split hit tracks with all hits belonging to one track. (b) Secondary particle hit mixed into correct track. (c) Exchange of hits between correct tracks (can also occur because of time mixing).

two tracks. In principle both of these tracks could be defined as correctly reconstructed tracks. If all tracks of elastically scattered antiprotons are found this would lead to efficiencies higher than 100%. In these cases one track is arbitrarily classified as a correct track and the other as a ghost track. In addition to elastically scattered antiprotons secondary particles can also pass the sensors of the luminosity detector (see figure 7.1 (b)). Should hits caused by these secondary particles be near the path of an elastically scattered antiproton the track finding algorithm reconstructs an additional track substituting one of the original hits with a secondary hit. These ghost tracks contribute a similar amount of ghost tracks as the split hits.

Sometimes tracks are spatially close enough to each other for hits to satisfy the $\delta\psi$ requirement for multiple triplets. This means a hit will be used in the reconstruction of the correct track it belongs to and additionally in the reconstruction of a mixed ghost track consisting out of hits from different particle tracks (see figure 7.1 (c)). This can also be caused by the spread of the hits over different time stamps. This means that mixing of hits from correct tracks does not only occur when they are spatially close together in one event but also when tracks in neighboring time stamps are spatially close together. These ghost tracks are the main contribution to the total amount of reconstructed ghost tracks. All the described sources of ghost tracks can in principle be mixed in one track. Only the number of ghost tracks caused by time mixing and secondary particles at the same time has been distinctly counted as these mixed source ghost tracks are in general negligible in comparison to the total number of ghost tracks. In the case of time mixing and secondaries it is about $\approx 0.26\%$.

The efficiency and ghost track percentage of the track finding algorithm are influenced by multiple parameters. The most obvious one is the allowed angle between two cells making up a triplet represented as $\delta\Psi_{max}$. The number of tracks generated in one event $n_{generatedTracks}$ is also relevant as it results in more hits per time stamp and therefore introduces more potential hit combinations. The amount of multiple scattering is dependent on the momentum of the antiprotons and thus must also be taken into account as a parameter. The lack of high level data containers in CUDA and performance considerations on GPU lead to a fixed number of potentially found triplets per timestamp $n_{tmpTriplets}$ and detector layer combination. This also has to be taken into account as a parameter.

Figure 7.2 exemplary shows the influence of the maximum triplet number on the efficiency for $P_{beam} = 15 \text{ GeV}/c$, $\delta\Psi_{max} = 5 \cdot 10^{-6}$ and for two and three generated tracks per event. It can be seen that the efficiency saturates at 97.5% for about 15 triplets. If it is chosen too low additional triplets overwrite the memory where the already reconstructed triplets reside. Thus the efficiency drops as part of correct tracks might be dropped. For more generated tracks per event the e.g. three tracks (see figure 7.2 red dots) efficiency drop is larger as there are more potential triplets filling the available memory space faster. Therefore it is important to choose a sufficiently high number for the maximum number of triplets to avoid overwriting. Although the number should also be small enough to avoid any adverse effects on computing performance.

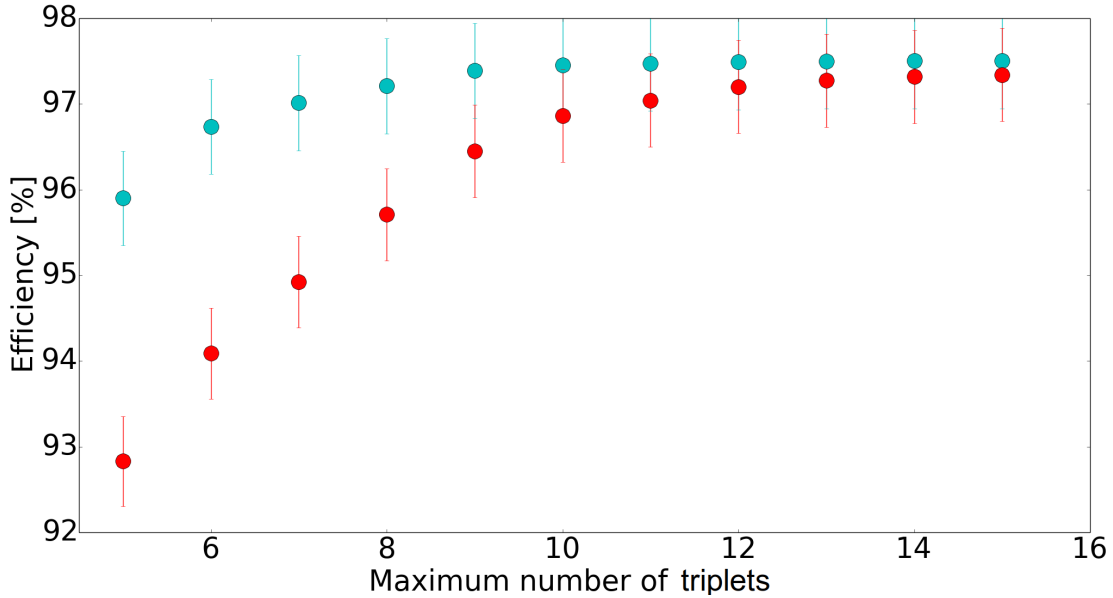


FIGURE 7.2: Efficiency depending on the maximum available number of reconstructable triplets per time window for $P_{beam} = 15 \text{ GeV}/c$, $\delta\Psi_{max} = 5 \cdot 10^{-6}$, $n_{generatedTracks} = 2$ (blue) and $n_{generatedTracks} = 3$ (red). The efficiency saturates at about 97.5%

To study the general influence of each parameter on the efficiency some parameters have been locked while one has been used as a variable. These data points are shown as differently colored symbols. Figure shows 7.3 the efficiency dependent on the beam momentum of the HESR. The number of tracks per simulated event is $n_{generatedTracks} = 3$. For the parameter related to the allowed scattering angle $\delta\Psi_{max}$ three different data

sets are shown. It can be seen that the efficiency varies between 99% – 96% and that it increases with higher momenta. The cause for the increasing momenta is that the multiple scattering angle is lower. In figure 7.4 the efficiency is shown depending on the number of tracks generated per event $n_{generatedTracks}$ for $\delta\Psi_{max} = 0.5 \cdot 10^{-5}$ and different beam momenta. It varies between 98.5% – 95.5% and decreases slightly with the number of generated tracks. The last exemplary figure 7.5 shows the efficiency dependent on $\delta\Psi_{max}$ with $n_{generatedTracks} = 1$ and at different beam momenta. Unsurprisingly a wider angle leads to an increase in efficiency as tracks more strongly affected by multiple scattering can be found. Other figures showing the efficiency behaviour for different parameter combinations can be found in appendix A.

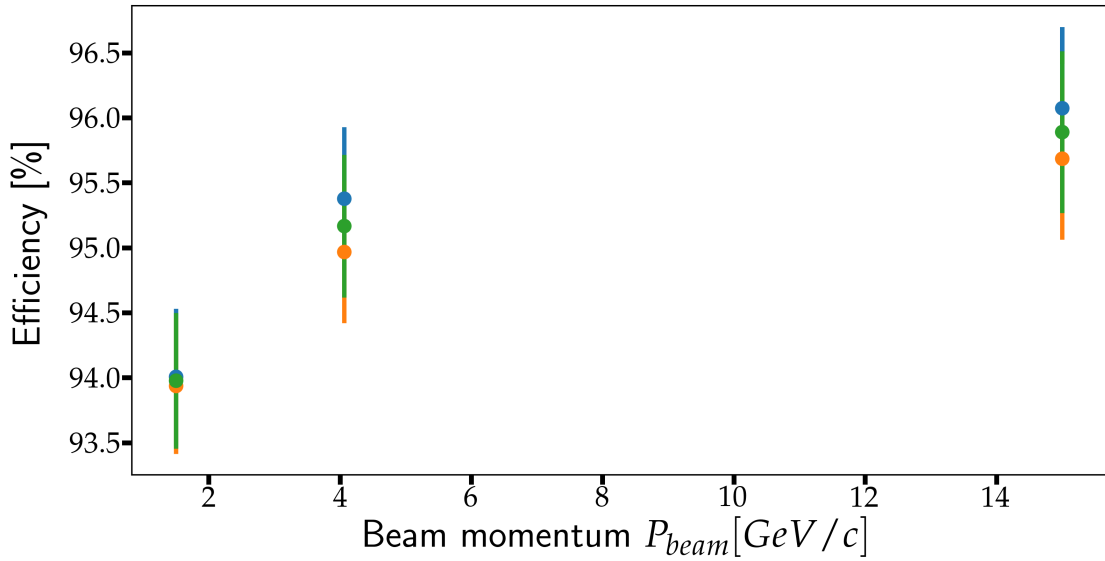


FIGURE 7.3: Track reconstruction efficiency for varying beam momenta P_{beam} and fixed parameters $n_{generatedTracks} = 3$, $n_{tmpTriplets} = 15$. Different $\delta\Psi_{max}$ are shown by different colors: $2 \cdot 10^{-5}$ (blue), $1 \cdot 10^{-5}$ (green), $5 \cdot 10^{-6}$ (orange).

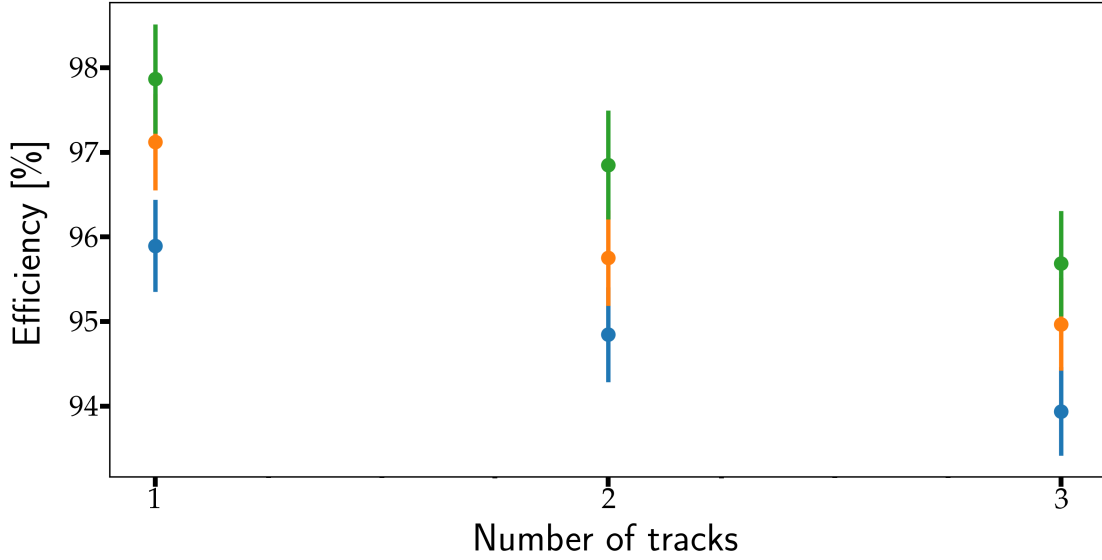


FIGURE 7.4: Track reconstruction efficiency for a varying number of generated tracks and fixed parameters $\delta\Psi_{max} = 0.5 \cdot 10^{-5}$, $n_{tmpTriplets} = 15$. Different beam momenta P_{beam} are shown by different colors: 1.5 GeV/c (blue), 4.06 GeV/c (orange), 15 GeV/c (green).

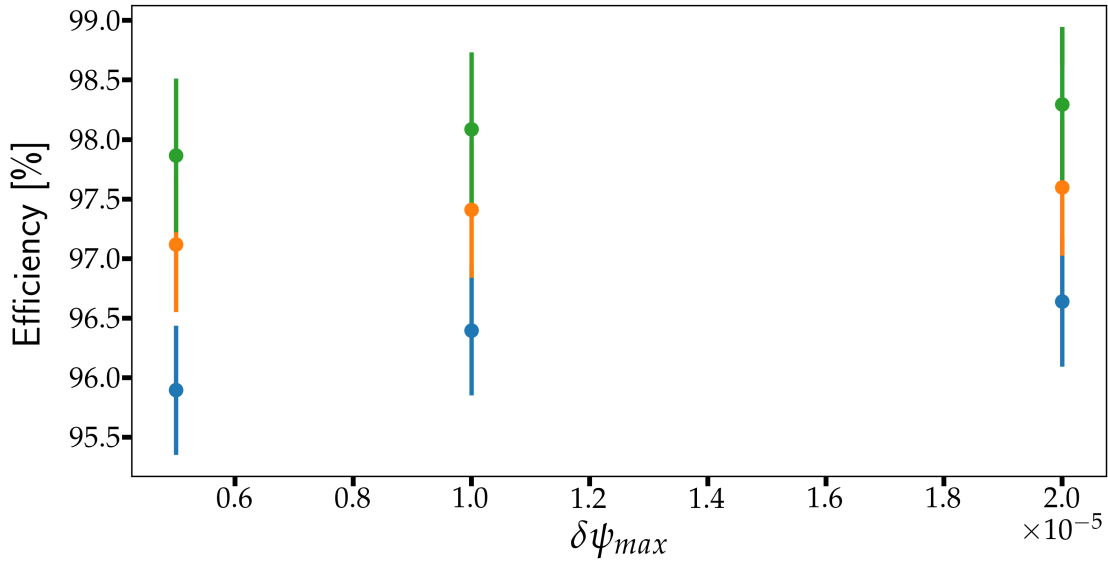


FIGURE 7.5: Track reconstruction efficiency for varying $\delta\Psi_{max}$ and fixed parameters $n_{generatedTracks} = 1$, $n_{tmpTriplets} = 15$. Different beam momenta P_{beam} are shown by different colors: 1.5 GeV/c (blue), 4.06 GeV/c (orange), 15 GeV/c (green).

The amount of ghost tracks depending on several parameters is studied in the same way as the reconstruction efficiency. Figure 7.7 shows the amount of ghosts dependent on the number of tracks with fixed $\delta\Psi_{max} = 2 \cdot 10^{-5}$ and various beam momenta. It varies from $\approx 1\%$ to $\approx 5\%$ and shows an expected increase with a higher number of tracks as the chances for hits originating from multiple tracks being closer together also

increases. At first glance the ghost percentage of $\approx 1\%$ seems unreasonably high if there is only one track per event. To understand this one must take into account that the time mixing can lead to multiple tracks per analyzed time window at this minimum number of simulated tracks. Figure 7.6 illustrates the worst case scenario for time mixing with $n_{generatedTracks} = 1$. Due to time walk individual hits are assumed to potentially move up to two time stamps away from their original time stamp. Therefore the current time stamp can contain up to two additional tracks from past events and the track generated for the current event can have hits spread into the next two future time stamps. The time window for the current time stamp extends to these two future time stamps to allow for the reconstruction of the current track but they can also contain a complete track each. For all those reasons a single time window for reconstruction can end up with five distinct tracks leading to many possible hit combinations even though only one track has been generated per event. With $n_{generatedTracks} = 3$ and multiple beam momenta the percentage of ghosts depending on $\delta\Psi_{max}$ is shown in figure 7.8. As expected the ghost track percentage rises with wider allowed angles due to more hit combinations being accepted as valid triplets but it does so only slightly while the beam momentum causes a larger increase.

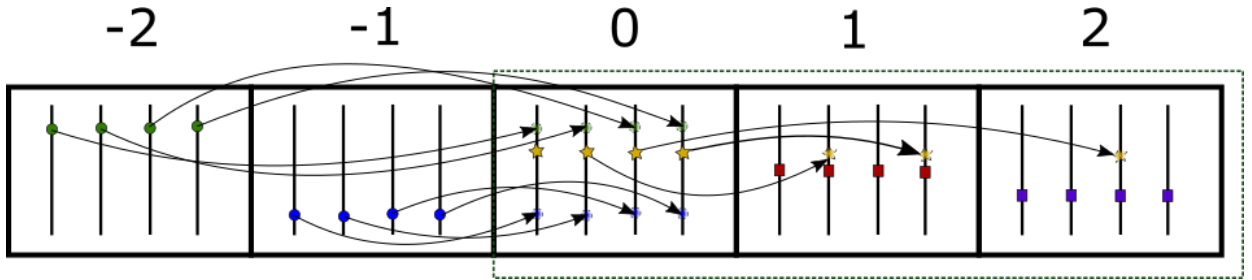


FIGURE 7.6: Worst case scenario for time mixing with $n_{generatedTracks} = 1$. Current time stamp marked with 0, past time stamps by negative numbers and future time stamps by positive numbers. Arrows and faded markers show which time stamps of hits deviating from there original time stamp because of time walk. Past tracks are marked in green and blue, future tracks in red and purple. Present track is marked in yellow and the time window for the present track is shown by the green dotted rectangle.

When looking at the momentum dependence in figure 7.9 and 7.10 a difference can be seen between a different fixed number of generated tracks. For $n_{generatedTracks} = 3$ the percentage of ghosts decreases with higher momenta while it increases for $n_{generatedTracks} = 1$. It has to be noted though that the overall ghost percentage is still a lot lower for a low number of generated tracks. This behavior change can be explained by the generally lower reconstruction efficiencies at higher momenta caused by more particle tracks in the edged area of the detector. Less hits in these areas means that there is also less potential for wrongly reconstructed ghost tracks. While this is also true in general for a lower number of generated tracks per event the contribution of ghost tracks caused by secondary particles dominates in this case leading to a higher overall number of ghost tracks. Except for the last case all shown plots represent the general trends of ghost tracks and reconstruction efficiencies regardless of the actual parameter combinations.

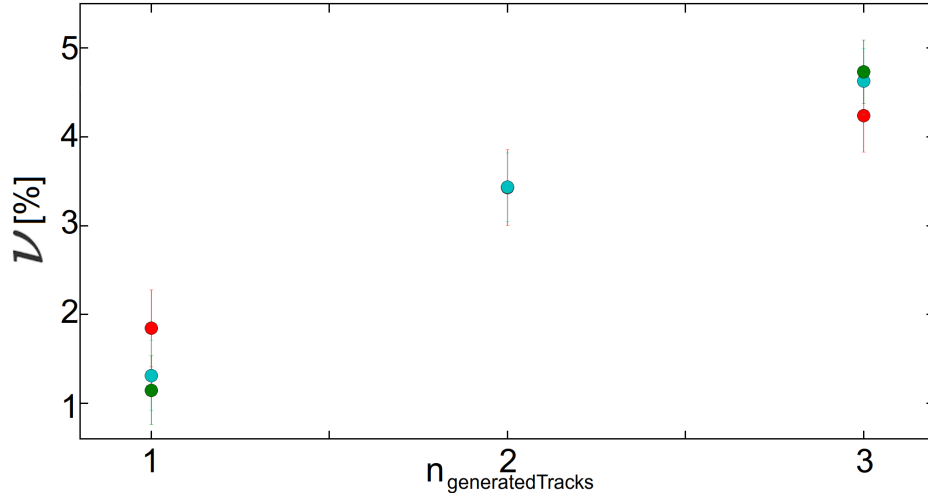


FIGURE 7.7: Percentage of ghost tracks ν in dependence on number of generated tracks. The parameters $\delta\Psi_{\text{max}} = 5 \cdot 10^{-6}$, $n_{\text{tmpTriplets}} = 15$. Different beam momenta P_{beam} are shown by different colors: 1.5 GeV/c (green), 4.06 GeV/c (cyan), 15 GeV/c (red).

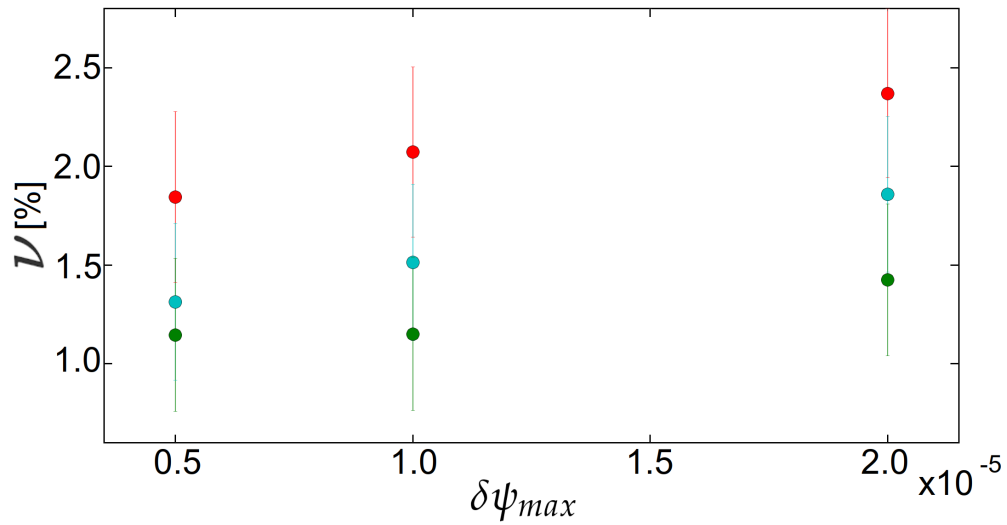


FIGURE 7.8: Percentage of ghost tracks ν in dependence on $\delta\Psi_{\text{max}}$. The parameters $n_{\text{generatedTracks}} = 1$, $n_{\text{tmpTriplets}} = 15$. Different beam momenta P_{beam} are shown by different colors: 1.5 GeV/c (green), 4.06 GeV/c (cyan), 15 GeV/c (red).

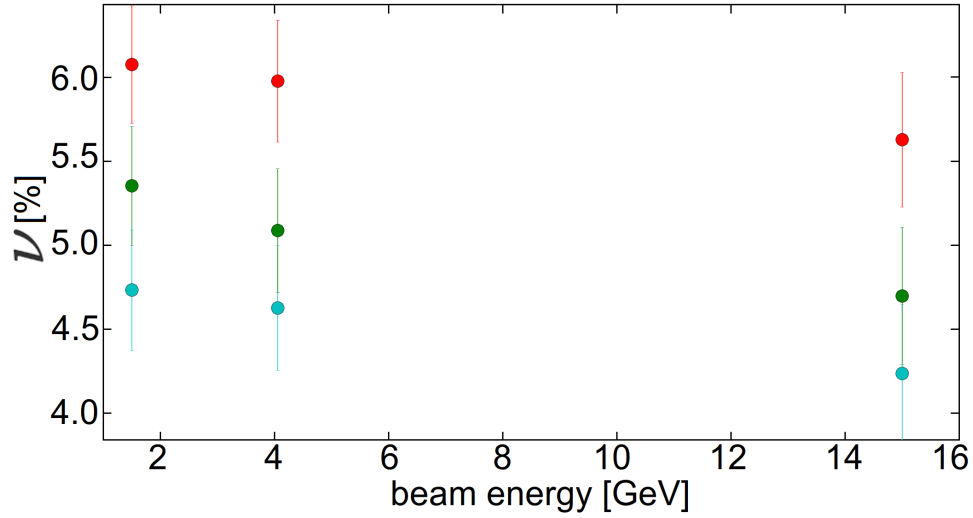


FIGURE 7.9: Percentage of ghost tracks ν in dependence on the beam momentum. The parameters $n_{generatedTracks} = 3$, $n_{tmpTriplets} = 15$. Different $\delta\Psi_{max}$ are shown by different colors: $2 \cdot 10^{-5}$ (red), $1 \cdot 10^{-5}$ (green), $5 \cdot 10^{-6}$ (cyan).

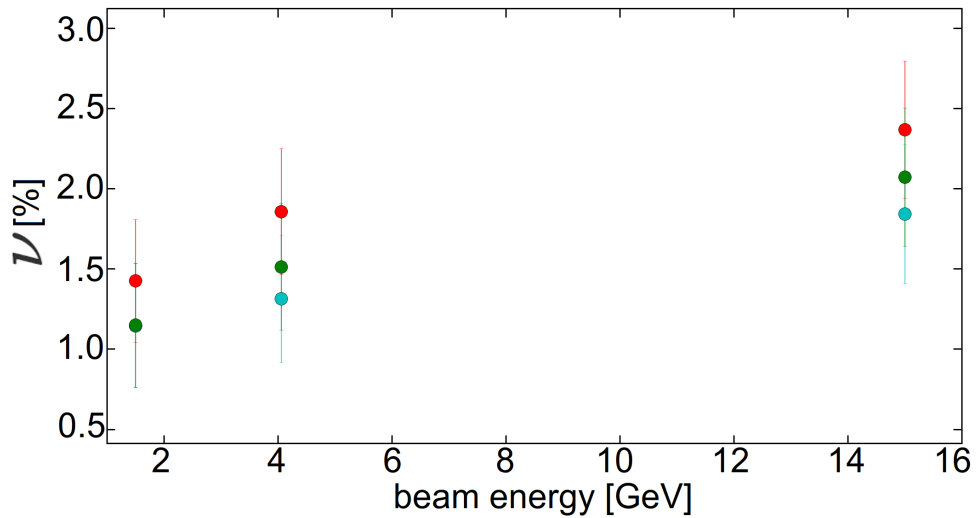


FIGURE 7.10: Percentage of ghost tracks ν in dependence on the beam momentum. The parameters $n_{generatedTracks} = 1$, $n_{tmpTriplets} = 15$. Different $\delta\Psi_{max}$ are shown by different colors: $2 \cdot 10^{-5}$ (red), $1 \cdot 10^{-5}$ (green), $5 \cdot 10^{-6}$ (cyan) The percentage of ghost tracks increases with higher momenta. The reason for this is the increased number of secondary particles passing the detector leading to more hits available for the track reconstruction.

Comparing the efficiencies and ghost percentages with results from offline analysis performed at $\delta\Psi = 0.5 \cdot 10^{-5}$ with the original cellular automaton algorithm [106] shows some overall decrease in performance for the online track finding algorithm. It must be noted that the values can not be compared directly as the offline analysis defines

percentages of events with either missed tracks or ghosts and an average number for each missed tracks and ghosts in events which contain at least one of such a track. As the given averages are only slightly larger than one all comparison will be made with the event percentages. For the percentage of events with missed tracks in case of five or less tracks per event the offline analysis results in $< 2\%$ for $1.5 \text{ GeV}/c$ and $< 3\%$ for $15 \text{ GeV}/c$. This is quite similar to the efficiencies of $\approx 99\%$ at $15 \text{ GeV}/c$ and $\approx 96\%$ at $1.5 \text{ GeV}/c$ for $n_{generatedTracks} = 3$ and $\delta\Psi_{max} = 0.5 \cdot 10^{-5}$. As expected in both cases the efficiency is slightly lower for higher beam momentum. However, the percentage of events containing ghosts is a lot lower in the offline analysis for less than five tracks per event with $< 0.02\%$ at $1.5 \text{ GeV}/c$ and $< 0.1\%$ at $15 \text{ GeV}/c$. Using the online track finding algorithm the percentage of ghosts rises from $\approx 1\%$ to $\approx 4.5\%$ for $n_{generatedTrack} = 1$ to $n_{generatedTrack} = 3$ at $1.5 \text{ GeV}/c$. One possible explanation for this is the removed step of iterating over cell states which was necessary to reduce processing times. Another reason is that the spread of hits over several time stamp has been considered for the online track finding algorithm while it is absent in the offline analysis. Time mixing basically increases the possible amount of tracks leaving hits in an event to five for $n_{generatedTracks} = 1$ and to 13 for $n_{generatedTracks} = 3$. Although the main reason is probably found in the different definition of ghost tracks. In the offline analysis a reconstructed track with 65% of its hits caused by the same particle is considered a good track while for the online algorithm all hits of a track must be caused by the same particle for not being counted as a ghost track.

7.2 Float versus Double precision performance

When using a GPU for the track finding algorithm in the DAQ chain either a consumer GPU or a professional version can be used. The difference between the two is the amount of resources available for single and double precision calculations. While both are capable of calculations using either precision modern consumer GPUs are slower than professional GPUs when double precision is used. The most crucial calculation in this respect is the determination of the angle between the triplet segments. Therefore It is necessary to check if there is any difference between single and double precision when calculating efficiencies. In table 7.2 the differences in efficiency can be seen for a couple of parameter combinations. Compared to the overall efficiency the difference is basically negligible so the use of a consumer GPUs is a valid concept.

P_{Beam} [GeV/ c^2]	$n_{generatedTracks}$	$\delta\Psi_{max}$	Efficiency difference [%]
1.5	1	$2 \cdot 10^{-5}$	0.0043
1.5	3	$5 \cdot 10^{-6}$	0.0015
1.5	3	$2 \cdot 10^{-5}$	0
15	3	$5 \cdot 10^{-6}$	0.0055
15	1	$2 \cdot 10^{-5}$	0

TABLE 7.2: Examples for the efficiency difference of the tracking algorithm between single and double precision for different parameter combinations. The maximum number of possible tracklets is 15 for all cases.

7.3 Processing times

To get an idea which kind of hardware to use for online track reconstruction the implementation of the algorithm described in chapter 6 has to be tested for calculation speed. The goal to be aimed for is 25 ns processing time per event as this is the current expected readout rate for the sensors of the detector. The principle structure of the implementation of the algorithm is the same for both the GPU and the CPU. In case of the GPU CUDA [127] has been used while the CPU version is implemented with openMP [136, 137]. To get the calculation time for the GPU kernels the *StopWatchInterface* class from CUDA and on a CPU *std::chrono::high_resolution_clock* from the standard library is used. Both classes allow getting the current clock tick at certain steps in the code and therefore allow to extract the processing time between these clock ticks.

7.3.1 GPU

The tracking algorithm has been tested on an Nvidia GTX 980 Ti and the number of blocks and threads has been varied to find the optimal working point for the two main algorithm steps triplet building and triplet combining. Each test run has been done with 10000 time stamps and the average calculation time per track has been calculated for various steps in the algorithm. The GPU has its own memory different from the main memory which the CPU uses. Thus the first step is to transfer the data from the main memory to the GPU memory. In general it is advisable to have fewer large memory transfers instead of lots of smaller ones. For this reason the data is organized in a Structure of Arrays (SoA) which is illustrated in figure 7.11. The structure contains one array for each hit information (e.g. x and y coordinates) and is accessible directly via index. This is contrary to an Array of Structures (AoS) in which each structure would contain all data for one hit. The latter usually results in longer memory transfers if each individual data is small compared to the overall amount of data. As the data is not organized in the way the track finding algorithm requires it has to be sorted first. This is done on the GPU with an algorithm provided by the thrust library [138]. Copying this structure from the host memory to the GPU global memory takes 0.02 μ s while sorting the data takes 0.07 μ s which is negligible compared to later processing steps. CUDA only offers simple data containers by default and the amount of hits per time stamp

and sensor plane can vary. This variation of the amount of hits makes it necessary to calculate an offset for the index used for the array access as the distribution of the actual data in memory is irregular. In the final DAQ the last two steps are expected to be unnecessary on software level as the individual components sending each piece of data can already presort and count hits for each part of the detector.

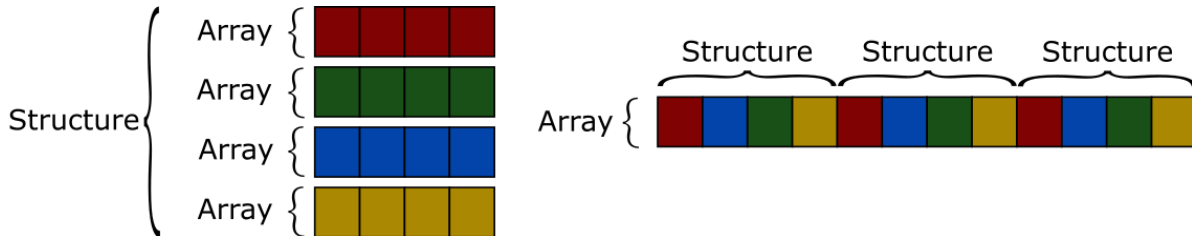


FIGURE 7.11: Illustration showing two possibilities to arrange data. Each color represents different data e.g. x and y coordinates of hits. On the left an Array of Structures (AoS) is shown while the right shows a Structure of Arrays (SoA).

After this the two main algorithm steps are executed and timed individually. Both are tested with 1 and 2 tracks generated per time stamp. The average triplet calculation and triplet combination times per track depending on the number of threads and blocks are shown in figure 7.12 and 7.13 respectively. The amount of threads per block is increased in steps of 32 as smaller steps necessarily lead to unused GPU hardware resources.

It can be seen that the computation time drops quickly from the non parallel case when only one thread and block is running. It can also be seen that the gain of parallelizing the computation further is negligible relatively fast. This is the case for more threads and also for more blocks. A typical saw tooth structure resulting from non optimal occupancy of the GPU resources can not be observed clearly. Besides that no structures can be observed in the histograms which means that no significant occupancy effects of the used hardware have to be taken into account. Simply increasing the degree of parallelism of the computation is enough to receive optimal results for the chosen algorithm implementation on the tested GPU.

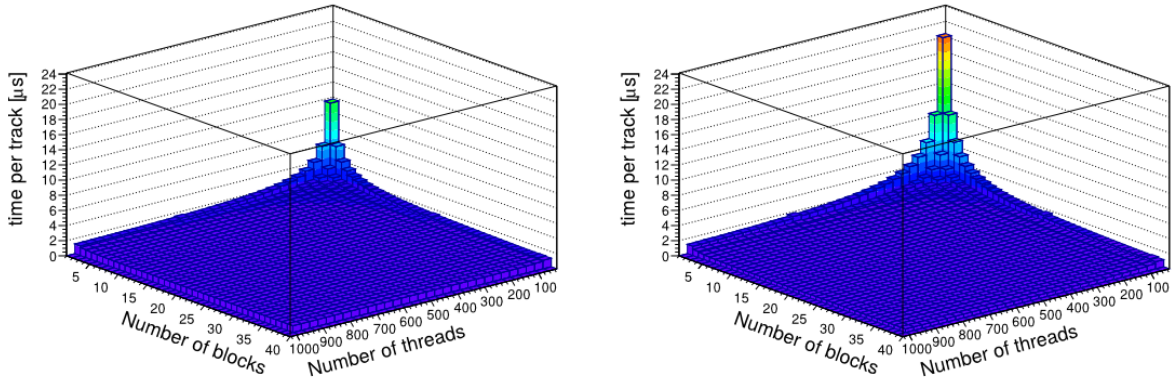


FIGURE 7.12: Time for triplet building with $n_{generatedTrack} = 1$ (left) and $n_{generatedTrack} = 2$ (right) depending on the number of threads and blocks on the GPU. The minimum time per track is $t_{minPerTrackCalculate} = 0.91 \mu s$ for $n_{generatedTrack} = 1$ and $t_{minPerTrackCalculate} = 0.48 \mu s$ for $n_{generatedTrack} = 2$

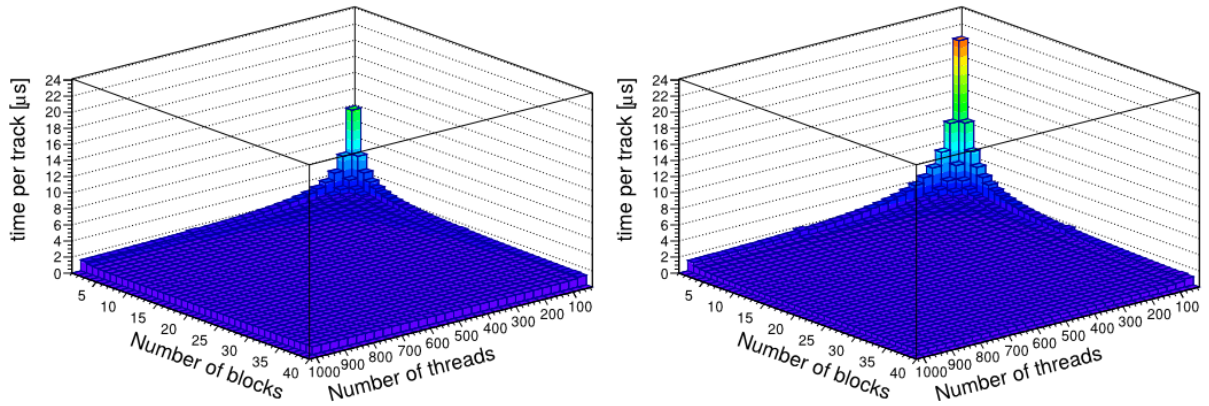


FIGURE 7.13: Time for triplet combination with $n_{generatedTrack} = 1$ (left) and $n_{generatedTrack} = 2$ (right) depending on the number of threads and blocks on the GPU. The minimum time is $t_{minPerTrackCombine} = 0.99 \mu s$ for $n_{generatedTrack} = 1$ and $t_{minPerTrackCombine} = 0.54 \mu s$ for $n_{generatedTrack} = 2$

The resulting minimal average computation times per track if only one track per event was generated are $0.91 \mu s$ for triplet building and $0.99 \mu s$ for the triplet combination. In comparison the memory transfer time of $0.02 \mu s$ and the time of $0.07 \mu s$ needed to sort the complete data are negligible. Calculating the offset of the position of the different time stamps and planes in the memory takes $0.86 \mu s$ per track. This is in the same order of magnitude as the two main computation steps but no effort has been made to optimize this as this is assumed to be already done in previous steps of the final DAQ. The total time per track of $2.76 \mu s$ is about a factor of 100 larger than the optimal target of $25 ns$ per track based on the readout frequency of the detector. In the case of two tracks per event the time per track for triplet building and combining is reduced to $0.48 \mu s$ and $0.54 \mu s$ respectively. The total processing time per event $t_{total} = n_{generatedTracks} \cdot t_{minPerTrackCombine} + n_{generatedTracks} \cdot t_{minPerTrackCalculate}$ for the two triplet processing steps increases slightly from $1.90 \mu s$ to $2.04 \mu s$ when more tracks are

present in an event. Taken for itself a $\approx 7\%$ increase in processing time for 100% increase in data is a good result. Unfortunately it does not change the fact that the baseline target of 25 ns for the processing time has not been met. The main reason for non optimal performance is probably the underestimated effect of the data structure of the tracking algorithm. The potential combinatorics of hits from different planes and different time stamps combined with the varying amount of hits for each of those make it difficult to provide a memory access scheme optimal for the GPU architecture. It was expected that the simple nature of the calculations and the sheer amount of possible parallelization on a GPU would offset this drawback. Other pitfalls like thread divergence in a group of 32 threads could be successfully avoided.

7.3.2 CPU

The main difference between the code running on a GPU and a CPU is that there is no separation into threads and blocks and that the number of threads is greatly reduced. The openMP version of the algorithm has been tested on a compute node equipped with two Intel Xeon Gold 6130 processors with 16 cores each. It offers Hyperthreading which makes it possible to increase the number of threads running simultaneously up to 32 threads per processor and 64 threads for the complete compute node. To get the average processing time per track with a specific number of threads 100000 time stamps with 1 track per time stamp have been processed per run. Each run with a specific number of threads has been repeated 10 times to check for systematic effects not visible in an average computation time. When allowing the compute node complete freedom to schedule the threads to different CPU cores the full 64 threads available with Hyperthreading can be used. The complete processing time per track depending on the number of threads can be seen in figure 7.14. The result of each of the 10 runs is inserted individually in the plot. Up until 10 threads running at the same time the expected behavior can be seen. The processing time drops exponentially with increasing number of threads starting from the slow sequential case of one thread. With more than about 10 threads the results are erratic. Up to roughly 32 threads (the number of physically available cores available on the complete compute node) a few runs still result in the minimal processing time already achieved with about 10 threads. In addition to this minimal runtime some runs finish with longer processing times even longer than the sequential processing time. These values are scattered without a clear underlying structure. The spread to longer processing times gets larger with an increasing number of threads. The spread gets even worse after the number of threads gets larger than the number of physical cores on the node. The baseline for the minimal processing time is not present any more. This behavior can be explained by the fact that the used processor has a non-uniform memory access (NUMA) design. NUMA means that memory access times depend on memory locations relative to the processor. The first thread accessing some data leads to a larger chunk of data containing the accessed data is being moved to memory closest to the core running the thread. This is called first touch. Subsequent threads accessing the same data now have longer access times depending on their spatial position relative to the memory where the data resides. Combining the freely distributed threads with the fact that the distribution of data in each run looks different explains the large spread in overall processing times.

When the number of threads is larger than the number of physical cores on one processor data access is spread over two processors. This can explain the quickly deteriorating performance when $n_{threads} > 16$. At more than 32 threads more threads are active via Hyperthreading than there are physical cores worsening the situation even further. To circumvent this problem threads can be assigned to specific physical cores via thread affinity. This deactivates Hyperthreading and limits the amount of threads to 32 in total. In figure 7.15 the processing times per track depending on the amount of threads running in parallel with each thread pinned to physical core is shown. The same exponential drop can be seen but the processing times are reduced in general compared to the runs with completely free thread scheduling and Hyperthreading. The erratic behavior is completely absent and after the initial drop in processing time there are no more performance improvements with more than about 16 threads. This is most likely due to memory limitations. In this context memory limitations means that the time needed to get a new set of data from the memory into the processor is larger than the time needed for track reconstruction computations. In this case increasing the degree of parallelism only leads to shorter overall processing times if an additional separate memory system is available e.g. another node with its own processors and memory. The minimal limit on reached processing times is about 100 ns. This only a factor of four larger than the maximum readout frequency used by the sensors.

In the worst case scenario of no further improvements being reached by using more powerful hardware splitting the incoming stream of data into four parts would be enough to ensure real time processing. As newer more powerful processors and other computer hardware components become available it is expected that the necessary amount of data splitting will be reduced further until the final detector is running.

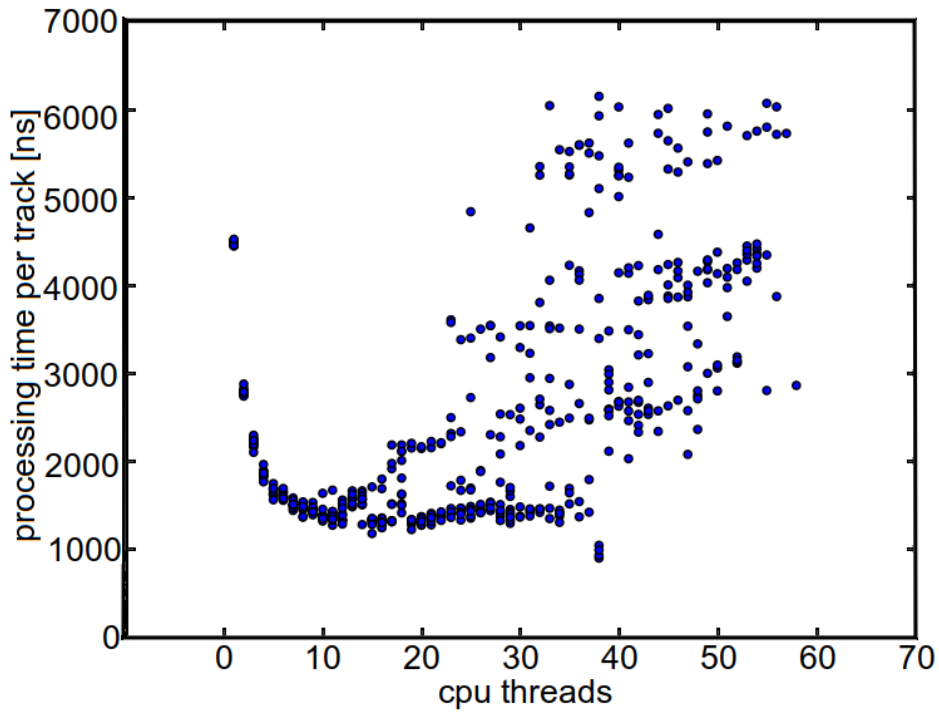


FIGURE 7.14: Processing time per track depending on number of CPU threads. Hyperthreading is enabled

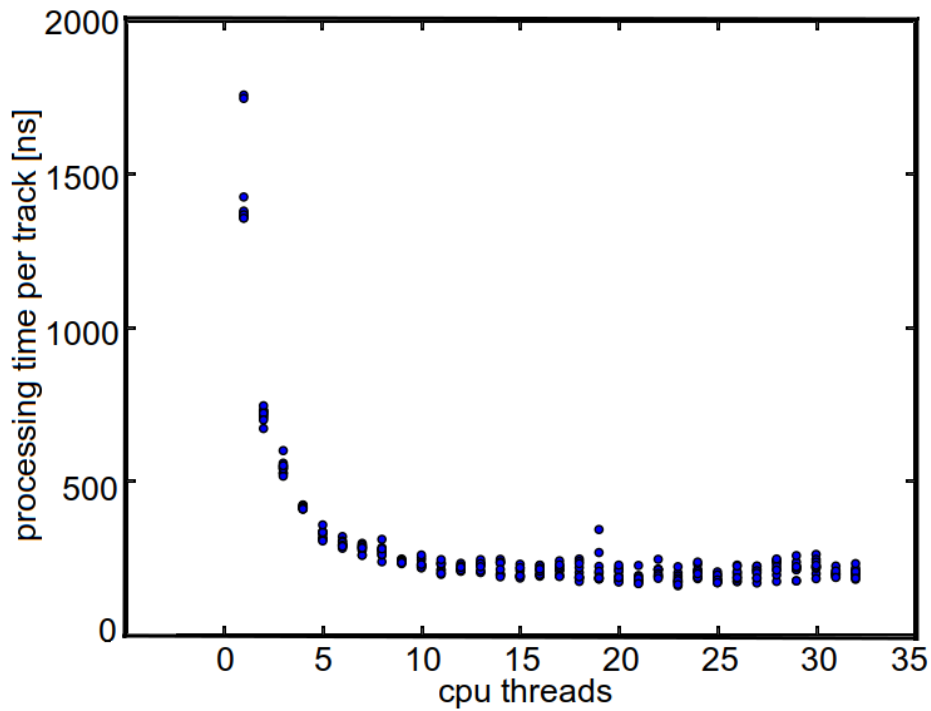


FIGURE 7.15: Processing time per track depending on number of CPU threads. Hyperthreading is disabled

7.4 Summary and Discussion

In order to be able to reduce the amount of data the luminosity detector at \bar{P} ANDA collects an online track finding algorithm has been developed. This track finding algorithm is based on a track finding algorithm that uses a cellular automaton. The newly developed track finding algorithm has been implemented in a GPU and a CPU version. Hits measured by the active silicon pixel sensors of the luminosity detector include a time stamp with a resolution of 25 ns. In the high luminosity case the expected rate of tracks is one track per time stamp. This low track multiplicity is not ideal to exploit the parallel computing capacities of either a GPU or CPU. Therefore the data of a large number of time stamps is collected before it is processed in large bunches. When processing these large bunches the average processing time per time stamp must be 25 ns to be able process all data in real time as there can be new data for every 25 ns. Hits caused by the same antiproton can be attributed to three different adjacent time stamps. This is caused by the distribution of the time walk. While the total spread is 75 ns the majority of hits falls into 50 ns and a time window including hits from three adjacent time stamps is introduced for each time stamp. Triplets containing hits from three different detector layers are calculated for each time window. Triplets sharing two hits are combined into tracks while uncombined triplets are saved as short tracks. To avoid duplicate reconstructions of tracks each triplet is assigned to the first time stamp it contains. Even though the original cellular automaton has been simplified and the new tracking algorithm has lower processing times per time stamp than the version used in the offline analysis has per event the implementation on the GPU (Nvidia GTX 980 Ti) misses the target of 25 ns by a factor of about 100. Computation times might be improved by a different arrangement of data in the memory but this is not certain. The problem with memory arrangement is that in order to achieve peak performance with a GPU it is necessary that adjacent threads on the GPU only access data in a limited memory range. As hit data is spread over time and space this access to a limited memory range can not be achieved without massive duplication of data. The fact that two tracks generated per individual time stamp increase the overall processing time per time stamp only marginally suggests that the structure of the algorithm is not really suited for a GPU in the low track environment of the luminosity detector. Comparing the GPU with the CPU implementation results shows a significant improvement when using a CPU (Intel Xeon Gold 6130) with a large number of physical cores as the computation time per time stamp of slightly above 100 ns misses the design target of 25 ns by only a factor of four. Using more than one of the CPUs on the node used for testing shows no overall improvement suggesting either a memory bottleneck or computational overhead when first creating all threads to process the data. This memory bottleneck or computational overhead can be circumvented by splitting the datastream into four streams each going to separate CPUs.

In terms of efficiency the new simplified algorithm implementation performs similar to the cellular automaton in the offline analysis showing that dropping the iterative cell state evolution step is a reasonable way of reducing computation time in the low track environment of the luminosity detector. The percentage of ghost tracks is larger than in the offline analysis though the different criteria of what is considered a good track prevent an exact comparison. However, considering that the online track finding

algorithm is only used in the DAQ chain as a selection criteria and the data will be processed further in offline processing steps the achieved ghost track percentages do not pose a problem.

One result of this chapter is that the algorithm could be simplified while maintaining a reasonable efficiency and ghost percentage. As the CPU used for these tests is an expensive server CPU the cost factor and simplified algorithm give sufficient reason why one should consider investigating an FPGA based implementation of the track finding algorithm.

Chapter 8

Event selection for the decay $e^+e^- \rightarrow h_c\eta\pi^+\pi^-$ at BESIII

As mentioned in the beginning of this thesis exotic charmonium-like states as the $Z_c(3900)^{\pm/0}$ and $Z_c(4020)^{\pm/0}$ motivate the existence of a related singlet that might decay to $h_c\eta$. In the years 2013, 2014 and recently several datasets with center of mass energies higher than 4.2 GeV have been collected by the BESIII collaboration. This includes the dataset of $\sqrt{s} = 4599.53(81)$ MeV with a luminosity of $586.9(40)$ pb⁻¹ which has been used to search for the decay $e^+e^- \rightarrow h_c\eta\pi^+\pi^-$ in this analysis. The methods to select events for this decay and to estimate background events are described in this chapter.

8.1 Datasets and Monte Carlo Simulations

The analysis of the reaction chain

$$e^+e^- \rightarrow h_c\eta\pi^+\pi^-$$

is performed with the subsequent decays $h_c \rightarrow \eta_c\gamma$, $\eta_c \rightarrow K^+K^-\pi^+\pi^-$ and $\eta \rightarrow \gamma\gamma$. This η decay has been used as it is the most prominent branch with a fraction of $\approx 39\%$ and has a clean signature in the detector with less chances for background contributions. As the η decays into two photons and the h_c decay also contributes one photon an η_c decay without photons in the final state has been chosen to prevent combinatorial background contribution from misattributed photons. For the same reasons a channel with a larger branching fraction of $\mathcal{B} = 6.9 \pm 1.1 \cdot 10^{-3}$ [20] but a limited number of π^\pm has been selected out of remaining η_c decays to serve as the target of this analysis. A Monte Carlo dataset of $26 \cdot 10^4$ events with the described sub decays has been generated.

The development of event selection criteria and study of efficiency, correctness of the reconstruction of the reaction channel and possible background channel contributions has been performed with Monte Carlo simulations. These simulations and the analysis of BESIII data have been done within the BOSS¹ framework version 7.0.3. To simulate the propagation and interaction of particles with the BESIII detector GEANT4 [139] is used. The initial charmonium resonances are generated with KKMC [140] including beam spread and, in the case it is used, initial state radiation up to 2nd order QED calculations. One Monte Carlo sample has been generated without initial state radiation to

¹BESIII Offline Software System

optimize event selection and calculate its efficiency. Additionally another Monte Carlo sample has been generated with initial state radiation to allow for the calculation of initial state radiation correction. To simulate daughter particle decays following the initial resonances BESEvtGen is used [141]. BESEvtGen is based on EvtGen [142] which has originally been developed for B-Physics experiments. For the BESIII detector it has been adapted to be usable for tau-charm physics.

After the generation of the signal events the particles are given to the BESIII detector simulation and are propagated through the full geometry model of it. Further decays of the final state particles are simulated. Any energy losses of particles and interactions with the detector material will be saved. For all energy deposits a detector response is simulated and digitized. Calibration data from the front end electronics of the detector are loaded from a database for this purpose.

Reconstruction of the tracks of charged particles is then performed with a hough tracking algorithm. The resulting data samples of charged tracks and candidates of neutral particles and photons have been used to develop the event selection described in the following.

To study background contributions two inclusive Monte Carlo datasets provided by the BESIII collaboration are used. One is a sample of hadronic reactions consisting of open charm and charmonium channels, vector charmonium states produced in initial state radiation processes, and non resonant $q\bar{q}$ events. The second background sample contains QED processes like e^+e^- , $\mu^+\mu^-$, $\tau^+\tau^-$, $\gamma\gamma$ -reactions.

8.2 Criteria for Particle Selection

The criteria for selecting particles in this analysis follow the standard criteria used by the BESIII collaboration and are described in more detail in the following sections. A representation of the complete selection work flow is shown in figure 8.1. In the first step of event selection charged particle candidates tracks are reconstructed from hit information from the MDC and photon candidates are selected from clusters reconstructed in the EMC.

Good Track Selection

A track is considered a good track when two criteria are fulfilled. A track must lie in the acceptance area of the MDC (this can be seen in figure 3.8) which means that the polar angle of the charged track to the beam fulfills the condition $|\cos\theta| < 0.93$. As the analysed decay does not contain any particles with a life time long enough to produce secondary vertices all tracks must have their origin close to the interaction point of the e^+ and e^- beam. This is satisfied when the closest point of the track lies within a cylindrical area around the interaction point. The radius of the cylindrical area in the xy plane perpendicular to the beam direction is $V_{xy} = 1$ cm while the length along the beam axis has a value of $V_z = \pm 10$ cm.

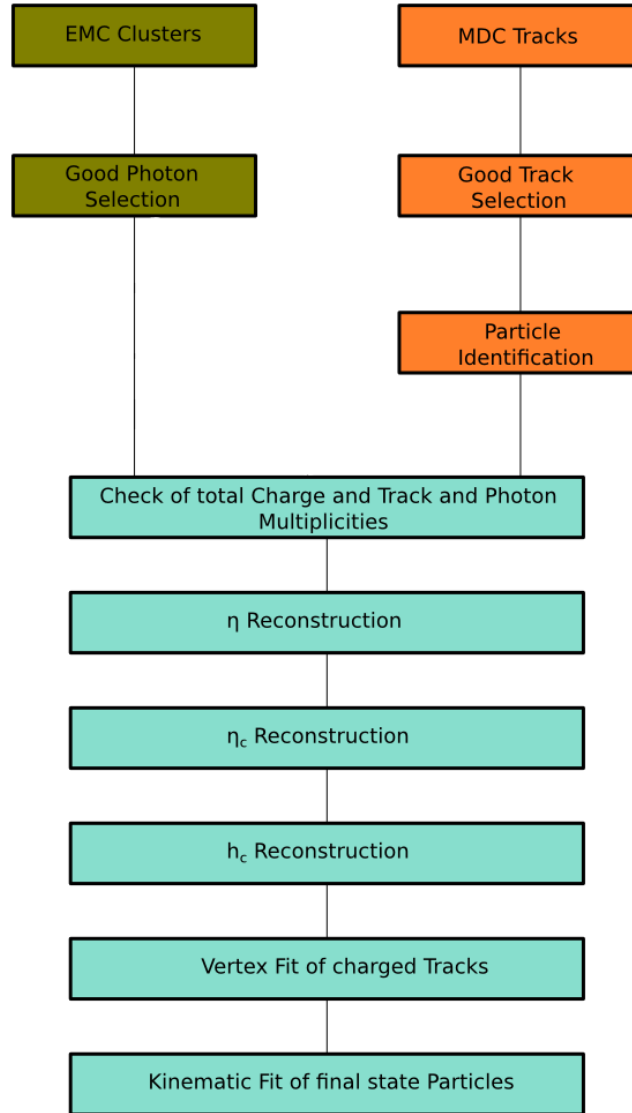


FIGURE 8.1: Work flow of the event selection of the decay $e^+e^- \rightarrow h_c \eta \pi^+ \pi^-$.

Particle Identification

As the pions and kaons have overlapping energy and momentum distributions and to prevent cross feed between other η_c decay modes which have the same number of charged tracks it is necessary to identify and separate pions and kaons. To achieve this identification and separation between pions and kaons a particle identification is performed on all good track candidates after they have been selected. The energy loss of the track in the MDC and the corresponding time-of-flight information of the TOF-detector are used to calculate a joint probability. This probability by the PID-algorithms must be larger than 0.1%. This is done for both pions and kaons and removes tracks with an uncertain particle identification. The amount of actual pion and kaon tracks

lost this way is low. In case of pions the probability to be a pion must be higher than the probability to be a kaon $P(\pi) > P(K)$. For kaons the inverse requirement $P(K) > P(\pi)$ must be fulfilled.

Good Photon Selection

Photons entering the EMC cause electromagnetic showers. These showers usually spread in more than one crystal. Hits in neighbouring crystals are consolidated to clusters and the center of mass of their energy depositions is calculated to get a spatial coordinate. If these clusters of energy in the EMC have no connected track in the drift chamber they are used to reconstruct photons and they must realize the following criteria to be regarded as a photon. In the barrel region of the EMC (the polar angle to the beam axis must satisfy $|\cos\theta| < 0.8$) the reconstructed energy of the cluster must be at least $E_\gamma > 25\text{ MeV}$. Alternatively if the cluster lies in the end cap region of the EMC defined by $0.86 < |\cos\theta| < 0.92$ it must have at least a total energy of $E_\gamma > 50\text{ MeV}$. This requirement in the end cap is set to a higher value to decrease the amount of background hits caused by the accelerator beams being incorrectly identified as low energy photons. Additionally the time difference between the event start time and the EMC timing information of $0\text{ ns} \leq t_{EMC} \leq 700\text{ ns}$ is required. The event start time is based on the clock of the accelerator. The stop time is set to a fixed value. All these requirements serve to suppress noise from the front end electronics. As splitoffs from clusters caused by charged particles might be misidentified as clusters in the EMC caused by photons a certain distance of a cluster in the EMC is required to the projections of the tracks of charged particles. For a cluster of a neutral particle to be identified as a good photon it must lie outside of a cone with an opening angle of at least 10° around any track of a charged particle candidate.

8.3 Event Selection

Pre-Selection

After all particle selection criteria have been applied events are pre-selected based on the multiplicity of the candidates for photons, kaons and pions. The number of good photons must be three. Four good tracks must be identified as pions and two as kaons. Additionally the net charge of all six charged tracks has to be zero. Candidates for the η_c are constructed out of $\pi^+\pi^-K^+K^-$ candidates. It can not be differentiated directly if a pion originated from the η_c or if they are prompt pions. Therefor there are four possibilities to combine the two positively and the two negatively charged pions. In case of the photons it is also not directly possible to distinguish between the photons originating from the η decay and the single photon from the h_c decay. This results in three distinct possibilities to combine the three photons and the η_c candidate into an h_c and an η candidate. Only combinations in which each particle candidate is used once are considered for further selection. To remove some of these combinatorics mass windows are applied. As the η has an invariant mass of $m_\eta = 547.862 \pm 0.017\text{ MeV}/c^2$ [20] a large window of $448\text{ MeV}/c^2 < m_{\gamma\gamma} < 648\text{ MeV}/c^2$ on this mass is used to select the photon pairs reconstructed as η candidates. This window is large enough not to influence any

results but to decrease computation time by removing some photon pairs early which never pass selection criteria in later calculation steps. In figure 8.2 the invariant mass spectrum of η reconstructed from $\gamma\gamma$ can be seen. The shape of the distribution is asymmetric with a long tail towards lower masses. The cause of this is that the EMC cannot measure the full photon energy due to insensitive material like holding structures of the crystals and shower leakage due to finite size of the detector. For the selection of the h_c candidates the invariant mass has to lie in the window of $|m_{h_c} - m_{h_c}^{PDG}| < 0.45 \text{ GeV}/c^2$ around the nominal mass $m_{h_c}^{PDG} = 3.525 \text{ GeV}/c^2$ [20]. The h_c mass distribution of the selected events can be seen in figure 8.3. In figure 8.4 the mass distribution of the underlying η_c is shown.

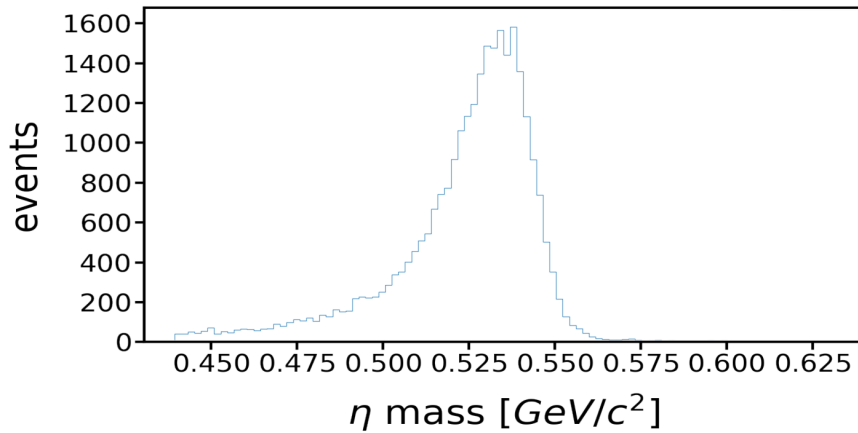


FIGURE 8.2: Reconstructed η mass distribution from signal Monte Carlo simulations.

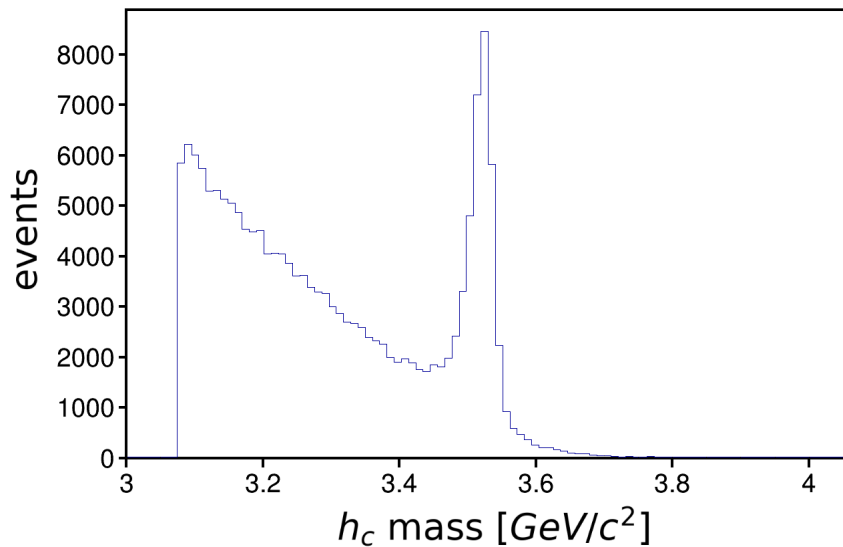


FIGURE 8.3: Reconstructed h_c mass distribution from signal Monte Carlo simulations.

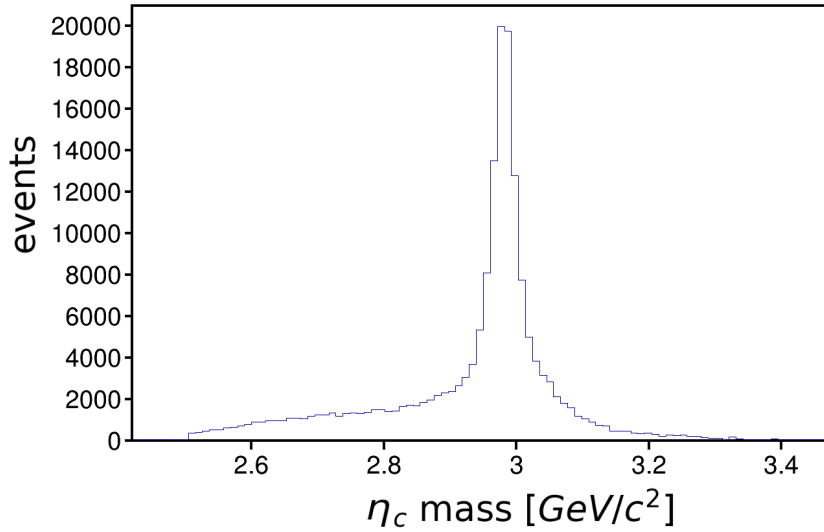


FIGURE 8.4: Reconstructed η_c mass distribution from signal Monte Carlo simulations.

Vertex Fit

All initial particles in the decay $e^+e^- \rightarrow h_c\eta\pi^+\pi^-$ originate from the same vertex but due to limited detector resolution the measured tracks do not reflect this. Therefore a vertex fit is performed. As h_c and η_c have a very short life time and the detector resolution is too low to differentiate a second vertex the pions and kaons from the η_c decay and the prompt pions have to originate from the same point for any valid event. The parameters of the six reconstructed particle tracks are varied within their uncertainties to minimize the distance between the nominal interaction point and point where all of these particle tracks are closest to each other. If the vertex fit converges the event is kept for further analysis while it is rejected when it does not converge.

Kinematic Fit

Even if the tracks are now constrained to a common vertex the kinematics of the event might not be correct. A kinematic fit can be used to determine how much the tracks of an event have to be modified in order to fulfill a set of constraints. The most commonly used constraint is the conservation of the total energy and momentum. Additional criteria as mass constraints can also be required while fitting. The measure of the deviation (χ^2) from perfect kinematics can be used for selecting possible candidates.

In this analysis the constraints used for the kinematic fit are constraints on the mass $m_\eta = 547.862 \pm 0.017 \text{ MeV}/c^2$ [20] of the η and the conservation of the total energy and momentum. The former means that the invariant mass of the two photons used to reconstruct the η candidate should be equal to m_η after the kinematic fit. The latter demands that the energy and the three components of the momentum of the initial e^+e^- system must be the same as the ones of the system of final state particles. This means the conservation of the total energy and momentum corresponds to four constraints. These types of fit are usually named by the amount of constraints used so a fit with only

the total energy and momentum conservation would be called a 4C-fit. As the invariant mass of the η is used as another constraint here the fit performed in this analysis is a 5C-fit.

In the BOSS framework the kinematic fit is based on the least squares method using lagrange multipliers is explained in the following and it is described in detail in [143]. A measurement with normally distributed uncertainties $\vec{\delta} = (\delta_1, \delta_2, \dots, \delta_n)^T$ of a number n parameters results in measured values of $\vec{y} = (y_1, y_2, \dots, y_n)^T$. These values deviate from the true values $\vec{\eta} = (\eta_1, \eta_2, \dots, \eta_n)^T$ in such a way that

$$\vec{y} = \vec{\eta} + \vec{\delta} \quad (8.1)$$

The true values $\vec{\eta}$ depend on r unknown parameters $x = (x_1, x_2, \dots, x_r)^T$ resulting in m boundary conditions

$$f_i(\vec{x}, \vec{\eta}) = f_i(\vec{x}, \vec{y} - \vec{\delta}) = 0, i = 1, \dots, m. \quad (8.2)$$

Expanding equation 8.2 around a point $(\vec{x}_0, \vec{\eta}_0)$ produces

$$f_i(\vec{x}, \vec{\eta}) \approx f_i(\vec{x}_0, \vec{\eta}_0) + \sum_{j=0 \dots r} \left. \frac{\partial f_i}{\partial x_j} \right|_{\vec{x}_0, \vec{\eta}_0} (x_j - x_{j,0}) + \sum_{k=0 \dots n} \left. \frac{\partial f_i}{\partial \eta_k} \right|_{\vec{x}_0, \vec{\eta}_0} (\eta_k - \eta_{k,0}) \quad (8.3)$$

The partial derivatives of the function f_i to the unknown parameters x_j and the true values η_j evaluated at $(\vec{x}_0, \vec{\eta}_0)$ shall be contained in the matrices A and B which are defined as

$$A_{ij} = \left. \frac{\partial f_i}{\partial x_j} \right|_{\vec{x}_0, \vec{\eta}_0} \quad \text{and} \quad B_{ij} = \left. \frac{\partial f_i}{\partial \eta_j} \right|_{\vec{x}_0, \vec{\eta}_0} \quad (8.4)$$

with $i = 1, \dots, m$ and $j = 1, \dots, r$. With additionally defining

$$\vec{\xi} = \vec{x} - \vec{x}_0 \quad \text{and} \quad \vec{\tau} = \vec{\eta} - \vec{\eta}_0 \quad (8.5)$$

approximation 8.3 can be written as

$$f_i(\vec{x}, \vec{\eta}) \approx f_i(\vec{x}_0, \vec{\eta}_0) + A\vec{\xi} + B\vec{\tau} = 0 \quad (8.6)$$

To fulfill equation 8.6 while minimizing the quadratic distance of the measured to the true values. To do this χ^2 is used. It is defined as

$$\chi^2 = \vec{\tau}^T C_y^{-1} \vec{\tau} \quad (8.7)$$

where C_y is the covariance matrix of the measured values \vec{y} . The method of lagrange multipliers states that 8.7 is minimized and 8.6 is fulfilled at the same time when the following expression

$$\begin{aligned}
\mathcal{L} &= \chi^2 + 2\vec{\lambda}^T \cdot \vec{f}(\vec{x}, \vec{\eta}) \\
&= \vec{\tau}^T C_y^{-1} \vec{\tau} + 2\vec{\lambda}^T \cdot (\vec{f}(\vec{x}_0, \vec{\eta}_0) + A\vec{\xi} + B\vec{\tau}) \\
&\stackrel{!}{=} 0,
\end{aligned} \tag{8.8}$$

where $\vec{\lambda} = (\lambda_1, \dots, \lambda_m)$ contains the lagrange multipliers, is fulfilled. With $G_B = (B^T C_y B)^{-1}$ the definitions $\vec{\xi}$ and $\vec{\tau}$ in 8.5 can be written as

$$\vec{\xi} = -(A^T G_B A)^{-1} A^T G_B \vec{f}(\vec{x}_0, \vec{\eta}_0) \tag{8.9}$$

and

$$\vec{\tau} = -C_y B^T G_B (\vec{f}(\vec{x}_0, \vec{\eta}_0) + A\vec{\xi}) \tag{8.10}$$

Expression 8.7 which needs to be minimized is a χ^2 distribution with $m - r$ degrees of freedom. When there are no unknown parameters \vec{x} so $r = 0$ the number of degrees of freedom becomes m and is equal to the number of constraints enforced. Determining the goodness of the fit is done with the χ^2 value which reflects the deviations from the kinematic correct solution. Signal events are expected to have mainly small values whereas background events are expected to have a flat distribution.

Every candidate of the complete decay undergoes two steps of kinematic fitting. At first only the total energy and momentum of the candidate is constraint to the initial energy and momentum of the e^+e^- . Candidates for which the kinematic fit converges with $\chi^2 < 200$ are then subjected to the 5C kinematic fit with the invariant mass of the two photons used to reconstruct the η candidate constraint to the η mass $m_\eta = 547.862 \pm 0.017 \text{ MeV}/c^2$ [20]. The distribution of the χ^2 values of the 5C kinematic fit of signal Monte Carlo events is shown in figure 8.5. A cut on the χ^2 of the fit is applied. Restricting candidates to $\chi^2 < 50$ retains 80% of reconstructed signal events. For each event the candidate with the lowest χ^2 is kept as a best candidate. In some events there are multiple best candidates. An example for this is the case when prompt pions can be exchanged with pions from the η_c decay without changing the total four momentum which leads to multiple candidates with effectively identical χ^2 values. In these cases all candidates are kept which fulfill $|\chi_{candidate}^2 - \chi_{best}^2| < 10^{-5}$.

Additional η_c -cut

Applying a cut on the mass of the reconstructed η_c $|m_{\eta_c}^{PDG} - m_{\eta_c}^{reconstructed}| < 100 \text{ MeV}/c^2$ with the nominal mass $m_{\eta_c}^{PDG} = 2.9839 \pm 0.0005 \text{ GeV}/c^2$ [20] reduces the number of events with multiple candidates significantly. This can be seen in figure 8.6 which shows the distribution of the number of selected best candidates in an event with $\chi^2 < 50$ in blue. The orange curve show the number of best candidates per event without the additional mass window cut and it can be seen that there are more events with multiple best candidates compared to the blue curve showing the number of best candidates with the η_c mass window cut applied. Furthermore the amount of background events is also reduced by this cut as described in the next section.

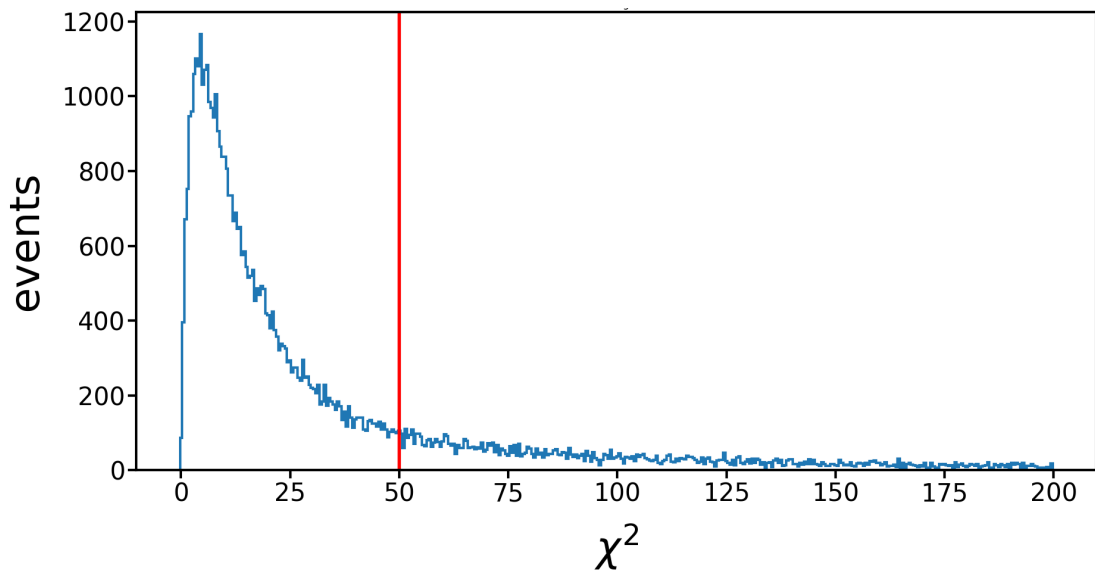


FIGURE 8.5: Distribution of the χ^2 from the kinematic fit for all candidates. χ^2 values of the fitted signal Monte Carlo events are represented by the blue curve. The red line shows the applied cut $\chi^2 < 50$

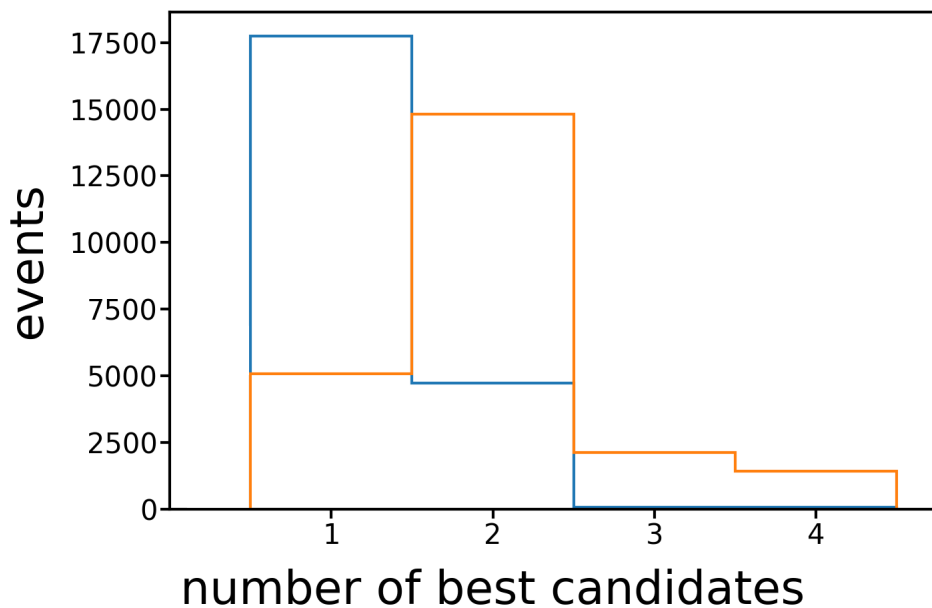


FIGURE 8.6: Number of selected best candidates. The orange curve shows the number of selected best candidates per event with $\chi^2 < 50$. The blue curve shows them with an additional η_c $|m_{\eta_c}^{PDG} - m_{\eta_c}^{reconstructed}| < 100 \text{ MeV}/c^2$ mass window cut applied.

8.4 Background Estimation

As described in chapter 8.1 two inclusive Monte Carlo samples are used to estimate the background contribution for the analyzed decay channel. While the QED sample

corresponds to the measured integrated luminosity of the dataset at $\sqrt{s} = 4.6\text{ GeV}$, the hadronic Monte Carlo sample is five times larger. As expected there is no contribution from the QED processes e^+e^- , $\mu^+\mu^-$, $\tau^+\tau^-$, $\gamma\gamma$. The investigated hadronic Monte Carlo sample contains all hadronic processes known so far and even more which are assumed to exist.

Figure 8.7 shows both χ^2 distribution of events from signal and inclusive Monte Carlo samples. The χ^2 distribution of the background candidates surviving all selection criteria is almost flat χ^2 . In figure 8.8 the h_c mass distribution is shown after all cuts applied. It can be seen that there is no h_c signal in the Monte Carlo background. From all background Monte Carlo samples 308 events belonging to 182 different reaction channels survived all cuts. By normalizing to the luminosity of data only ≈ 62 events remain.

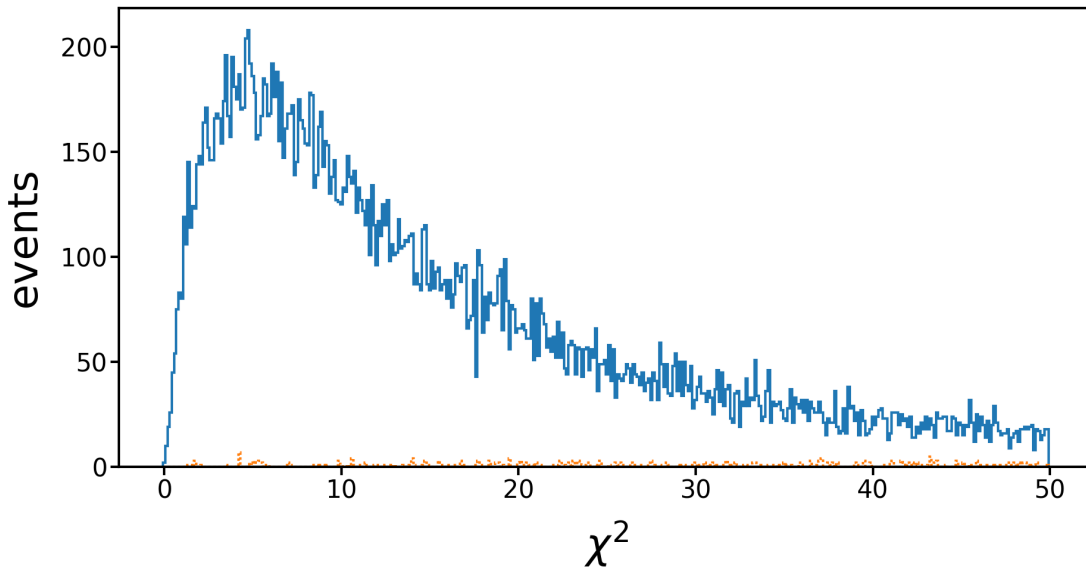


FIGURE 8.7: χ^2 distributions for all best candidates after $\chi^2 < 50$ and $|m_{\eta_c} - m_{\eta_c}^{PDG}| < 100\text{ MeV}/c^2$ cut have been applied. χ^2 values of background events from inclusive Monte Carlo samples are shown in orange and of signal Monte Carlo samples in blue.

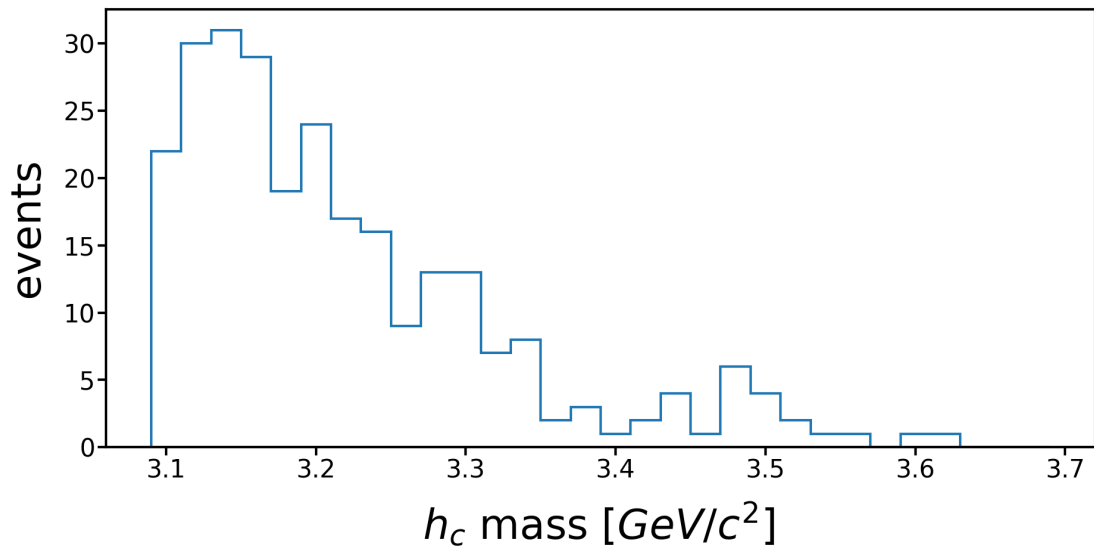


FIGURE 8.8: h_c mass distributions of the best candidates of background events from inclusive Monte Carlo sets. A $\chi^2 < 50$ and $|m_{\eta_c} - m_{\eta_c}^{PDG}| < 100 \text{ MeV}/c^2$ cut have been applied.

Chapter 9

Results of the Analysis

In this chapter the event reconstruction performance is evaluated in terms of the correctness of the reconstruction of the complete event, the global event reconstruction efficiency and mass resolution. Furthermore the Bukin function used as a fit function to determine the cross section is described. Additionally the η_c channel crossfeed is assessed. Since the sum of the mass of the $h_c\eta\pi^+\pi^-$ final state is 4.35 GeV, the phase space available at $\sqrt{s} < 4.6$ GeV is small. This results in very slow prompt pions which lead to very low reconstruction efficiencies. Therefore only the dataset at $\sqrt{s} = 4.6$ GeV is investigated.

9.1 Correctness

To get the correctness of the event reconstruction Monte Carlo samples were used. An event is considered correct if it contains at least one candidate which matches the generated decay tree. Remaining candidates are classified as mismatched candidates as they have not been reconstructed correctly. The correctness is defined as $\frac{\text{matchedCandidates}}{\text{generatedCandidates}}$ and reaches 71%. In figure 9.1 the h_c mass distribution of all best candidates is shown in blue. In addition it is separated in candidates which perfectly match the generated event (orange) and candidates which don't match the generated event (green). This background contribution is caused by so called combinatorial background events. For example photons from the h_c and η decay can be attributed to the wrong mother particle or initial pions can be switched with pions from the η_c decay. Another part of this distribution consists of correctly reconstructed h_c candidates for which the Monte Carlo truth matching has failed. As the combinatorial background is not peaking underneath the h_c peak it does not cause any complications.

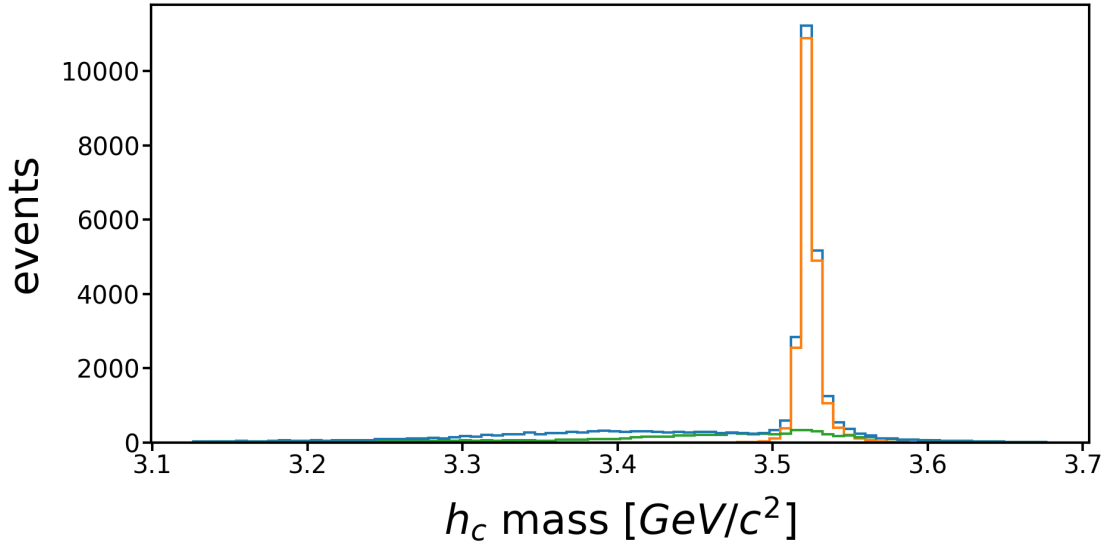


FIGURE 9.1: h_c mass distributions. The blue curve shows all candidates reconstructed from signal Monte Carlo events after all selections and cuts applied. The orange curve represents only h_c candidates which have been reconstructed as they were initially simulated. h_c candidates which are reconstructed wrongly are indicated in green.

9.2 Method for cross section determination

In this analysis the cross section for the channel $e^+e^- \rightarrow h_c\eta\pi^+\pi^-$ will be determined with a fit. Cross sections and angular distributions are mostly unknown in the relevant energy range of this analysis. Therefore a data based approach is used. The background in the signal region is estimated via fitting the background distribution in a wider area including the signal region. For this it is preferable to have some non-peaking background left in the invariant h_c mass and describe both the signal and the background shape with a composite fit. For the signal shape a Bukin function [144] has been chosen as it describes the signal shape of the Monte Carlo generated signal better than a Gaussian distribution. It is specifically designed for modeling asymmetric tails which is achieved by a convolution of a Gaussian function with exponential functions modeling the tails separately. In RooFit [145] it is implemented in 3 different ranges given by

$$x_{1,2} := x_p + \sigma_p \sqrt{2 \ln 2} \left(\frac{\xi}{\sqrt{\xi^2 + 1}} \mp 1 \right) \quad (9.1)$$

for the left tail $x < x_1$ the function is defined by

$$\mathcal{P}(x; x_p, \sigma_p, \xi, \rho) := A_p \exp \left[\frac{\xi \sqrt{\xi^2 + 1} \frac{(x-x_1)\sqrt{2 \ln 2}}{\sigma_p}}{(\sqrt{\xi^2 + 1} - \xi)^2 \ln(\sqrt{\xi^2 + 1} - \xi)} + \rho_1 \left(\frac{x - x_1}{x_p - x_1} \right)^2 - \ln 2 \right] \quad (9.2)$$

in the center region $x_1 < x \leq x_2$ it is defined by

$$\mathcal{P}(x; x_p, \sigma_p, \xi, \rho) := A_p \exp \left[-\ln 2 \left(\frac{\ln \left(1 + 2\xi \sqrt{\xi^2 + 1} \frac{(x-x_p)}{\sigma_p \sqrt{2 \ln 2}} \right)}{\ln \left(1 + 2\xi \left(\xi - \sqrt{\xi^2 + 1} \right) \right)} \right)^2 \right] \quad (9.3)$$

and for the right tail $x \geq x_2$ it is defined by

$$\mathcal{P}(x; x_p, \sigma_p, \xi, \rho) := A_p \exp \left[\frac{-\xi \sqrt{\xi^2 + 1} \frac{(x-x_2) \sqrt{2 \ln 2}}{\sigma_p}}{\left(\sqrt{\xi^2 + 1} - \xi \right)^2 \ln \left(\sqrt{\xi^2 + 1} + \xi \right)} + \rho_2 \left(\frac{x - x_2}{x_p - x_2} \right)^2 - \ln 2 \right] \quad (9.4)$$

A_p is the amplitude, x_p is the peak position and σ_p the peak width (FWHM/2.35). ξ is a parameter describing the asymmetry and $\rho_{1,2}$ are parameters for the individual tails. Figure 9.2 shows some example curves for different parameters.

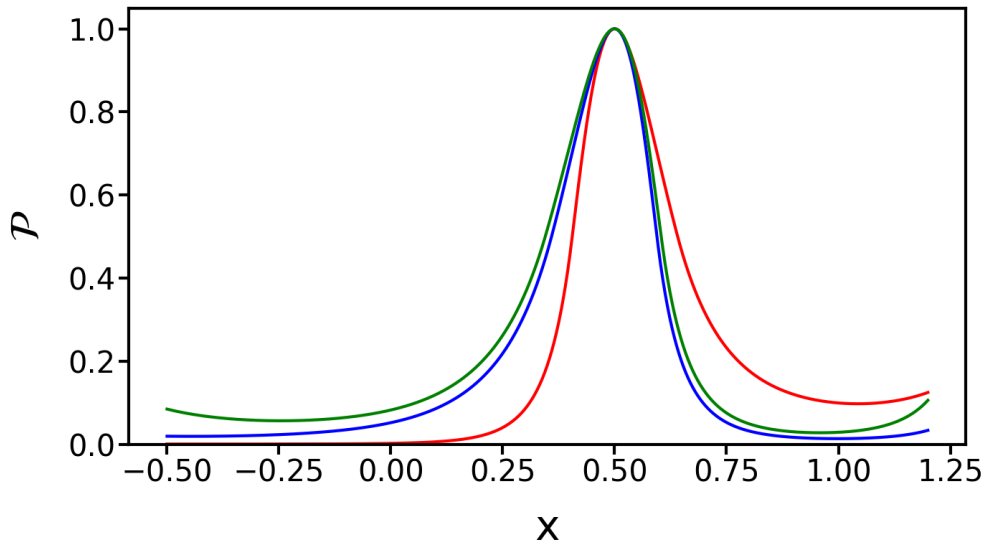


FIGURE 9.2: Examples curves for the Bukin function for different parameters. The following parameters are used for the curves: red ($x_p = 0.5$, $\sigma_p = 0.1$, $\rho_1 = 0.1$, $\rho_2 = 0.2$, $\xi = 0.2$), blue ($x_p = 0.5$, $\sigma_p = 0.1$, $\rho_1 = 0.1$, $\rho_2 = 0.2$, $\xi = -0.2$), green ($x_p = 0.5$, $\sigma_p = 0.11$, $\rho_1 = 0.15$, $\rho_2 = 0.25$, $\xi = -0.2$)

The distribution of background candidates resulting from wrongly reconstructed signal events can be described with a very broad Gaussian function. The fitting function depending on the mass is then

$$f_{fit}(m) = n_{sig} \mathcal{P}(m, x_p, \sigma_p, \xi, \rho) + n_{comb} \frac{1}{\sqrt{2\pi}\sigma^2} e^{-\frac{(x-\mu)^2}{2\sigma^2}} \quad (9.5)$$

with n_{sig} being the number of correctly reconstructed signal events and n_{comb} the number of combinatorial background events. To determine the parameters of both the Bukin and the Gaussian function (9.5) is fitted to the h_c mass distribution of the best candidates from signal Monte Carlo events. In addition to these parameters the fraction of $\frac{n_{sig}}{n_{comb}}$ is also determined. In figure 9.3 the result of this fit is shown. The blue curve is the combined function for the signal while the red curve shows only the broad Gaussian function describing the combinatorial background. With a $\chi^2/dof = 0.99$ the fit model describes the signal Monte Carlo very well.

The background estimated in 8.4 is described with an exponential function and the complete fit model depending on the mass m is therefore given by

$$f_{fit}(m) = n_{sig} \mathcal{P}(m, x_p, \sigma_p, \xi, \rho) + n_{comb} \frac{1}{\sqrt{2\pi\sigma^2}} e^{-\frac{(x-\mu)^2}{2\sigma^2}} + n_{bkg} e^{(am)} \quad (9.6)$$

in which n_{bkg} is the number of background events unrelated to the signal decay mode. The parameter a is the slope of the exponential function. As the goal of this analysis is to extract a cross section and an upper limit in case of an insignificant signal yield the change of the mean and the width of the peak position that might be caused by using a Bukin function is not relevant. All parameters and the fraction $\frac{n_{sig}}{n_{comb}}$ are fixed to the values extracted from the fit to the signal distribution (shown in figure 9.3) when the complete fit model (equation 9.6) is fitted to data. From n_{sig} determined this way the observed cross section σ is calculated with:

$$\sigma = \frac{n_{sig}}{\mathcal{L} \cdot \epsilon \cdot \mathcal{B}} \quad (9.7)$$

where \mathcal{L} is the integrated Luminosity, ϵ the global reconstruction efficiency determined from Monte Carlo simulations and $\mathcal{B} = \mathcal{B}(\eta \rightarrow \gamma\gamma) \cdot \mathcal{B}(h_c \rightarrow \eta_c\gamma) \cdot \mathcal{B}(\eta_c \rightarrow K^+K^- \pi^+ \pi^-)$ the product of the branching ratios of all decays used in this analysis.

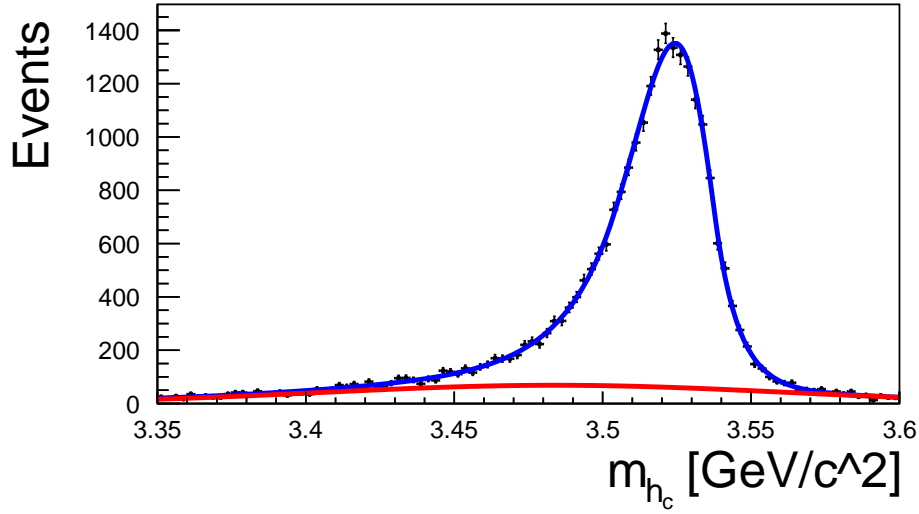


FIGURE 9.3: Distribution of the h_c mass after candidate selection from signal Monte Carlo samples. The distribution is fitted with a Bukin function modeling the signal and a Gaussian function (red curve) modeling the combinatorial background distribution.

9.3 Efficiency and Resolution

The reconstruction efficiency is determined by dividing the number of signal events n_{sig} obtained with the fit shown in figure 9.3 by the number of originally generated signal Monte Carlo events n_{gen} . This results in an efficiency $\epsilon = 8.28\%$.

The resolution of the h_c mass is estimated by fitting the residuals of the originally simulated mass and the mass reconstructed after all selection steps. In this way the natural width of the h_c is separated from the resolution. To accurately describe the distribution of these residuals two Gaussian functions have to be used as a resolution function. Figure 9.4 shows the residuals and the corresponding fit result. The distribution is slightly shifted from zero to $3.77 \pm 0.21 \text{ MeV}/c^2$ and additionally, slightly asymmetric with a tail to higher reconstructed masses which is modeled by the second Gaussian. The resolution is defined as the width of the central Gaussian function which corresponds to the resolution of the mass of the h_c and has a value of $12.35 \pm 0.20 \text{ MeV}/c^2$

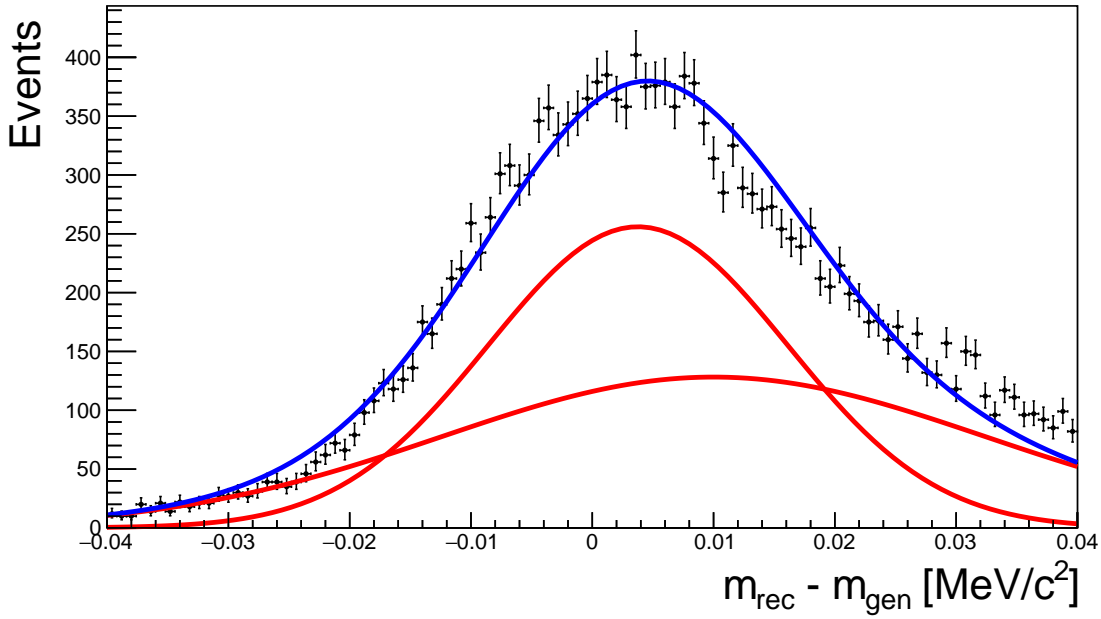


FIGURE 9.4: Residual distribution of the h_c mass. The fitted resolution function constructed out of two Gaussian functions is represented in blue. The red curves are the individual functions.

9.4 Channel Cross Feed

Particle misidentification and the uncertainties in the event reconstruction can result in non-signal η_c decay modes to be reconstructed as the specific η_c decay of this analysis. This can result in an inflated number of reconstructed events and is called cross feed. To determine the size of this effect Monte Carlo simulations have been used.

10^5 events have been simulated by allowing the η_c to decay to all known decay modes as listed by lundcharm [146]. These sum up to 69% of the total η_c branching fraction as listed by the PDG [20].

As soon as one event of a certain η_c decay passes the complete reconstruction chain this decay was simulated again with 10^5 events each. This is done to save computing time and can be done as some channels are not reconstructed incorrectly at all. The number of events of each of these extra simulated decays are counted after reconstruction and summarized in table 9.1. No branching ratios for the η_c final states have been taken into account. The remaining η_c decay modes passing the selection steps are $\eta_c \rightarrow K^- \pi^+ K^0$, $\eta_c \rightarrow K^+ \pi^- \bar{K}^0$ and $\eta_c \rightarrow K^- \pi^0 K^+$. The main source for the wrong reconstruction of η_c decays are the additional π^\pm in the decay originating from the K^0 decays. In rare cases it is possible for the e^\pm originating from a π^0 decay to be misidentified as π^\pm . Normalizing the numbers of the remaining events by the branching ratios leads to a total cross feed frequency of less than 0.01%. Therefore these cross feed events can be neglected for the rest of this analysis.

$K^- \pi^+ K^0$	$K^+ \pi^- \bar{K}^0$	$K^- \pi^0 K^+$	total
16	14	5	35

TABLE 9.1: Cross feed to the the analyzed η_c decay mode $K^+ K^- \pi^+ \pi^-$ at the center of mass energy of 4.6 GeV from other η_c channels. Only channels with a non-zero contribution are listed. 10^5 events have been simulated for each decay mode.

9.5 Cross section

The data set available from the BESIII collaboration at a center of mass energy of 4.6 GeV is analyzed with the event selection described in chapter 8.

The distribution of all events surviving the selection are shown in form of h_c the mass distribution in figure 9.5. No peaking structure can be seen and using the frequentist calculator of RooStats on the fit result leads to a significance of 0σ . Since the background distribution in data looks very similar to the distribution from the Monte Carlo simulation (see figure 8.8) the function 9.6 is fitted to data to extract the signal and background yields. The function is the sum of an exponential function describing the background distribution, a Bukin function for the signal events and a wide Gaussian function for the description of the combinatorial background component. The peak position and width as well as the parameters describing the asymmetry of the Bukin function are fixed to the values obtained through fitting the signal Monte Carlo set at 4.6 GeV. The slope of the exponential function as well as the number of background and signal events are determined by the fit.

The number n_{sig} of observed h_c candidates in data gives the cross section of the analyzed channel with the following equation

$$\sigma = \frac{n_{sig}}{\mathcal{B}(h_c \rightarrow \gamma \eta_c) \cdot \mathcal{B}(\eta \rightarrow \gamma \gamma) \cdot \mathcal{B}(\eta_c \rightarrow K^+ K^- \pi^+ \pi^-) \cdot \epsilon \cdot \mathcal{L}} \quad (9.8)$$

in which \mathcal{L} is the integrated luminosity of the analyzed data set, ϵ is the reconstruction efficiency of this reaction channel, $\mathcal{B}(\eta \rightarrow \gamma \gamma) = 39.41 \pm 0.20\%$ is the branching ratio of η decaying to two photons, $\mathcal{B}(h_c \rightarrow \gamma \eta_c) = 51 \pm 6\%$ is the branching ratio of h_c decaying into a photon and an η_c and $\mathcal{B}(\eta_c \rightarrow K^+ K^- \pi^+ \pi^-) = 0.69 \pm 0.10\%$ is the branching ratio of the η_c decay into two charged kaons and two charged pions. All branching ratios are taken from the PDG [20]. The integrated luminosity is measured from the observed rate of Bhabha scattering events [147] after correcting for detector acceptance and efficiency. It is cross checked with the reaction channels $e^+ e^- \rightarrow \mu^+ \mu^-$ and $e^+ e^- \rightarrow \gamma \gamma$.

The resulting cross section is

$$\sigma_{4.6 \text{ GeV}} = -2.2_{-20.3}^{+27.9} \text{ pb} \quad (9.9)$$

The statistical uncertainties for this value are a confidence interval for a parameter of interest θ in the presence of a nuisance parameter ν obtained by calculating the values for which

$$\max \ln L(\theta, \nu) = \ln L(\hat{\theta}, \hat{\nu}) - \lambda$$

$\hat{\theta}$ and $\hat{\nu}$ are values for which the log-likelihood L is at a maximum and $\lambda = 0.5$ for a 68% confidence interval. Within the statistical uncertainties the extracted cross section is compatible with 0, no significant signal is observed. Therefore an upper limit is estimated on the cross section. This is done with a scan of the likelihood function depending on the cross section which is described in section 9.8.

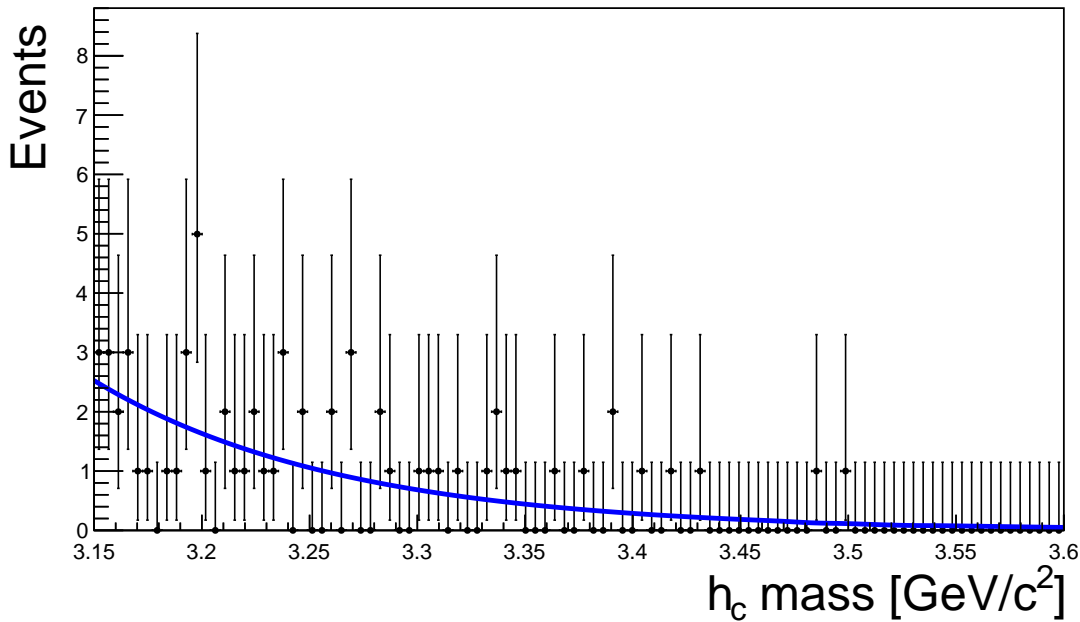


FIGURE 9.5: h_c invariant mass distribution of the decay $e^+e^- \rightarrow h_c\eta\pi^+\pi^-$ for BESIII data at $\sqrt{s} = 4.6\text{ GeV}$. Selected data is represented by the black points. The blue line is the result of the fit of the combination of signal and background model.

9.6 Systematic Uncertainties

This section describes how the systematic uncertainties in the cross sections measurement are estimated for this analysis. The systematic uncertainties are important to calculate an accurate upper limit.

9.6.1 Fit Bias

To test if the fitting procedures leads a possible bias of the extracted cross section an input-output check is performed. A certain signal and background shape is taken and toy Monte Carlo samples are created with these. The signal distribution is described by a Bukin function whose parameters were fixed by a fit to the signal Monte Carlo sample. The background shape is determined by a fit to data of the complete model consisting

of the Bukin function and an exponential function. The number of events sampled from the background shape match the number of background events in the fit to data. To determine if there is any bias for any signal cross section the number of signal events sampled from the Bukin function is varied. For each number of signal events 10000 distributions are generated and fitted with the complete model and the cross section is determined. All resulting cross section values are filled into a histogram as shown in figure 9.6 for the simulated cross section of 154 pb. This distribution is fitted with a Gaussian function to estimate its mean and width. The obtained mean values are very accurate but the widths of the distributions are very large.

Figure 9.7 shows the determined mean values of the signal cross sections as a function of the cross section used to generate the toy Monte Carlo samples. The width of the single histogram is taken as the uncertainty of the cross section determination. As a linear relation is expected a linear function is fitted to the mean values of the signal cross sections to quantify if there is any bias. The slope of the linear function is 1.0034 ± 0.0008 and the offset is -0.76 ± 0.13 pb. Compared to the statistical uncertainty on the measured cross section $\sigma_{obs} = -2.2^{+27.9}_{-20.3}$ pb the offset is very small and the slope has also almost no effect. Therefore no fit bias will be taken into account in this analysis.

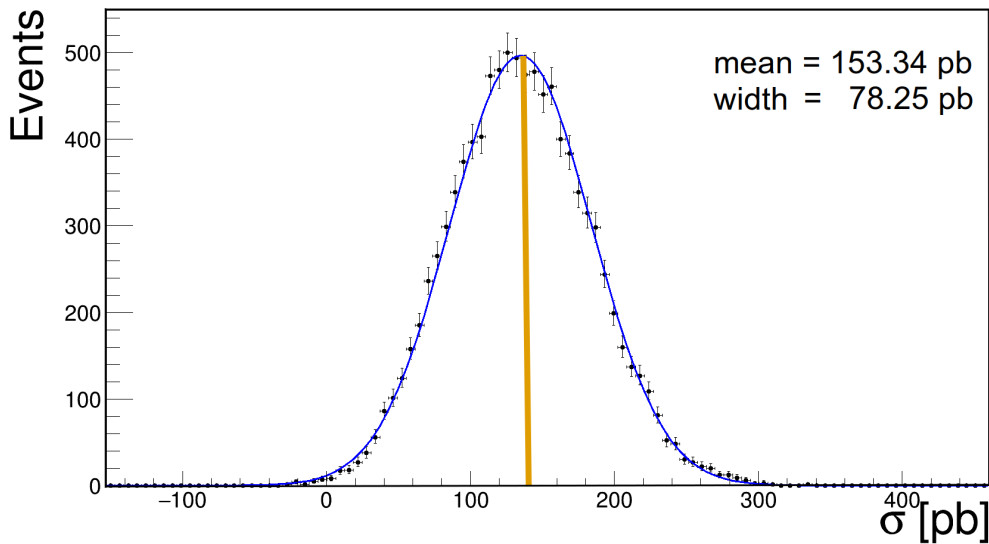


FIGURE 9.6: Exemplary Gaussian distribution of the fitted cross sections with the complete fit model for an input cross section of 154 pb

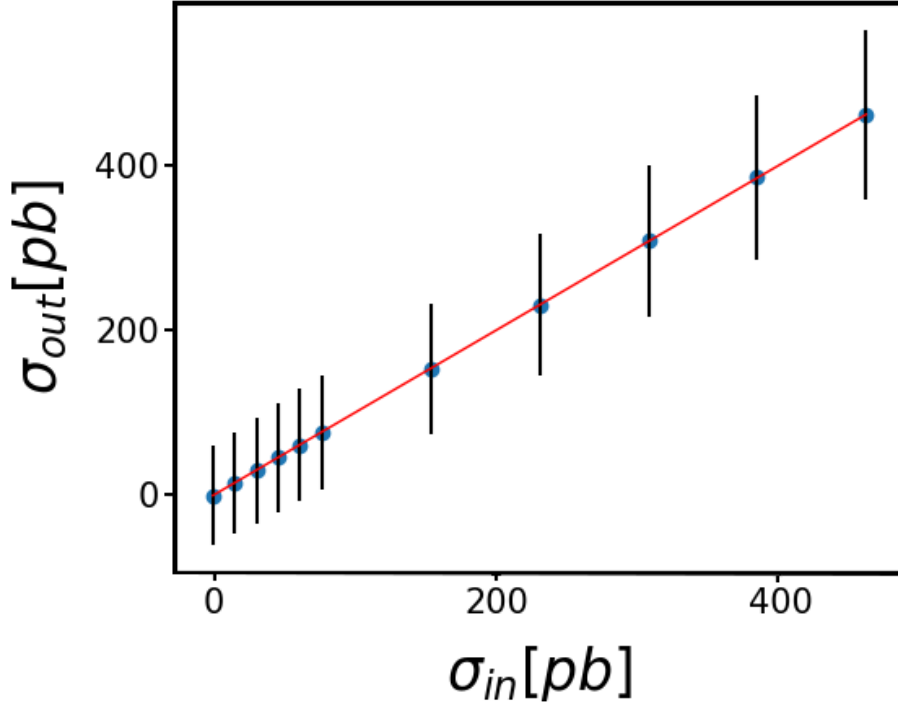


FIGURE 9.7: Test of a fit bias: The mean values and width (error bars) of the Gaussian distributions of the cross section extraction of 10000 toy Monte Carlo fits is plotted in dependence on the generated cross section. The line is a fit to the mean values. The slope is 1.0034 ± 0.0008 and the offset is -0.76 ± 0.13 pb

9.6.2 Fit Range of h_c mass

For the extraction of the yield of signal events and therefore the cross section the fit function 9.6 was used and the range from 3.15 GeV to 3.6 GeV was fitted. To study the influence of the fit range used for the fit of h_c candidates the range is narrowed and widened by 10% of the original range. With this the narrow fit range for the h_c mass is $3.175 \text{ GeV}/c^2 < m_{h_c} < 3.575 \text{ GeV}/c^2$ and the wide fit range is $3.125 \text{ GeV}/c^2 < m_{h_c} < 3.625 \text{ GeV}/c^2$. For the wide range the cross section is extracted to be $-2.76^{+19.23}_{-13.47}$ pb and for the narrow range $-4.16^{+19.70}_{-15.04}$ pb. The larger difference between the cross sections obtained by the nominal fit $-2.23^{+27.90}_{-20.32}$ pb and the values obtained with the modified fit ranges is taken as systematic uncertainty. This results in a systematic uncertainty on the cross section of $\Delta\sigma_{fitRange} = 1.93$ pb.

9.6.3 Background Shape

The background shape was determined by the fit to data where the function e^{am} was used. The influence of the model used to fit the background shape is studied by using another model with a similar shape. As replacing the exponential function in the fit

with Chebychev polynomials does not yield good results the following model using a hyperbolic tangents has been used $f_{background} = a \cdot \tanh(-m + b) + c$ with a, b and c being free parameters in the fit. The resulting cross section of using this background function is $\sigma_{tanh} = -30.02$ pb. Both the fit with the nominal exponential function to describe the background and the fit with the hyperbolic tangents are shown in figure 9.8. The difference between the cross sections obtained via fitting the two models containing distinct functions describing the background is taken as systematic uncertainty of the background shape. Its value is $\Delta\sigma_{background} = 27.79$ pb.

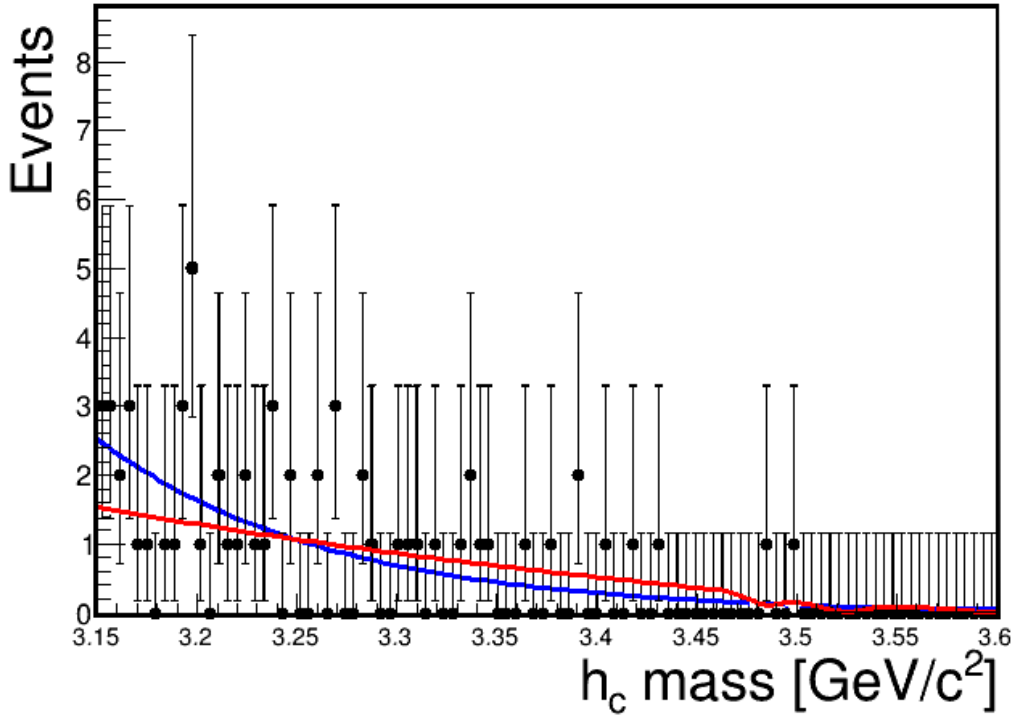


FIGURE 9.8: Fits to data with two different background functions. The blue curve shows the nominal fit using the exponential function with a reduced $\chi^2 = 0.53$ and the red curves shows the fit based on the tangents hyperbolicus with a reduced $\chi^2 = 0.49$

9.6.4 h_c Parameters

The starting parameters for Bukin function used in the fit model 9.6 are obtained by fitting the signal Monte Carlo sample. As no clear signal can be seen in data the parameters are fixed to the values obtained by the Monte Carlo fit. To take the uncertainties of this fit model into account 1000 fits on the data sample are performed with each parameter taken from a Gaussian distribution with the mean value at the fixed value and a width by taking the fit error. The distribution of the cross section resulting from these 1000 fits is shown figure 9.9 together with a Gaussian fit. The standard deviation of $\Delta\sigma_{parameters} = 0.21$ pb of this fit is used as the systematic uncertainty related to the signal function.

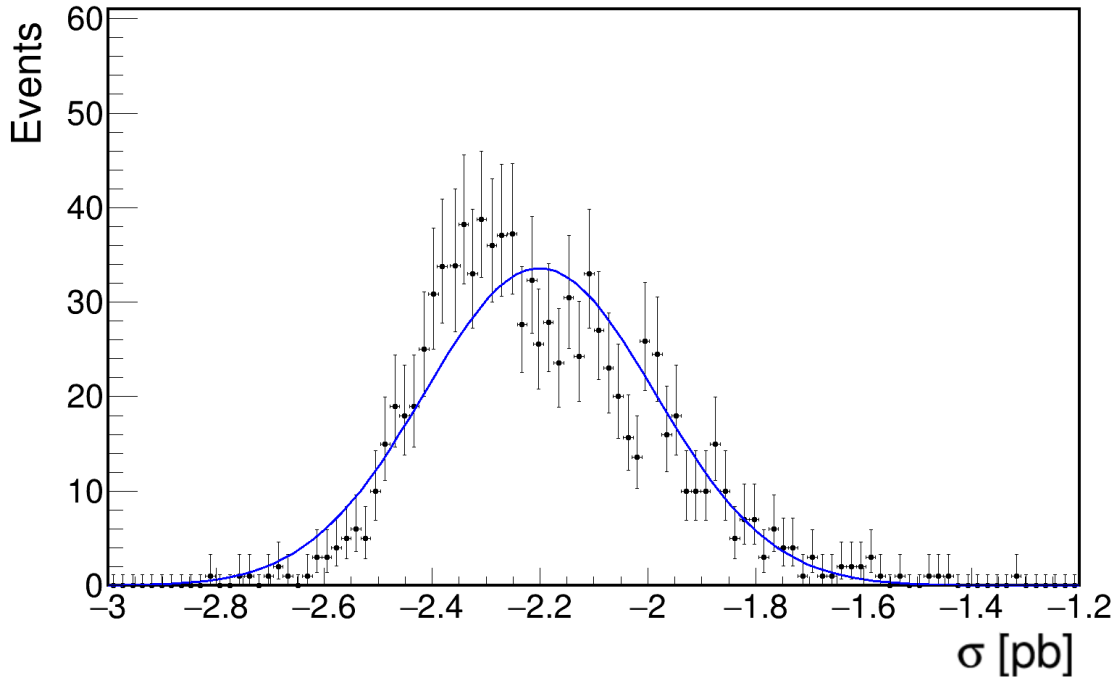


FIGURE 9.9: Distribution of fitted cross section values for the determination of the systematic uncertainty of the h_c Parameters. The blue curve shows a fit with a Gaussian function with a mean of $\sigma = -2.20$ pb and a standard deviation of $\Delta\sigma_{parameters} = 0.21$ pb

9.6.5 Branching Ratio

To measure the cross section it is necessary to know the branching ratios of the decays leading to the analyzed final state (see equation 9.8). Therefore the uncertainties of the branching ratios also influence the cross section and need to be taken into account as systematic uncertainty. As only one specific decay channel of the η_c is used for this analysis the uncertainty is calculated directly. The uncertainties of the involved branching fractions $\mathcal{B}(h_c \rightarrow \gamma\eta_c)$, $\mathcal{B}(\eta \rightarrow \gamma\gamma)$, $\mathcal{B}(\eta_c \rightarrow K^+K^-\pi^+\pi^-)$ are independent of each other and therefore quadratically summed. The change of the cross section when varying the complete branching fraction by this amount is taken as the systematic uncertainty. The values for the η , h_c and η_c decay channels as given in the PDG [20] result in a systematic uncertainty of $\Delta\sigma_{branching} = 1.36$ pb.

9.6.6 Reconstruction Efficiency

For data and for Monte Carlo samples the efficiency for the reconstruction of charged tracks, neutral particles and certain composite particles is not exactly the same. The difference between data and Monte Carlo is taken as the uncertainty of the reconstruction method. This systematic uncertainty on the reconstruction efficiency has multiple different sources. The uncertainty caused by the description of the track reconstruction in Monte Carlo simulations has been estimated as 1% per track [148].

To get the systematic uncertainty of the photon detection the missing momentum and the π^0 decay angle method has been used [149]. In the former the missing momentum of a photon is calculated to predict the energy and direction of a photon. For this a control sample $\psi' \rightarrow \pi^+ \pi^- J/\psi$ with $J/\psi \rightarrow \rho^0 \pi^0$ is used. For the decay angle method a $J/\psi \rightarrow \rho^0 \pi^0$ control sample is used. The π^0 decays to two photons and thus the energy distribution of the photons can be predicted. With both methods the resulting difference between data and Monte Carlo simulations is smaller than 1%.

The systematic uncertainty of the particle identification used to distinguish between pions and kaons is 1% which is studied with a control sample of the reaction channel $ee \rightarrow \pi^+ \pi^- K^+ K^-$ [150]. The systematic uncertainty caused by the reconstruction of the η is estimated in [151]. A control sample $J/\psi \rightarrow \pi^+ \pi^- \pi^0$ and $J/\psi \rightarrow \eta p \bar{p}$ leads to a systematic uncertainty of 1% per η .

The influence of the systematic uncertainties described above is taken into account by multiplying the reconstruction efficiency with a factor α which is calculated as

$$\alpha = (\kappa_T)^{n_T} (\kappa_P)^{n_P} (\kappa_{\pi^\pm})^{n_{\pi^\pm}} (\kappa_{K^\pm})^{n_{K^\pm}} (\kappa_\eta)^{n_\eta}. \quad (9.10)$$

In this n is the number of tracks T, photons P, K^\pm , π^\pm and η in the final state of the decay. The κ are individually drawn from a Gaussian probability distribution with the mean equal to one and the uncertainty of the corresponding value as a width. With each combination of κ a cross section is calculated. This is repeated 1000 times and the resulting distribution and a Gaussian fit is shown in figure 9.10. The standard deviation $\Delta\sigma_{reco} = 0.24$ pb of the fitted Gaussian function is taken as systematic uncertainty.

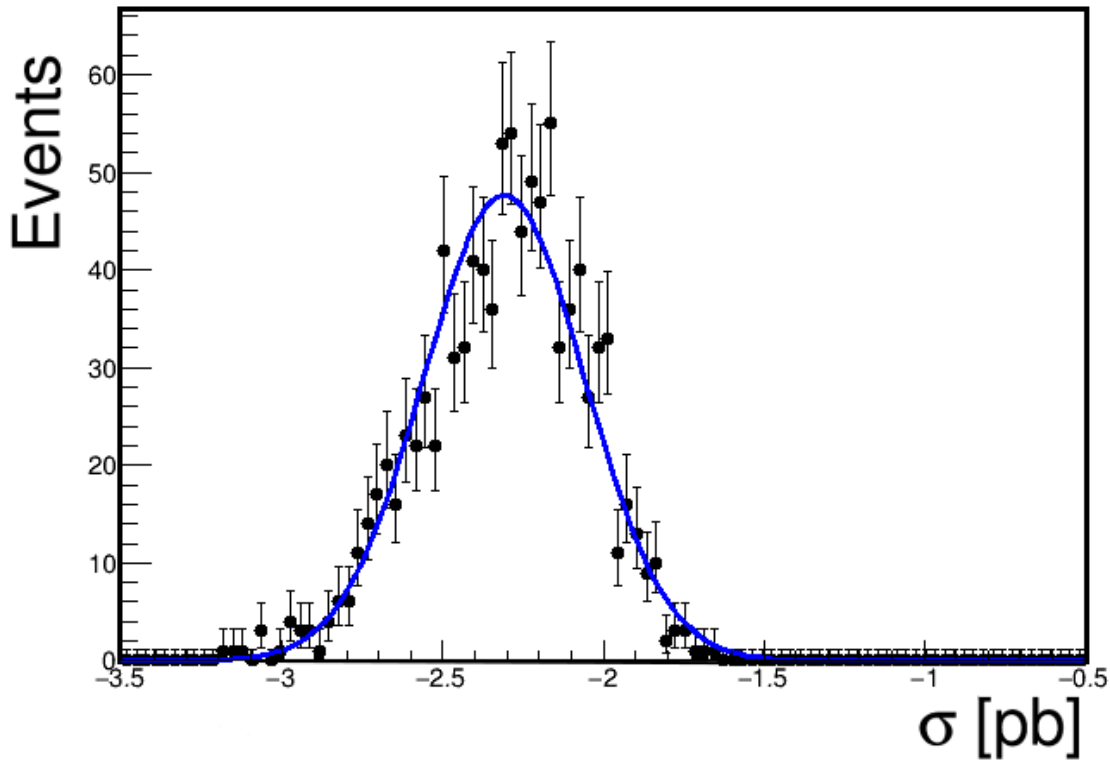


FIGURE 9.10: Distribution of fitted cross section values for the determination of the systematic uncertainty of the reconstruction efficiency. The blue curve shows a fit with a Gaussian function with a mean of $\sigma = -2.29$ pb and a standard deviation of $\Delta\sigma_{reco} = 0.24$ pb

9.6.7 η_c mass cut

To reduce the number of events with two best h_c candidates significantly an η_c mass cut is introduced. Only candidates which have an η_c mass in a window of 100 MeV around the nominal η_c mass $m_{\eta_c}^{PDG} = 2.9839 \pm 0.0005$ MeV/ c^2 [20] are selected for further analysis. To study the systematic uncertainty caused by the cut on the η_c mass window $|m_{\eta_c}^{PDG} - m_{\eta_c}| < 100$ MeV/ c^2 it is varied by 10% in total. Both edges are varied symmetrically. This leads to a wider cut of $|m_{\eta_c}^{PDG} - m_{\eta_c}| < 110$ MeV/ c^2 and narrower cut of $|m_{\eta_c}^{PDG} - m_{\eta_c}| < 90$ MeV/ c^2 . Both variations are applied to data and a fit to data was performed. The wider cut results in a cross section of $\sigma_{wide} = 0.96$ pb and the narrower one yields $\sigma_{narrow} = 0.76$ pb. The larger one of the absolute difference between these two results and the nominal fit value is taken as the systematic uncertainty $\Delta\sigma_{m_{\eta_c}} = 3.19$ pb for the η_c mass cut.

9.6.8 Kinematic fit χ^2 cut

To reduce background contributions and crossfeed between channels a cut of $\chi^2 < 50$ on the χ^2 distribution is used. The systematic uncertainty caused by this cut is studied by varying its value by 10% in each direction. This gives a wider cut with $\chi^2 < 55$ and a narrower cut with $\chi^2 < 45$. A fit to the data is performed with both variations of the

cut. This leads to the cross sections $\sigma_{\chi^2_{wide}} = 3.52$ pb and $\sigma_{\chi^2_{narrow}} = 6.01$ pb. These results are subtracted from the nominal cross section value and the larger absolute difference of $\Delta\sigma_{\chi^2} = 8.24$ pb is then taken as the systematic uncertainty of the χ^2 -cut.

9.6.9 Luminosity Measurement

The integrated luminosity used for the determination of the cross section is measured by using Bhabha events.

As there are differences between Monte Carlo Simulations and reality the integrated luminosity has an uncertainty. These differences are caused mainly by radiative effects of non-perturbative hadronic vacuum polarisation near the J/ψ peak, differences in how particles propagate the detector material and the specific choice of cuts when selecting events. The corresponding relative uncertainty of the measurement of the integrated luminosity is 1% [147]. This corresponds to a systematic uncertainty of $\Delta\sigma_{luminosity} = 0.02$ pb.

9.6.10 Total Systematic Uncertainty

The total systematic uncertainty and its contributing parts are summarized in table 9.2. Assuming that all the systematic uncertainties discussed in this chapter are uncorrelated, the square root of the quadratic sum of these systematic uncertainties is taken as the total systematic uncertainty. It is dominated by the contribution of the background shape and the cut on the χ^2 of the kinematic fit. These values are very large in comparison to the fitted cross section itself but are in the same order of magnitude as the statistical error of the cross section measurement.

source	$\Delta\sigma$ [pb]
Fit range	1.93
Fit parameters	0.21
Branching ratio	1.36
Background shape	27.79
Reconstruction efficiency	0.24
η_c cut	3.19
Kinematic fit χ^2 cut	8.24
Luminosity	0.02
Total systematic uncertainty	29.26

TABLE 9.2: Summary of systematic uncertainties and total systematic uncertainty at the center of mass energy of 4.6 GeV

9.7 Initial State Radiation and Vacuum Polarization

Normally it would be assumed that the center of mass energy is the complete energy of the reaction channel which is analyzed. However, the cross section which is directly observed is not the actual cross section of the process as the observed cross section is influenced by two effects. These two effects are Initial State Radiation (ISR) and vacuum polarization.

Initial State Radiation

At particle colliders one or both incoming particles can emit photons before they interact which is called ISR. Therefore the actual energy E available for the collision is reduced compared to the nominal center of mass energy E_0 . This reduced collision energy has to be taken into account as it influences the observed cross section. The cross section calculated in chapter 9.5 does not contain a correction for ISR but for the upper limit in chapter 9.8 it is included. In this section the calculation of a correction factor δ_{ISR} for ISR is described. The number of observed events N is given by:

$$N = \mathcal{L} \int \sigma(x)\epsilon(x)W(x)dx \quad (9.11)$$

where x is the fraction of the summed energy E_γ of all ISR photons in an event and E_{beam} the nominal beam energy

$$x = \frac{E_\gamma}{E_{beam}} \quad (9.12)$$

while $\sigma(x)$ is the cross section, $\epsilon(x)$ the efficiency and \mathcal{L} the integrated luminosity. $W(x)$ is the radiator function taken from [152]. This radiator function is a description of the probability that an ISR photon is emitted at a certain center of mass energy and serves the purpose of a weight. For a center of mass energy \sqrt{s} the radiator function $W(x)$ can be written as:

$$\begin{aligned} W(s, x) &= \Delta \beta x^{\beta-1} - \frac{\beta}{2}(2-x) \\ &\quad + \frac{\beta^2}{8} [(2-x)(3\ln(1-x) - 4\ln(x)) - 4\frac{\ln(1-x)}{x} - 6 + x], \\ \Delta &= 1 + \frac{\alpha}{\pi} \left(\frac{3}{2}L + \frac{1}{3}\pi^2 - 2 \right) + \left(\frac{\alpha}{\pi} \right)^2 \delta_2, \\ \delta_2 &= \left(\frac{9}{8} - 2\xi_2 \right) L^2 - \left(\frac{45}{16} - \frac{11}{2}\xi_2 - 3\xi_3 \right) L \\ &\quad - \frac{6}{5}\xi_2^2 - \frac{9}{2}\xi_3 - 6\xi_2 \ln(2) + \frac{3}{8}\xi_2 + \frac{57}{12}, \\ \beta &= \frac{2\alpha}{\pi} (L-1), \xi_2 = 1.644493407, \xi_3 = 1.2020569, L = 2\ln \frac{\sqrt{s}}{m_e}, \end{aligned} \quad (9.13)$$

with the electron mass m_e and the fine structure constant $\alpha = \frac{1}{137}$. In figure 9.11 an example for the shape of the radiator function $W(x)$ is shown at 4.36 GeV for a flat cross section.

Introducing the efficiency ϵ_0 and and cross section σ_0 at $x = 0$ into equation 9.13 gives:

$$N = \mathcal{L}\sigma_0\epsilon_0 \int \frac{\sigma(x)}{\sigma_0} \frac{\epsilon(x)}{\epsilon_0} W(x) dx \quad (9.14)$$

The correction factor δ_{ISR} is then defined as

$$\delta_{ISR} := \int \frac{\sigma(x)}{\sigma_0} \frac{\epsilon(x)}{\epsilon_0} W(x) dx \quad (9.15)$$

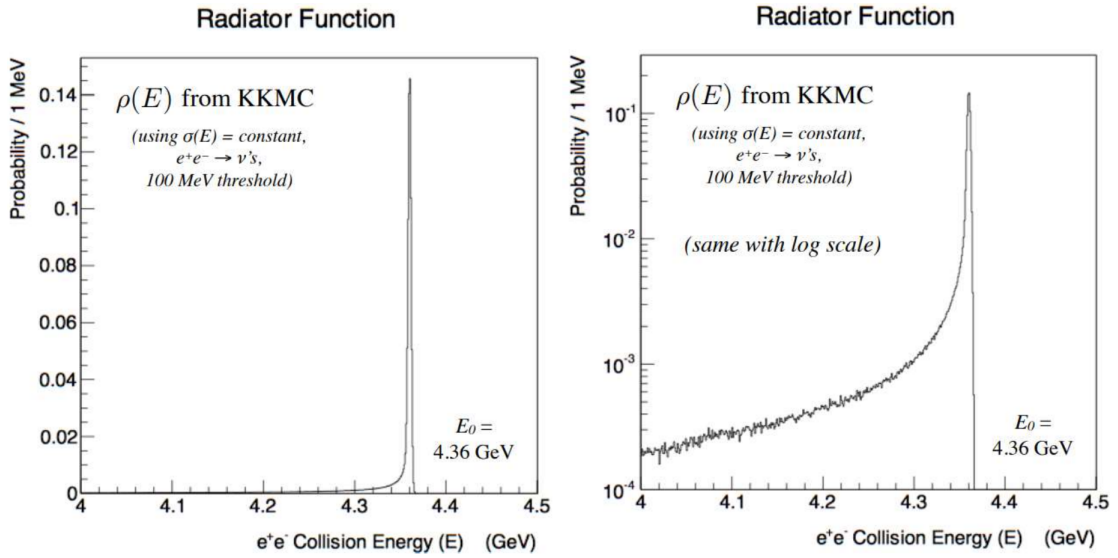


FIGURE 9.11: Example for the radiator function $W(x)$ ($W(x) \equiv \rho(x)$) for a flat cross section at a center of mass energy of 4.36 GeV [153]

and transforms equation 9.14 into

$$N = \mathcal{L}\sigma_0\epsilon_0\delta_{ISR}. \quad (9.16)$$

The normalized efficiency $\frac{\epsilon(x)}{\epsilon_0}$ depends on the ratio of the total energy of ISR photons emitted in an event the beam energy. To extract the normalized efficiency signal Monte Carlo simulations are used. Monte Carlo sets including ISR photons are simulated with the KKMC generator. With these simulations the efficiency ϵ_x can be extracted. Resonant structures in the vicinity of the center of mass energy of a reaction channel influence the radiator function $W(x)$. The cross section for e^+e^- is not precisely known in the energy range of the BESIII datasets. Therefore a narrow resonance near the actual center of mass energy is used as an input cross section. The $Y(4260)$ resonance is modeled as a Breit-Wigner distribution with a mean value at 4.26 GeV/ c^2 and a width of 10 MeV. In figure 9.12 the normalized efficiency distribution is shown together with a fit. The fit function to obtain this fit is chosen empirically as an S-curve described with:

$$\epsilon(x) = A(1 - \operatorname{erf}(\frac{x - \mu}{\sigma})) \quad (9.17)$$

where μ and σ are fit parameters and $\operatorname{erf}(y)$ is the Gauss error function

$$\operatorname{erf}(y) = \frac{2}{\sqrt{\pi}} \int_0^y e^{-r^2} dr. \quad (9.18)$$

It can be seen that the chosen model for the distribution of $\frac{\epsilon(x)}{\epsilon_0}$ describes it reasonably well. Figure 9.13 shows the correction factor δ_{ISR} in dependence on the center of mass energy after the normalized efficiency has been fitted and the integral has been solved numerically. The correction factor δ_{ISR} varies significantly near the region of the resonant structure.

Thus the efficiency is mainly dependent on the behaviour of the cross section of the initial state e^+e^- . For narrower resonant structures the variations of δ_{ISR} are even larger. Should the resonant structure shift, the structure of δ_{ISR} also changes. As the behavior of the cross section e^+e^- is not known the minimum value $\delta_{ISR} = 0.66$ leading to the largest correction is chosen.

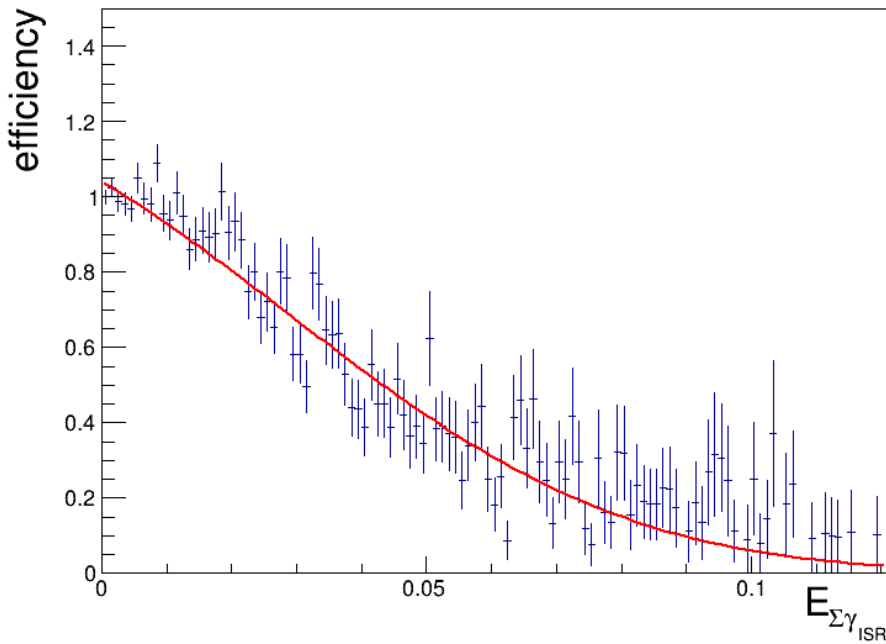


FIGURE 9.12: Normalized efficiency as a function of the energy sum of all ISR photons per event fitted with an S-curve

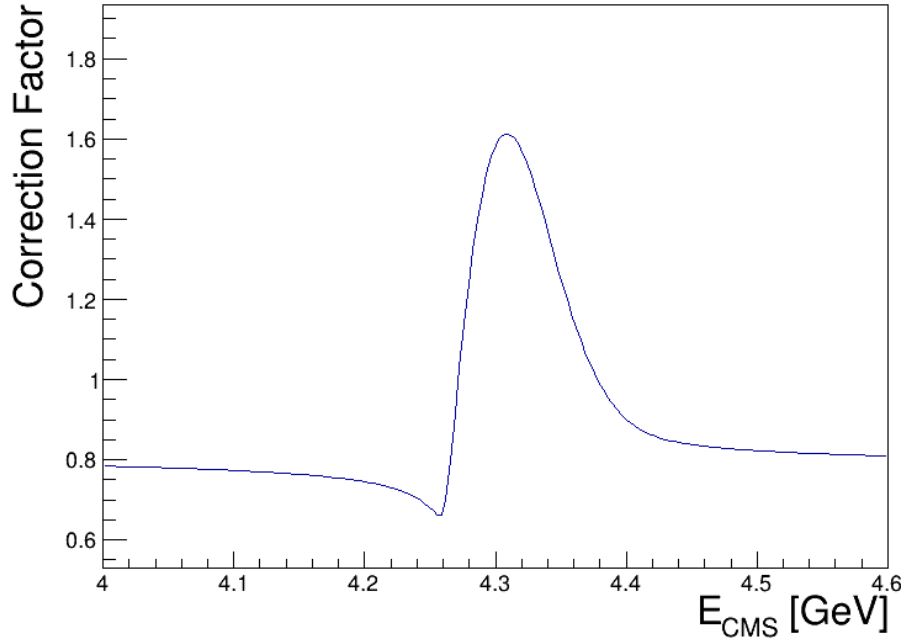


FIGURE 9.13: Correction factor as a function of the center of mass energy. The minimum of the function which is used as a static correction factor is 0.66

Vacuum Polarization

As the resonances which are searched for in this analysis couple to the e^+e^- system through a virtual photon further QED corrections have to be taken into account. A process which has an effect here is vacuum polarization. It describes the modification of the photon propagator through the spontaneous creation of particle anti-particle pairs. The cross section has to be modified to include this process with the correction factor δ_{vp} .

This correction factor is given by:

$$\delta_{vp} := |1 - \hat{\Pi}(s)|^2 = |1 - [\Pi(s) - \Pi(0)]|^2 = \frac{\tilde{\sigma}^0(s)}{\sigma^0(s)} \quad (9.19)$$

with $\sigma^0(s)$ as the theoretical cross section and $\tilde{\sigma}^0(s)$ as the total cross section [154]. In Quantum field theories it is possible that short lived virtual particle anti-particle pairs are spontaneously created in a vacuum which are called vacuum bubbles. In the case of e^+e^- reactions these vacuum bubbles modify the photon propagator which is equivalent to a modified coupling strength between two electrical charges. To calculate the photon propagator including the vacuum polarization a so called One-Particle-Irreducible (1PI) chain approximation is used. In this approximation an infinite series of 1PI diagrams is summed and the photon propagator changed from

$$\gamma^* : \frac{-ig_{\mu\nu}}{q^2} \quad (9.20)$$

to

$$\tilde{\gamma}^* : \frac{-ig_{\mu\nu}}{q^2[1 - \Pi(q^2)]} \quad (9.21)$$

where $g_{\mu\nu}$ is the metric tensor, $\Pi(q^2)$ the vacuum polarization function and $q^2 = s$ for an e^+e^- annihilation [155]. Figure 9.14 illustrates such a replacement of the basic photon propagator γ^* through the modified photon propagator $\tilde{\gamma}^*$.

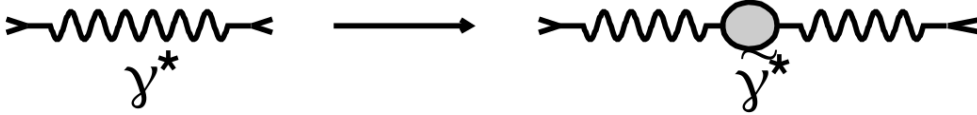


FIGURE 9.14: Basic propagator γ^* is replaced by the propagator $\tilde{\gamma}^*$ which includes the vacuum polarization correction [154]

The vacuum polarization function $\Pi(q^2)$ represents an infinite integral of fermion loops in the four-momentum space in which fermions have odd half integer spins. For QED loops this integral can be solved perturbatively using Feynman rules[155]. To cancel the divergence of the infinite integral the bare electric charge e_0 in the Lagrangian is renormalized with the renormalization constant $Z_3 \equiv \frac{1}{1-\Pi(0)}$ to $\sqrt{Z_3}e_0$. The finite part of $\Pi(s)$ is used to redefine the running coupling constant $\alpha(s)$ to the leading order, resulting in:

$$\alpha(s) = \frac{\frac{e_0^2}{4\pi}}{1 - \Pi(s)} = \frac{\alpha}{1 - [\Pi(s) - \Pi(0)]} \equiv \frac{\alpha}{1 - \hat{\Pi}(s)}, \quad (9.22)$$

where $\hat{\Pi}(s) = \Pi(s) - \Pi(0)$. With the redefined running coupling constant an uncorrected measured total cross section is changed from $\sigma^0(s)$ to a corrected total cross section $\tilde{\sigma}^0(s)$. In this case "total" is used to describe the coherent summation of a resonant (σ_ψ^0) and a non-resonant ($\sigma_{\gamma^*}^0(s)$) process $\sigma^0(s) = \sigma_\psi^0 + \sigma_{\gamma^*}^0(s)$. The non-resonant cross section is

$$\sigma_{\gamma^*}^0(s) = \frac{4\pi\alpha^2}{3s}, \quad (9.23)$$

in which QED fine structure constant is $\alpha \approx \frac{1}{137}$. In its Breit-Wigner form the non resonant part is given as

$$\sigma_\psi^0(s) = \frac{4\pi\alpha^2}{3s} |\mathcal{A}_{BW}|^2 \quad (9.24)$$

where

$$\mathcal{A}_{BW} = \frac{F r e^{i\delta}}{\Delta + i r} \quad (9.25)$$

with the intrinsic phase angle δ of the time dependent wave function $\Phi(t=0)$ and

$$\Delta = \frac{s - M^2}{M^2}, r = \frac{\Gamma}{M}, F = \frac{3\sqrt{s\Gamma_e\Gamma_f}}{a\Gamma M}. \quad (9.26)$$

M is the mass of the resonance, Γ the total decay width while Γ_e and Γ_f are the bare electronic and final state widths. Now the total cross section $\sigma^0(s)$ can be written in the form:

$$\sigma^0(s) = \frac{4\pi\alpha^2}{3s} |\mathcal{A}_{eff}|^2 \quad (9.27)$$

with

$$\mathcal{A}_{eff} = 1 + \frac{Fre^{i\delta}}{\Delta + ir}. \quad (9.28)$$

Replacing α with the running coupling constant $\alpha(s)$ results in the vacuum polarization corrected total cross section

$$\tilde{\sigma}^0(s) = \frac{\sigma_{\gamma^*}^0(s) + \sigma_{\psi}^0(s)}{|1 - \hat{\Pi}(s)|^2} = \frac{\sigma^0(s)}{|1 - \hat{\Pi}(s)|^2}. \quad (9.29)$$

In this analysis the correction factor $|1 - \hat{\Pi}(s)|^2$ is calculated with the Fortran based alphaQED package [156]. In figure 9.15 an example for the theoretical and vacuum polarization corrected cross section line shapes near the J/ψ (left) and $\psi(2s)$ (right) can be seen which shows the significant effect the vacuum polarization has. When comparing the corrections near the J/ψ ($\Gamma_{PDG} = 92.9$ keV) and $\psi(2s)$ ($\Gamma_{PDG} 294$ keV) shows that the narrower J/ψ resonance has much stronger effect than the broader $\psi(2s)$. The correction factor for the center of mass energy $\sqrt{s} = 4.6$ GeV was calculated to be $\delta_{vp} = 1.055$ using the $Y(4260)$ ($\Gamma_{PDG} = 55$ MeV) as nearby resonance.

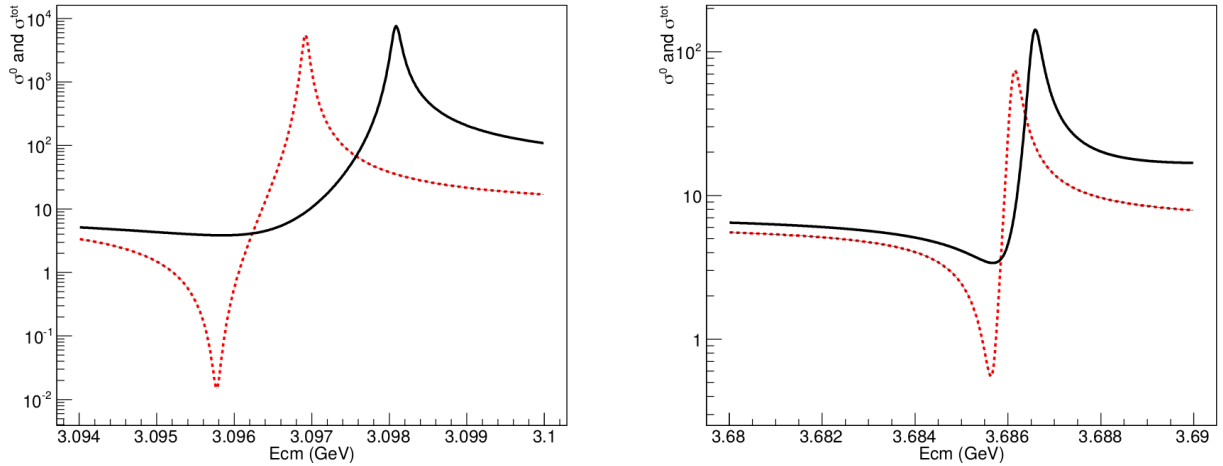


FIGURE 9.15: Line shapes of $\sigma^0(s)$ (dashed red line) and $\tilde{\sigma}^0(s)$ (solid black line) close to $J\psi$ (left) and $\psi(2s)$ (right) [154]

9.8 Upper Limit

In this analysis the cross section of $e^+e^- \rightarrow h_c\eta\pi^+\pi^-$ has been measured as $\sigma_{4.6\text{GeV}}^{obs} = -2.2^{+27.9}_{-20.3} \pm 29.3$ pb not including ISR and vacuum polarization corrections. It has a

significance of 0 and thus an upper limit of the cross section at 90% confidence level has to be calculated. To achieve this a Bayesian approach is used. The upper limit θ^{up} on a parameter θ at the confidence level C e.g. 90% is given by

$$C(\theta^{up}) = \frac{\int_{-\infty}^{\theta^{up}} L(\theta)\pi(\theta)d\theta}{\int_{-\infty}^{\infty} L(\theta)\pi(\theta)d\theta} \quad (9.30)$$

$L(\theta)$ is the likelihood function and $\pi(\theta)$ the prior distribution [157]. For this analysis it is assumed that the prior distribution is zero for all negative cross section values and is constant for all values greater zero. This assumption modifies the equation to

$$C(\sigma^{up}) = \frac{\int_0^{\sigma^{up}} L(\sigma)d\sigma}{\int_0^{\infty} L(\sigma)d\sigma} \quad (9.31)$$

This is equal to choosing an upper limit θ^{up} in such a way that the probability of finding a value $\theta > \theta^{up}$ is lower than $1 - C$

$$P(\theta > \theta^{up}) < 1 - C$$

The likelihood curve as a function of the cross section is determined by calculating the negative log-likelihood curve obtained by a fit minimizer for different values of the cross section. This is done with the software package RooFit [145]. Shifting the minimum of the log-likelihood curve so that the minimum value is zero and taking the exponential of it yields the likelihood curve which can be seen in figure 9.16. Shifting the minimum of the log-likelihood curve to zero leads to the maximum of the likelihood curve being one. For a confidence level of 90% this method and integrating from 0 up to 90% of the area of the curve yields an upper limit of $\sigma^{up} = 61.5$ pb.

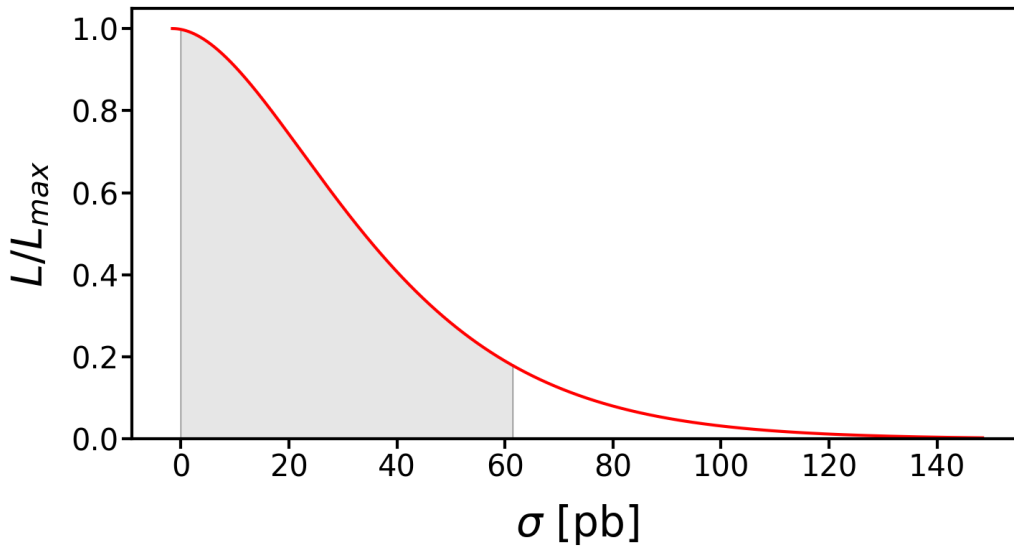


FIGURE 9.16: Likelihood curve for the cross section measurement for $\sqrt{s} = 4.6$ GeV. The interval of 0 up to the upper limit at a 90% confidence level is shown as a gray shaded area.

The calculated likelihood curve and therefore the upper limit only contains statistical uncertainties of the cross section measurement but no systematic uncertainties. These have to be included separately. This is done by convolving the likelihood curve with a Gaussian distribution with the width equal to the total systematic uncertainty determined in section 9.6 and the mean at 0. The likelihood function in equation (9.31) becomes

$$L_{sys}(\sigma) = \int_{-\infty}^{\infty} L(\sigma') \cdot G(\sigma'|\sigma, \sigma_{sys}) d\sigma'.$$

Roofit has problems calculating the log-likelihood curve below cross sections obtained by the nominal fit of this analysis. This leads to a likelihood curve which is cut off after a value slightly below the nominal cross section. A numerical convolution of this cut off likelihood curve leads to a shift of the resulting curve maximum instead of only a broadening the curve. The likelihood curve and the upper limit including the systematic uncertainties are depicted in figure 9.17. For the cross section measurement of $e^+e^- \rightarrow h_c\eta\pi^+\pi^-$ the resulting likelihood curve leads to an upper limit at 90% confidence level with the value of $\sigma_{sys}^{up} = 76.2$ pb. Dividing the upper limit including systematic uncertainties by the initial state radiation correction factor $\delta_{ISR} = 0.66$ and vacuum polarization factor $\delta_{VP} = 1.055$ yields a corrected upper limit including systematic uncertainties of $\sigma_{corr}^{up} = 109.5$ pb.

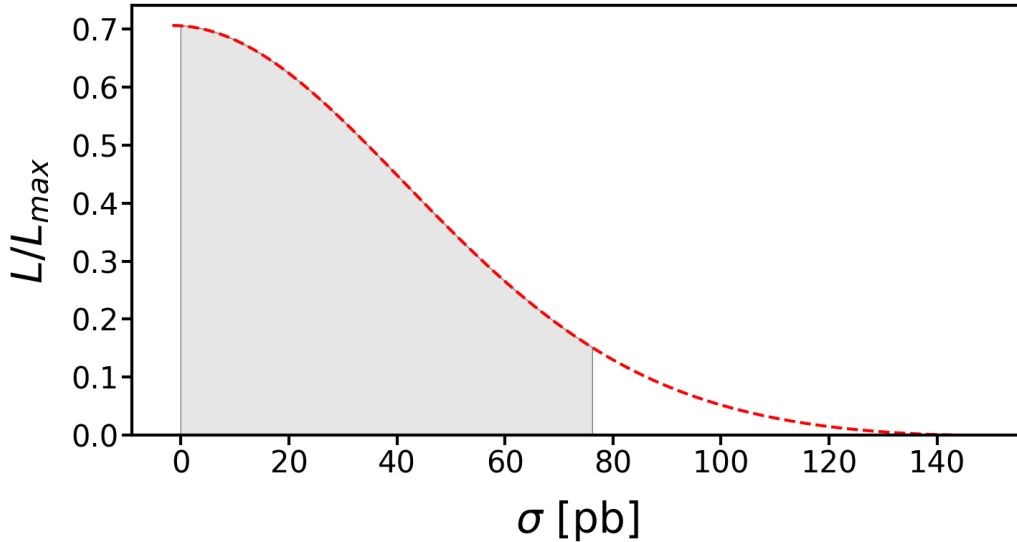


FIGURE 9.17: Likelihood curve convoluted with a Gaussian function representing the systematic uncertainties for the cross section measurements for $\sqrt{s} = 4.6$ GeV. The interval of 0 up to the upper limit at a 90% confidence level is shown as a gray shaded area.

9.9 Summary and Discussion

In this thesis the cross section of the reaction $e^+e^- \rightarrow h_c\eta\pi^+\pi^-$ at a center of mass energy of 4.6 GeV was measured to be $\sigma = -2.2^{+27.9}_{-20.3} \pm 29.3$ pb. As this result is statistically compatible with zero an upper limit on the cross section has been calculated at 90%

confidence level. Without any corrections this upper limit is $\sigma^{up} = 61.5$ pb. Including systematic uncertainties into the calculation increases the upper limit to $\sigma_{sys}^{up} = 76.2$ pb. Further correcting this upper limit for the initial state radiation and vacuum polarization leads to a result of $\sigma_{corr}^{up} = 109.5$ pb. The resulting cross section and upper limits are summarized in table 9.3.

σ	$-2.2_{-20.3}^{+27.9} \pm 29.3$ pb
σ^{up}	61.5 pb
σ_{sys}^{up}	76.2 pb
σ_{corr}^{up}	109.5 pb

TABLE 9.3: Summary of the resulting observed cross section and the upper limits with pure statistical uncertainties, statistical and systematical uncertainties.

As no significant signal was observed in the reaction channel $e^+e^- \rightarrow h_c\eta\pi^+\pi^-$ there is no evidence of a resonant structure which might be a Z_c singlet state decaying to h_c . When comparing the upper limits with and without systematic uncertainties it becomes clear that the largest contribution is the low statistics. One way to mitigate this would be a data set with a much higher luminosity. As the reconstruction efficiency in this analysis is very low because of the very slow prompt pions statistics could also be increased by extending the search to data sets with higher center of mass energies which would have a larger available phase space especially for these pions. This would be possible now since additional data at $\sqrt{s} = 4.7$ GeV was recorded recently. In addition it is planned to increase the center of mass energy further to up to $\sqrt{s} = 4.9$ GeV [158]. For this reason other viable data sets will be available for this search in the near future. Another approach to reach higher statistics would be to include more decay modes of the η_c . Since almost no events were found in the signal region a larger data set and a higher center of mass energy would be crucial to finding a possible resonance by analysing the reaction $e^+e^- \rightarrow h_c\eta\pi^+\pi^-$. As the background shape is by far the largest contribution to the systematic uncertainty a more detailed understanding of the possible background contributions is needed. Another approach would be to use the cut and count method.

In table 9.4 the upper limit established in this thesis for the reaction channel $e^+e^- \rightarrow h_c\eta\pi^+\pi^-$ is listed in comparison to a few other similar reaction channels. The reaction channel $e^+e^- \rightarrow h_c\pi^+\pi^-$, in which the $Z_c(4020)^\pm$ was discovered, has also been investigated using BESIII data sets [159]. In figure 9.18 the dressed cross section (including vacuum polarization effects) of the process $e^+e^- \rightarrow h_c\pi^+\pi^-$ at different center of mass energies can be seen. The distribution of the cross sections is fitted with two Breit-Wigner functions. The result is shown as a red curve. The two individual Breit-Wigner functions are shown as dashed curves. The error bars shown in the plot are the statistical uncertainties and do not include systematic uncertainties. At a center of mass energy of $\sqrt{s} = 4.6$ GeV the cross section of the reaction channel is $\sigma = 7.2_{-3.5}^{+3.8}$ pb. This shows that it should be possible in principal to find reactions with such a low cross section

with statistical significance if they have similar signatures but a larger available phase space leading to more statistics.

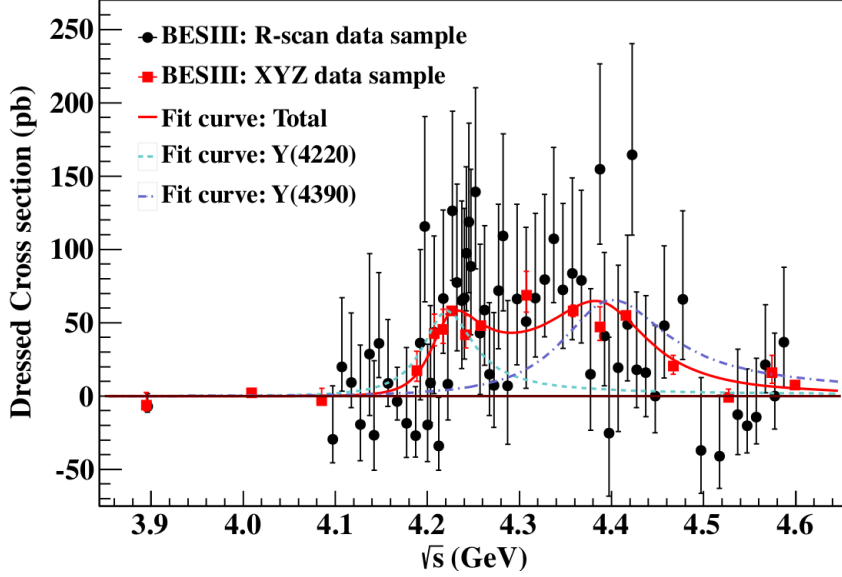


FIGURE 9.18: Dressed cross section (including vacuum polarization effects) of the process $e^+e^- \rightarrow h_c\pi^+\pi^-$ at different center of mass energies [159]. The solid red curve is a fit of two Breit-Wigner functions while the dashed curves are the individual Breit-Wigner functions of two structures ($Y(4220)$, $Y(4390)$). The error bars are exclusively statistical uncertainties.

Another similar process is $e^+e^- \rightarrow \eta_c\eta\pi^+\pi^-$ [160]. It has an η_c meson with $J^{PC} = 0^{-+}$ instead of the h_c ($J^{PC} = 1^{+-}$) in the reaction channel analysed in this work. This leads to one less photon in the final state. There has also been no significant cross section found for $e^+e^- \rightarrow \eta_c\eta\pi^+\pi^-$ and an upper limit of $\sigma^{up} = 23.72$ pb has been determined at 4.6 GeV. At the same center of mass energy the reaction channel $e^+e^- \rightarrow h_c\eta$ [161] differing from $e^+e^- \rightarrow h_c\eta\pi^+\pi^-$ by two pions has an upper limit of $\sigma^{up} = 11.1$ pb. Looking at a reaction channel $e^+e^- \rightarrow J/\psi\pi^+\pi^-$ with J/ψ instead of h_c shows another small cross section of $\sigma = 6.4 \pm 1.1$ pb [49] close to the cross section of $e^+e^- \rightarrow h_c\pi^+\pi^-$. All these other reaction channels have either a very small cross section or a small upper limit compared to the upper limit of $\sigma_{corr}^{up} = 109.5$ pb of this work. However, it has to be noted that as all these similar reaction channels are not related through isospin symmetry to the reaction channel investigated in this thesis and thus the cross sections can in principle be very different from each other.

Decay	Cross section
$e^+e^- \rightarrow h_c\pi^+\pi^-$	$7.2^{+3.8}_{-3.5}$ pb
$e^+e^- \rightarrow J/\psi\pi^+\pi^-$	6.4 ± 1.1 pb
$e^+e^- \rightarrow h_c\eta$	< 11.1 pb
$e^+e^- \rightarrow \eta_c\eta\pi^+\pi^-$	< 23.72 pb
$e^+e^- \rightarrow h_c\eta\pi^+\pi^-$	< 109.49 pb

TABLE 9.4: Cross section comparison of $e^+e^- \rightarrow h_c\eta\pi^+\pi^-$ with similar processes at the studied center of mass energy $\sqrt{s} = 4.6$ GeV. The given uncertainties combine statistical and systematic uncertainties. The values are taken from [159], [49], [161] and [160]

Chapter 10

Summary

Since the publication of the quark model states with other internal configurations than the conventional mesons ($q\bar{q}$) and baryons (qqq) have always been a theoretical option but no strong experimental evidence has been found for the longest time. However, in the last two decades charmonium-like states like the $X(3872)$, $Y(4260)$ and the $Z_c(3900)^{\pm/0}$ and the $Z_c(4020)^{\pm/0}$ which deviate from the conventionally expected states have been discovered, thus granting an opportunity to improve QCD through the findings in charmonium spectroscopy. There are many possibilities how their internal structure looks like but so far evidence for a conclusive answer remains incomplete. To determine their exact nature and answer many more open questions about QCD it is vital to study the properties of these states and find further new states in the charmonium region. Two key experiments in these efforts are the BESIII experiment in Beijing and the future PANDA experiment at FAIR in Darmstadt. The high statistics dataset of BESIII allows for the opportunity to find more new states as is evident by the fact that BESIII was one of the two experiments where the charged $Z_c(3900)^{\pm}$ has been found. The PANDA experiment will be able to search for new states in formation reactions which are not accessible through e^+e^- collisions as the antiproton-proton annihilation process allows for arbitrary mesonic quantum numbers to be produced. In addition to this the high-quality antiproton beam of PANDA permits line shape scanning of resonances with a precision down to 100 keV which could potentially answer the question about the inner structure of the $X(3872)$ and other resonant structures.

Measuring the line shape of a resonance at PANDA is done with the energy scan method. To extract the line shape from the data collected with this scan method the relative luminosity is needed as a normalization factor. Furthermore the absolute integrated luminosity is required to perform any cross section measurement. Thus PANDA will use a dedicated luminosity detector to measure the luminosity with high precision to have a low systematic uncertainty for these cross section measurements. To reduce the uncertainty of the luminosity determination due to background contributions the luminosity detector is built as a tracking detector measuring the angular distribution of tracks of elastically scattered antiprotons. It is located 11 m downstream of the interaction point and it uses high-voltage monolithic active silicon pixel sensors. The sensors are organized in four layers covering the whole azimuthal range and the polar angle range of $3.5 - 8$ mrad. The data acquired by the 400 sensors is transferred to storage by the data acquisition system. To keep the amount of data collected at a manageable level a software trigger is used. Based on the existence of tracks reconstructed out of the hit information the trigger will form a decision whether to keep a package of data or not. For this purpose an online track finding algorithm is used with the goal of being able

to process data in real time. To reach this goal a cellular automaton which has shown promising results in earlier offline tracking studies has been taken as a basis for the new track finding algorithm for online data processing. It has been both simplified and modified for parallel processing to reduce the overall processing time. As the luminosity detector is a low track environment processing times are decreased by accumulating data over a large amount of time stamps before processing all possible hit combinations in parallel.

The pixel sensors used in the detector provide not only the spatial coordinates but also time stamps with a resolution of 25 ns. Due to time walk hits caused by the same particle can be distributed over a time of about 75 ns. In a first step triplets containing hits out of three different detector layers are formed out of all data in a time window spanning three consecutive time stamps. Triplets sharing two hits are combined to complete tracks and uncombined triplets will be saved as short tracks. To ensure that all tracks are found a time window is created for each time stamp. By associating each triplet with the earliest time stamp contained in it duplicate reconstruction of tracks is avoided.

The algorithm has been implemented on a GPU as well as a CPU to investigate which type of processor is more suited to the task of real time track finding in the specific case of the luminosity detector. A track finding efficiency of up to $\approx 98.5\%$ is reached while the percentage of ghost tracks is about 1% to 4.8% depending on the different beam momenta and parameters of the track finding algorithm. This is increased in comparison to the cellular automaton used in the offline studies. These offline studies use different less strict criteria of what is considered a correct track. On a GPU a minimum track processing time of $\approx 2 \mu\text{s}$ per track has been reached while on a CPU it could be reduced to $\approx 100 \text{ ns}$. Both processing times fail to reach the target of 25 ns. However, the factor of four in speed for the CPU implementation could be overcome by simply dividing the data into four different streams which could be processed on parallel CPUs. As the slow GPU processing times are most likely caused by the suboptimal memory access patterns further investigations into these might yield improved results. Alternatively an FPGA implementation of the track finding implementation could also be a viable solution as the algorithm has been simplified from its original version. Regardless of which implementation is chosen for the luminosity detector it needs to be integrated into the current DAQ system for testing in a realistic online scenario.

The observation of the charmonium like state $Z_c(3900)^{\pm,0}$ decaying into $J/\psi\pi^{\pm,0}$ and the solid evidence for a decay $Z_c(4020)^{\pm/0} \rightarrow \pi^{\pm/0}h_c$ suggest both could be isospin triplets. If this is the case isospin singlet states decaying to $J/\psi\eta$ or $h_c\eta$ might also exist. In this work a resonant structure decaying to $h_c\eta$ has been searched for in the reaction channel $e^+e^- \rightarrow h_c\eta\pi^+\pi^-$. Only the high luminosity dataset at a center of mass energy of 4.6 GeV gathered by the BESIII collaboration has been used for the search as a minimum energy of the recoiling pions is required. The analysis of the reaction was performed using the subsequent decays $\eta_c \rightarrow K^+K^-\pi^+\pi^-$ and $\eta \rightarrow \gamma\gamma$. For lower energies the available phase space for pions is too small and thus the momentum of the pions is too low to be measured. To extract the signal cross section the h_c mass distribution of all selected events has been fitted with a maximum likelihood fit. This fit results in an observed cross section of

$$\sigma_{4.6\text{ GeV}} = -2.2^{+27.9}_{-20.3} \pm 29.3 \text{ pb}$$

where the first error gives the statistical uncertainty and the second the total of the systematic uncertainties. Both the statistical and systematic uncertainty are an order of magnitude larger than the cross section value itself and the result is statistically compatible with no events observed. As there is no significant signal an upper limit at 90% confidence level, including systematic uncertainties as well as ISR and vacuum polarization corrections, has been calculated on the cross section:

$$\sigma^{up} = 109.5 \text{ pb}$$

As this upper limit is very large it is not possible to completely exclude the existence of the reaction channel $e^+e^- \rightarrow h_c\eta\pi^+\pi^-$. The reaction $e^+e^- \rightarrow Z_c\pi^+\pi^-$ with the possibly existing resonant substate $Z_c \rightarrow h_c\eta$ is a subsample of the investigated decay channel. Therefore the extracted upper limit on it is also an upper limit on the $Z_c \rightarrow h_c\eta$ production within the reaction channel $e^+e^- \rightarrow h_c\eta\pi^+\pi^-$.

To improve the result higher statistic datasets at 4.6 GeV are needed as the large statistical uncertainty leads to a large upper limit. The search should also be extended to higher center of mass energies as this would lead to a larger available phase space and therefore a larger efficiency. This might also result in a higher number of reconstructed events at the same luminosity if the cross section is in the same order. Another option is to include more decay channels of the η_c which might help to reduce the statistical uncertainties and thus the upper limit of this measurement. Additional decay channels of the η could also be included but these will most likely introduce more combinatorial background because of the large pion multiplicity.

List of Abbreviations

1PI	One-Particle-Irreducible
AoS	Array of Structures
ALICE	A Large Ion Collider Experiment
ALU	Arithmetic Logic Unit
ANKE	Apparatus for Studies of Nucleon and Kaon Ejectiles
APPA	Atomic, Plasma Physics and Applications
API	Application Programming Interface
ASIC	Application-Specific Integrated Circuit
BEPCII	Beijing Electron-Positron Collider
BESIII	Beijing Spectrometer III
boPET	Biaxially-oriented polyethylene terephthalate
BPM	Beam Position Monitors
CA	Cellular Automaton
CAD	Computer-aided design
CBM	Compressed Baryonic Matter
CKM	Cabibbo-Kobayashi-Maskawa
CMS	Center of Mass System
CMOS	Complementary Metal-Oxide-Semiconductor
CPU	Central Processing Unit
COSY	Cooler Synchrotron
CR	Collector Ring
CVD	Chemical Vapor Deposition
DAQ	Data Acquisition

DIRC Detector of Internally Reflected Cherenkov light

DPM Dual Parton Model

DRAM Dynamic Random Access Memory

DRY Don't Repeat Yourself

EMC Electromagnetic Calorimeter

FAIR Facility for Antiproton and Ion Research

FPGA Field-Programmable Gate Array

FT Forward Tracker

FToF Forward Time of Flight

GEANT4 Geometry and tracking

GEM Gas electron multiplier

GIM Glashow–Iliopoulos–Maiani

GPU Graphics Processing Unit

GSI GSI Helmholtzzentrum für Schwerionenforschung GmbH

HESR High Energy Storage Ring

HERA-B Hadron-Electron Ring Accelerator B

HVMAPS High Voltage Monolithic Active Pixel Sensors

IC Integrated Circuit

ICP Iterative Closest Point Algorithm

ILP Instruction Level Parallelism

I/O Input/Output

IP Interaction point

ISR Initial State Radiation

IHEP Institute of High Energy Physics

KOALA Key experiment for PANDA Luminosity determination

LHCb Large Hadron Collider beauty

LMD Luminosity Detector

LUT Look-Up-Table

LSM	Linear Shift Mechanism
LVDS	Low-voltage differential signaling
MAPS	Monolithic Active Pixel Sensors
MC	Monte Carlo
MDC	Multilayer Drift Chamber
MDT	Mini drift tube
MVD	Micro Vertex Detector
NUMA	non-uniform memory access
NMOS	n-type metal-oxide-semiconductor
NEMO-2	Neutrino Ettore Majorana Observatory - 2
NUSTAR	Nuclear Structure, Astrophysics and Reactions
OZI	Okubo-Zweig-Iizuka
PCA	Point of Closest Approach
PCIe	Peripheral Component Interconnect Express
PID	Particle Identification
PMOS	p-type metal-oxide-semiconductor
PMT	Photomultiplier tube
p-LINAC	Proton linear accelerator
QFT	Quantum Field Theory
QED	Quantum Electrodynamics
QCD	Quantum Chromodynamics
RAM	Random Access Memory
RESR	Recuperated experimental storage ring
RF	Radio Frequency
RICH	Ring Imaging Cherenkov
RMS	Root Mean Square
RPC	Resistive plate chamber
SFU	Special Function Unit

SHE Super Heavy Elements
SIMD Single Instruction Multiple Data
SIS Schwerionen Synchrotron
SLAC Stanford Linear Accelerator Center
SM Standard Model
SM Streaming Multiprocessor
SMT Simultaneous Multithreading
SoA Structure of Arrays
SODA Synchronisation of Data Acquisition
SPARC Stored Particles Atomic Physics Research Collaboration
SRAM Static Random Access Memory
STT Straw Tube Tracker
SVD Singular Value Decomposition
TDR Technical Design Report
ToT Time over Threshold
TLP Thread Level Parallelism
TOF Time of Flight
UML Unified Modeling Language
UNILAC Universal Linear Accelerator

Bibliography

- [1] S. L. Glashow. "Partial Symmetries of Weak Interactions". In: *Nucl. Phys.* 22 (1961), pp. 579–588.
- [2] S. Weinberg. "A Model of Leptons". In: *Phys. Rev. Lett.* 19 (1967), pp. 1264–1266.
- [3] P. W. Higgs. "Broken symmetries and the masses of gauge bosons". In: *Physical Review Letters* 13.16 (1964), p. 508.
- [4] F. Englert and R. Brout. "Broken Symmetry and the Mass of Gauge Vector Mesons". In: *Phys. Rev. Lett.* 13 (9 1964), pp. 321–323.
- [5] G. Aad et al., (ATLAS Collaboration). "Observation of a new particle in the search for the Standard Model Higgs boson with the ATLAS detector at the LHC". In: *Phys. Lett.* B716 (2012), pp. 1–29.
- [6] S. Chatrchyan et al., (CMS Collaboration). "Observation of a New Boson at a Mass of 125 GeV with the CMS Experiment at the LHC". In: *Phys. Lett.* B716 (2012), pp. 30–61.
- [7] Wikipedia. *Standard Model*. 2006. URL: https://en.wikipedia.org/wiki/Standard_Model (visited on 08/18/2019).
- [8] M. Gell-Mann. "A Schematic Model of Baryons and Mesons". In: *Phys. Lett.* 8 (1964), pp. 214–215.
- [9] S.-K. Choi et al., (Belle Collaboration). "Observation of a Narrow Charmonium-like State in Exclusive $B^\pm \rightarrow K^\pm \pi^+ \pi^- J/\psi$ Decays". In: *Phys. Rev. Lett.* 91 (26 2003), p. 262001.
- [10] B. Aubert et al., (BABAR Collaboration). "Observation of a broad structure in the $\pi^+ \pi^- J/\psi$ mass spectrum around 4.26 GeV/c²". In: *Physical review letters* 95.14 (2005), p. 142001.
- [11] M. Ablikim et al., (BESIII Collaboration). "Observation of a Charged Charmoniumlike Structure in $e^+e^- \rightarrow \pi^+ \pi^- J/\psi$ at $\sqrt{s}=4.26$ GeV". In: *Phys. Rev. Lett.* 110 (25 2013), p. 252001.
- [12] Z. Q. Liu et al., (Belle Collaboration). "Study of $e^+e^- \rightarrow \pi^+ \pi^- J/\psi$ and Observation of a Charged Charmoniumlike State at Belle". In: *Phys. Rev. Lett.* 110 (25 2013), p. 252002.
- [13] T. Xiao et al. "Observation of the charged hadron $Z_c^\pm(3900)$ and evidence for the neutral $Z_c^0(3900)$ in $e^+e^- \rightarrow \pi\pi J/\psi$ at $s=4170$ MeV". In: *Physics Letters B* 727.4-5 (2013), pp. 366–370.
- [14] M. Ablikim et al., (BESIII Collaboration). "Observation of $Z_c(3900)^0$ in $e^+e^- \rightarrow \pi^0 \pi^0 J/\psi$ ". In: *Phys. Rev. Lett.* 115 (11 2015), p. 112003.

- [15] M. Ablikim et al., (BESIII Collaboration). "Observation of a Charged Charmoniumlike Structure $Z_c(4020)$ and Search for the $Z_c(3900)$ in $e^+e^- \rightarrow \pi^+\pi^-h_c$ ". In: *Phys. Rev. Lett.* 111 (24 2013), p. 242001.
- [16] M. Ablikim et al., (BESIII Collaboration). "Observation of $e^+e^- \rightarrow \pi^0\pi^0h_c$ and a Neutral Charmoniumlike Structure $Z_c(4020)^0$ ". In: *Phys. Rev. Lett.* 113 (21 2014), p. 212002.
- [17] G. Zweig. "An SU(3) model for strong interaction symmetry and its breaking. Version 1". In: (1964).
- [18] O. W. Greenberg. "Spin and Unitary Spin Independence in a Paraquark Model of Baryons and Mesons". In: *Phys. Rev. Lett.* 13 (1964), pp. 598–602.
- [19] M. Y. Han and Y. Nambu. "Three Triplet Model with Double SU(3) Symmetry". In: *Phys. Rev.* 139 (1965), B1006–B1010.
- [20] M. Tanabashi et al., (Particle Data Group). "Review of Particle Physics". In: *Phys. Rev. D* 98 (3 2018), p. 030001.
- [21] D. Griffiths. *Introduction to Elementary Particles*. Wiley-VCH, 2. edition, 2008.
- [22] T. Weber. *High-Voltage Monolithic Active Pixel Sensors for the PANDA Luminosity Detector and Search for the Decay $e^+e^- \rightarrow \eta_c\eta\pi^+\pi^-$ at Center of Mass Energies between 4.23 - 4.36 GeV at BESIII*. Phd-thesis, Johannes Gutenberg-Universität Mainz, 2016.
- [23] K. A. Olive. "Review of particle physics". In: *Chinese physics C* 38.9 (2014), pp. 090001–090001.
- [24] K. G. Wilson. "Confinement of Quarks". In: *Phys. Rev. D* 10 (1974), pp. 2445–2459.
- [25] S. Scherer. "Introduction to chiral perturbation theory". In: *Advances in Nuclear Physics, Volume 27*. Springer, 2003, pp. 277–538.
- [26] F. Halzen and A. D. Martin. *Quark & Leptons: An Introductory Course In Modern Particle Physics*. 2008.
- [27] C. Patrignani et al., (Particle Data Group). "Review of Particle Physics". In: *Chin. Phys.* C40.10 (2016), p. 100001.
- [28] J. J. Aubert et al. "Experimental Observation of a Heavy Particle J ". In: *Phys. Rev. Lett.* 33 (23 1974), pp. 1404–1406.
- [29] J. E. Augustin et al. "Discovery of a Narrow Resonance in e^+e^- Annihilation". In: *Phys. Rev. Lett.* 33 (23 1974), pp. 1406–1408.
- [30] S. L. Glashow, J. Iliopoulos, and L. Maiani. "Weak Interactions with Lepton-Hadron Symmetry". In: *Phys. Rev. D* 2 (1970), pp. 1285–1292.
- [31] K. A. Olive et al., (Particle Data Group). "Review of Particle Physics". In: *Chin. Phys.* C38 (2014), p. 090001.
- [32] S. Dubynskiy and M. B. Voloshin. "Hadro-charmonium". In: *Physics Letters B* 666.4 (2008), pp. 344–346.
- [33] M. Michel. *Extraction of the scalar wave in $J/\psi \rightarrow \gamma\pi^0\pi^0$ using the CompPWA Framework*. Johannes Gutenberg-Universität Mainz, 2016.

- [34] G. S. Bali. "Lattice calculations of hadron properties". In: *Eur. Phys. J. A* 19 (2004), pp. 1–8.
- [35] R. Aaij et al., (LHCb Collaboration). "Determination of the X(3872) Meson Quantum Numbers". In: *Phys. Rev. Lett.* 110 (22 2013), p. 222001.
- [36] G. Barucca et al., (PANDA Collaboration). "Precision resonance energy scans with the PANDA experiment at FAIR - Sensitivity study for width and line shape measurements of the X(3872)". In: *Eur. Phys. J. A* 55.3 (2019), p. 42.
- [37] B. Aubert et al., (BABAR Collaboration). "Observation of a Broad Structure in the $\pi^+\pi^-J/\psi$ Mass Spectrum around $4.26\text{ GeV}/c^2$ ". In: *Phys. Rev. Lett.* 95 (14 2005), p. 142001.
- [38] B. Aubert et al., (BABAR Collaboration). "Evidence of a Broad Structure at an Invariant Mass of $4.32\text{ GeV}/c^2$ in the Reaction $e^+e^- \rightarrow \pi^+\pi^-\psi(2S)$ Measured at BABAR". In: *Phys. Rev. Lett.* 98 (21 2007), p. 212001.
- [39] C. Z. Yuan et al., (Belle Collaboration). "Measurement of the $e^+e^- \rightarrow \pi^+\pi^-J/\psi$ Cross Section Via Initial-State Radiation at Belle". In: *Phys. Rev. Lett.* 99 (18 2007), p. 182004.
- [40] X. L. Wang et al., (Belle Collaboration). "Observation of Two Resonant Structures in $e^+e^- \rightarrow \pi^+\pi^-\psi(2S)$ via Initial-State Radiation at Belle". In: *Phys. Rev. Lett.* 99 (14 2007), p. 142002.
- [41] T. E. Coan et al., (CLEO Collaboration). "Charmonium Decays of $Y(4260)$, $\psi(4160)$, and $\psi(4040)$ ". In: *Phys. Rev. Lett.* 96 (16 2006), p. 162003.
- [42] M. Ablikim et al., (BESIII Collaboration). "Observation of $e^+e^- \rightarrow \gamma X(3872)$ at BESIII". In: *Phys. Rev. Lett.* 112 (9 2014), p. 092001.
- [43] T. Barnes, F. Close, and E. Swanson. "Hybrid and conventional mesons in the flux tube model: Numerical studies and their phenomenological implications". In: *Physical Review D* 52.9 (1995), p. 5242.
- [44] L. Liu et al. "Excited and exotic charmonium spectroscopy from lattice QCD". In: *Journal of High Energy Physics* 2012.7 (2012), p. 126.
- [45] L. Maiani et al. "Four quark interpretation of $Y(4260)$ ". In: *Physical Review D* 72.3 (2005), p. 031502.
- [46] D. Ebert, R. Faustov, and V. Galkin. "Excited heavy tetraquarks with hidden charm". In: *The European Physical Journal C* 58.3 (2008), pp. 399–405.
- [47] M. Cleven et al. " $Y(4260)$ as the first S-wave open charm vector molecular state?" In: *Physical Review D* 90.7 (2014), p. 074039.
- [48] X. Li and M. B. Voloshin. " $Y(4260)$ and $Y(4360)$ as mixed hadrocharmonium". In: *Modern Physics Letters A* 29.12 (2014), p. 1450060.
- [49] M. Ablikim et al., (BESIII Collaboration). "Precise Measurement of the $e^+e^- \rightarrow \pi^+\pi^-J/\psi$ Cross Section at Center-of-Mass Energies from 3.77 to 4.60 GeV ". In: *Phys. Rev. Lett.* 118 (9 2017), p. 092001.
- [50] M. Ablikim et al., (BESIII Collaboration). "Observation of a Charged ($D D^*$) \pm Mass Peak in $e^+e^- \rightarrow \pi(D\bar{D}^*)$ at $s = 4.26\text{ GeV}$ ". In: *Physical review letters* 112.2 (2014), p. 022001.

- [51] M Ablikim et al., (BESIII Collaboration). “Observation of a Charged Charmoniumlike Structure in $e^+e^- \rightarrow (D^*\bar{D}^*)^\pm\pi^\mp$ at $s=4.26$ GeV”. In: *Physical review letters* 112.13 (2014), p. 132001.
- [52] H. H. Gutbrod et al. *FAIR Baseline Technical Design Report, Executive Summary*. FAIR publications, 2006.
- [53] L. Groening et al. *The 70-MeV Proton Linac for the Facility for Antiproton and Ion Research FAIR*. Proceedings of the Linear Accelerator Conference LINAC2006, pp. 186–188, 2006.
- [54] N. Tahir et al. *Design of a Target for Antiproton Production at the Future FAIR Facility*. GSI Annual Report, 2007.
- [55] F. Nolden et al. *TDR - Collector Ring (CR)*. 2008.
- [56] C. Donlinski et al. *TDR - Recuperated Experimental Storage Ring (RESR)*. 2008.
- [57] Q. Hu et al. “A recoil detector for the measurement of antiproton-proton elastic scattering at angles close to 90° ”. In: *The European Physical Journal A* 50.10 (2014), p. 156.
- [58] T. Stöhlker et al., (SPARC Collaboration). “SPARC collaboration: new strategy for storage ring physics at FAIR”. In: *Hyperfine Interactions* 227.1-3 (2014), pp. 45–53.
- [59] A. Lehrach et al. “Beam performance and luminosity limitations in the high-energy storage ring (HESR)”. In: *Nuclear Instruments and Methods in Physical Research Section A: Accelerators, Detectors and Associated Equipment Spectrometers* 561.2 (2006), pp. 289–296.
- [60] D. Prasuhn. “private communications”. In: (2018).
- [61] R. Maier et al. *The high energy storage ring (HESR)*. Proceedings of PAC2011, New York, USA, 2011.
- [62] H. Leithoff. *Ein Kühlsystem für den PANDA Luminositätsdetektor und Suche nach dem Zerfall $e^+e^- \rightarrow \gamma\eta\chi_{c0}$ bei der Schwerpunktsenergie von 4.26 GeV an BESIII*. Phd-thesis, Ruhr Universität Bochum, 2019.
- [63] G. Barucca et al., (PANDA Collaboration). “Precision resonance energy scans with the PANDA experiment at FAIR”. In: *The European Physical Journal A* 55.3 (2019), p. 42.
- [64] M. Lutz et al., (PANDA Collaboration). *Physics performance report for PANDA: strong interaction studies with antiprotons*. Tech. rep. 2009.
- [65] A. V. Belitsky and A. Radyushkin. “Unraveling hadron structure with generalized parton distributions”. In: *Physics reports* 418.1-6 (2005), pp. 1–387.
- [66] M. Danysz and J. Pniewski. “Delayed disintegration of a heavy nuclear fragment: I ”. In: *The London, Edinburgh, and Dublin Philosophical Magazine and Journal of Science* 44.350 (1953), pp. 348–350.
- [67] *RN-DET-2017-001. Release note, PANDA Collaboration, Darmstadt 2017*.
- [68] A. Khoukaz et al., (PANDA Collaboration). “Technical Design Report for the PANDA Internal Targets”. In: (2012). URL: https://panda.gsi.de/system/files/user_uploads/u.kurilla/RE-TDR-2012-002.pdf.

- [69] W. Erni et al. *Technical Design Report for the: PANDA Micro Vertex Detector*. arxiv:1207.6581, 2012. URL: https://panda.gsi.de/system/files/user_uploads/u.kurilla/RE-TDR-2011-001.pdf.
- [70] P. Winz et al., (PANDA Collaboration). “Technical Design Report for the PANDA Straw Tube Tracker”. In: (2012). URL: https://panda.gsi.de/system/files/user_uploads/u.kurilla/RE-TDR-2012-001.pdf.
- [71] R. Novotny et al., (PANDA Collaboration). “Technical Design Report for the PANDA Electromagnetic Calorimeter”. In: (2008). URL: https://panda.gsi.de/system/files/user_uploads/u.kurilla/RE-TDR-2008-001.pdf.
- [72] B. Singh et al., (PANDA Collaboration). “Technical Design Report for the PANDA Barrel DIRC Detector”. In: (2017). URL: https://panda.gsi.de/system/files/user_uploads/j.schwiening/RE-TDR-2016-001.pdf.
- [73] M. Düren et al., (PANDA Collaboration). “Technical Design Report for the PANDA Endcap Disc DIRC”. In: (2019). URL: https://panda.gsi.de/system/files/user_uploads/j.schwiening/RE-TDR-2018-006.pdf.
- [74] K. Suzuki et al., (PANDA Collaboration). “Technical Design Report for the PANDA Barrel Time-of-Flight”. In: (2016). URL: https://panda.gsi.de/system/files/user_uploads/ken.suzuki/RE-TDR-2016-003_0.pdf.
- [75] G. Alexeev et al., (PANDA Collaboration). “Technical Design Report for the PANDA Muon System”. In: (2012). URL: https://panda.gsi.de/system/files/user_uploads/u.kurilla/RE-TDR-2012-003.pdf.
- [76] J. Smyrski et al., (PANDA Collaboration). “Technical Design Report for the PANDA Forward Tracker”. In: (2018). URL: https://panda.gsi.de/system/files/user_uploads/admin/RE-TDR-2017-001.pdf.
- [77] S. Belostotski et al., (PANDA Collaboration). “Technical Design Report for the PANDA Forward Time of Flight detector (FTof wall)”. In: (2018). URL: https://panda.gsi.de/system/files/user_uploads/admin/RE-TDR-2016-004.pdf.
- [78] H. Xu et al., (PANDA Collaboration). “Introduction to PANDA Data Acquisition System”. In: *Physics Procedia* 37 (2012), pp. 1855–1860.
- [79] K. Korcyl et al., (PANDA Collaboration). “Modeling event building architecture for the triggerless data acquisition system for PANDA experiment at the HESR facility at FAIR/GSI”. In: *Journal of Physics: Conference Series*. Vol. 396. 1. 2012, p. 012027.
- [80] I. Konorov et al. “SODA: Synchronization Of Data Acquisition”. In: *Presentation at PANDA FE-DAQ workshop Bodenmais* (2009).
- [81] C. Yu et al. “BEPCII Performance and Beam Dynamics Studies on Luminosity”. In: *Proc. of International Particle Accelerator Conference (IPAC'16)* (2016), pp. 1014–1018.
- [82] E. Abakumova et al. “The beam energy measurement system for the Beijing electron–positron collider”. In: *Nuclear Instruments and Methods in Physics Research Section A: Accelerators, Spectrometers, Detectors and Associated Equipment* 659.1 (2011), pp. 21–29.

- [83] D. M. Asner et al., (BESIII Collaboration). “Physics at BES-III”. In: *Int. J. Mod. Phys. A* 24 (2009), S1–794.
- [84] M. Ablikim et al., (BESIII Collaboration). “Future Physics Programme of BESIII”. In: *Chinese Physics C* 44.4 (2020), p. 040001.
- [85] Y.-B. Yang et al., (CLQCD Collaboration). “Lattice study of radiative J/ψ decay to a tensor glueball”. In: *Physical review letters* 111.9 (2013), p. 091601.
- [86] L.-C. Gui et al., (CLQCD Collaboration). “Scalar glueball in radiative J/ψ decay on the lattice”. In: *Physical review letters* 110.2 (2013), p. 021601.
- [87] M. Ablikim et al., (BESIII Collaboration). “Partial wave analysis of $J/\psi \rightarrow \gamma \eta \eta$ ”. In: *Physical Review D* 87.9 (2013), p. 092009.
- [88] M. Ablikim et al., (BESIII Collaboration). “Erratum: Amplitude analysis of the $\pi^0 \pi^0$ system produced in radiative J/ψ decays [Phys. Rev. D 92, 052003 (2015)]”. In: *Physical Review D* 93.3 (2016), p. 039906.
- [89] M. Ablikim et al., (BESIII Collaboration). “Amplitude analysis of the $K^+ K^- K^0$ system produced in radiative J/ψ decays”. In: *Physical Review D* 98.7 (2018), p. 072003.
- [90] M. Tanabashi et al., (Particle Data Group). “Review of particle physics”. In: *Physical Review D* 98.3 (2018), p. 030001.
- [91] L. Riggio, G. Salerno, and S. Simula. “Extraction of $|V_{cd}|$ and $|V_{cs}|$ from experimental decay rates using lattice QCD $D \rightarrow \pi(K)\ell\nu$ form factors”. In: *The European Physical Journal C* 78.6 (2018), p. 501.
- [92] M. Ablikim et al., (BESIII Collaboration). “Measurement of the branching fraction for the semileptonic decay $D^{0(+)} \rightarrow \pi^{-(0)}\mu^+\nu_\mu$ and test of lepton flavor universality”. In: *Physical review letters* 121.17 (2018), p. 171803.
- [93] M. Ablikim et al., (BESIII Collaboration). “Precision measurement of the mass of the τ lepton”. In: *Physical Review D* 90.1 (2014), p. 012001.
- [94] M. A. Sanchis-Lozano. “On the search for weak decays of heavy quarkonium in dedicated heavy-quark factories”. In: *Zeitschrift für Physik C Particles and Fields* 62.2 (1994), pp. 271–279.
- [95] A. Datta et al. “Flavor changing processes in quarkonium decays”. In: *Physical Review D* 60.1 (1999), p. 014011.
- [96] C. Hill. “Topcolor assisted technicolor”. In: *Physics Letters B* 345.4 (1995), pp. 483–489.
- [97] H.-B. Li and S.-H. Zhu. “Mini-review of rare charmonium decays at BESIII”. In: *Chinese Physics C* 36.10 (2012), pp. 932–940.
- [98] Y. Aditya, K. J. Healey, and A. A. Petrov. “Searching for super-WIMPs in leptonic heavy meson decays”. In: *Physics Letters B* 710.1 (2012), pp. 118–124.
- [99] L. Calibbi et al. “Minimal axion model from flavor”. In: *Physical Review D* 95.9 (2017), p. 095009.
- [100] M. Ablikim et al., (BESIII Collaboration). “Dark photon search in the mass range between 1.5 and 3.4 GeV/c²”. In: *Physics Letters B* 774 (2017), pp. 252–257.

- [101] J. Lees et al., (BABAR Collaboration). “Search for a Dark Photon in e^+e^- Collisions at B a B ar”. In: *Physical review letters* 113.20 (2014), p. 201801.
- [102] M. Ablikim et al., (BESIII Collaboration). “Design and Construction of the BESIII Detector”. In: *Nucl. Instrum. Meth. A* 614 (2010), pp. 345–399.
- [103] (BESIII Collaboration). *BESIII Detector Drawing*. URL: <http://english.ihep.cas.cn/bes/doc/2124.html> (visited on 08/22/2019).
- [104] H. Stein et al. “Determination of target thickness and luminosity from beam energy losses”. In: *Physical Review Special Topics-Accelerators and Beams* 11.5 (2008), p. 052801.
- [105] T. Armstrong et al. “Precision measurements of antiproton-proton forward elastic scattering parameters in the 3.7 to 6.2 GeV/c region”. In: *Physics Letters, Section B: Nuclear, Elementary Particle and High-Energy Physics* 385.1-4 (1996), pp. 479–486.
- [106] A. Karavdina. *Preparation for the accurate luminosity measurement by antiproton-proton elastic scattering and feasibility study for observation of h_c hadronic decay modes at the PANDA experiment*. Phd-thesis, Johannes Gutenberg-Universität Mainz, 2015.
- [107] A. Galoyan et al. “Parametrization of the $\bar{P}P$ Elastic Scattering Differential Cross Section Between $2 \text{ GeV}/c \leq P_{lab} \leq 16 \text{ GeV}/c$ ”. In: *arXiv preprint arXiv:0809.3804* (2008).
- [108] A. Capella and other. “Dual parton model”. In: *Physics Reports* 236.4 (1994), pp. 225–329.
- [109] M. Fritsch et al., (PANDA Collaboration). “Technical Design Report for the PANDA Luminosity Detector (LMD)”. In: (2019). URL: https://panda.gsi.de/system/files/user_uploads/m.fritsch/RE-TDR-2015-001_1.pdf.
- [110] H. Leithoff. “private communications”. In: (2020).
- [111] I. Perić. “A novel monolithic pixelated particle detector implemented in high-voltage CMOS technology”. In: *Nuclear Instruments and Methods in Physics Research Section A: Accelerators, Spectrometers, Detectors and Associated Equipment* 582.3 (2007), pp. 876–885.
- [112] R. Turchetta et al. “A monolithic active pixel sensor for charged particle tracking and imaging using standard VLSI CMOS technology”. In: *Nuclear Instruments and Methods in Physics Research Section A: Accelerators, Spectrometers, Detectors and Associated Equipment* 458.3 (2001), pp. 677–689.
- [113] L. Greiner et al. “A MAPS based vertex detector for the STAR experiment at RHIC”. In: *Nuclear Instruments and Methods in Physics Research Section A: Accelerators, Spectrometers, Detectors and Associated Equipment* 650.1 (2011), pp. 68–72.
- [114] N. Berger et al., (Mu3e Collaboration). “The mu3e experiment”. In: *Nuclear Physics B-Proceedings Supplements* 248 (2014), pp. 35–40.
- [115] K. Korcyl et al. “Modeling event building architecture for the triggerless data acquisition system for PANA experiment at the HESR facility at FAIR/GSI”. In: *Journal of Physics* 396 (2012), p. 012027.

- [116] M. Traxler et al. "A compact system for high precision time measurements (< 14 ps RMS) and integrated data acquisition for a large number of channels". In: *Journal of Instrumentation* 6.12 (2011), p. C12004.
- [117] Intel Corporation. *Microprocessor Quick Reference Guide*. URL: <https://www.intel.com/pressroom/kits/quickreffam.htm> (visited on 10/14/2019).
- [118] Intel Corporation. *Intel Core i7-7740X X-series Processor Specification*. URL: <https://ark.intel.com/content/www/us/en/ark/products/121499/intel-core-i7-7740x-x-series-processor-8m-cache-up-to-4-50-ghz.html> (visited on 10/14/2019).
- [119] Intel Corporation. *Intel Xeon Processor E3-1290 v2 Specification*. URL: <https://ark.intel.com/content/www/us/en/ark/products/65722/intel-xeon-processor-e3-1290-v2-8m-cache-3-70-ghz.html> (visited on 10/14/2019).
- [120] G. E. Moore et al. *Cramming more components onto integrated circuits*. 1965.
- [121] Intel Corporation. *Enhanced Intel SpeedStep Technology for the Intel Pentium M Processor (White Paper)*. 2004. URL: <https://web.archive.org/web/20150812030010/http://download.intel.com/design/network/papers/30117401.pdf>.
- [122] J. L. Hennessy and D. A. Patterson. *Computer architecture: a quantitative approach*. Elsevier, 2011.
- [123] R. M. Russell. "The CRAY-1 computer system". In: *Communications of the ACM* 21.1 (1978), pp. 63–72.
- [124] Arm Holdings. *SIMD ISAs | Neon - Arm Developer*. URL: <https://developer.arm.com/architectures/instruction-sets/simd-isas/neon> (visited on 10/14/2019).
- [125] N. Weber. *GPU Array Access Auto-Tuning*. Phd-thesis, Technische Universität Darmstadt, 2017.
- [126] T. Ungerer, B. Robic, and J. Silc. "A survey of processors with explicit multi-threading". In: *ACM Comput. Surv.* 35 (2003), pp. 29–63.
- [127] Nvidia Corporation. *Programming Guide :: CUDA Toolkit Documentation*. URL: <https://docs.nvidia.com/cuda/cuda-c-programming-guide/index.html> (visited on 10/16/2019).
- [128] Nvidia Corporation. *Whitepaper: NVIDIA's Next Generation CUDA Compute Architecture: Fermi*. URL: http://www.nvidia.com/content/PDF/fermi_white_papers/NVIDIA_Fermi_Compute_Architecture_Whitepaper.pdf (visited on 10/16/2019).
- [129] Nvidia Corporation. *Best Practices Guide :: CUDA Toolkit Documentation*. URL: <https://docs.nvidia.com/cuda/cuda-c-best-practices-guide/index.html> (visited on 10/16/2019).
- [130] P. V. Hough. *Method and means for recognizing complex patterns*. 1962.

- [131] I. Kisel et al., (NEMO Collaboration). “Cellular automaton and elastic net for event reconstruction in the NEMO-2 experiment”. In: *Nuclear Instruments and Methods in Physics Research Section A: Accelerators, Spectrometers, Detectors and Associated Equipment* 387.3 (1997), pp. 433–442.
- [132] I. Abt et al. “CATS: a cellular automaton for tracking in silicon for the HERA-B vertex detector”. In: *Nuclear Instruments and Methods in Physics Research Section A: Accelerators, Spectrometers, Detectors and Associated Equipment* 489.1-3 (2002), pp. 389–405.
- [133] S. Gorbunov et al., (ALICE Collaboration). “ALICE HLT high speed tracking on GPU”. In: *IEEE Transactions on Nuclear Science* 58.4 (2011), pp. 1845–1851.
- [134] I. Kisel. “Event reconstruction in the CBM experiment”. In: *Nuclear Instruments and Methods in Physics Research Section A: Accelerators, Spectrometers, Detectors and Associated Equipment* 566.1 (2006), pp. 85–88.
- [135] S. Spataro et al., (PANDA Collaboration). “The PandaRoot framework for simulation, reconstruction and analysis”. In: *Journal of Physics: Conference Series*. Vol. 331. 3. 2011, p. 032031.
- [136] L. Dagum and R. Menon. “OpenMP: an industry standard API for shared-memory programming”. In: *Computational Science & Engineering, IEEE* 5.1 (1998), pp. 46–55.
- [137] OpenMP Architecture Review Board. *OpenMP Application Program Interface Version 3.0*. 2008. URL: <https://www.openmp.org/wp-content/uploads/spec30.pdf> (visited on 10/16/2019).
- [138] Nvidia Corporation. *Thrust :: CUDA Toolkit Documentation*. URL: <https://docs.nvidia.com/cuda/thrust/index.html> (visited on 10/16/2019).
- [139] S. Agostinelli et al., (GEANT Collaboration). “GEANT4—a simulation toolkit”. In: *Nucl. Instrum. Meth. A* 506.25 (2003), p. 0.
- [140] S. Jadach, B. Ward, and Z. Was. “Coherent exclusive exponentiation for precision Monte Carlo calculations”. In: *Physical Review D* 63.11 (2001), p. 113009.
- [141] R.-G. Ping, (BESIII Collaboration). “Event generators at BESIII”. In: *Chinese Physics C* 32 (2008), p. 599.
- [142] A. Ryd et al. “A Monte Carlo Generator for B-Physics”. In: (2004). URL: <http://cern.ch/robbep/EvtGen/GuideEvtGen.pdf>.
- [143] Y. Liang et al. “Lagrange multiplier method used in BESIII kinematic fitting”. In: *Chinese Physics C* 34.2 (2010), p. 204.
- [144] A. D. Bukin. “Fitting function for asymmetric peaks”. In: *arXiv e-prints*, arXiv:0711.4449 (2007), arXiv:0711.4449.
- [145] W. Verkerke and D. P. Kirkby. “The RooFit toolkit for data modeling”. In: *eConf C0303241* (2003), MOLT007.
- [146] J. C. Chen et al. “Event generator for J/ψ and $\psi(2S)$ decay”. In: *Phys. Rev. D* 62 (3 2000), p. 034003.

- [147] M. Ablikim et al., (BESIII Collaboration). "Precision measurement of the integrated luminosity of the data taken by BESIII at center-of-mass energies between 3.810 GeV and 4.600 GeV". In: *Chinese Physics C* 39.9 (2015), p. 093001.
- [148] M. Ablikim et al., (BESIII Collaboration). "Observation of $\eta' \rightarrow \pi^+ \pi^- \pi^+ \pi^-$ and $\eta' \rightarrow \pi^+ \pi^- \pi^0 \pi^0$ ". In: *Phys. Rev. Lett.* 112 (25 2014), p. 251801.
- [149] M. Ablikim et al., (BESIII Collaboration). "Study of χ_{cJ} radiative decays into a vector meson". In: *Phys. Rev. D* 83 (11 2011), p. 112005.
- [150] M. Ablikim et al., (BESIII Collaboration). "Measurements of the branching fractions of $\eta_c \rightarrow K^+ K^- \pi^0$, $K_S^0 K^\pm \pi^\mp$, $2(\pi^+ \pi^- \pi^0)$, and $p\bar{p}$ ". In: *Phys. Rev. D* 100 (1 2019), p. 012003.
- [151] M. Ablikim et al., (BESIII Collaboration). "Branching fraction measurements of χ_{c0} and χ_{c2} to $\pi^0 \pi^0$ and $\eta\eta$ ". In: *Phys. Rev. D* 81 (5 2010), p. 052005.
- [152] P. Rong-Gang. "An exclusive event generator for e+ e- scan experiments". In: *Chinese Physics C* 38.8 (2014), p. 083001.
- [153] R. Mitchell. "Efficiencies and ISR Corrections for Cross Section Measurements." In: *Internal presentation at BESIII workshop* (2014).
- [154] J. Hong-Dou. "A discussion on vacuum polarization correction to the cross-section of $e^+ e^- \rightarrow \gamma^* / \psi \rightarrow \mu^+ \mu^-$ ". In: *Chinese Physics C* 43 (2018), p. 013104.
- [155] M. Peskin et al. *An Introduction to Quantum Field Theory*. CRC Press, 1995.
- [156] F. Jegerlehner. " α QED, eff (s) for precision physics at the FCC-ee/ILC". In: *CERN Yellow Reports: Monographs* 3 (2020), p. 9.
- [157] G. Zech and G. Bohm. *Einfuehrung in Statistik und Messwertanalyse fuer Physiker*. Deutsches Elektron Synchrotron in der Helmholtz Gemeinschaft Zentralbibliothek, 2006.
- [158] C. H. Yu. "BEPCII operation status and topup progress". In: *Presentation at the BESIII Collaboration 2019 Summer meeting July 1st – 5th , 2019 , Fudan University* (2019).
- [159] M. Ablikim et al. "Evidence of Two Resonant Structures in $e^+ e^- \rightarrow \pi^+ \pi^- h_c$ ". In: *Phys. Rev. Lett.* 118 (9 2017), p. 092002.
- [160] M. Ablikim et al. "Search for the decay $e^+ e^- \rightarrow \eta_c \eta \pi^+ \pi^-$ at Center of Mass Energies between 4.23-4.60 GeV at BESIII". In: *Unpublished* ().
- [161] M. Ablikim et al., (BESIII Collaboration). "Observation of $e^+ e^- \rightarrow \eta h_c$ at center-of-mass energies from 4.085 to 4.600 GeV". In: *Phys. Rev. D* 96 (1 2017), p. 012001.

Appendix A

Track Reconstruction Efficiencies

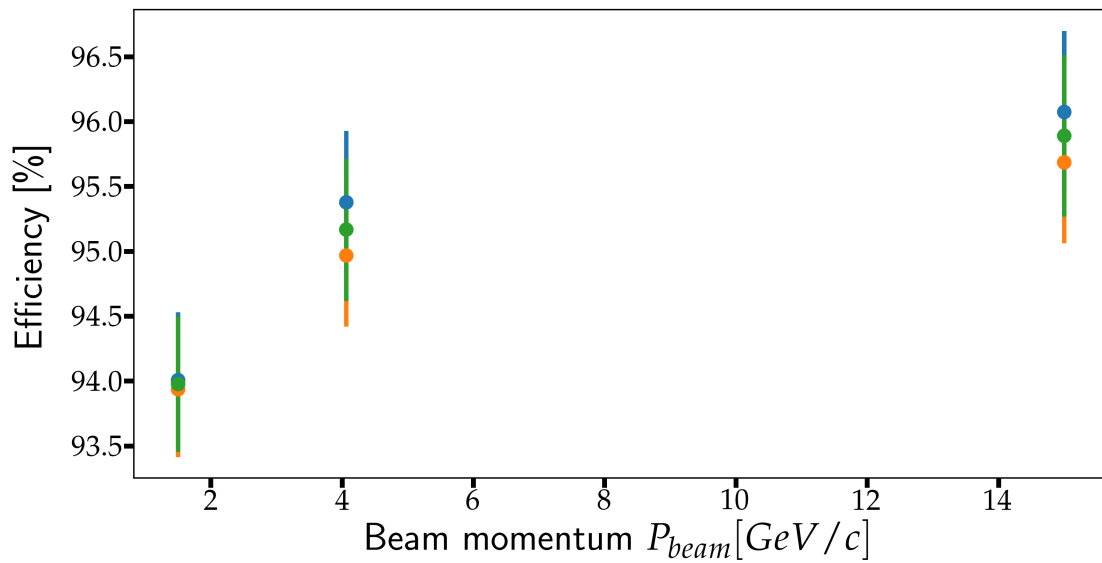


FIGURE A.1: Track reconstruction efficiency for varying beam momenta P_{beam} and fixed parameters $n_{generatedTracks} = 3$, $n_{tmpTriplets} = 15$. Different $\delta\Psi_{max}$ are shown by different colors: $2 \cdot 10^{-5}$ (blue), $1 \cdot 10^{-5}$ (green), $0.5 \cdot 10^{-5}$ (orange).

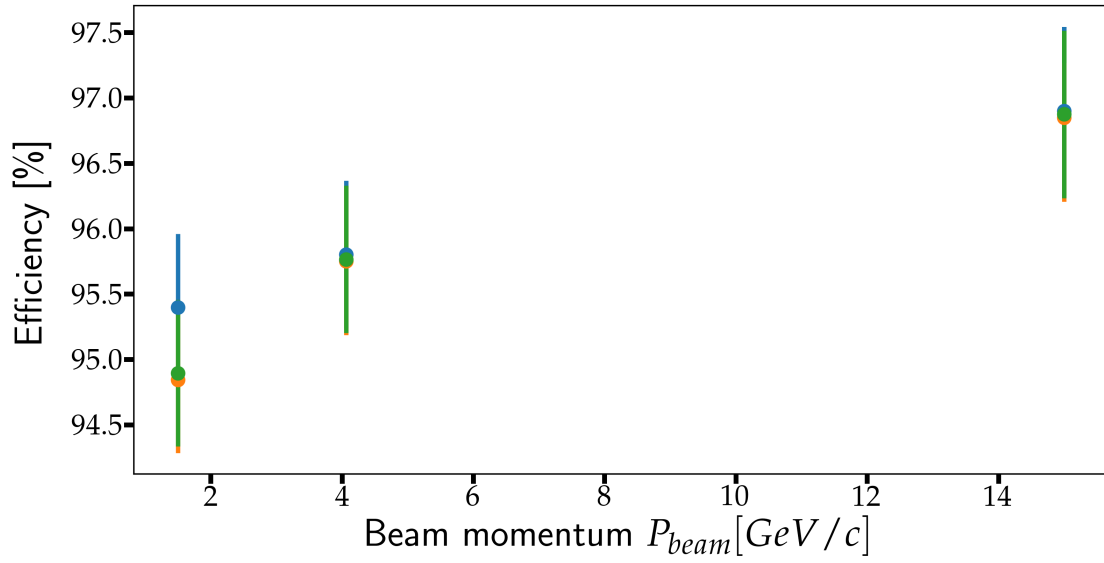


FIGURE A.2: Track reconstruction efficiency for varying beam momenta P_{beam} and fixed parameters $n_{generatedTracks} = 2, n_{tmpTriplets} = 15$. Different $\delta\Psi_{max}$ are shown by different colors: $2 \cdot 10^{-5}$ (blue), $1 \cdot 10^{-5}$ (green), $0.5 \cdot 10^{-5}$ (orange).

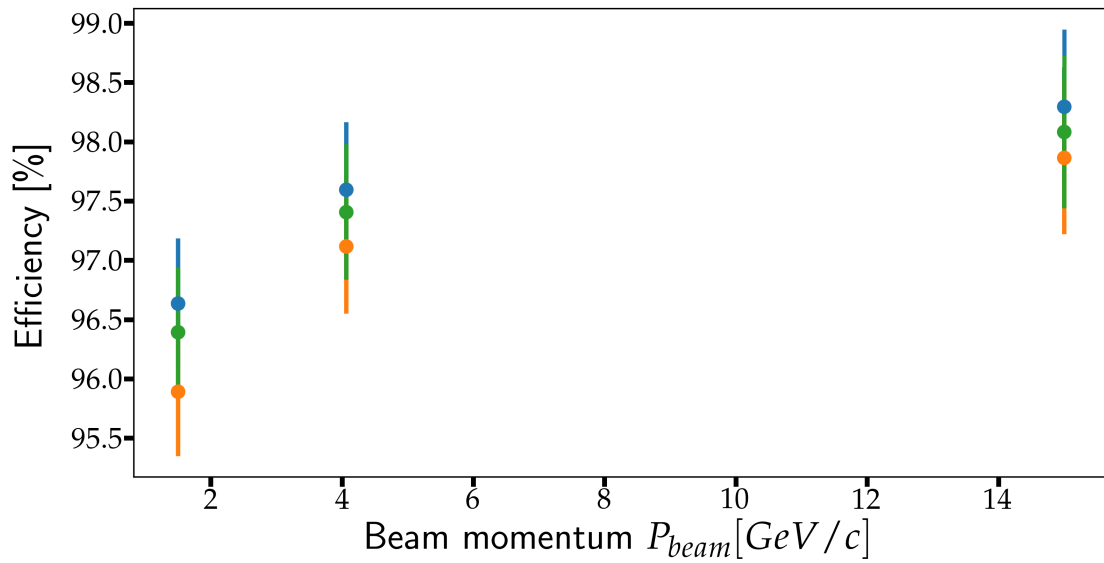


FIGURE A.3: Track reconstruction efficiency for varying beam momenta P_{beam} and fixed parameters $n_{generatedTracks} = 1, n_{tmpTriplets} = 15$. Different $\delta\Psi_{max}$ are shown by different colors: $2 \cdot 10^{-5}$ (blue), $1 \cdot 10^{-5}$ (green), $0.5 \cdot 10^{-5}$ (orange).

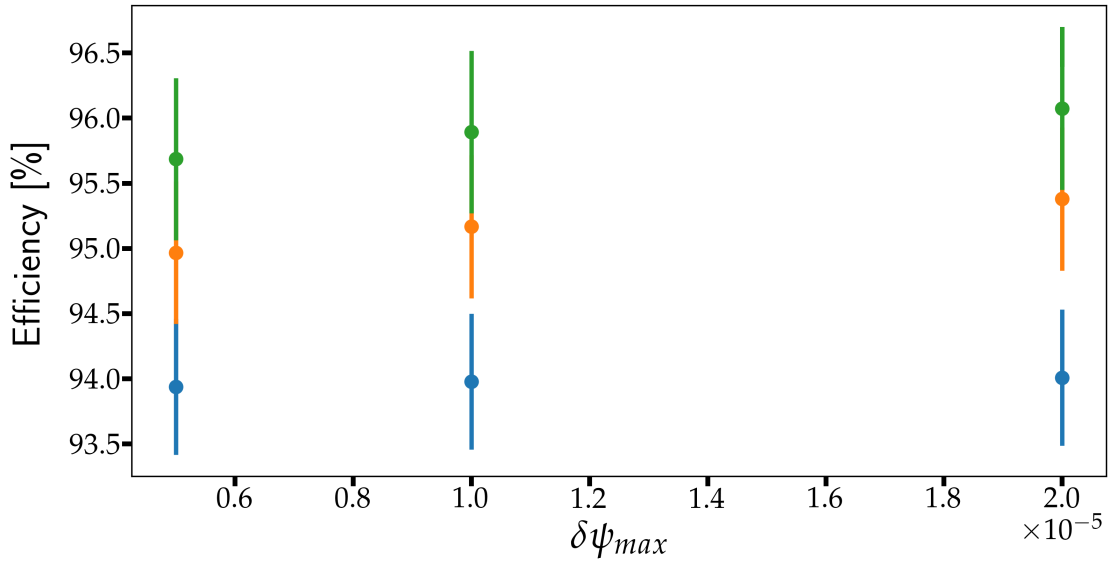


FIGURE A.4: Track reconstruction efficiency for varying $\delta\Psi_{max}$ and fixed parameters $n_{generatedTracks} = 3, n_{tmpTriplets} = 15$. Different P_{beam} are shown by different colors: $P_{beam} = 1.5$ GeV (blue), $P_{beam} = 4.06$ GeV (orange), $P_{beam} = 15$ GeV (green).

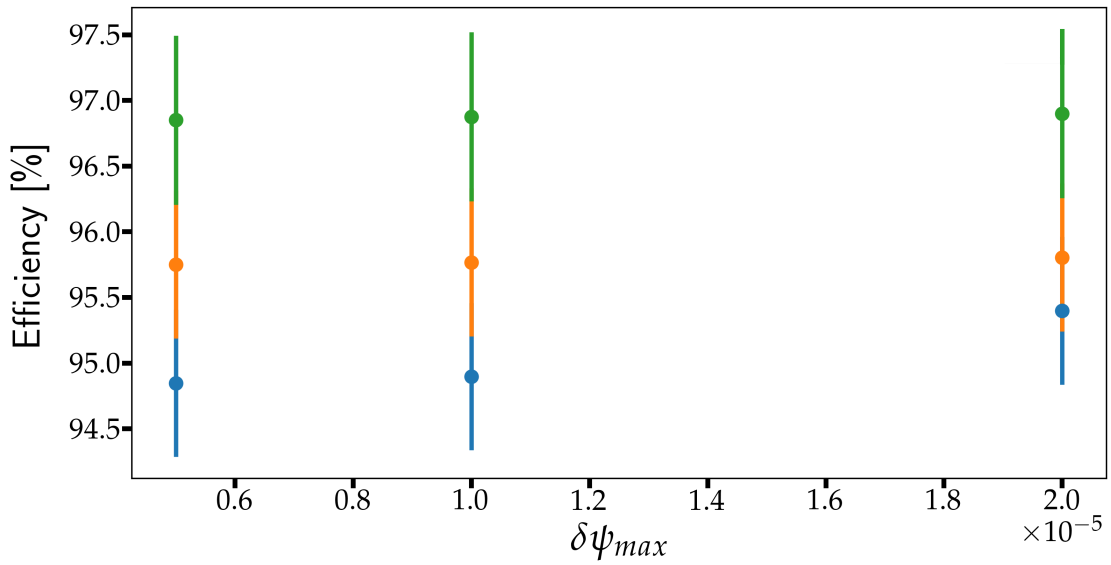


FIGURE A.5: Track reconstruction efficiency for varying $\delta\Psi_{max}$ and fixed parameters $n_{generatedTracks} = 2, n_{tmpTriplets} = 15$. Different P_{beam} are shown by different colors: $P_{beam} = 1.5$ GeV (blue), $P_{beam} = 4.06$ GeV (orange), $P_{beam} = 15$ GeV (green).

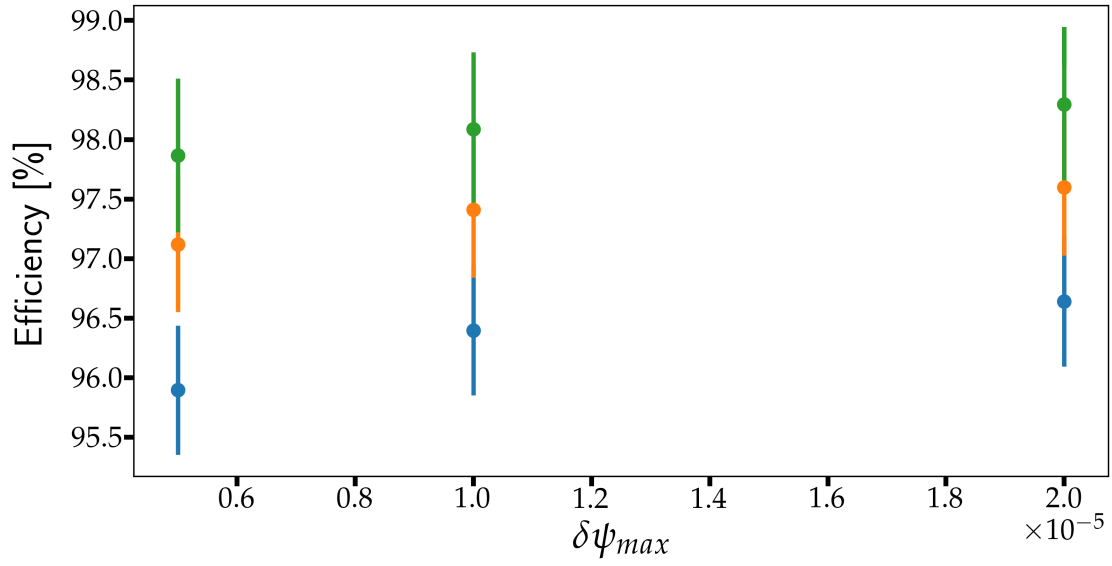


FIGURE A.6: Track reconstruction efficiency for varying $\delta\Psi_{max}$ and fixed parameters $n_{generatedTracks} = 1$, $n_{tmpTriplets} = 15$. Different beam momenta P_{beam} are shown by different colors: $P_{beam} = 1.5 \text{ GeV}$ (blue), $P_{beam} = 4.06 \text{ GeV}$ (orange), $P_{beam} = 15 \text{ GeV}$ (green).

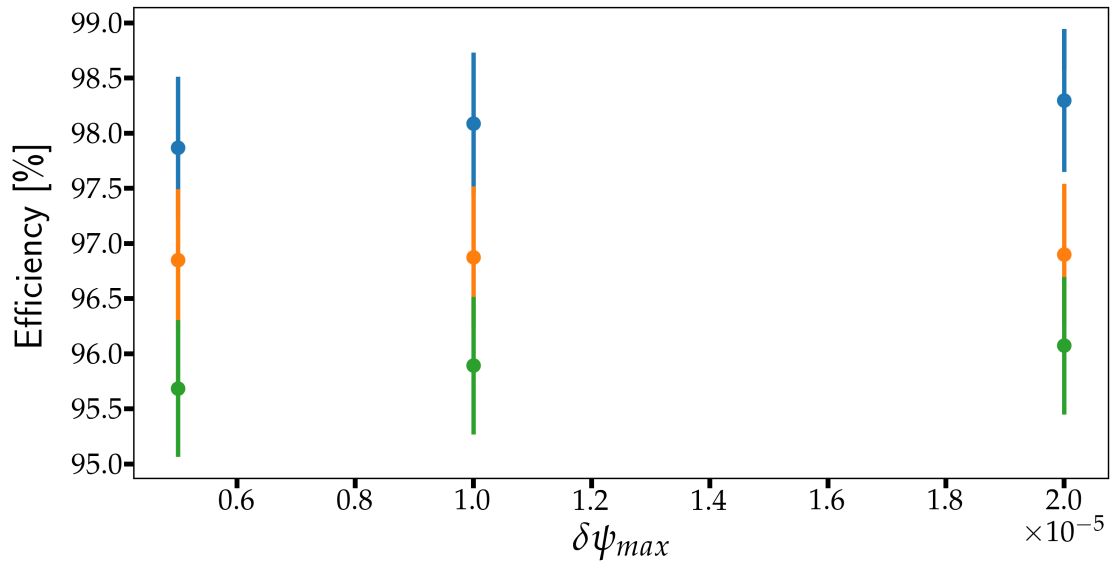


FIGURE A.7: Track reconstruction efficiency for varying $\delta\Psi_{max}$ and fixed parameters $P_{beam} = 15 \text{ GeV}$, $n_{tmpTriplets} = 15$. Different $n_{generatedTracks}$ are shown by different colors: 1 (blue), 2 (orange), 3 (green).

aaaa

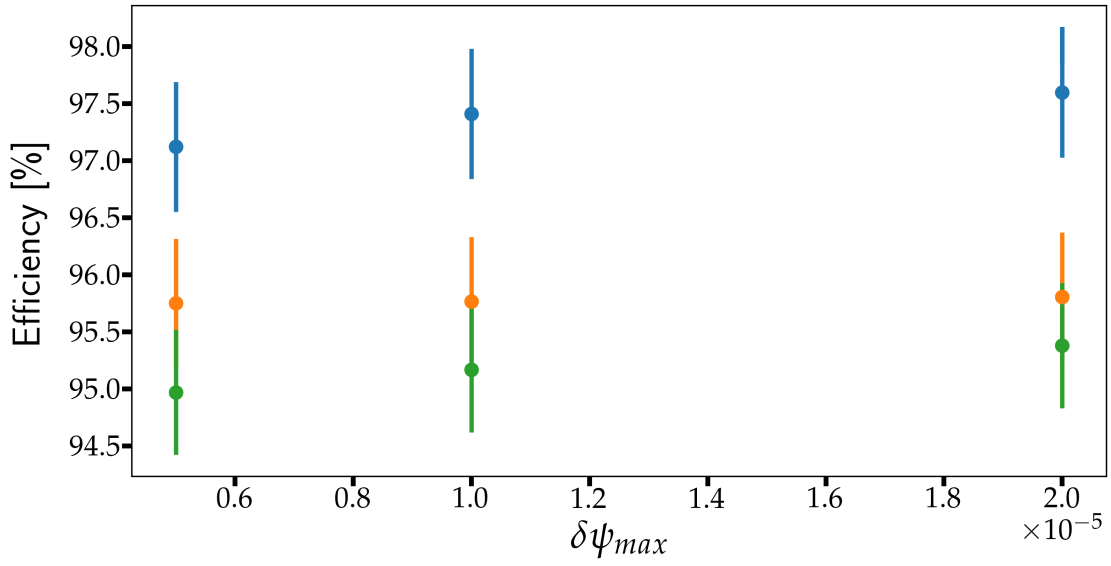


FIGURE A.8: Track reconstruction efficiency for varying $\delta\Psi_{max}$ and fixed parameters $P_{beam} = 4.06$ GeV, $n_{tmpTriplets} = 15$. Different $n_{generatedTracks}$ are shown by different colors: 1 (blue), 2 (orange), 3 (green).

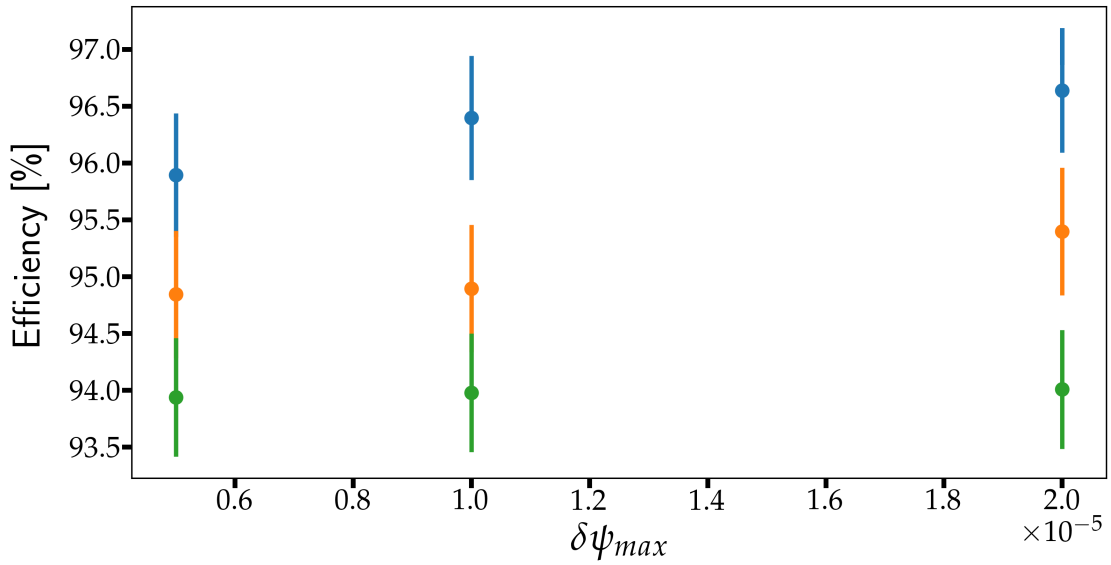


FIGURE A.9: Track reconstruction efficiency for varying $\delta\Psi_{max}$ and fixed parameters $P_{beam} = 1.5$ GeV, $n_{tmpTriplets} = 15$. Different $n_{generatedTracks}$ are shown by different colors: 1 (blue), 2 (orange), 3 (green).

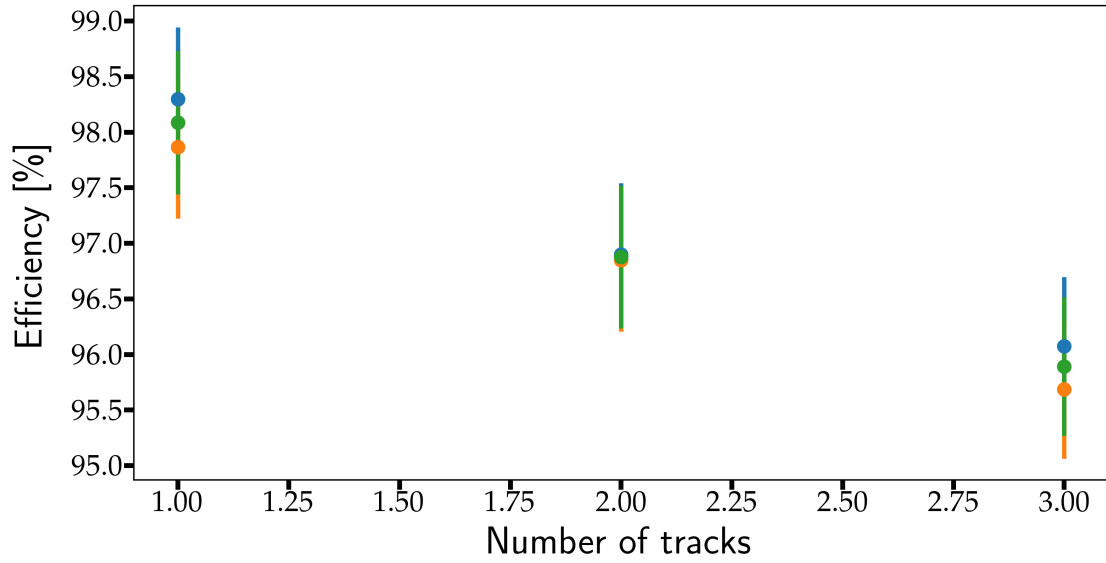


FIGURE A.10: Track reconstruction efficiency for varying $n_{generatedTracks}$ and fixed parameters $P_{beam} = 15 \text{ GeV}$, $n_{tmpTriplets} = 15$. Different $\delta\Psi_{max}$ are shown by different colors: $2 \cdot 10^{-5}$ (blue), $1 \cdot 10^{-5}$ (green), $5 \cdot 10^{-6}$ (orange).

FIGURE A.11: Track reconstruction efficiency for varying $n_{generatedTracks}$ and fixed parameters $P_{beam} = 4.06 \text{ GeV}$, $n_{tmpTriplets} = 15$. Different $\delta\Psi_{max}$ are shown by different colors: $2 \cdot 10^{-5}$ (blue), $1 \cdot 10^{-5}$ (green), $5 \cdot 10^{-6}$ (orange).

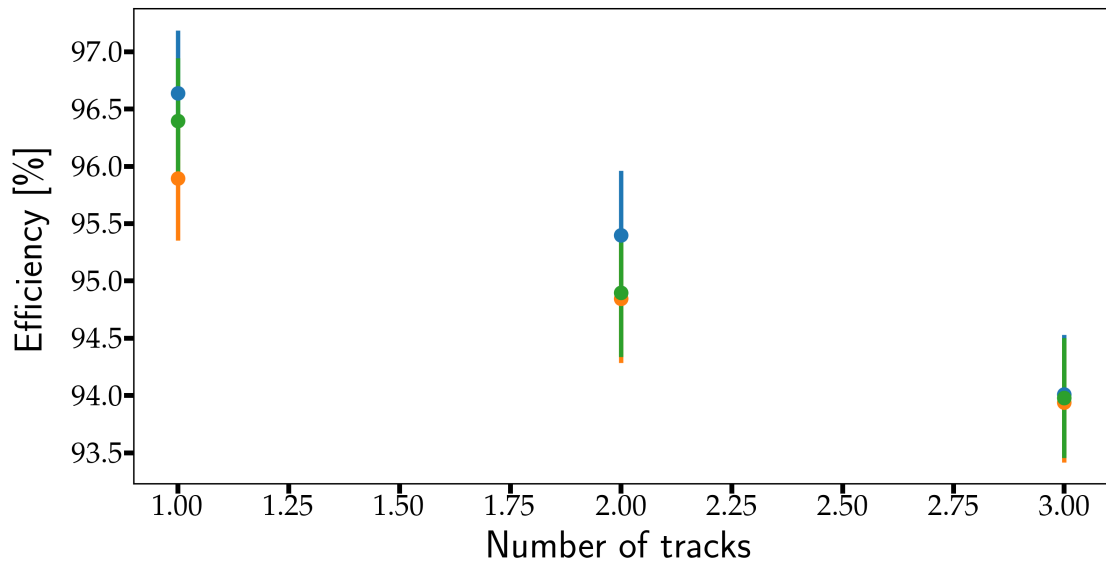


FIGURE A.12: Track reconstruction efficiency for varying $n_{generatedTracks}$ and fixed parameters $P_{beam} = 1.5 \text{ GeV}$, $n_{tmpTriplets} = 15$. Different $\delta\Psi_{max}$ are shown by different colors: $2 \cdot 10^{-5}$ (blue), $1 \cdot 10^{-5}$ (green), $5 \cdot 10^{-6}$ (orange).

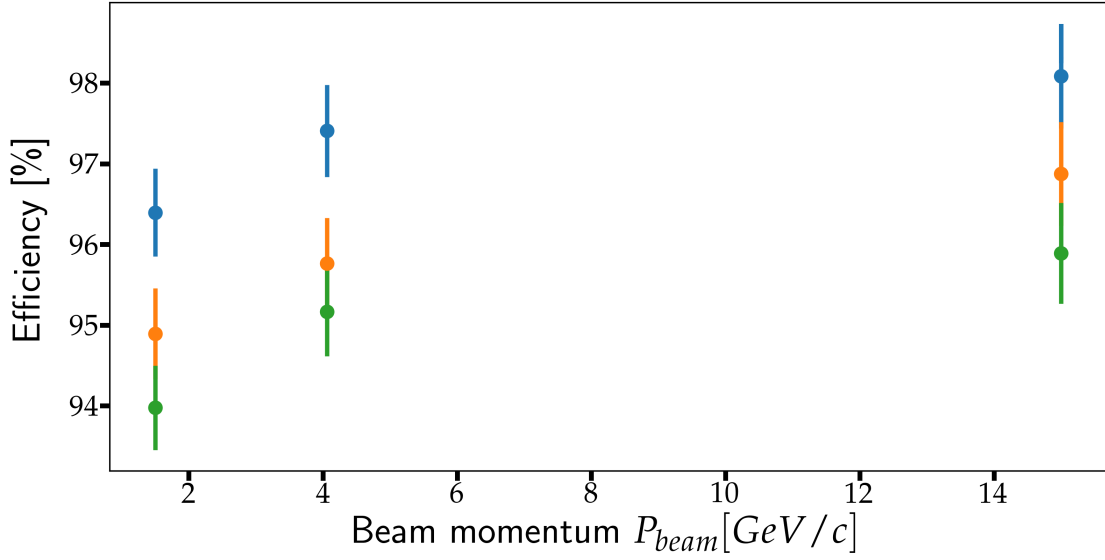


FIGURE A.13: Track reconstruction efficiency for varying beam momenta P_{beam} and fixed parameters $\delta\Psi_{max} = 1 \cdot 10^{-5}$, $n_{tmpTriplets} = 15$. Different $n_{generatedTracks}$ are shown by different colors: 1 (blue), 2 (orange), 3 (green).

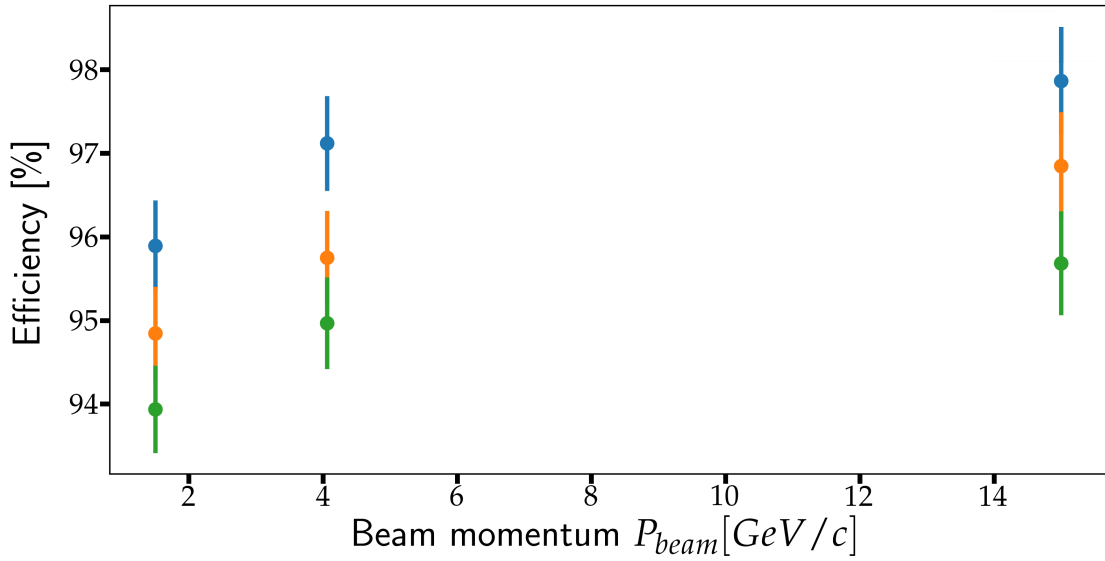


FIGURE A.14: Track reconstruction efficiency for varying beam momenta P_{beam} and fixed parameters $\delta\Psi_{max} = 0.5 \cdot 10^{-5}$, $n_{tmpTriplets} = 15$. Different $n_{generatedTracks}$ are shown by different colors: 1 (blue), 2 (orange), 3 (green).

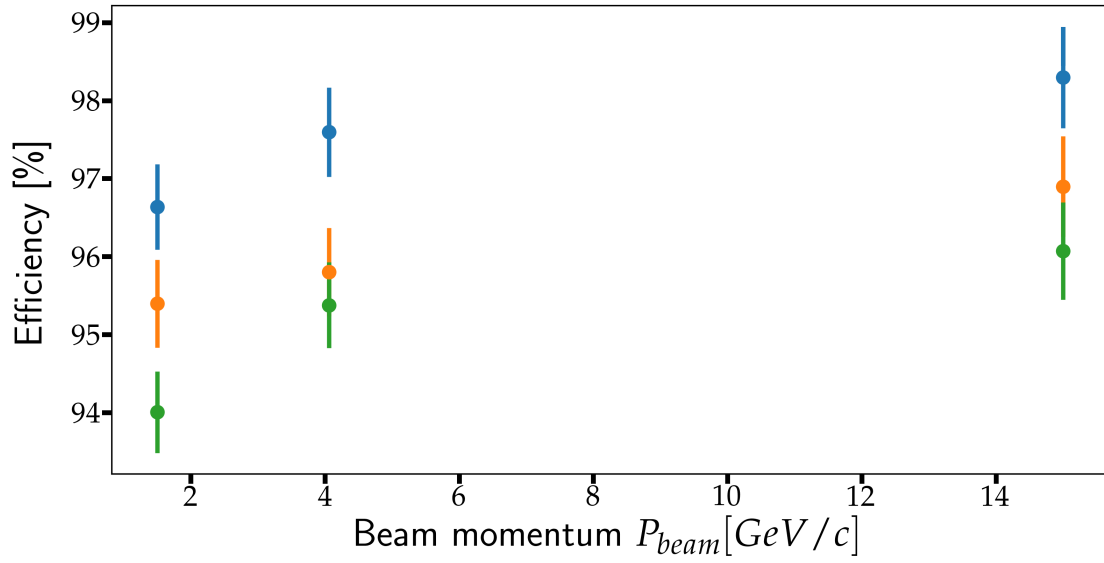


FIGURE A.15: Track reconstruction efficiency for varying beam momenta P_{beam} and fixed parameters $\delta\Psi_{max} = 2 \cdot 10^{-5}$, $n_{tmpTriplets} = 15$. Different $n_{generatedTracks}$ are shown by different colors: 1 (blue), 2 (orange), 3 (green).

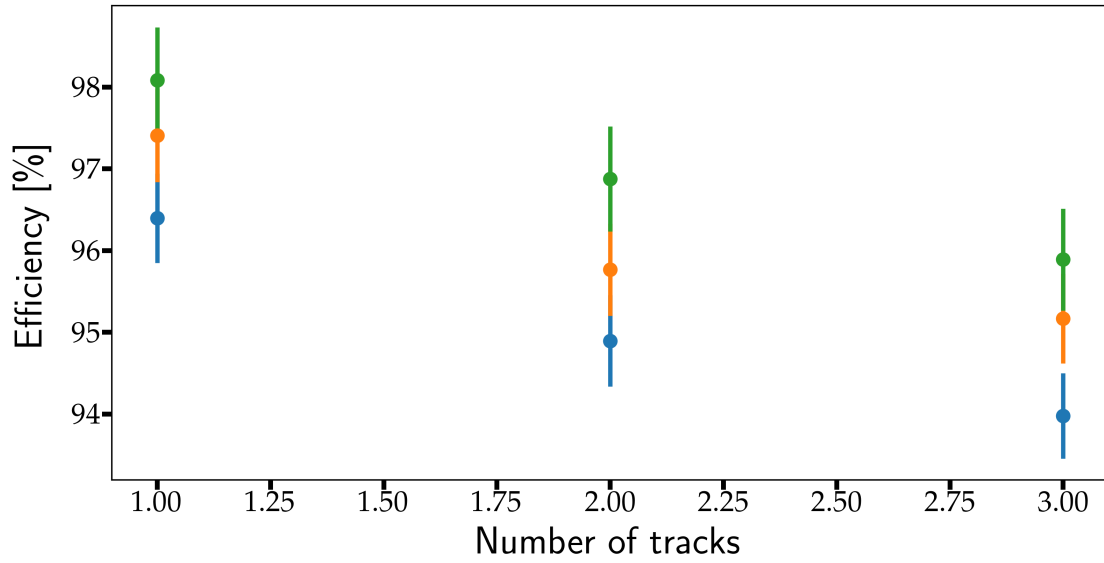


FIGURE A.16: Track reconstruction efficiency for varying $n_{generatedTracks}$ and fixed parameters $\delta\Psi_{max} = 1 \cdot 10^{-5}$, $n_{tmpTriplets} = 15$. Different P_{beam} are shown by different colors: $P_{beam} = 1.5$ GeV (blue), $P_{beam} = 4.06$ GeV (orange), $P_{beam} = 15$ GeV (green).

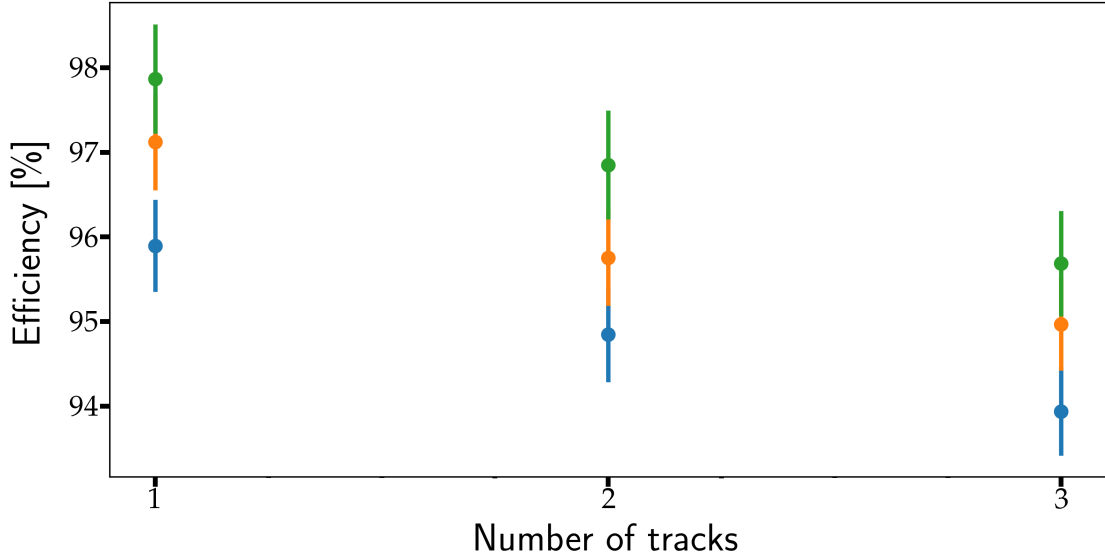


FIGURE A.17: Track reconstruction efficiency for varying $n_{generatedTracks}$ and fixed parameters $\delta\Psi_{max} = 0.5 \cdot 10^{-5}$, $n_{tmpTriplets} = 15$. Different P_{beam} are shown by different colors: $P_{beam} = 1.5 \text{ GeV}$ (blue), $P_{beam} = 4.06 \text{ GeV}$ (orange), $P_{beam} = 15 \text{ GeV}$ (green).

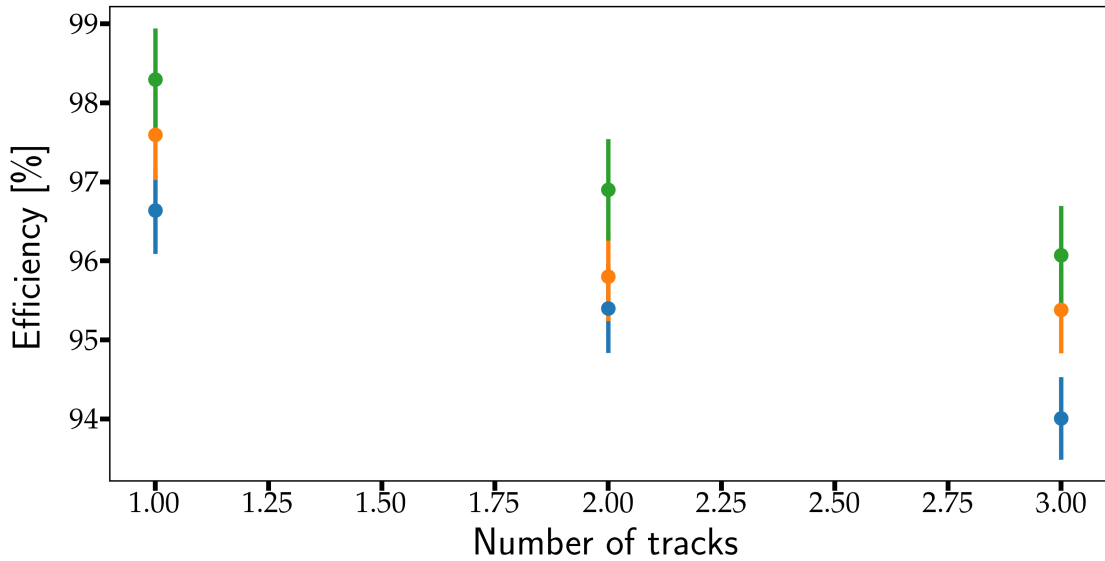


FIGURE A.18: Track reconstruction efficiency for varying $n_{generatedTracks}$ and fixed parameters $\delta\Psi_{max} = 2 \cdot 10^{-5}$, $n_{tmpTriplets} = 15$. Different P_{beam} are shown by different colors: $P_{beam} = 1.5 \text{ GeV}$ (blue), $P_{beam} = 4.06 \text{ GeV}$ (orange), $P_{beam} = 15 \text{ GeV}$ (green).

Stephan Maldaner

Curriculum Vitae

Personal Information

Name Stephan Maldaner
Date of Birth 30 March 1988
Place of Birth Mainz, Germany
Nationality German

Education

2014–2020 **PhD studies in Physics**, *Ruhr Universität Bochum/Helmholtz Institute Mainz, Germany.*
2007–2013 **Diploma in Physics**, *Johannes Gutenberg Universität Mainz, Germany.*
2004–2007 **General qualification for university entrance**, *Technisches Gymnasium - BBS1 Mainz, Germany.*
1998–2004 , *Sebastian-Münster-Gymnasium Ingelheim, Germany.*
1994–1998 **Elementary School**, *Pestalozzischule Ingelheim, Germany.*

Diploma Thesis

Title Algorithmenentwicklung für den topologischen Trigger am ATLAS Detektor
Supervisors Professor Stefan Tapprogge

PhD Thesis

Title Development of an Online Track Finding Algorithm for the $\bar{\text{PANDA}}$ Luminosity Detector and Search for the decay channel $e^+e^- \rightarrow h_c \eta \pi^+ \pi^-$ at the Center of Mass Energy of 4.6 GeV at BESIII
Supervisors Professor Miriam Fritsch